University of Kentucky
UKnowledge

Theses and Dissertations--Mechanical Engineering

Mechanical Engineering

2023

# MECHANICAL ENERGY HARVESTER FOR POWERING RFID SYSTEMS COMPONENTS: MODELING, ANALYSIS, OPTIMIZATION AND DESIGN

Alireza Babaei
*University of Kentucky*, alireza.babaei@uky.edu
Author ORCID Identifier:
https://orcid.org/0000-0002-7803-8418
Digital Object Identifier: https://doi.org/10.13023/etd.2023.036

Right click to open a feedback form in a new tab to let us know how this document benefits you.

## Recommended Citation

Babaei, Alireza, "MECHANICAL ENERGY HARVESTER FOR POWERING RFID SYSTEMS COMPONENTS: MODELING, ANALYSIS, OPTIMIZATION AND DESIGN" (2023). *Theses and Dissertations--Mechanical Engineering*. 208.
https://uknowledge.uky.edu/me_etds/208

This Doctoral Dissertation is brought to you for free and open access by the Mechanical Engineering at UKnowledge. It has been accepted for inclusion in Theses and Dissertations--Mechanical Engineering by an authorized administrator of UKnowledge. For more information, please contact UKnowledge@lsv.uky.edu.

STUDENT AGREEMENT:

I represent that my thesis or dissertation and abstract are my original work. Proper attribution has been given to all outside sources. I understand that I am solely responsible for obtaining any needed copyright permissions. I have obtained needed written permission statement(s) from the owner(s) of each third-party copyrighted matter to be included in my work, allowing electronic distribution (if such use is not permitted by the fair use doctrine) which will be submitted to UKnowledge as Additional File.

I hereby grant to The University of Kentucky and its agents the irrevocable, non-exclusive, and royalty-free license to archive and make accessible my work in whole or in part in all forms of media, now or hereafter known. I agree that the document mentioned above may be made available immediately for worldwide access unless an embargo applies.

I retain all other ownership rights to the copyright of my work. I also retain the right to use in future works (such as articles or books) all or part of my work. I understand that I am free to register the copyright to my work.

REVIEW, APPROVAL AND ACCEPTANCE

The document mentioned above has been reviewed and accepted by the student's advisor, on behalf of the advisory committee, and by the Director of Graduate Studies (DGS), on behalf of the program; we verify that this is the final, approved version of the student's thesis including all changes required by the advisory committee. The undersigned agree to abide by the statements above.

Alireza Babaei, Student

Dr. Johne Parker, Major Professor

Dr. Jesse Hoagg, Director of Graduate Studies

# MECHANICAL ENERGY HARVESTER FOR POWERING RFID SYSTEMS COMPONENTS: MODELING, ANALYSIS, OPTIMIZATION AND DESIGN

DISSERTATION

A dissertation submitted in partial fulfillment of the
requirements for the degree of Doctor of Philosophy in the
College of Engineering
at the University of Kentucky

By
Alireza Babaei
Lexington, Kentucky
Director: Dr. Johné Parker, Associate Professor of Mechanical Engineering
Lexington, Kentucky
2022

Copyright © Alireza Babaei 2022
https://orcid.org/0000-0002-7803-8418

ABSTRACT OF DISSERTATION

MECHANICAL ENERGY HARVESTER FOR POWERING RFID SYSTEMS COMPONENTS: MODELING, ANALYSIS, OPTIMIZATION AND DESIGN

Finding alternative power sources has been an important topic of study worldwide. It is vital to find substitutes for finite fossil fuels. Such substitutes may be termed renewable energy sources and infinite supplies. Such limitless sources are derived from ambient energy like wind energy, solar energy, sea waves energy; on the other hand, smart cities megaprojects have been receiving enormous amounts of funding to transition our lives into smart lives. Smart cities heavily rely on smart devices and electronics, which utilize small amounts of energy to run. Using batteries as the power source for such smart devices imposes environmental and labor cost issues. Moreover, in many cases, smart devices are in hard-to-access places, making accessibility for disposal and replacement difficult. Finally, battery waste harms the environment.

To overcome these issues, vibration-based energy harvesters have been proposed and implemented. Vibration-based energy harvesters convert the dynamic or kinetic energy which is generated due to the motion of an object into electric energy. Energy transduction mechanisms can be delivered based on piezoelectric, electromagnetic, or electrostatic methods; the piezoelectric method is generally preferred to the other methods, particularly if the frequency fluctuations are considerable. In response, piezoelectric vibration-based energy harvesters (PVEHs), have been modeled and analyzed widely. However, there are two challenges with PVEH: the maximum amount of extractable voltage and the effective (operational) frequency bandwidth are often insufficient. In this dissertation, a new type of integrated multiple system comprised of a cantilever and spring-oscillator is proposed to improve and develop the performance of the energy harvester in terms of extractable voltage and effective frequency bandwidth. The new energy harvester model is proposed to supply sufficient energy to power low-power electronic devices like RFID components. Due to the temperature fluctuations, the thermal effect over the performance of the harvester is initially studied. To alter the resonance frequency of the harvester structure, a rotating element system is considered and analyzed. In the analytical-numerical analysis, Hamilton's principle along with Galerkin's decomposition approach are adopted to derive the governing equations of the harvester motion and corresponding electric circuit. It is observed that integration of the spring-oscillator subsystem alters the boundary condition

of the cantilever and subsequently reforms the resulting characteristic equation into a more complicated nonlinear transcendental equation. To find the resonance frequencies, this equation is solved numerically in MATLAB. It is observed that the inertial effects of the oscillator rendered to the cantilever via the restoring force effects of the spring significantly alter vibrational features of the harvester. Finally, the voltage frequency response function is analytically and numerically derived in a closed-from expression. Variations in parameter values enable the designer to mutate resonance frequencies and mode shape functions as desired. This is particularly important, since the generated energy from a PVEH is significant only if the excitation frequency coming from an external source matches the resonance (natural) frequency of the harvester structure. In subsequent sections of this work, the oscillator mass and spring stiffness are considered as the design parameters to maximize the harvestable voltage and effective frequency bandwidth, respectively. For the optimization, a genetic algorithm is adopted to find the optimal values. Since the voltage frequency response function cannot be implemented in a computer algorithm script, a suitable function approximator (regressor) is designed using fuzzy logic and neural networks. The voltage function requires manual assistance to find the resonance frequency and cannot be done automatically using computer algorithms. Specifically, to apply the numerical root-solver, one needs to manually provide the solver with an initial guess. Such an estimation is accomplished using a plot of the characteristic equation along with human visual inference. Thus, the entire process cannot be automated. Moreover, the voltage function encompasses several coefficients making the process computationally expensive. Thus, training a supervised machine learning regressor is essential. The trained regressor using adaptive-neuro-fuzzy-inference-system (ANFIS) is utilized in the genetic optimization procedure. The optimization problem is implemented, first to find the maximum voltage and second to find the maximum widened effective frequency bandwidth, which yields the optimal oscillator mass value along with the optimal spring stiffness value. As there is often no control over the external excitation frequency, it is helpful to design an adaptive energy harvester. This means that, considering a specific given value of the excitation frequency, energy harvester system parameters (oscillator mass and spring stiffness) need to be adjusted so that the resulting natural (resonance) frequency of the system aligns with the given excitation frequency. To do so, the given excitation frequency value is considered as the input and the system parameters are assumed as outputs which are estimated via the neural network fuzzy logic regressor. Finally, an experimental setup is implemented for a simple pure cantilever energy harvester triggered by impact excitations. Unlike the theoretical section, the experimental excitation is considered to be an impact excitation, which is a random process. The rationale for this is that, in the real world, the external source is a random trigger. Harmonic base excitations used in the theoretical chapters are to assess the performance of the energy harvester per standard criteria. To evaluate the performance of a proposed energy harvester model, the input excitation type consists of harmonic base triggers. In summary, this dissertation discusses several case studies and addresses key issues in the design of optimized piezoelectric vibration-based energy harvesters (PVEHs). First, an advanced model of the integrated systems is presented with equation derivations. Second, the proposed model is decomposed and analyzed in terms of mechanical and electrical frequency response functions. To do so, analytic-numeric methods are adopted. Later, influential parameters of the integrated system are detected. Then the proposed model is optimized with respect

to the two vital criteria of maximum amount of extractable voltage and widened effective (operational) frequency bandwidth. Corresponding design (influential) parameters are found using neural network fuzzy logic along with genetic optimization algorithms, i.e., a soft computing method. The accuracy of the trained integrated algorithms is verified using the analytical-numerical closed-form expression of the voltage function. Then, an adaptive piezoelectric vibration-based energy harvester (PVEH) is designed. This final design pertains to the cases where the excitation (driving) frequency is given and constant, so the desired goal is to match the natural frequency of the system with the given driving frequency. In this response, a regressor using neural network fuzzy logic is designed to find the proper design parameters. Finally, the experimental setup is implemented and tested to report the maximum voltage harvested in each test execution.

KEYWORDS: Piezoelectric vibration-based energy harvester (PVEH), harvestable electric voltage, effective (operational) frequency bandwidth, genetic optimization, neural network fuzzy inference system, soft computing algorithms

Alireza Babaei

*(Name of Student)*

11/30/2022

Date

MECHANICAL ENERGY HARVESTER FOR POWERING RFID SYSTEMS COMPONENTS: MODELING, ANALYSIS, OPTIMIZATION AND DESIGN

By
Alireza Babaei

Johné Parker, Ph.D.
Director of Dissertation

Jesse Hoagg, Ph.D.
Director of Graduate Studies

11/30/2022
Date

# DEDICATION

To my beloved parents. A special feeling of gratitude to my loving parents, whose words of persistence, patience, love, emotion, struggle, inspiration, ambition, tenacity, pacify and motivate my mind and my soul. Words cannot express my sincere appreciation to you, mom and dad.

ACKNOWLEDGMENTS

The following dissertation, while an individual work, benefited from the insights and direction of several people. First, my Dissertation Chair, Dr. Johné Parker, whose guidance and mentorship led me throughout this process. In addition, Dr. Johné Parker provided timely, detail-oriented and instructive comments and evaluation at every stage of the dissertation process, allowing me to complete this project on schedule. Next, I wish to thank the complete Dissertation Advisory Committee: Dr. David Herrin, Dr. Peter Perry, and Dr. Peng (Edward) Wang. Each individual provided insights that guided and challenged my thinking, substantially improving the finished product.

In addition to the technical and instrumental assistance above, I received equally important and supportive assistance from my family and friends.

TABLE OF CONTENTS

ACKNOWLEDGMENTS ..... iii

LIST OF TABLES ..... vii

LIST OF FIGURES ..... ix

CHAPTER 1. Introduction ..... 1

1.1 Introduction and Motivation for the Proposed Research ..... 1

1.2 Preliminaries to Energy Harvesting Technology ..... 2

1.3 Preliminaries to RFID Technology ..... 6

1.4 Overview and Goals of the Proposed Research Project ..... 7

1.5 Major Contributions (Problem Statement) of the Proposed Research Project ..... 11

CHAPTER 2. State of the Art (Literature Review) ..... 14

2.1 Background and Preliminaries ..... 14

2.2 Size Competency and Considerations ..... 17

2.3 Material Gradation and Modifications ..... 18

2.4 Temperature Fluctuations Effect Over the Dynamic Response ..... 18

2.5 State of the Art ..... 19

2.6 Energy Harvesting Integrated with IoT ..... 26

CHAPTER 3. Preliminaries to Dynamical Analysis of Beam Elements ..... 37

3.1 Temperature Effects over Oscillatory Response of Beam Elements ..... 37

3.1.1 Kinematic Relations and Kinetics ..... 38

3.1.2 Solution Procedure and Results ..... 42

3.1.3 Conclusion ..... 53

3.2 Higher-Order Shear Effect and Rotation Effect over Oscillatory Response of Beam Elements ..... 55

3.2.1 Navier's Method and Discretizing Procedure ..... 59

3.2.2 Results and Verification ..... 60

3.2.3 Conclusion ..... 63

3.3 Deriving System of Coupled Electromechanical Integral-Partial Differential Equations ..... 64
3.3.1 Analytical-Numerical Solution Approach Based on Modal Decomposition Method ..... 70
3.3.2 Results and Discussion ..... 72

CHAPTER 4. Analytical Numerical Analysis of Oscillator-Spring Subsystem Integration... ..... 78

4.1 Reinforced Piezoelectric Vibration Energy Harvester Using Cantilever-Spring-Oscillator System - Pure Mechanical Analysis ..... 78

4.2 Governing Equations of Motion, Boundary Conditions and Kinematics of Cantilever-Oscillator-Spring ..... 79

4.3 Variational Terms and Extended Hamilton's Principle ..... 80

4.4 Solution Procedure ..... 82
4.4.1 Free Vibrations: Natural Frequency, Mode Shape Functions ..... 82
4.4.2 Forced Vibrations: Harmonic Base Excitations ..... 85

4.5 Results and Discussion ..... 87
4.5.1 New Eigenvalues and Restoring Force of the Spring ..... 88
4.5.2 Effect of Mass and Stiffness Ratios over Natural Frequencies ..... 90
4.5.3 Mechanical Frequency Response of Beam Vibration ..... 95

4.6 Conclusion ..... 98

CHAPTER 5. Optimization of the Energy Harvester ..... 101

5.1 Introduction and Background ..... 101

5.2 Mathematical Modeling ..... 102

5.3 Analytical Solution Approach Based on Galerkin's Modal Decomposition Method… ..... 108

5.4 Results and Discussion ..... 112

5.5 Optimizing the Energy Harvester via Soft Computing Techniques ..... 113
5.5.1 Optimizing the Extractable Voltage Amount at the First Resonance: ..... 118
5.5.2 Optimizing the Effective (Operational) Frequency Bandwidth (EFBW) ..... 164

5.6 Conclusion ..... 196

CHAPTER 6. Adaptive Piezoelectric Vibration-Based Energy Harvester (PVEH) ..... 200

6.1 Introduction and Background to Adaptive PVEH ..... 200

6.2 Training the Fuzzy Inference System for the Adaptive PVEH ..... 203

6.3 Designing the Fuzzy Inference System (FIS) ..... 219

6.4 Conclusion ..... 241

CHAPTER 7. Experimental Setup ..... 243

7.1 Preliminaries of Statistical Data Visualization ..... 243

7.2 Exploratory data analysis ..... 244

7.3 Clustering the dataset. ..... 256

7.4 Conclusion ..... 268

CHAPTER 8. Conclusion ..... 270

8.1 Overview ..... 270

8.2 Improvements in understanding the vibration response of a configuration. ..... 270

8.3 Importance of integrating a sub-system of oscillator-spring to the cantilever ..... 272

8.4 Importance of optimizing the cantilever-oscillator-spring energy harvester ..... 275

8.5 Importance of designing an adaptive PVEH according to a given excitation ..... 278

8.6 Importance of experimental setup to observe the amount of harvestable voltage and energy ..... 279

8.7 Summary of contributions ..... 281

8.8 Future work ..... 282

APPENDICES ..... 285

APPENDIX 1. Technical Parameters and Terminology ..... 285

APPENDIX 2. Dataset ..... 290

REFERENCES ..... 297

VITA ..... 302

LIST OF TABLES

Table 1. Comparison of different frequencies ..... 43

Table 2. Different frequencies for different length ratios ..... 60

Table 3. Geometric and mechanical properties of beam [35] ..... 72

Table 4. Proportional damping values for first three modes of vibration [35] ..... 73

Table 5. Geometrical, and mechanical parameters of the cantilever-oscillator-spring [35] ..... 87

Table 6. First eigenvalue and dimensionless resonant frequency of cantilever-oscillator-spring system ..... 88

Table 7. Second eigenvalue and dimensionless resonant frequency of cantilever-oscillator-spring system ..... 89

Table 8. Third eigenvalue and dimensionless resonant frequency of cantilever-oscillator-spring system ..... 89

Table 9. geometric and mechanical properties of beam [35] ..... 112

Table 10. Proportional damping values for first three modes of vibration [35] ..... 113

Table 11. ANFIS training properties ..... 131

Table 12. Comparison of various built-in membership functions (MFs) ..... 131

Table 13. Evaluation of Gaussian MF, 300 epochs ..... 133

Table 14. Evaluation of Generalized-Bell shaped MF, 300 epochs ..... 135

Table 15. Optimization algorithm properties and information ..... 157

Table 16. Optimization algorithm properties and information ..... 158

Table 17. Evaluation of the proposed optimization algorithm using ‘readfis’ for various values of inputs (design) values ..... 159

Table 18. Numerically-solved eigenvalues by means of VPASOLVE ..... 162

Table 19. Membership function type evaluation for the first resonance ..... 167

Table 20. Membership function type evaluation for the third resonance ..... 168

Table 21. Gaussian membership function number evaluation for first resonance ..... 169

Table 22. Gaussian membership function number evaluation for third resonance ..... 171

Table 23. Optimization algorithm properties and information ..... 191

Table 24. Numerically-solved eigenvalues using VPASOLVE ..... 194

Table 25. Resonance frequency of the cantilever-spring-oscillator system found analytically ($rm = 1$) ..... 204

Table 26. Resonance frequency of the cantilever-spring-oscillator system found analytically ($rs = 0.1$) ..... 206

Table 27. Disparate types of built-in membership functions (MFs) ..... 209
Table 28. Triangular MF evaluation with respect to RMSE..... 210
Table 29. Trapezoidal MF evaluation with respect to RMSE ..... 210
Table 30. GeneralizedBell shaped (G-bell) MF evaluation with respect to RMSE..... 211
Table 31. Gaussian MF evaluation with respect to RMSE..... 211
Table 32. Gaussian2 (double Gaussian) MF evaluation with respect to RMSE..... 212
Table 33. Polynomial MF evaluation with respect to RMSE ..... 213
Table 34. Double sigmoid MF evaluation with respect to RMSE..... 213
Table 35. Polynomial-sigmoid MF evaluation with respect to RMSE..... 214
Table 36. Generalized-Bell shaped (G-bell) MF evaluation with respect to RMSE ..... 215
Table 37. Triangular MF evaluation with respect to RMSE..... 215
Table 38. Trapezoidal MF evaluation with respect to RMSE ..... 216
Table 39. Gaussian MF evaluation with respect to RMSE..... 216
Table 40. Gaussian2 (double Gaussian) MF evaluation with respect to RMSE..... 217
Table 41. Polynomial MF evaluation with respect to RMSE ..... 217
Table 42. Double sigmoid MF evaluation with respect to RMSE..... 218
Table 43. Polynomial MF evaluation with respect to RMSE ..... 218
Table 44. Desired excitation (driving) frequency and corresponding design parameters ..... 236
Table 45. Eigenvalues solved numerically via VPASOLVE..... 238
Table 46. Angular and linear frequencies found via closed-form expression ..... 239
Table 47. Box plot summary of information ..... 251
Table 48. Box plot summary for the electric power generated from the PVEH in experimental setup. ..... 256
Table 49. Harvested voltage by oscillator-spring sub-system integration. ..... 274
Table 50. Estimated values of the resonance frequency using ANFIS..... 279
Table 51 Harvested power by oscillator-spring integration..... 280

LIST OF FIGURES

Figure 1. Energy harvesting flowchart ..... 4
Figure 2. Distributed parameter (cantilever) energy harvester ..... 24
Figure 3. Internet of Things (IoT) principal components ..... 27
Figure 4. IoT principal components (2nd outlook) ..... 28
Figure 5. Layers of IoT ..... 28
Figure 6. IoT applications in technologies ..... 29
Figure 7 . IoT and smart city ..... 32
Figure 8. IoT and security issues ..... 34
Figure 9. Schematic of a simply-supported beam ..... 39
Figure 10. Variation of fundamental frequency with temperature ..... 45
Figure 11. Variation of fundamental frequency with rotation factor ..... 46
Figure 12. Frequency response function of a system under thermal stress and rotation effects ..... 47
Figure 13. Static deflection ratio with respect to temperature ..... 48
Figure 14. Dynamic deflection ratio with respect to excitation frequency and temperature ..... 50
Figure 15. Dynamic deflection ratio with respect to excitation frequency and rotation factor ..... 51
Figure 16. Steady-state time response with respect to rotation factor ..... 52
Figure 17. Steady-state time response with respect to temperature ..... 53
Figure 18. Comparison between EBBT and RLBT for different values of slenderness ratio ..... 61
Figure 19. Impression of coupled rotation over fundamental frequency for thin and thick RLBT beams ..... 62
Figure 20. Frequency shift based on rotation effects for thin and thick RLBT beams ..... 63
Figure 21. Cantilever beam with piezoelectric layers at the top and bottom ..... 65
Figure 22. Verification of current results ..... 74
Figure 23. Voltage frequency response function (V-FRF) ..... 75
Figure 24. Shunted vibration frequency response function (Wrel-FRF) ..... 76
Figure 25. Schematic of cantilever-oscillator-spring system ..... 80
Figure 26. Characteristic equations' graphs for different values of mass ratio and stiffness ratio ..... 84

Figure 27. Variations of dimensionless frequencies versus mass ratio with soft spring (r_s=0.01; a. first mode, b. second mode, c. third mode) ..... 91

Figure 28. Variations of dimensionless frequencies versus mass ratio with stiff spring (r_s=100; a. first mode, b. second mode, c. third mode) ..... 92

Figure 29. Variations of dimensionless frequencies versus stiffness ratio with light oscillator ($rm$=0.01; a. first mode, b. second mode, c. third mode) ..... 93

Figure 30. Variations of dimensionless frequencies versus stiffness ratio with heavy oscillator ($rm$ =10; a. first mode, b. second mode, c. third mode) ..... 94

Figure 31. Mode shape functions of reference system and extreme cases of mass and stiffness ratios (a. mode one; b. mode two; c. mode three) ..... 95

Figure 32. Relative tip motion FRF versus dimensionless excitation frequency (reference system and extreme cases of mass and stiffness ratios)..... 96

Figure 33. Schematic of the cantilever-spring-mass energy harvester ..... 103

Figure 34. Tuned PVEH perspective ..... 116

Figure 35. FIS schematic structure ..... 123

Figure 36. Fuzzy inference structure to make the aggregated output. ..... 124

Figure 37. FIS editors and viewers in MATLAB ..... 125

Figure 38. Schematic of the 5 layers in ANFIS ..... 127

Figure 39. Voltage frequency response function with respect to excitation frequency (constant mass ratio) ..... 128

Figure 40. Neuro Fuzzy designer..... 130

Figure 41. RMSE with respect to the Gaussian fuzzy rule numbers ..... 134

Figure 42. RMSE with respect to the Gaussian fuzzy membership function numbers .. 135

Figure 43. RMSE with respect to the Generalized-Bell shaped fuzzy rule numbers ..... 136

Figure 44. RMSE with respect to the Generalized-Bell shaped fuzzy membership function numbers ..... 137

Figure 45. Fuzzy logic designer application setting ..... 138

Figure 46. Fuzzy logic membership function editor – first input ..... 139

Figure 47. Fuzzy logic designer application setting – second input ..... 140

Figure 48. Fuzzy logic rule viewer ..... 141

Figure 49. Fuzzy inference verbose rule editor ..... 142

Figure 50. Fuzzy inference symbolic rule editor ..... 143

Figure 51. Fuzzy inference indexed rule editor ..... 144

Figure 52. Fuzzy inference surface viewer..... 145

Figure 53. Fuzzy logic designer application setting ..... 146

Figure 54. Fuzzy logic membership function editor – first input ..... 147
Figure 55. Fuzzy logic membership function editor – second input..... 148
Figure 56. Fuzzy inference verbose rule editor ..... 149
Figure 57. Fuzzy inference symbolic rule editor ..... 150
Figure 58. Fuzzy inference indexed rule editor ..... 151
Figure 59. Fuzzy logic rule viewer ..... 152
Figure 60. Fuzzy inference surface viewer ..... 153
Figure 61. Objective function (resonance voltage) optimizing track – Gaussian FIS .... 156
Figure 62. Objective function (resonance voltage) optimizing track – Generalized-Bell FIS ..... 158
Figure 63. Plotting the characteristic equation at the vicinity of the first eigenvalue .... 160
Figure 64. Plotting the characteristic equation at the vicinity of the second eigenvalue 161
Figure 65. Plotting the characteristic equation at the vicinity of the third eigenvalue ... 161
Figure 66. Voltage frequency response function (FRF) ..... 162
Figure 67. Voltage frequency response function (FRF) ..... 163
Figure 68. RMSE with respect to the Gaussian fuzzy rule numbers ..... 170
Figure 69. RMSE with respect to the Gaussian fuzzy MF numbers..... 171
Figure 70. RMSE with respect to the Gaussian fuzzy rule numbers ..... 172
Figure 71. RMSE with respect to the Gaussian fuzzy MF numbers..... 173
Figure 72. Fuzzy logic designer application setting ..... 174
Figure 73. Fuzzy logic membership function editor – first input ..... 175
Figure 74. Fuzzy logic membership function editor – second input..... 176
Figure 75. Fuzzy logic verbose rule viewer..... 177
Figure 76. Fuzzy inference symbolic rule editor ..... 178
Figure 77. Fuzzy inference indexed rule editor ..... 179
Figure 78. Fuzzy inference rule viewer ..... 180
Figure 79. Fuzzy inference surface viewer ..... 181
Figure 80. Fuzzy logic designer application setting – third resonance..... 182
Figure 81. Fuzzy logic membership function editor – third resonance ..... 183
Figure 82. Fuzzy logic membership function editor – third resonance ..... 184
Figure 83. Fuzzy inference verbose rule editor ..... 185
Figure 84. Fuzzy inference indexed rule editor ..... 186
Figure 85. Fuzzy inference symbolic rule editor ..... 187

Figure 86. Fuzzy inference rule viewer ..... 188
Figure 87. Fuzzy inference surface viewer ..... 189
Figure 88. Objective function (operational frequency bandwidth) optimizing track ..... 190
Figure 89. Plotting the characteristic equation at the vicinity of the first eigenvalue .... 193
Figure 90. Plotting the characteristic equation at the vicinity of the second eigenvalue 193
Figure 91. Plotting the characteristic equation at the vicinity of the third eigenvalue ... 194
Figure 92. Voltage frequency response function (FRF) ..... 195
Figure 93. ANFIS toolbox chart in MATLAB ..... 203
Figure 94. Analytical-numerical voltage FRF procedure ..... 207
Figure 95. Fuzzy logic designer application setting ..... 220
Figure 96. Fuzzy logic membership function editor ..... 221
Figure 97. Fuzzy inference rule viewer ..... 222
Figure 98. Fuzzy inference verbose rule viewer ..... 223
Figure 99. Fuzzy inference symbolic rule viewer ..... 224
Figure 100. Fuzzy inference indexed rule viewer ..... 225
Figure 101. Fuzzy inference surface viewer ..... 226
Figure 102. Fuzzy logic designer application setting ..... 227
Figure 103. Fuzzy logic membership function editor ..... 228
Figure 104. Fuzzy logic rule viewer ..... 229
Figure 105. Fuzzy inference verbose rule editor ..... 230
Figure 106. Fuzzy inference symbolic rule editor ..... 231
Figure 107. Fuzzy inference indexed rule editor ..... 232
Figure 108. Fuzzy inference surface viewer ..... 233
Figure 109. ANFIS model structure ..... 234
Figure 110. Schematic of constant spring stiffness and varying oscillator mass ..... 235
Figure 111. Schematic of constant oscillator mass and spring stiffness ..... 236
Figure 112. First eigenvalue around the desired frequencies ..... 238
Figure 113. Voltage frequency Response function (FRF) ..... 240
Figure 114. Experimental setup of the piezoelectric energy harvester ..... 245
Figure 115. Harvested AC voltage with respect to the experiment iteration ..... 246
Figure 116. Scatter plot of impact-driven excitation ..... 247
Figure 117. Box plot features ..... 248
Figure 118. Box plot for the experiment iteration ..... 249

Figure 119. Box plot for the harvested voltage ..... 250
Figure 120. Box plot highlights ..... 251
Figure 121. Histogram of the impact-driven experiment dataset ..... 253
Figure 122. Scatter-Histogram of the impact-driven experiment dataset ..... 254
Figure 123. Scatter-Histogram of the impact-driven experiment dataset in parent container ..... 255
Figure 124. C-Means clustering objective function improvement. ..... 259
Figure 125 experimental data clusters ..... 260
Figure 126 Fuzzy logic designer for C-Means clustering ..... 261
Figure 127 Fuzzy membership function editor for C-Means clustering ..... 261
Figure 128 Rule editor for fuzzy C-Means clustering ..... 262
Figure 129 Rule viewer in fuzzy C-Means clustering ..... 263
Figure 130 Exponent of fuzzy partition matrix effect over overlap in clusters ..... 264
Figure 131 Fuzzy logic designer for subtractive clustering ..... 265
Figure 132 Fuzzy membership function editor for subtractive clustering ..... 266
Figure 133 Rule editor for fuzzy subtractive clustering ..... 267
Figure 134 Rule viewer for subtractive fuzzy clustering ..... 268

# CHAPTER 1. INTRODUCTION

## 1.1 Introduction and Motivation for the Proposed Research

The primary motivation of this dissertation is to investigate energy harvesting modules for low-power electronics such as RFID systems. One of the driving forces behind the research for novel energy harvesting modules is the ubiquitous demand for energy sources to power devices ranging from small-scaled (micro-electro-mechanical-systems) MEMS devices (sensors, actuators, accelerometers, resonators, etc.), wearable electronics, wireless sensor networks (WSNs), and internet of thing devices (IOT) to large-scale applications in industrial sectors. Many RFID components associated with the Internet of Things (IoT) generally require power on the order of a few watts. Considering the fact that RFID tags and associated sensors mostly require small amounts of energy, it is timely to find reliable alternative power sources. One such source is the vibration-based energy harvester. In an RFID system, several components usually need very small amounts of energy to operate. Replacing the conventional power sources with an energy harvester module provides the required energy for such components. This also results in financial benefits. Furthermore, there may be a reduced need for regular maintenance as the mentioned energy harvester module has a long lifespan. Such strengths are great benefits for numerous RFID-based applications. In other words, it is of high interest to devise a free vibration energy harvester to augment the power requirements of RFID components due to economic benefits. As the last incentive and impetus, coincidence and overlapping of excitation frequency with the system's resonant frequency is a challenge with current energy harvesters which requires in-depth and profound investigation in terms of effective frequency bandwidth, modal and vibrational feature analysis. In other words, frequency

widening is another important stimulus to adapt (adjust) the harvesting system with the excitation frequency available in the background. Thus, this dissertation aims to investigate and improve the efficacy of piezoelectric vibration energy harvesters, to augment the energy requirements of a RFID fixture, yielding a more reliable system, less energy usage from non-renewable sources and more efficient developed RFID fixtures in several sectors.

## 1.2 Preliminaries to Energy Harvesting Technology

Energy harvesting, also called power harvesting, energy scavenging, energy harnessing, or ambient power, mainly pertains to the process by which energy is obtained from external sources such as wind energy, thermal energy, solar power and kinetic or mechanical energy. Such energy can be harnessed for small-sized, low-powered autonomous devices. The historical roots of energy harvesting date back to the waterwheel and windmill. Scavenging energy from available sources has been an everlasting challenge for human beings. The evolutionary path of this technology has enabled us to potentially power sensor networks and mobile devices. Powering such devices enables us to eliminate batteries from the target fixtures or platforms. Another distinct application of energy harvesting lies in the field of climate change and global warming. Harnessed energy can also be implemented to power small-sized autonomous sensors such as those developed using micro-electro-mechanical and nano-electro-mechanical systems (MEMS, and NEMS) technology. Although MEMS and NEMS elements require a small amount of energy, their operation and performance is limited to battery lifespan. A harvested energy source could lead to a much longer lifespan. Energy harvesting devices converting free,

clean, and available ambient energy into electrical energy have attracted significant interest in commercial, industrial, and medical sectors. Most majority of harvesting systems are established based on the concept of converting ubiquitous mechanical motion into electricity useable in several disparate applications. A main source for energy is often vibrational-mechanical energy; however, electromagnetic energy, thermal energy, sound energy, and light energy are all available as energy resources. Generally, captured energy is stored in battery, capacitor, or super capacitor. Battery is a proper fit for long-term usage and super-capacitor for short-term applications. Less energy is dissipated with a battery and it is suitable for devices requiring steady energy flow. A capacitor is a good choice, if an application necessitates huge energy spikes. Super capacitors have virtually unlimited charge-discharge cycles, so it can perform efficiently for an extended period of time. Such feature of super capacitor provides a maintenance-free operation with internet of things (IoT), wireless sensor network (WSN) devices, and RFID systems' components [1]. In the following section there are some examples of energy harvesting in different approaches [2]:

- Some wristwatches (also called automatic watches) are powered by kinetic energy derived from arm and hand locomotion.
- Micro wind turbines scavenge wind energy and put out the supply for WSNs.
- Piezoelectric fibers (crystals) generate small amount of electrical voltage as they are mechanically deformed.

Electrostatic and piezoelectric techniques are often common and well-accepted regarding mechanical and vibration-based energy harvesting systems. In electrostatic energy harvesters, a variable capacitor modulates a change in capacitance to either increase

voltage or electric charge. Based on the principles of electrostatics, such variations including mechanical mobility can be converted into electricity. However, electromagnetic approach may be impractical or ill-advised under certain circumstances. The piezoelectric approach is a well-accepted and widely used method among researchers and industrial sectors. In the scope of this research, a key focus is to better understanding and improving piezoelectric energy harvesting technology [3].

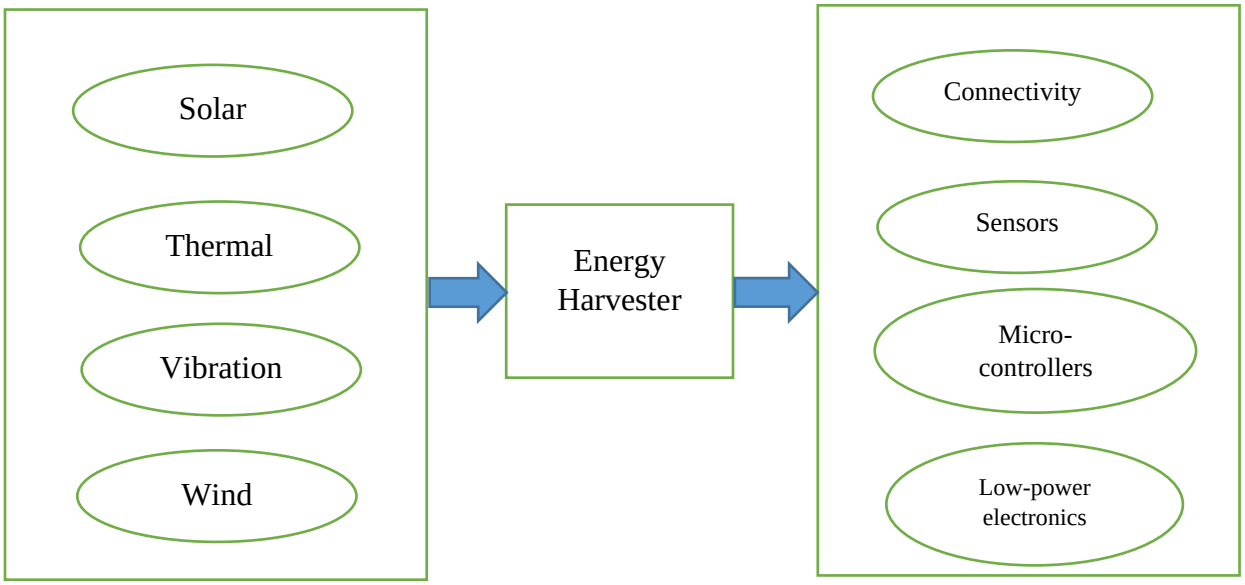


Figure 1. Energy harvesting flowchart

Figure 1 demonstrates the above-mentioned energy harvesting methods, with a schematic process view ranging from energy sources up to applications. Piezoelectricity is the electric charge accumulating in certain types of materials in response to applied mechanical stress. Materials with this specific trait include certain ceramics, crystals, humans bone, DNA and various protein. Piezoelectricity was discovered by French physicists Jacques and Pierre Curie [1].

An applied force to an element of a material equipped with piezoelectric materials can generate electrical voltage. It is assumed that the element is connected to the electrical circuit with a resistance through the electrodes. Perfect bonding of electrodes to the element surfaces at the top and bottom creates a uniform electric field. A linear electromechanical interaction between the mechanical and electrical states in crystalline materials leads to the piezoelectric effect. The piezoelectric effect is a reversible process conveying that materials exhibiting the piezoelectric effect demonstrate reverse piezoelectric field as well. The piezoelectric effect pertains to the internal electrical charge due to applied mechanical force(s); respectively, reverse piezoelectric effect refers to the internal mechanical strain generation due to applied electrical field. Such inverse feature of piezoelectric materials is utilizable in ultrasonic sound wave production [2]. In addition to applications tied to energy harvesting, piezoelectricity is also exploited in several further applications such as: sound production and detection, piezoelectric inkjet printing, generation of high voltages, electronic frequency generation, microbalances, driving ultrasonic nozzles, and ultrafine focusing of optical assemblies. During World War I, the first practical application of piezoelectric materials was accomplished by Paul Langevin in France. He would utilize these phenomena for sonar applications. After this successful implementation of piezoelectricity, during World War II and afterwards, researchers in United States, Russia and Japan devoted significant effort to study and apply piezoelectricity for several applications [2]. In a piezoelectric Material, the atoms distribution and electric charge distribution are unique. It means that atoms distribution is not symmetric. So, positive and negative charge distribution exist in the unit cell. In static equilibrium such dipoles cancel each other out. But if the unit is stretched, the dipoles no

longer cancel each other out and positive and negative charges emerge on opposite sides of the crystal. Opposite charges can be directed through the electrical circuit which generates electricity.

### 1.3 Preliminaries to RFID Technology

Radio frequency identification system (RFID) is a suite of technologies with significant versatility and simplicity. RFID technologies can be adopted in a wide range of applications such as industrial, system monitoring, biomedical applications, etc. [4].

The advent of RFID technology seeks its roots in World War II. Léon Theremin, a scientist from the Soviet Union devised a covert listening device capable of being powered by means of radio waves. This listening device was essentially a long-range passive RFID tag [5]. In the 1940's, the Allies were developing a similar ID device for tracking applications of incoming airplanes. The Scottish physicist Sir Robert Alexander Watson-Watt invented an active tracking system named identify friend or foe (IFF). Subsequently, airplanes were equipped with radio transmitter which would respond back to the signal broad-casted by the radar stations at the ground [6]. After such inspiring research-based efforts, several improvements have arisen to develop tracking systems for several applications ranging in different industries. The prominent superiority of RFID systems pertains to the fact that RFID systems do not require a line of sight to access the targeted information [7]. A tag with the bar code printed on the back is shown in Figure 1. There are numerous practical applications for RFID currently and the list continues to grow. An example list of companies integrating RFID as an essential component of operations is given in [8]. There is an ever-growing rate of research projects and journal publications in

the field of RFID technology. Such RFID systems have several advantages over conventional tracking methods (printed ID), making RFID very attractive from both manufacturing and research aspects. Several industries deploy RFID technology to minimize operational costs [9]. After such inspiring research-based efforts, several improvements have arisen to develop tracking systems for several applications ranging in different industries. The prominent superiority of RFID systems pertains to the fact that RFID systems do not require a line of sight to access the targeted information [7]. A tag with the bar code printed on the back is shown in Figure 1. One of the practical applications of such RFID tags systems may lay in the example of finding out if a specific object or goods is out of stock or not. Walmart is one of the biggest retail companies which utilizes RFID and integration technologies [8]. There is an ever-growing rate of research projects and journal publications in the field of RFID technology. Such RFID systems have several advantages over conventional tracking methods (printed ID), making RFID very attractive from both manufacturing and research aspects. Several industries deploy RFID technology to minimize operational costs [9].

### 1.4 Overview and Goals of the Proposed Research Project

Based on the information provided in the motivation section, it is worth to establish effort in the frame of academic research to propose and devise more efficient, improved, and developed energy harvester systems applicable and integrable with targeted tag RFID systems and internet of things (IOTs). Upon successful modeling, analysis, optimization, and design; it is expected that research results will suggest a framework to power selected RFID components using efficient piezoelectric vibration-based energy harvester (PVEH)

and save energy consequently. Moreover, it was remarked that energy harvesters have challenges and potential drawbacks. Such systems need to be efficient enough to produce and generate acceptable amounts of energy, and to keep an admissible lifespan simultaneously. For example, energy harvester systems used with RFID might be expected to experience temperature fluctuations. Operation of antenna during reading process and backscattering leads to temperature shifts. To get a precise prediction and estimation of temperature effects on harvester performance (i.e., the amount of harvestable power and the frequency bandwidth), temperature effects will be perused theoretically and modeled via energy and variational approaches. From longevity viewpoint, energy harvesters could be anticipated to face severe and harsh excitations. Regardless of controlled harmonic (deterministic), impact-driven, or random and stochastic motivations as the inputs to the harvester system; large-amplitude mechanical forces would mostly end up in desirable and bigger electrical energies. However, two main obstacles exist for severe and large-amplitude mechanical forcing conditions: natural restriction with the exciting force (input excitation), and durability and harvester's failure problem. Natural restriction points to the fact that excitation source is limited and cannot be intensified at any level. Durability deals with the fact that any mechanical system has a specific and bounded lifespan. Based on the concepts in strength of materials and machine component design; force magnitude and load cycles expedite rupture and failure. As a result, extracting more energy and lifespan of the harvester are in inverse (contrary) relationship. In other words, extracting more electrical energy usually leads to less durability and lifespan of the device. Another issue alludes to the fact that, if the excitation frequency from the external source (operator) is not at close vicinity of the resonant frequency of the energy harvester beam, an

insignificant amount of energy will be generated. This is known as tuning and effective frequency bandwidth issues which is a drawback with conventional energy harvesters. Conventional energy harvesters simply consist of a beam and tuning mass (oscillator) welded to the tip end of the beam. To compensate and obviate tuning and frequency bandwidth issues, in this research a new theoretical modeling is presented which consists of the oscillator held and hung by the beam using an elastic support like a spring rather than using welding. In other words, the new modeling encompasses system integration of oscillator-spring to the cantilever beam. As a result of such novel modeling design of cantilever joined with elastically restrained oscillator, the spring restoring forces will generate a new vibration mode much smaller than the first mode of conventional systems, increase the degrees of freedom and the degree of generalized modal coordinates. The newly generated minimal vibration mode is between the fundamental resonance of the conventional system and zero. Such manipulation will significantly widen the effective frequency bandwidth and overcome the prevalent issue. Furthermore, the new model of cantilever-spring-oscillator system will overcome the inefficient amount of generated energy as for a given frequency bandwidth, one further vibration mode is being augmented in a given bandwidth which generates another maximum value of electric voltage (and power). So, the novel cantilever-spring-oscillator model enhances the piezoelectric vibration-based energy harvesters' efficacy both in terms of the amount of power and effective (operational) frequency bandwidth. Moreover, such a system demonstrates great adapting capability meaning that based on the input excitations coming from an external source, the PVEH can be adjusted to match the external driving (excitation) frequency by taking decent oscillator mass or spring stiffness values. Such an adaptive PVEH is

particularly helpful in cases where the external source cannot be modified, and the energy harvester's substrate needs to compensate. Besides the mentioned theoretical modeling, experimental setup is implemented for the conventional model of cantilever to gather the maximum amount of harvested voltage for disparate values of beam length. The experiment is implemented with random impact-driven impulse inputs to conduct the randomness of the generated power. Thus, the experiment setup only consists of a simple cantilever and does not have the oscillator and the tuning mass. Eventually, models considering thermal stress, and spring-oscillator system integration are proposed to improve the piezoelectric vibration-based energy harvesters from theoretical perspectives, while the experimentation is to be implemented with impact-driven stochastic input excitations.

Fundamental research problems in the modeling-analysis section of the research consist of: effects of temperature gradients, adjustable and elastically-mounted inertial effects of oscillator (dynamic magnifier), spring restoring force effect; upon electromechanical response of energy harvesters mountable to targeted tag RFID fixture. In the next step, the proposed model is optimized with respect to the adjustable design parameters to optimize and maximize the: amount of extractable electric energy and effective frequency bandwidth. Moreover, as for the natural frequency of the system to match the excitation frequency, the adjustable parameters are found to the particular values. The primary purpose of the current project can be extended to further industrial applications wherever energy sources are required for internet of things (IOTs), wireless sensor networks (WSNs), and radio frequency identification systems (RFID). The primary goals are summarized as follows:

- Reinforced and enhanced extractable energy from modeling.
- Widened effective frequency bandwidth from modeling.
- Optimized system with optimal characteristics using soft computing techniques.
- Studied the randomness of the impact-driven experimentation.

## 1.5 Major Contributions (Problem Statement) of the Proposed Research Project

In this research project, first, modeling of temperature effects is elaborated. Since, almost all of mechanical devices operating solely or in interaction with electrical, civil, chemical, or computer components; they face temperature shits, so it is imperative to study thermal effects over systems response from mechanical (vibrational-dynamical) and electrical viewpoints. Correspondingly, creating a decent temperature-dependent model of the electromechanical energy harvester is of concern. It is good to note that such a model addressing thermal effects can be extended and applied in further harvesting devices as long as accounting the corresponding governing equations integrated. In addition to temperature effects, it was implied that the challenge of matching the excitation frequency and the harvester's resonant frequency should be addressed to harness more energy, widen the effective frequency bandwidth, and soothing the harsh oscillations resulted from the oscillator's inertia. In this response, energy harvester models undergoing restoring spring forces originating from the elastic support, and dynamic magnifier's (oscillator) inertial effects are studied as well. In each of the mentioned case studies, governing coupled electro-mechanical dynamic-vibration equations are to be obtained and proper solution procedures including: Galerkin's based modal decomposition analysis, analytical-

numerical approaches along with soft computing algorithms will be adopted. Adaptive-neuro Fuzzy inference system (ANFIS) which takes the benefits of both fuzzy logic and neural network will be utilized to approximate the nonlinear model and then genetic optimization algorithm will find the optimal values of the oscillator mass and the spring stiffness. With such adjustable parameters, it is expected to develop and improve the efficiency and performance of the piezoelectric vibration-based energy harvesters. Such improvements and modifications refer to: reinforcing and maximizing the extractable amount of electric voltage, and to widening the effective (operational) frequency bandwidth. The mentioned improvement is rendered using the soft computing technique. In short, impact of: sudden temperature fluctuations, and elastically-attached dynamic magnifier will be theoretically addressed with focus on extractable electrical power, tip displacement and maximum vibration amplitudes of the harvester module, and effective frequency bandwidth widening. Graphical demonstrations of the mechanical and electrical frequency response functions (FRFs) will be provided to better and accurately understand the influential factors, and optimize such factors for the desired reinforced extractable energy along with widened bandwidth. Besides optimization, sub-system parameters (oscillator mass and spring stiffness values) will be designed to reach the specific excitation frequency and design a customized energy harvester. In the next step, experimental implementation will be set up with impact-driven random inputs for the purpose of studying the variance and dispersion of the generated voltage. Expected major contributions are summarized as follows:

- Modeling temperature effects via energy and variational concepts
- Studying thermal effects over harvester's electro-mechanical response

- Modeling elastically restrained dynamic magnifier (cantilever-spring-oscillator)
- Studying spring restoring forces effects over: extractable power, and operational frequency bandwidth
- Studying oscillator mass effects over: extractable power, frequency bandwidth
- Optimizing the PVEH using soft computing techniques and finding the optimal design parameters (oscillator mass and spring constant)
- Designing a well-tuned fuzzy inference system (FIS) as a regressor model via neural networks
- Developing a proper genetic optimization algorithm using the designed regressor
- Adjusting the PVEH according to the given excitation (driving) frequency of the external source
- Running experimentation to record the maximum extractable voltage in a conventional energy harvester (cantilever)

# CHAPTER 2. STATE OF THE ART (LITERATURE REVIEW)

## 2.1 Background and Preliminaries

In this section, literature review regarding vibration-based (mechanical) energy harvesting via different transduction mechanisms including piezoelectric materials is presented. Vibration-based energy harvesting from ambient indefinite sources has gained remarkable attention among researchers, research-based institutes, research and development (R&D) sectors of several industries and corporations all around the world. Vibration-based energy scavenging is almost anywhere since the whole universe, creatures, human bodies, and machines are all in motion. The evolution of harvesting devices covers several areas, mostly including mechanical aspects along with some modifications to the electrical aspect. Vibration energy is prevalent not only in the environment due to wind, and fluid flow; but also, in operational conditions wherever rotating, or any other type of machinery is in progress. Conversion of dynamic motion into electrical energy via piezoelectricity effect is often called piezoelectric energy harvesting. Contrary to the thermal and solar energy harvesting approaches that can generate hundreds of watts; small-size piezoelectric vibration energy harvesting method mostly can generate only microwatts or even milli-watts. The good thing with piezoelectric energy harvesting is due to general improvement in technology, there are several electronics requiring low-level energy. In other words, new generations of electronic devices are operational with low power sources. On the other hand, piezoelectric vibration-based energy harvesters are mostly smaller than wind energy harvesters in the shape of wind turbine or solar panels. Such compactness in size means less cost of manufacturing, easy setup, and simple replacement. A further positive point is the fact that they are functional regardless of

atmospheric condition, which is a big drawback for solar panels and wind turbines. With all this in mind, it seems reasonable why worldwide annual revenue of piezoelectric devices has increased from $22 billion in 2012 to $37 billion in 2017 [10]. Examples in which vibration-based piezoelectric energy harvesting can be deployed include civil infrastructures such as bridges and buildings, human body, and aerospace systems ([11], [12], [13], [14], [15], [16]). Converting vibratory energy into electrical energy via piezoelectric phenomena has advantages over other transduction mechanisms such as magnestrictive, electrostatic, triboelectric, and electromagnetic converters, since piezoelectric approach include factors like: inherent transduction capacity, the preservation of efficiency, higher power density, and capacity to function in high frequency applications [17], [18], [19]. Most of the mentioned points are derived since the scale in the system is reduced to smaller orders. In order to harness dynamic motion and energy via the harvester element, piezoelectric harvester is to be attached to the host system. Then, the mentioned interface can be set up in several approaches considering design constraints and system characteristics imposed to the harvester device. Given the fact that most piezoelectric harvesting systems operate at the microwatt to milliwatt scale, the most common application of piezoelectric energy harvesting is to provide energy for low-power electronics including embedded electronics, implantable biomedical devices, wireless sensor nodes (WSNs), internet of things (IoT), and portable and wearable electronics as well as RFID components. Piezoelectric energy harvesting systems can provide a permanent, autonomous power source that does not need replacement or maintenance. Compared to traditional energy sources, like batteries, autonomous operation can reduce costs associated with battery replacement and labor expenses. Furthermore,

autonomous power supplies allow electronic devices to be embedded into structures or placed in remote locations. With recent growth in low-power electronics (e.g., wireless sensors, microelectronics), piezoelectric energy harvesting has drawn significant attention in the research community over the past decade. From a material viewpoint, several piezoelectric material structures have been improved and a diverse range of such materials is presented. Amongst the most prevalent piezoelectric material is the perovskite lead zirconate titanate, which is known as PZT that is stupefied with lanthanum or niobium to form hard or soft materials, respectively. Moreover, piezoelectric ceramics (piezo-ceramics) have been widely used in sensors and actuators due to their direct coupling which enables operation without bias voltages, and their ability to output large voltages on the order of 50 V to 100 V.

Table 1 is presented to refer to typical research efforts carried out in the field of windmill-type energy harvesters which are all modeled as beam elements as mechanical elements. It is good to mention that most of such energy harvester devices are made up of PZT as the base material type [10].

As mentioned in the above sections, piezoelectric vibration-based energy harvesting systems perform based on the mechanical motions. Such motions mostly exhibit in the form of oscillations and vibrations. In mechanical engineering, vibrations pertain to phenomena whereby oscillations take place around the equilibrium points, resulting in unbalanced systems from dynamical viewpoint. Vibration can be desired, such as the case pertinent to musical instruments, cone of loudspeakers, or even in mobile phones. However, vibration can be pernicious and unwanted; especially in electric motors, mechanical engines, rotating and non-rotating machinery. Such vibrations usually lead to waste of significant amount of energy and even failure and rupture of the electrical or

mechanical element. Vibration in industrial category usually is the resultant of imbalances, misalignments, uneven friction, or meshing of the gear teeth in gear boxes in coupling with each other. It was implicitly mentioned that devising harvesting systems helps us to take advantage of such dynamic vibratory motions. Such harvesting systems are supposed to take advantage of the unwanted vibrations and convert them to electrical energy. In order to improve performance of current energy harvesters, in-depth understanding of mechanical vibrational-dynamical analysis of such systems is essential, otherwise the amount of generated energy is insignificant. This means that reaching goals such as increasing maximum power or voltage extractable as well as an environmentally robust and durable system; vibration, modal and dynamic analysis of systems should be perused in detail. In this regard, concise literature review is presented. One of the most efficient mechanical elements with attractive mode shape functions is beams.

## 2.2 Size Competency and Considerations

As the size and dimension of the system is scaled down, classical mechanics theorems usually fail to capture anticipated accuracy. To handle this issue, non-classical theories have been developed. Modified couple stress theory (MCST) and non-local strain gradient theory (NLSG) are among the theories with significant and high attention [20]. In modified couple stress theory, it is assumed that besides to Cauchy stress-strain tensors conjugated; couple stress tensor is also conjugated with curvature tensor and a material length scale parameter is included consequently. In non-local strain gradient theory, it is assumed that stress of a point of an infinitesimal element is not only function of strain of that point but also is a function of strain of all points in the domain. This assumption is

joined with strain gradient theory noting that stress accounts for higher order strain gradient as well. Such theories are highly applicable and efficient in modeling, analysis, simulation and design of micro-electro-mechanical-systems and nano-electro-mechanical-systems (MEMS and NEMS) which can be deployed in small-scaled (MEMS-NEMS) energy harvesters as well ([21], [22]).

### 2.3 Material Gradation and Modifications

Another feature with high attraction among several researchers refers to the material gradation throughout the main element axis or the one perpendicular to it. Technically this is called axially functionally graded (AFG) or functionally graded (FG) materials. The design of AFGMs is tied to geometrical modification. So that cross-sectional area perpendicular to the axis of beam is changing with respect to $x$-direction. AFGMs; however, are the result of more complicated technology than changing cross sectional areas and geometry solely. With the help of centrifugal forces, mixture of two different material types is adopted. FGMs usually consist of two constituents: metal alloy, and ceramic. Metal constituent helps the system in terms of toughness and increases its strength in deformations and vibrations. On the other hand, ceramic portion enhances system's resistance to potential thermal fluctuations available in most operation sites. Furthermore, ceramic provides another benefit to the system by keeping weight quite lighter than pure metal system ([23], [24]).

### 2.4 Temperature Fluctuations Effect Over the Dynamic Response

Another key point with electromechanical and even pure mechanical systems pertains to the presence of temperature fluctuations. This hypothesis is derived from

realistic adoptions of various systems in operational machinery conditions. Temperature mutations are an unavoidable process with almost all of the machinery, either harvesters or pure functional machines. Since; almost all machines waste some amount of energy via thermal energy, it sounds essential to address thermal effects over the dynamic response and performance of energy harvesters and electro-mechanical elements ([25], [26], [27], [28]). Eventually, since some electro-mechanical systems fall in the placement and interface of another host substructure, the effects of such host element over the performance and operations of devised electro-mechanical systems is of importance. To bring up such an idea, elastic and viscoelastic effects of host structures need to be covered. Ranging from simple dynamic support to complicated static-dynamic supports; several foundation-shape models have been perused ([29], [30]).

## 2.5 State of the Art

In this section, concise review of research efforts accomplished within the dynamic analysis of electro-mechanical systems and models is presented:

Zannosi [31] investigated dynamic response of porous small-scaled beams based on the modified couple stress theory. Presented model in this study is made up of material mutations and the effects of such factors are addressed as well. Li et al. [32] carried out research addressing dynamic response of beams submerged in fluid. Authors utilized added mass method to obtain effects of hydrodynamic load induced from fluid as well as material gradation profile. Temperature-dependent model of MCST beam is presented by Babaei et al. [33]. Authors prove that it is essential to address thermal stress imposition effects on the sensor models. Besides, a proper model of electro-mechanical system with

continuously varying thermo-mechanical properties is proposed. Axially functionally graded electro-mechanical model is suggested based on the modified couple displacement field [34]. Results demonstrate that mutation of cross-sectional area of the model ends up in gradations of flexural rigidity, and oscillatory response of the system. Such traits can be adopted in the design and analysis of gyroscopes and energy harvesters as well as sensors. As one of the key research articles published in the field of piezoelectric energy harvesting using beam elements, Erturk and Inman investigated dynamic importance within energy harvesting design procedure [35]. Su et al. [36] carried out a research for energy harvesting of rotating systems. Authors considered centrifugal forces effects upon harvester model in several orientations. Results of this paper illustrate that tilt angle of the tip mass mounted at the end of the beam can be used to adjust resonant frequency with respect to the excitation frequency. Effects of two hard base accelerations upon harvester performance model is reported by Rezaei et al. [37]. Authors present a nonlinear model which can be solved using multiple scales method. Results point to the higher accuracy of nonlinear resonator-harvesters contingent to the proper mechanical parameter adoption. Since most of the energy harvesters operate with quite weak excitations, several researchers have tried to improve and enhance the input excitation or improve the operational aspect of the harvester by means of mechanical or electrical modifications. Fan et al. [38] proposed mechanical stoppers in combination with electrical magnetic field to make mono-stable model which finally yields more extractable power in comparison to conventional harvesters. The model is also tested under random excitations by means of White Gaussian noise. Dehsaraji et al. [39] perused size-dependent models integrated with energy harvesters. They proposed that small-scaled energy harvesters can be modeled based on

the non-classical theories. In this regard, modified couple stress theory is utilized to predict more accurate results. In extension to remedy the size-dependency issue, Tadi Beni et al. [40] improved nonlinearity within the system of energy harvester. Interactions between size-dependent models and nonlinear forcing terms have also been reported in this model. Shifting the harvesters more towards material engineering, Tan et al. [41] devised a composite-based structure as the harvester. They addressed material effects over dynamic and electrical response of the system. Several numerical methods and approaches have been adopted by researchers regarding investigation of oscillatory response of nonlinear complicated energy harvesters. Zhou et al. [42] used harmonic balance method to solve nonlinear equations derived from electro-mechanical energy harvester model. Results of this research prove the accuracy and validity of harmonic balance method for analyzing nonlinear harvester models. Incorporating electromagnetic and piezoelectric methods in harvesting energy; Bolat et al. [43] proposed a hybrid model to harness energy of low-frequency moving aerodynamic elements. Authors considered air flow as the main reason and source for dynamic motions. Stephen and Renno et al. [44], [45] reported sequel of electro-mechanical coupling coefficient and load resistance on electrical amount of extractable power. Erturk and Inman [46], [47] carried out performance evaluation of cantilever beam energy harvester analytically and experimentally. Another category of energy harvesters falls in small-scale systems. Although it is proved that in such miniaturized systems, non-classical theorems should be adopted; for the sake of energy scavenging, most research skip size-dependency and only concentrate on electromechanical aspects, but several researchers establish energy harvester model based on size-dependent models. Tao et al. [13] proposed a 2DOF MEMS vibration-based energy

harvester comprising environmental-friendly material. This model includes two subsystems; the primary system is set for energy conversion from mechanical into electrical energy forms, and the second one is an auxiliary subsystem for the purpose of frequency adjustment. Such frequency adjustment can be employed properly to increase operational frequency bandwidth. Designing a cantilever energy harvester based on seesaw mechanism is reported by Asthana et al. [48]. Using the finite element method (FEM), this novel type of harvester enables covering wider bands of operational frequency. Incorporating graded material into the harvester design enables mechanical property variations. Property profile gradation directly impresses bending stiffness (flexural rigidity) which alters resonance and fundamental frequency range. Heshmati and Amini [49] investigated model parameter effects along with multi-moving oscillators located on a functionally graded (FG) beam. Model parameters are affected by material property gradation according to graded pattern. Rotational effect in dynamic response of beams has been of great importance among researchers. Fu and Yeatman [50] incorporated rotating beam with electromechanical dynamics to remedy the issue of harnessing energy from low-frequency operations as long as enhancing frequency bandwidth. Authors proposed rotational energy scavenger model considering bi-stability and frequency-up conversion which is suitable for wide bandwidth systems. Tang and Wang [51] developed a new type of harvesting systems by means of mobile end effects and dynamic magnifiers. This new type of dynamic magnifier widens the frequency bandwidth and results in increased power output. Besides, the effect of mass offsets has been perused. Mass offsets are basically resultant of considerable magnifier width. Authors suggest a more efficient energy harvester design with proper mass offset and spring stiffness ratio values. Fan et al.[33],

devised a new type of piezoelectric energy harvester with stoppers enabling the harvester to generate enough power from low-frequency harmonic or low-intensity random excitations. This new type of energy scavenger is a guarantee for low-level ambient excitation usage under both harmonic and random excitations. Besides the mentioned research papers, some industrial elements are supposed to work in ambient with temperature fluctuations. Devising new-type dynamic magnifier is carried out by Tang and Wang [52]. Authors propose elimination of clamped-type support of a cantilever beam and employing translational spring with linear characteristics at the clamped end. Such elastically restrained harvesters are allowed to translate vertically and harness more energy from the same input conditions. Aladwani et al. [53], [54] proposed similar type of dynamic magnifier to extract more energy. Authors proved that providing two inertial effects at clamped and free ends of the system enables the system to scavenge more energy. Moreover, it is mentioned in the paper that proper selection of design factors and parameters with such dynamically magnified system leads to increased frequency bandwidth. In lumped-parameter energy harvesters, mass, spring's constant, and the damping constants are the dominant factors determining the oscillatory response of the mass, which renders the amount of extractable voltage [10].

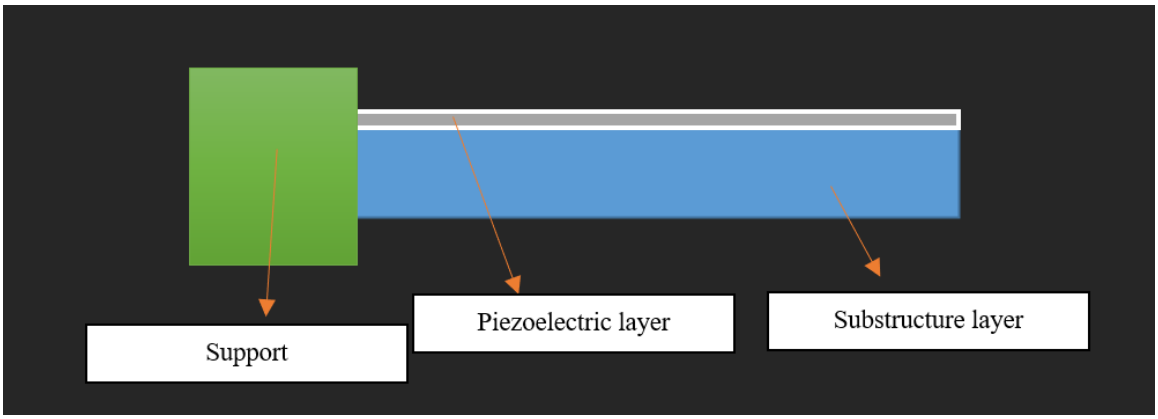

Figure 2. Distributed parameter (cantilever) energy harvester

As mentioned in the above sections, lumped-parameter model was improved into a distributed-parameter model which mainly consisted of a cantilever beam with piezoelectric patches bonded on top of the beam. This type of energy harvester is shown in figure 2. The generated electrodes due to vibrations and on the piezoelectric surface are directed to the electric circuit ([35]-[49]).

There are specific types of energy harvesters in which the harvested energy is enhanced with dynamic magnifiers. The rotational spring provides rotations, and the translational spring enables the beam to move translationally. The mass at the right end (also called the tip mass, proof mass, end mass, attached mass) acts as a tuning inertia. The mass on the left end plays the main role as the dynamic magnifier and yields more harvestable energy ([51]-[54]). Cantilever beam configurations play a predominant role in piezoelectric vibration-based energy harvesters (PVEH) [55]. Roundy and Wright [56] employed a lumped-parameter configuration for harvesting mechanical energy using the piezoelectric phenomena. This model encompasses only one vibration mode and lacks the electromechanical coupling effects in terms of higher vibration mode shapes and strain distribution. In contrast, scholars employed distributed-parameter models (e.g. cantilever

beams) to address the mentioned drawbacks of lumped-parameter systems and improve the harvesters efficacy ([47], [35]). As a result, it seems essential to scrutinize the dynamical response and analysis of mechanical beams. There are multiples of technical articles covering this scope ([57], [58], [25]) and for the purpose of brevity we only focus on the energy harvesting analysis. Naseer et al. [59] investigated the analysis of piezo-electric vibration-based energy harvesters (PVEH) considering the vortex phenomena. In this study, vortex-induced vibrations are the origin of energy harvesting. Zhang et al. [55] studied the PVEH made up of composites. Nonlinearities in this study are derived from magnetic force and restoring forces. A harmonic balance approach is taken to find the semi-analytical response of the energy harvester. To improve the efficiency of PVEH exposed to small-frequencies (low excitation frequencies). Asthana et al. [60] conducted a research addressing the optimization of a cantilever beam. Moon et al. [61] reported the efficacy of the tuning mass in widening the operational frequency bandwidth of a cantilever-based energy harvester. Dechant et al. [62] carried out research concerning the application of tuning masses integrated with cantilever beam arrays to reinforce the outcome voltage. Such arrays of energy harvesters reinforced with tuning masses can be highly helpful for wireless sensor networks. Jia and Seshia [63] conducted an experimental investigation to find the optimal tuning mass ratio to the mass of the cantilever beam. They also verified their experimental results with numerical analysis. Staaf et al. [64] adopted a sliding tuning mass mechanism to enhance the effective frequency bandwidth of the energy harvesters. They proposed such a model for functionality in wireless sensor networks (WSN) under stochastic excitations which are known as random vibrations. Zhao et al. [65] proposed a novel 2D energy harvester with self-tuning capability. They studied

the effects of the vibration direction on the performance of the harvester module. Nonlinear energy harvester analysis under mounted on a rotating element is studied by Mei et al. [66].

## 2.6 Energy Harvesting Integrated with IoT

Sine the energy harvesting topic is highly attractive to the small emerging technologies such as: internet of things (IoT), wireless sensor networks (WSNs), and micro-electro-mechanical-systems (MEMS); it sounds helpful to provide a brief literature review and fundamentals about such integrated technologies: new dynamic of networks connecting different objects, in various places and in constant timespan, was first created by the invention of internet of things (IoT). The first report in this response was first published by the International Telecommunications Union (ITU) [67]. Nowadays, IoT is integrated with disparate industries encompassing transportation, civil structures, defense and aerospace, manufacturing, energy generation and management, healthcare, environment and condition monitoring, and smart cities. Ever-growing IoT technology has been expected to creep into all aspects of human beings in close future, life without IoT technology will be impossible [68]. IoT major components can be visualized in the following figure:

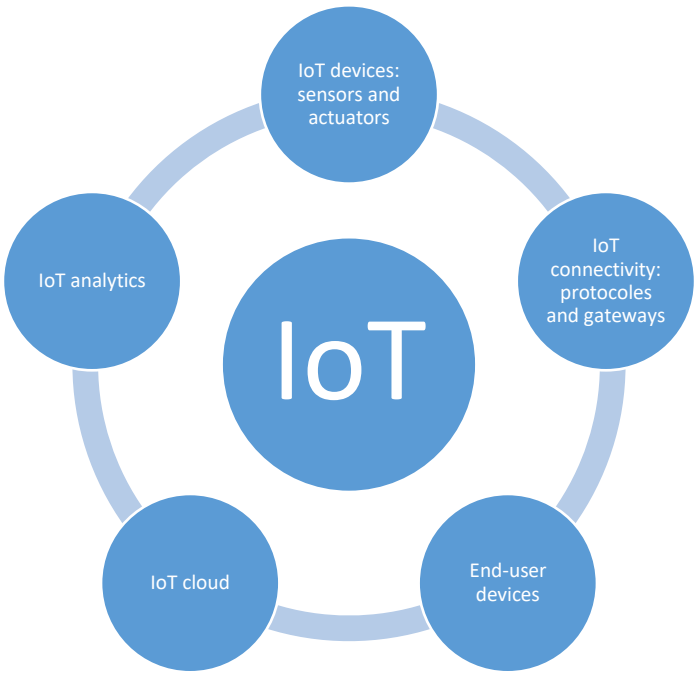


Figure 3. Internet of Things (IoT) principal components

Sensors and actuators integrated with IoT, operate data collection and control a desired process. Protocols and gateways transfer data in the online world. The data is stored in the IoT cloud. Decisions are also taken in this section. The gathered data is processed and analyzed in the data management and IoT analytics section. Eventually, the user interfaces control the system [69]. In a different fashion, IoT can be classified with following parts:

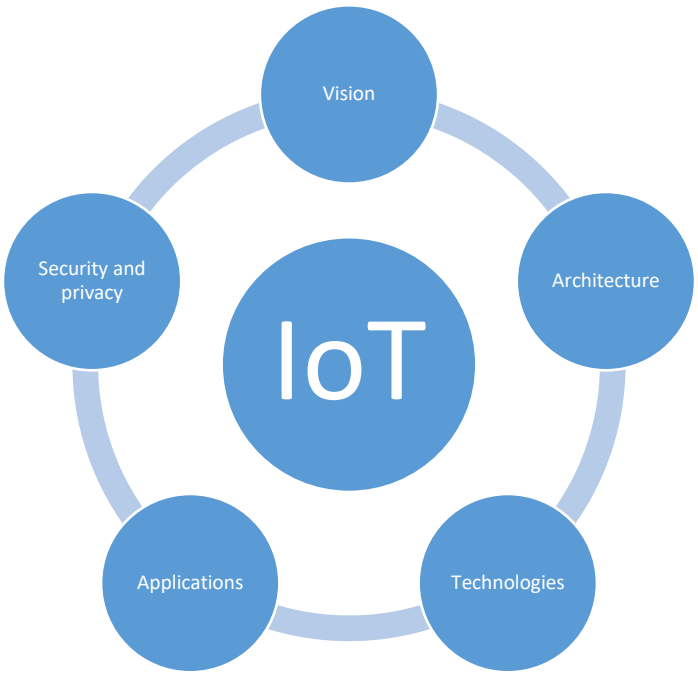


Figure 4. IoT principal components (2nd outlook)

In this outlook, classification mainly pertains to the capability of objects communicating with each other and taking actions accordingly. Such comprehension and response are doable using machine learning or artificial intelligence. Architecture of IoT comprises the following layers:

Figure 5. Layers of IoT

Technology section is made up of the 7 well-known sub-divisions of technologies which are imperative to make IoT realistic and applicable:

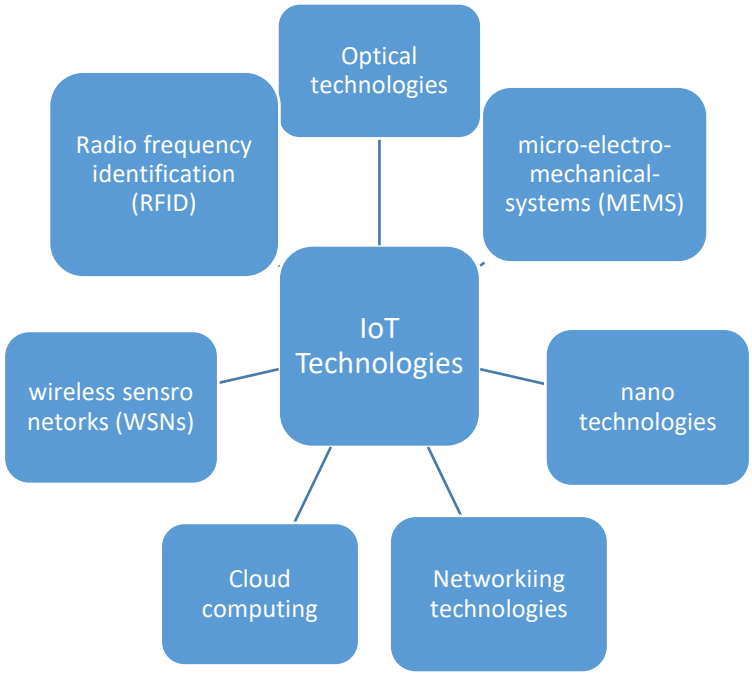


Figure 6. IoT applications in technologies

RFID is the heart of IoT as the technology of enabling objects to be identifiable. Objects equipped with RFID are uniquely detectable which enables the operator or the system to keep track of any object. Mostly the RFID system comprises of three elements: the reader, the antenna, and the tag. Tags are indeed the microchip transceiver which contains unique information of each object in it. Tags can be active or passive. If the RFID is equipped with an external power source (e.g., battery) the tag is called an active tag. If there are not any external power sources, the tag is passive. Passive tags get activated using the backscattering process in which, the signal emitted from the antenna, includes an amount of energy and triggers (activates) the tag to send the signal back to the antenna along with the unique information stored in it [70].

RFID tags can be divided into low frequency, high frequency, ultra-high frequency, and microwave frequency. Bar code technology performs in a similar fashion to RFID. However, RFID is a superior method since it works basically with radio frequency electro-magnetic waves. But the bar code is basically an optical method which requires the physical existence of the object. Moreover, RFID can be programmed to act as an actuator in contrast to the bar code. WSN is a wirelessly connected set of sensors which are connected to each other to pass on the target data such as: temperature, humidity, velocity, and displacement to the processing unit. Such a connected network requires power to operate. Such a power source can be battery. However, there are some issues with batteries. Batteries have limited lifespan and end up in replacement actions. This means a huge drawback, and labor costs. Besides, in some cases, the WSN is placed in hard-to-access (remote) locations making it arduous to reach the device. Besides, batteries waste causes environmental issues as they contribute to earth pollution. With this in mind, recently the adoption of energy harvester modules has gained significant attention among industries and research corporations. This topic is elaborated in detail in the preceding sections. Cloud computing is deemed to be the most vital IoT component. Considering the ever-growing number of IoT devices, a very powerful and strong computing technology is in demand to store and analyze such big data effectively. In cloud, several servers are converged on a single mother platform. This way, resources can be readily shared between all servers at any place and any time. Using cloud, all servers are converted into a single one, with stronger processing capabilities [67].

Connecting technologies are designed to connect different objects to each other. Already for wide-range transmission, the 3G, and 4G are taken. As for mobile traffic, since we usually have usual tasks, it is predictable which bandwidth is required. But, with creeping into the ubiquitous computing era; it is no longer predictable to estimate the right bandwidth. Nano technology is mainly defined to reinforce a system operation quality, while decreasing the dimensions in nano scale. Such a decrement renders smaller usage of material and lower manufacturing cost, higher resistance to mechanical noise and vibrations, better packing ability, and more accuracy. Adoption of nano technology results in nano IoT devices called internet of nano-things. Optical technology developments such as: Li-Fi and Bi-Di have made various breakthrough improvements in IoT. Li-Fi and epoch-making visible light communication is capable of providing big connectivity on high bandwidth which is useful for interconnections applied in IoT. Similar to Li-Di, bi-directional (Bi-Di) technology makes the 40G ethernet connectivity feasible. With the advent of micro technology and miniaturization, Micro-electro-mechanical-systems (MEMS) have been introduced with widespread applications in engineering and medical sectors. MEMS sensors and actuators, gyroscopes and resonators have been studied in big volume by different researchers all around the world. There are several appliances and devices in our daily life that are intelligent and smart. The main concept behind IoT is to connect all such devices with each other, so that the data will be shared within a single cloud and decision-making system. Six symbolic examples of IoT applications are brought in the following picture [69], [71]:

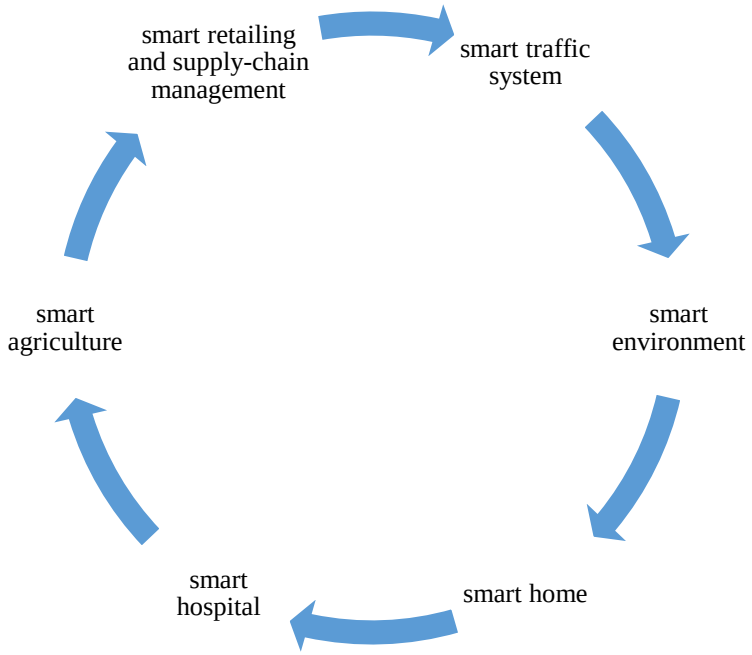


Figure 7 . IoT and smart city

Replacing image processing techniques with IoT-enabled traffic systems leads to much better and more efficient traffic monitoring in smart cities. Using IoT, automatic identification of vehicles, and all traffic-related factors is doable. This technology can render theft detection, traffic issues, road conditions, accidents. IoT enables the smart traffic monitoring system to be adaptive with respect to weather and climatic changes which results in less cost and a more efficient system. It is evident that discerning an environmental phenomenon like an earthquake is of crucial importance. Smart environment is doable by innovative IoT which enables us to predict natural disasters like fire, tsunami, and flood. With IoT, smart homes are reachable. This way, we can control our homes and appliances remotely. Home automation is expected to save a significant amount of time and energy for residential complex residents. Additionally, the monitoring of water and electricity usage per house can reveal potential technical issues like leakage.

This has the potential to result in great economic savings. IoT-enabled security cameras and systems will guarantee house security against burglaries. Smart hospitals: one of the technologies helping doctors and nurses to monitor patient conditions (temperature, heart rate, pulse rate, respiration rate) is based on the integration of wearable monitoring devised. Also, in case of a medical emergency (cardiac arrest), it takes a time for the ambulance to reach the target point, while using drone ambulances, they can rapidly reach the patient with an emergency kit and doctors using the monitoring system can provide proper medical care and survive the patient until the ambulance arrives. In smart agriculture, the product will be mostly optimized by monitoring humidity, temperature, light, water, and fertilizers. In retailing, IoT integrated with RFID helps to track specific objects to see whether the item is in stock or not. Besides, placing online orders is doable by this method, which is widely stated in the preceding parts. Finally, statistical charts and information will be available for effective analysis and future decisions. Security and privacy challenges with IoT: as IoT makes everyone and any object detectable and identifiable at any time at any place, there are some privacy issues and concerns arising among society. Specifically, thinking about abuse of IoT intensifies such a concern. There are three symbolic issues addressed with IoT [71]:

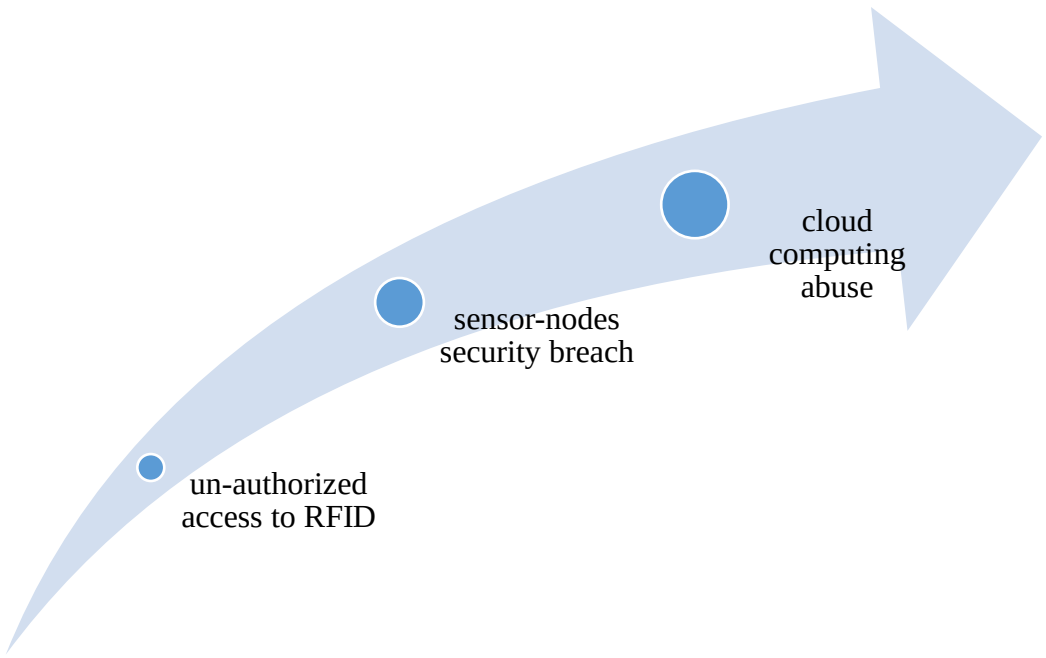


Figure 8. IoT and security issues

Accessing a RFID tag can expose and reveal confidential information, the tag can be read by a miscreant reader and damaged. With WSNs, there are issues regarding data manipulation and acquisition: by interfering with the nodal frequencies, Jamming obstructs the whole network system. In Tampering, the node is controlled by the attacker. If multiple pseudonymous identities are attributed to a node, Sybil attack takes place. In this case the target node is adversely influenced. In Flooding, the memory is exhausted and exploited as big data traffic is being operated. As mentioned earlier, in cloud computing, big servers' networks are converged to share resources in between. Man-in-the-middle attack (MIMA), Phishing. Cloud Security Alliance (CSA) have announced some threats: Malicious Insider attack is a type of attack in which there is an individual inside the system and can manipulate the data. Data Loss refers to the threat where the user can delete the data by accessing it. Man-in-the-middle pertains to an Account Hijacking

threat that the attacker can interfere with the messages and data being transmitted between two parties. Cloud computing can be very dangerous as if the attacker can access the entire servers on the cloud, he can upload malicious software and control many devices. IoT has shown the capability to impact on today's life intensively and at an ever-growing pace. Several training projects and initiatives have been incorporating with IoT to benefit this technology and thrive in different aspects. IoT impacts disparate facets of life. IoT has gained remarkable attention and attract from research institutes worldwide. Thus, it is expectable the technology will boost several job opportunities and affect future economy. Such a striking impact is mentioned to be directed toward the information technology (IT) based applications and software domains. From hardware outlook and perspective, the consolidation and integration of microsystem technologies with IoT can guarantee its establishment and obviate its limits and restrictions in hardware and infrastructural assemblies. The accessible and sustainable infrastructure for globalizing IoT is still in shortage. Such an issue seems to be solvable by providing scalable and small-size infrastructures with self-powering trait. This solution pertains to the proper integration of various technologies and interdisciplinary research areas pointing to autonomous devices. With autonomous devices, energy harvesting, and ultra-low power electronics play the key role. IoT European Research Cluster states the requirement for development in energy harvesting and energy storage plazas as the crucial demands in realization of ubiquitous connectivity that IoT proclaims. WSNs as a subdivision of IoT requires low-energy, miniaturized, and integrated nodes. Such nodes are typically powered by batteries. Batteries as non-renewable energy sources carry unavoidable issues like environment pollution, labor cost, and difficulty with replacements particularly in hard-to-access

locations. Considering the growing development in electronics technology, low-power electro-mechanical devices run on minimal and small amounts of energy. Besides, there are several energy conversion mechanisms to exploit the ubiquitous energy forms available in the universe generating small amounts of energy. Thus, integration of electronics with microsystem energy harvesting technologies result in energy-autonomous technology enabling the electro-mechanical systems (e.g., WSN nodes, IoT devices) to supply their own required energy and operate without any external power sources. Such a triumph in interdisciplinary technology plaza promises mass production and pervasiveness meaning that IoT-related devices and subsidiaries are independent from energy restrictions and render robust infrastructures. As mentioned comprehensively in the preceding sections, energy scavenging (ES) or energy harvesting (EH) is the technology of utilizing and exploiting different forms of energy available in the environment and converting it to electric power. Such a new and emerging technology is highly attractive and helpful for IoT-related applications ([69], [71], [72], [73], [74])

# CHAPTER 3. PRELIMINARIES TO DYNAMICAL ANALYSIS OF BEAM ELEMENTS

In this chapter, the main focus is to provide preliminaries and in-depth study of beam elements undergoing various operational conditions and modifications. Such conditions are essential to be considered and modeled properly to understand the induced mutation and effects over the vibrational response of the electro-mechanical elements. In detail, studying the resonance frequency profiles, mode shapes in disparate vibration modes; are among the priorities. To do so, proper modeling is the very first step. Then, adopting the variational principle of Hamilton, governing equations of motion will be derived and discretized using the suitable discretization approach (e.g., Galerkin, Navier, etc.).

## 3.1 Temperature Effects over Oscillatory Response of Beam Elements

In this section, the main purpose is to model the thermal energy induced to the beam system and study how it alters the energy harvester's systems behavior particularly from dynamical and vibratory aspects. Electro-mechanical system is supposed to be placed inside an RFID fixture with temperature fluctuations due to the operation of antenna. So, we assume sudden temperature increments and decrements need to be modeled and taken into account. Different types of boundary conditions are considered to cover a wide range of applications. Since antenna works and stops regularly, heat generation is negligible. In other words, generated heat is not continuous with respect to time and only sudden fluctuations emerge. Consequently, due to the time gap between each operation cycle of the antenna, the beam fits to a steady-state condition and role of such thermal energies appear in the form of time-invariant energy. However, thermal energy still is big enough to alter thermo-mechanical properties of the beam specifically because of the compact

configuration and small sizes of the entire fixture. Top and bottom surfaces are the surfaces which are mostly imposed to the ambient, so temperature fluctuations start from the mentioned surfaces. Modulus of Young (E), modulus of rigidity (G), Poisson's ratio (ν), and thermal expansion coefficients are supposed to be varying due to temperature shifts. To use a proper mathematical model for such variations, following non-linear parameter-temperature equation is proposed ([28]):

$$P = P_0(P_{-1}T^{-1} + 1 + P_1T + P_2T^2 + P_3T^3) \tag{3.1}$$

in Eq. (3.1), $P_i$ are specific coefficients which are shown in Table 2.

### 3.1.1 Kinematic Relations and Kinetics

To model the system of a beam in oscillations, first one needs to define the displacements and the corresponding forces. Boundary conditions of electro-mechanical system presented is firstly considered as simply supported (pinned-pinned) beam with length L, width b and thickness h. In order to derive governing equation of motion, energy method along with Hamilton's variational principle is used. Energy method is independent of coordinates and is more useful for complicated systems where coordinate-dependent method is unable to be used. The energy method is established based on the variational principle expressing those variations of Lagrangian of any system with respect to time is zero. Based on classical continuum mechanics, strain energy of the infinitesimal element of beam configuration is:

$$U_s = \frac{1}{2}\int_V (\sigma_{ij} : \varepsilon_{ij})\, dV, \quad i=j=x,y,z \tag{3.2}$$

$$\sigma_{ij} = 2G\varepsilon_{ij} + \lambda tr(\varepsilon_{ij})I_d \tag{3.3a}$$

$$\varepsilon_{ij} = \frac{1}{2}(u_{i,j} + u_{j,i}) \tag{3.3b}$$

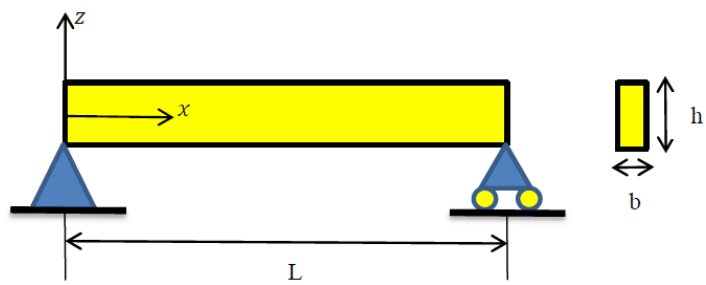


Figure 9. Schematic of a simply-supported beam

where σ and ε represent Cauchy stress and strain tensors, $I_d$ shows identity tensor, λ is Lame's constant, and G represents shear modulus of rigidity. Using Euler-Bernoulli theory, displacement field of a random point on the neutral axis is as follows:

$$u_x(x, z, t) = -z\emptyset(x, t) \tag{3.4a}$$

$$u_y(x, z, t) = 0 \tag{3.4b}$$

$$u_z(x, z, t) = w(x, t) \tag{3.4c}$$

in Eqs. (3.4), $\emptyset(x, t) = \frac{\partial w}{\partial x}$ is independent rotation, $w(x, t)$ is lateral displacement of neutral axis. Using Eqs. (3.4b) and (3.4c) following elements are found:

$$\varepsilon_{xx} = -z\frac{\partial^2 w}{\partial x^2} \tag{3.5a}$$

$$\sigma_{xx} = -z\frac{\partial^2 w}{\partial x^2}E \tag{3.5b}$$

substituting Eqs. (3.5a) and (3.5b) into Eq. (3.2) leads to the strain energy term:

$$U_s = \frac{1}{2}\int_V E\left(-z\frac{\partial^2 w}{\partial x^2}\right)^2 dV \tag{3.6}$$

variation of Eq. (3.6) is:

$$\int_{t_1}^{t_2} \delta U_s dt = \int_{t_1}^{t_2} \int_V [E(-z\frac{\partial^2 w}{\partial x^2})(-z\frac{\partial^2}{\partial x^2}(\delta w)]\, dVdt \tag{3.7}$$

by taking integration by parts from Eq. (3.7), it can be rewritten in the following form:

$$\int_{t_1}^{t_2} \delta U_s dt = \int_{t_1}^{t_2} \{\int_0^L EI\frac{\partial^4 w}{\partial x^4}\delta w dx\} dt \tag{3.8}$$

in Eq. (3.8), I represents second moment of inertia ($I = {bh^3}/{12}$) and A represents area of cross section ($A = bh$).

To consider the effects of temperature, temperature energy renders energy terms which need to be determined as well. In this response, reinforced strain energy derived from thermal stress is expressed in Eq. (3.9):

$$U_T = \frac{1}{2}\int_V {\sigma_x}^T \left(\frac{\partial w}{\partial x}\right)^2 dV \tag{3.9}$$

${\sigma_x}^T$ is thermal stress:

$${\sigma_x}^T = -E\alpha\Delta T \tag{3.10}$$

$\Delta T$ is temperature shift from reference temperature ($\Delta T = T - T_r$).

variation of Eq. (3.10) with respect to time is to be found:

$$\int_{t_1}^{t_2} \delta U_T\, dt = \int_{t_1}^{t_2} \int_0^L E\alpha\, \Delta T A \frac{\partial^2 w}{\partial x^2}\delta w dx dt \tag{3.11}$$

Kinetic energy of the beam is expressed in the following equation:

$$K_1 = \frac{1}{2}\int_V \rho(\frac{\partial w}{\partial t})^2 dV \tag{3.12}$$

in Eq. (3.12), ρ is density. Besides to translational kinetic energy, reinforced kinetic energy is augmented to the system due to relative rotation of beam elements with respect to the fixed axis. This is resultant from the concept of the rotating beams around an axis.

Corresponding coupled rotational displacement field is assumed to have a linear relation with the translational displacements.

$$x\theta(x,t) = aw(x,t) \tag{3.13}$$

$a$ is speed coefficient multiplied with lateral displacement. The resultant augmented kinetic energy is:

$$K_2 = \frac{1}{2}\int_V \rho\, x^2 \left(\frac{\partial\theta}{\partial t}\right)^2 dV \tag{3.14}$$

variations of total kinetic energy ($K = K_1 + K_2$) with respect to time is:

$$\int_{t_1}^{t_2} \delta K\, dt = \int_{t_1}^{t_2} -(1+a^2)\rho A \frac{\partial^2 w}{\partial t^2}\delta w dt \tag{3.15}$$

based on Hamilton's principle, Lagrangian of energy terms is constant with respect time:

$$\int_{t_1}^{t_2} (\delta K - \delta U_s - \delta U_T) dt = 0 \tag{3.16}$$

substituting Eqs. (3.8), (3.11), (3.15) into Eq. (3.16) yields following dynamic-vibration equation of thermally stressed rotating-element electro-mechanical beam under free vibrations:

$$(1+a^2)\rho A \frac{\partial^2 w}{\partial t^2} + E\alpha\Delta T A \frac{\partial^2 w}{\partial x^2} + EI\frac{\partial^4 w}{\partial x^4} = 0 \tag{3.17}$$

moreover, boundary conditions of the simply supported beam are as follows:

$$w|_{x=0,L} = 0, \quad \left.\frac{\partial^2 w}{\partial x^2}\right|_{x=0,L} = 0$$

for the case of forced vibrations, variation of Lagrangian is equal to variation of external load ($f(x,t)$ per unit length). Variation of external load is:

$$\int_{t_1}^{t_2} f(x,t)\delta w dt \tag{3.18}$$

thus, dynamic-vibration equation of thermally stressed rotating-element electro-mechanical model under the forced vibrations is:

$$(1+\mathrm{a}^2)\rho\mathrm{A}\frac{\partial^2\mathrm{w}}{\partial\mathrm{t}^2}+\mathrm{E}\alpha\Delta\mathrm{TA}\frac{\partial^2\mathrm{w}}{\partial\mathrm{x}^2}+\mathrm{EI}\frac{\partial^4\mathrm{w}}{\partial\mathrm{x}^4}=\mathrm{f} \tag{3.19}$$

### 3.1.2 Solution Procedure and Results

Eqs. (3.17) and (3.19) are linear partial differential equations with constant coefficients. Using modal decomposition concepts, lateral displacement can be expressed in following form:

$$w(x,t)=\sum_{n=1}^{\infty}\phi_n(x)\eta_n(t) \tag{3.20}$$

$\phi_n(x)$ is the eigenfunctions and $\eta_n(t)$ is modal time response for n'th vibration mode.

Free vibrations: in this case governing equation is homogenous and method of separation of variables is adopted. Besides, since there is no viscous damping effect, time response is equal to exponential function of natural frequency ($\omega_n$) times time variant ($t$). ($\zeta_n(t)=e^{j\omega_n t}$):

$$EI\frac{d^4\phi_n}{dx^4}+E\alpha\Delta TA\frac{d^2\phi_n}{dx^2}-\omega^2(1+a^2)\rho A\phi_n=0 \tag{3.21}$$

applying boundary conditions to the discretized equation, one may obtain following modal function and eigenvalues:

$$\phi_n(x)=sin\lambda_n(x),\ \ \lambda_n={}^{n\pi}/_{L} \tag{3.22}$$

substituting Eq. (3.22) into Eq. (3.21) one may find an explicit expression for natural frequency:

$$\omega_{nrt} = \sqrt{(EI{\lambda_n}^4 - E\alpha\Delta TA{\lambda_n}^2)/((1+a^2)\rho A)} \tag{3.23}$$

in Eq. (3.23) taking values of rotation effect and temperature shift equal to zero ($a, \Delta T = 0$) gives the frequency of a classical beam as presented in vibration books. Taking only the rotation factor equal to zero yields the thermally stressed natural frequency ($\omega_{n-th} = \sqrt{(EI{\lambda_n}^4 - E\alpha\Delta TA{\lambda_n}^2)/\rho A}$). To validate current model and results, one need to derive non-dimensional frequency:

$$\widehat{\omega}_{nrt} = \omega_{nrt} L^2 \sqrt{\rho A/EI} \tag{3.24}$$

Table 1. Comparison of different frequencies

| Dimensionless Frequency | Present |
|---|---|
| $\widehat{\omega}_1$ | 9.8696 |
| $\widehat{\omega}_2$ | 39.4784 |
| $\widehat{\omega}_3$ | 88.8264 |

Table 1 is presented to show the natural frequencies at the first three vibration modes.

Forced vibration-Harmonic motivations: For the forced vibration case, Eq. (3.19) is adopted which is a non-homogenous equation. Substitution of Eq. (3.20) into Eq. (3.19) yields:

$$EI\sum_{n=1}^{\infty}\frac{d^4}{dx^4}\phi_n(x)\eta_n(t) + E\alpha\Delta TA\sum_{r=1}^{\infty}\frac{d^2}{dx^2}\phi_n(x)\eta_n(t) + \rho A\sum_{r=1}^{\infty}\phi_n(x)\frac{d^2}{dt^2}\eta_n(t) = f(x,t) \tag{3.25}$$

considering a harmonic motivation as external force ($f(x,t) = f_0 e^{j\omega_e t}$) and noting orthogonality of modal displacement functions; by multiplying Eq. (3.25) by $\phi_s(x)$ and integrating over length of beam ($0 - L$), following equation is obtainable:

$$A_{1rt}\frac{d^2}{dt^2}\eta_n(t) + A_{2rt}\eta_n(t) = A_{3rt}e^{j\omega_e t} \tag{3.26}$$

where $\omega_e$ represents excitation frequency and $f_0$ is the external force amplitude. Coefficients are:

$$A_{1rt} = \frac{L}{2}\rho A(1 + a^2) \tag{3.27a}$$

$$A_{2rt} = \frac{{\lambda_n}^4 L}{2}EI - \frac{{\lambda_n}^2 L}{2}E\alpha\Delta TA \tag{3.27b}$$

$$A_{3rt} = \frac{2}{\lambda_n}f_0 \tag{3.27c}$$

solution of Eq. (3.26) encompasses the combination of homogeneous section and the particular one which can be written in the following form:

$$\eta_n(t) = a_0\cos(\omega_n t) + a_1\sin(\omega_n t) + a_{3rt}\,e^{j\omega_e t} \tag{3.28}$$

where:

$$a_{3rt} = \frac{A_{3rt}}{A_{2rt} - A_{1rt}{\omega_e}^2} \tag{3.29}$$

$a_0$ and $a_1$ are coefficients to be determined based on the initial conditions of the system. In this section we focus on response of system at rest ($\eta(0) = \dot{\eta}(0) = 0$) which is known as beating phenomena. It is a decent assumption when there is a concentration of system dynamics at initial steps and beginning of the performance of electro-mechanical system. Exerting initial conditions of beating status, leads to $a_0 = a_1 = 0$.

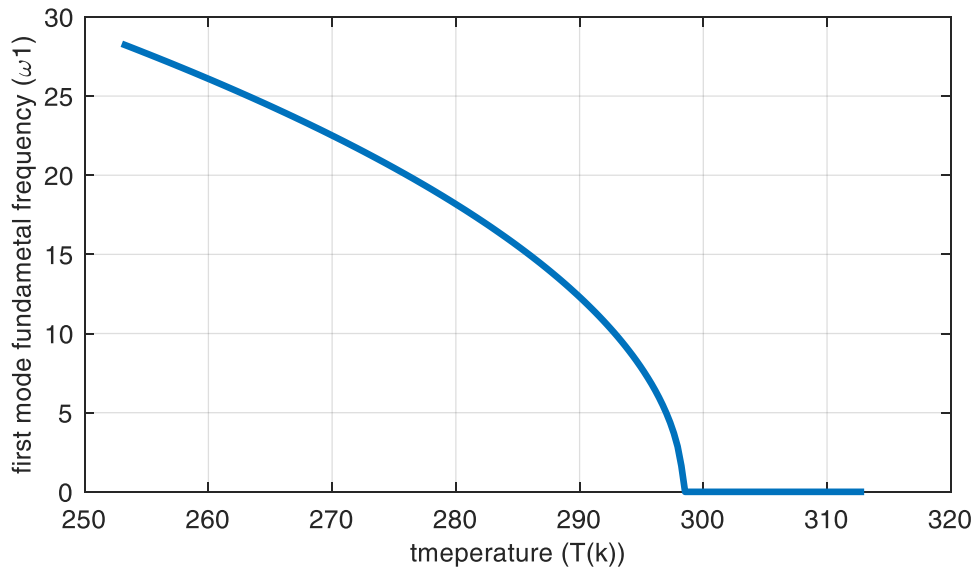


Figure 10. Variation of fundamental frequency with temperature

Figure 10 is provided to demonstrate variations of the first mode of vibration frequency with temperature mutations. It can be understood that increasing temperature results in frequency decrement with negative curve. Variations seem sharp at higher temperatures. It is good to note that passing a specific temperature, the first frequency of vibrations is suppressed. To find this specific temperature named as critical temperature ($T_{cr}$), one needs to solve Eq. (3.23) for zero value which leads to $T_{cr} = 298.3739\ k$.

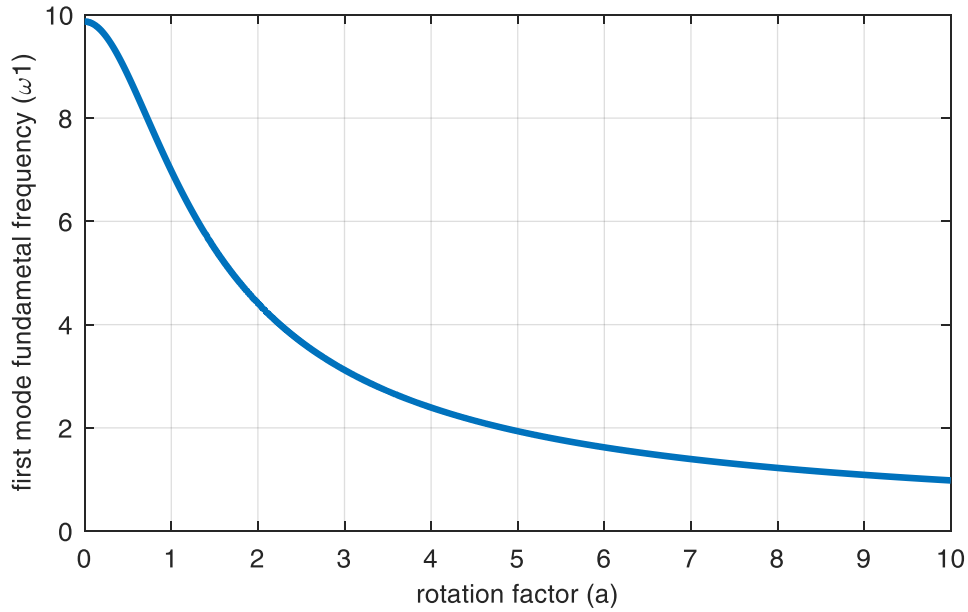


Figure 11. Variation of fundamental frequency with rotation factor

Impact of constrained rotations over frequency of the system is provided in Figure 11. One may conclude steep decrement of frequency for small values of $a$, meaning that small values of rotation factor ride severe role and makes system decrease in oscillations. Realistic expectations are assumed to remain for very small rotation effects. However, to accomplish mathematical conditions, taking the limit of Eq. (3.23) conveys no-vibration condition:

$$\lim_{n\to\infty} \omega_n = 0 \tag{3.30}$$

To get a decent quantitative measure of the output spectrum of the system under external stimuli, frequency response function (FRF) is a good measurement method. For this purpose, external force amplitude ratio with respect to response amplitude is to be obtained using Eqs. (3.26) and (3.29). After some mathematical operations, following FRF is obtained:

$$FRF = {}^{1}/_{(1 - \omega_{rrt}{}^{2})} \tag{3.31}$$

where $\omega_{rrt}$ is ratio of excitation frequency ($\omega_e$) to natural frequency bearing thermal stress and rotation effects ($\omega_{nrt}$):

$$\omega_{rrt} = {}^{\omega_e}/_{\omega_{nrt}} \tag{3.32}$$

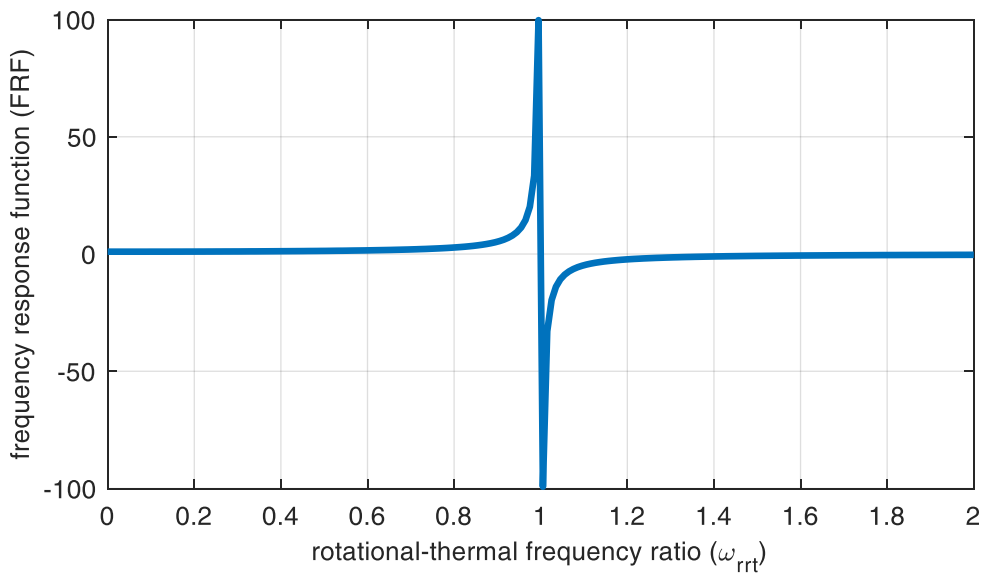


Figure 12. Frequency response function of a system under thermal stress and rotation effects

To present FRF of current model, Figure 12 has been included. Based on this figure, whenever excitation frequency is equal to fundamental frequency ($\omega_e = \omega_{nrt}$), FRF goes to infinity ($FRF \xrightarrow{yields} \infty$) which is named as resonance. In this case, ratio of response amplitude ($a_3$) to input amplitude ($A_3$) is infinitely large. An interesting finding refers to similar FRF for classical beam and current model which is bearing temperature shifts and rotation effects. In other words, the layout of FRF for the current model is identical to FRF of a classical model. Besides, static and dynamic deflection ratios of

thermally-stressed rotating-element model versus classical model ($a, \Delta T = 0$), also provide valuable information of the output spectrum in terms of temperature shift effects and rotation influence. Static deflection of classical and current models ($\delta_{st}$, $\delta_{strt}$) is ratio of applied force magnitude to system stiffness which can be obtained as following for both classical and current models:

$$\delta_{st} = {A_3}/{A_2} \tag{3.33}$$

$$\delta_{strt} = {A_{3rt}}/{A_{2rt}} \tag{3.34}$$

$D_{st}$ is a notation for static deflection ratio:

$$D_{st} = {\delta_{strt}}/{\delta_{st}} \tag{3.35}$$

substitution of coefficients and simplification of Eq. (3.35) leads to:

$$D_{st} = {\lambda_n{}^2 I}/{(\lambda_n{}^2 I - A\alpha\Delta T)} \tag{3.36}$$

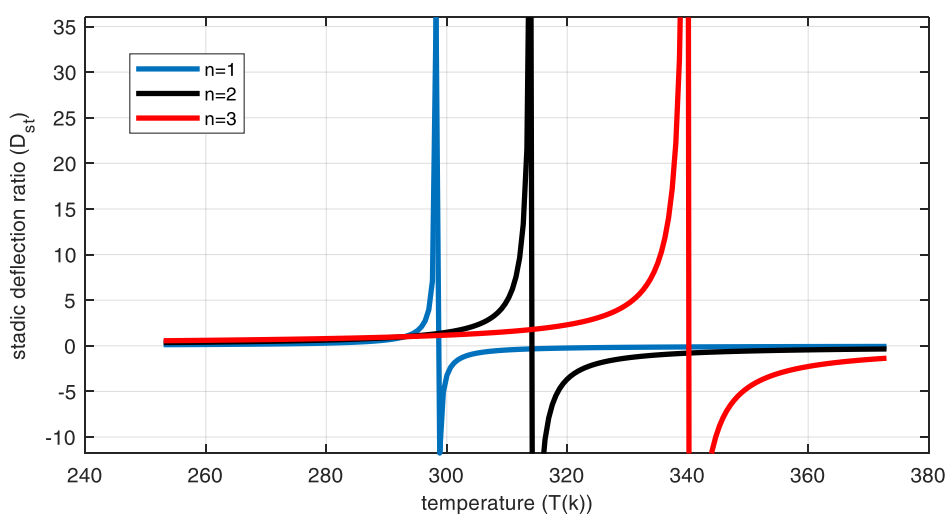


Figure 13. Static deflection ratio with respect to temperature

Based on Eq. (3.35), static deflection ratio spectrum is a function of temperature and frequency ratio, meanwhile rotation does not play a role. Thus, variation of this spectrum with temperature fluctuations is presented for the first three vibration modes in Figure 13. Obviously, each static deflection ratio spectrum shows sudden changes at specific temperatures. Such temperatures can be calculated using Eq. (3.35). ($T_{cr1} = 298.3739k, for\ second\ mode: T_{cr2} = 314.2753, third\ mode: T_{cr3} = 340.0858$)

Regarding dynamic deflection ratio ($D_{dyn}$); amplitude of response is to be divided by external force amplitude:

$$D_{dyn} = {a_{3rt}}/{a_3} \tag{3.37}$$

by substitution of Eqs. (3.27), (3.29), and (3.32) into Eq. (3.37); Eq. (3.38) is obtainable:

$$D_{dyn} = \left(\frac{{\lambda_n}^4 L}{2} EI - \frac{L}{2}\rho A {\omega_e}^2\right) \Big/ \left(\frac{{\lambda_n}^4 L}{2} EI - \frac{{\lambda_n}^2 L}{2} E\alpha\Delta T A - \frac{L}{2}\rho A(1 + a^2){\omega_e}^2\right) \tag{3.38}$$

Dynamic deflection ratio spectrum is function of temperature, rotation, and excitation frequency ($D_{dyn} = D_{dyn}(T, a, \omega_e)$). Practically it is impossible to plot variations of this spectrum with respect to all three independent variables simultaneously. Instead, separate plots are provided:

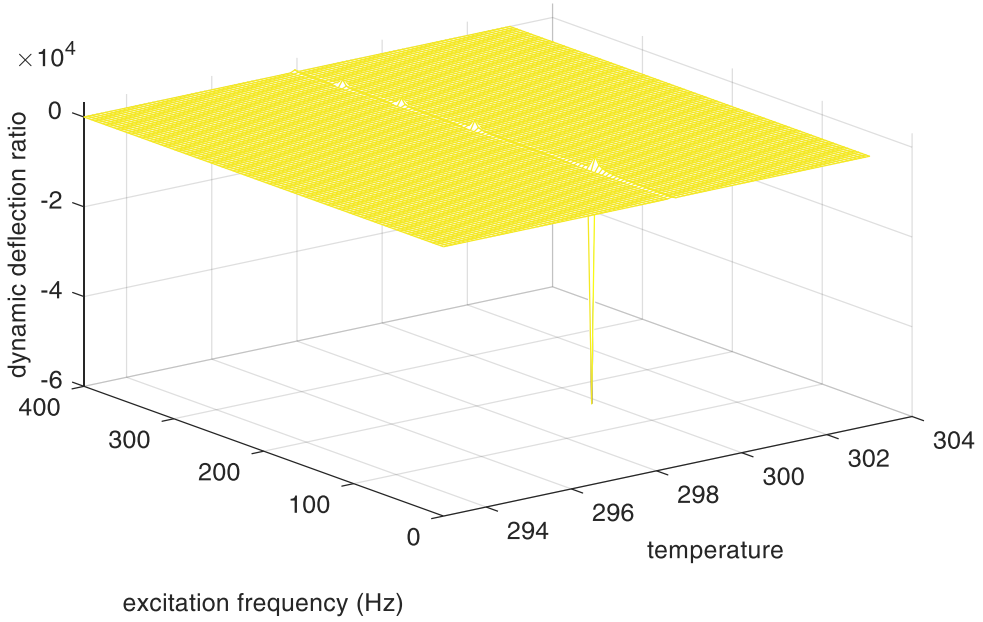


Figure 14. Dynamic deflection ratio with respect to excitation frequency and temperature

Figure 14 demonstrates dynamic deflection ratio spectrum variations with temperature and excitation frequency. Based on this figure, temperature changes do not affect dynamic deflection ratio unless at critical temperatures which was discussed earlier. In other words, dynamic deflections of a system undergoing temperature changes and a system free of thermal effects, are identical as far as temperature range excludes the critical value for each vibration mode.

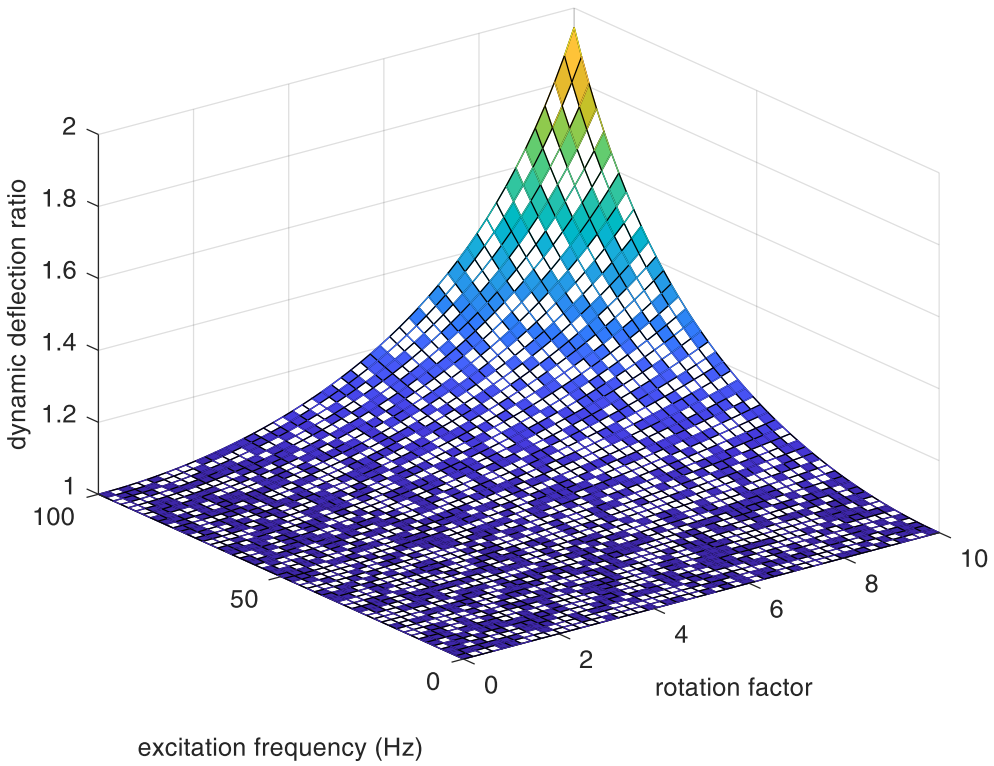


Figure 15. Dynamic deflection ratio with respect to excitation frequency and rotation factor

Figure 15 shows dynamic deflection spectrum ratio with excitation and rotation factor variations. Based on this figure, increasing rotation factor and excitation frequency lead to increment in dynamic deflection ratio. Meaning that exerting rotation into the system yields in higher dynamic deflections than the system of free of rotations.

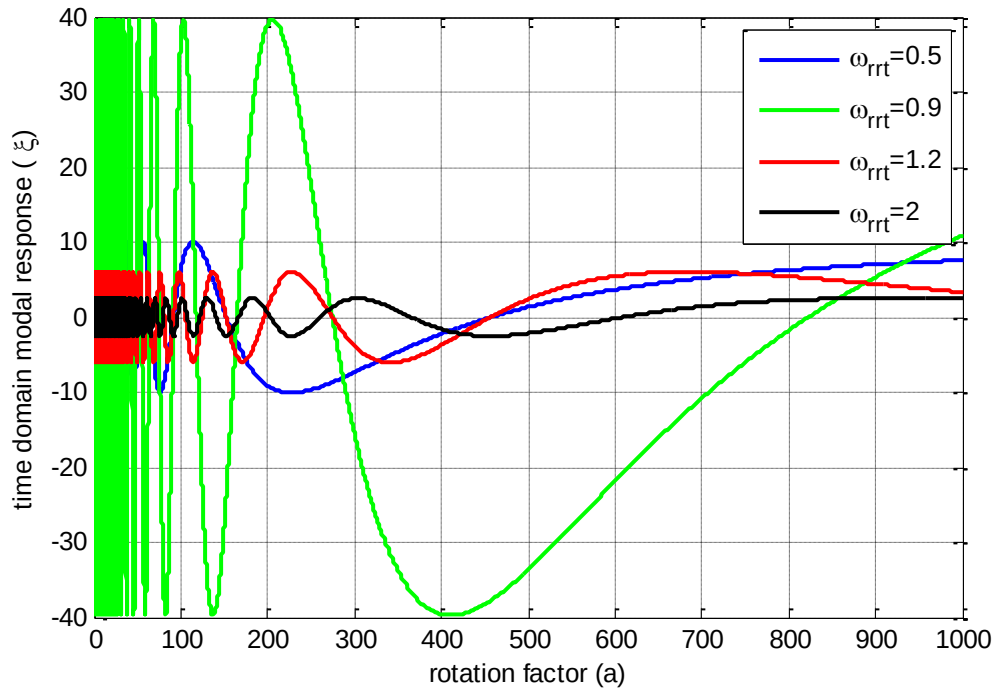


Figure 16. Steady-state time response with respect to rotation factor

In Figure 16, time modal response of the system based on rotation effect is shown. Increment in rotation factor, ends up in decreased time modal response. Depending on the value of frequency ratio of rotating-element thermally-stressed system, passing specific values of rotating factor leads to gradual decrement in response. For example, when excitation frequency is two times fundamental frequency, reaching $a > 300$ deforms oscillatory response to non-oscillatory one and eventually system time response reaches smooth-varying spectrum. Another finding reveals the fact that when $\omega_{rrt} < 1$, system oscillations are a lot more sever than large values of excitation frequency ($\omega_{rrt} > 1$).

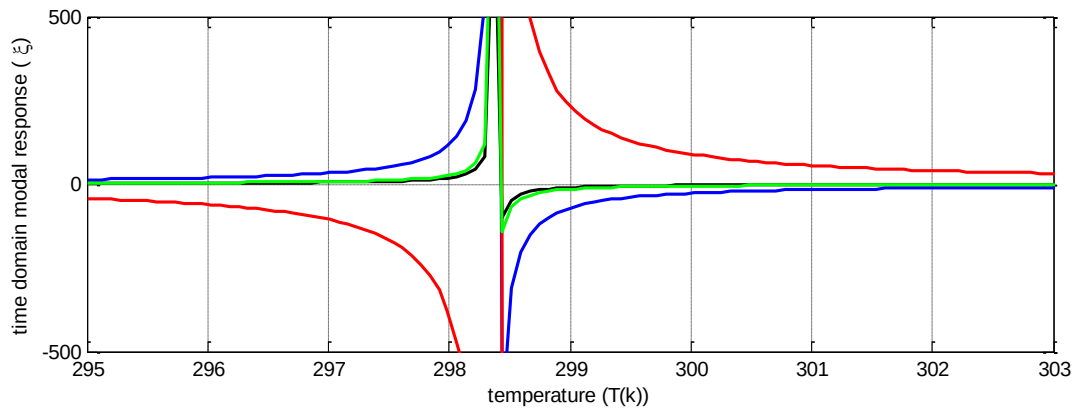


Figure 17. Steady-state time response with respect to temperature

This figure presents modal time response based on temperature variations. It can be observed that for temperature values far from critical value ($T_{cr1} = 298.3739k$), temperature has no effects on time response. However, at the vicinity of critical temperature, time response goes to infinity with different rates depending on the value of $\omega_{rrt}$.

### 3.1.3 Conclusion

In order to design a proper energy harvester element applicable in RFID components; primary step includes proposing a decent mechanical model, scrutinizing static and dynamical responses of the proposed model. The proposed model is a pinned-pinned beam with transverse displacements of main concern. To get a thorough analysis, realistic environmental impacts should be considered. Since the energy scavenger is to perform inside a fixture with sudden temperature fluctuations, the proposed model counts thermal stresses. To reach more precision, rotation of elements around the axis of lateral displacement is also counted. In this regard, modified coupled displacement field is used.

In the rotating-element thermally-stressed model, temperature and rotation influxes can be abbreviated in the following:

Static extent: Temperature fluctuations are effective around the critical temperature available at each vibration mode. At the vicinity of such critical temperatures, static deflection and the corresponding ratio reach infinity. Higher modes get bigger critical temperatures as well. Moreover, severity of temperature impression looks sharper as vibration mode increases. Element rotations do not play a role in static spectrums at all. In other words, static response of the system is independent of rotations around transverse axis.

Dynamic extent: Temperature gain results in gradual cutback of natural vibration frequency. This deduction is maintained up to the critical temperature. At the exact value of critical temperature, oscillations of the system are damped. Element rotations result in decrement of vibration frequencies but enhancement in dynamic deflection ratio. Another point is the fact that dynamic behavior of the system is a function of driving frequency along with both temperature and rotation.

Forced vibrations extent: Time response illustrates similar variations with temperature as those of static and dynamic deflections. In details: around critical temperature, the system shows severe responses towards infinity regardless of driving frequency value. Excitation frequency value however determines slope and shape of the response. It means at resonance condition, break process from horizontal to vertical lines in response plot, takes place through a single point and steeply. However, this whole process for values of driving frequency far away from natural frequency happens throughout smooth and gentle variations. It is also good to note that temperature does not

have any impact over modal response except around critical value. In contrast, element rotations show significantly more impressions over time modal response for all values of rotation factor. Increasing this factor, ends up in less oscillatory shape. In other words, rotation growth damps the system and leads to more stability.

### 3.2 Higher-Order Shear Effect and Rotation Effect over Oscillatory Response of Beam Elements

In this section some preliminaries about the shear effects on the oscillatory response of a beam are presented which is vital particularly for thick beam elements. More importantly, rotating-element method to alter the natural frequencies of beam elements is studied along with the interactions with shearing effect. Such a manipulations in resonant frequency can be highly attractive to energy harvesters as they can be matched to the excitation frequency available at the background to render more power. In more details, a piezoelectric vibration-based energy harvester is made up of a beam as the main substrate (element), it is good to find the influential factors over the oscillatory response of beams. A pinned-pinned (simply-supported) beam is considered to have length L and a width equal to h. In order to derive the mechanical equations of motion, elastic strain energy of the infinitesimal element of the beam is defined in Eq. (3.1), where σ and ε represent Cauchy stress and strain tensors, $I_d$ shows identity tensor, λ shows Lame's constant, and G is shear modulus of rigidity. To consider the shearing effects, Reddy-Levinson theory is adopted. Based on the Reddy-Levinson beam theory, displacement field of a random point on the neutral axis is defined according to the following relations

$$u_x(x,z,t) = -z\frac{\partial w(x,t)}{\partial x} + z\left(1 - \frac{4z^2}{3h^2}\right)\theta(x,t) \tag{3.39a}$$

$$u_y = 0 \tag{3.39b}$$

$$u_z(x, z, t) = w(z, t) \tag{3.39c}$$

where $w(x, t)$ represents lateral displacement of any point on the neutral axis and $\theta(x, t)$ shows the variation of lateral displacement with respect to x. Using Eqs. (2b)-(3c), the following stress and strain elements are found:

$$\varepsilon_{xx} = -z\frac{\partial^2 w}{\partial x^2} + z\left(1 - \frac{4z^2}{3h^2}\right)\frac{\partial\theta(x,t)}{\partial x} \tag{3.40a}$$

$$\varepsilon_{xz} = \frac{1}{2}\left(1 - \frac{4z^2}{h^2}\right)\theta(x, t)) \tag{3.40b}$$

$$\sigma_{xx} = (2G + \lambda)\ \varepsilon_{xx} \tag{3.40c}$$

$$\sigma_{xx} = 2G\ \varepsilon_{xz} \tag{3.40d}$$

Similar to the former section, Hamilton's principle is taken to obtain the governing equations. To use this method, variations of the strain energy should be found:

$$\int_{t_1}^{t_2}\int_0^L \delta U_s dt = \int_{t_1}^{t_2}\int_V (2G + \lambda)\ \varepsilon_{xx}\delta\varepsilon_{xx}\, dVdt \tag{3.41}$$

$2G + \lambda$ can be replaced by E. Substitution of Eqs (3.40a)-(3.41b) into Eq. (3.1) gives the following equation:

$$\int_{t_1}^{t_2}\int_0^L \delta U_s dt = \int_{t_1}^{t_2}\int_V E\ (-z\frac{\partial^2 w}{\partial x^2} + z\left(1 - \frac{4z^2}{3h^2}\right)\frac{\partial\theta(x,t)}{\partial x})(-z\frac{\partial^2}{\partial x^2}\delta w + z\left(1 - \frac{4z^2}{3h^2}\right)\frac{\partial}{\partial x}\delta\theta)\, dVdt \tag{3.42}$$

Eq. (3.42) can be simplified into Eq. (3.43) by using several numerical operations, including integration by parts:

$$\int_{t_1}^{t_2}\int_0^L \delta U_s dt = \int_{t_1}^{t_2}\int_0^L (\frac{\partial^2}{\partial x^2}\left(EI_1 \frac{\partial^2 w}{\partial x^2}\right)\delta w - \frac{\partial}{\partial x}\left(\left(\frac{4}{3h^2}EI_2 - EI_1\right)\frac{\partial^2 w}{\partial x^2}\right)\delta\theta + \frac{\partial^2}{\partial x^2}\left(\left(\frac{4}{3h^2}EI_2 - EI_1\right)\frac{\partial\theta}{\partial x}\right)\delta w - E\left(I_1 + \frac{16}{9h^4}I_3 - \frac{8}{3h^2}I_2\right)\frac{\partial^2\theta}{\partial x^2}\delta\theta + G(A - \frac{16}{h^4}I_2 - \frac{8}{h^2}I_1)\theta\delta\theta)\, dxdt \tag{3.43}$$

in Eq. (3.43), A shows area, E is Young's modulus, $I_1$is second moment of inertia, $I_2$ and $I_3$ are also defined as following:

$$A = bh \tag{3.44a}$$

$$I_1 = \int_A z^2 dA \tag{3.44b}$$

$$I_2 = \int_A z^4 dA \tag{3.44c}$$

$$I_3 = \int_A z^6 dA \tag{3.44d}$$

the translational kinetic energy of the Reddy-Levinson beam is defined in Eq. (3.44):

$$K_1 = \frac{1}{2}\int_V \rho(\left(-z\frac{\partial^2 w}{\partial t\,\partial x} + z\left(1 - \frac{4z^2}{3h^2}\right)\frac{\partial\theta}{\partial t}\right)^2 + (\frac{\partial w}{\partial t})^2)dV \tag{3.45}$$

in Eq. (3.45), ρ is density. Variations of this equation gives the following one:

$$\delta K_1 = \int_V \rho((-z\frac{\partial^2 w}{\partial t\,\partial x}\frac{\partial^2}{\partial t\,\partial x}\delta w + z\left(1 - \frac{4z^2}{3h^2}\right)\frac{\partial\theta}{\partial t}\frac{\partial}{\partial t}\delta\theta) + \frac{\partial w}{\partial t}\frac{\partial}{\partial t}\delta w)dV \tag{3.46}$$

Besides the translational kinetic energy displayed in Eq. (3.46), the coupled kinetic energy term should be considered. This additional term emerges at the time of rotations specifically associated with gyroscope applications. For this purpose, Reddy-Levinson beam is supposed to rotate around a fixed vertical axis. Based on Eq. (3.13) rotational displacement is assumed to have a linear relation with the translational displacements.

$$K_2 = \frac{1}{2}\int_V \rho\, x^2 \left(\frac{\partial\theta}{\partial t}\right)^2 dV \tag{3.47}$$

using a similar process for finding the variations of Eq. (3.47), following equation is found:

$$\delta K_2 = \int_V \rho\, x^2 \frac{\partial\theta}{\partial t}\frac{\partial}{\partial t}\delta\theta dV \tag{3.48}$$

taking variations with respect to time, integration by parts method, following relationships are obtained:

$$\int_{t_1}^{t_2} \delta K_s dt = \int_0^L (-\rho A(1+\alpha^2)\frac{\partial^2 w}{\partial t^2}\delta w + \frac{\partial^2}{\partial x\,\partial t}\Big(\rho I_1 \frac{\partial^2 w}{\partial x\,\partial t} - \rho I_1 \frac{\partial\theta}{\partial t} + \frac{4}{3h^2}\rho I_2 \frac{\partial\theta}{\partial t}\Big)\delta w - \frac{\partial}{\partial t}(-\rho I_1 \frac{\partial^2 w}{\partial x\,\partial t} + \frac{4}{3h^2}\rho I_2 \frac{\partial^2 w}{\partial x\,\partial t} + \rho I_1 \frac{\partial\theta}{\partial t} - \frac{8}{3h^2}\rho I_2 \frac{\partial\theta}{\partial t} + \frac{16}{9h^4}\rho I_3 \frac{\partial\theta}{\partial t})\delta\theta)\, dx \tag{3.49}$$

as a result, the dynamic-vibration equations of the Reddy-Levinson beam are expressed in the following system of coupled equations:

$$-\rho A(1+\alpha^2)\frac{\partial^2 w}{\partial t^2} + \rho I_1 \frac{\partial^4 w}{\partial x^2\,\partial t^2} + \left(\frac{4}{3h^2}\rho I_2 - \rho I_1\right)\frac{\partial^3\theta}{\partial x\,\partial t^2} - EI_1 \frac{\partial^4 w}{\partial x^4} - \left(\left(\frac{4}{3h^2}EI_2 - EI_1\right)\frac{\partial^3\theta}{\partial x^3}\right) = 0 \tag{3.50a}$$

$$\left(\frac{4}{3h^2}EI_2 - EI_1\right)\frac{\partial^3 w}{\partial x^3} + \left(\rho I_1 - \frac{4}{3h^2}\rho I_2\right)\frac{\partial^3 w}{\partial x\,\partial t^2} + \left(\frac{8}{3h^2}\rho I_2 - \rho I_1 - \frac{16}{9h^4}\rho I_3\right)\frac{\partial^2\theta}{\partial t^2} + \left(EI_1 + \frac{16}{9h^4}EI_3 - \frac{8}{3h^2}EI_2\right)\frac{\partial^2\theta}{\partial x^2} - \left(GA - \frac{16}{h^4}GI_2 - \frac{8}{h^2}GI_1\right)\theta = 0 \tag{3.50b}$$

the boundary conditions for this system are:

$$w|_{x=0,L} = 0, \quad \left.\frac{\partial^2 w}{\partial x^2}\right|_{x=0,L} = 0 \tag{3.51}$$

### 3.2.1 Navier's Method and Discretizing Procedure

Eqs. (3.50a) and (3.50b) indicate a linear coupled system of partial differential equations. The Navier method is one of the most efficient methods for discretizing such systems and finding numerical answers. Navier's method is established on the assumption of expressing the functions (translational and rotational field functions), including unknown coefficients and specific admissible functions, in terms of expansion series. Such admissible functions are adopted based on the type of boundary conditions satisfying the equations at the initial boundaries. Thus, for the translational functions, sinusoidal functions are used and, for the rotational function, cosine functions are employed in the series.

$$w(x,t) = \sum_{i=1}^{n} W_n \sin\,(m_n x) e^{i\omega_n t}, m_n = \frac{n\pi}{L} \tag{3.52a}$$

$$\theta(x,t) = \sum_{i=1}^{n} \Theta_n \cos(m_n x) e^{i\omega_n t} \tag{3.52b}$$

in Eqs. (3.52a) and (3.52b), $\Theta_n$ and $W_n$ are the unknown Fourier coefficients, i represents the complex number (i.e.g, $i = \sqrt{-1}$), and $\omega$ is the vibration frequency. Substituting the expansions presented in Eqs. (3.52a) and (3.52b) into Eqs. (3.50a) and (3.50b) results in the following system of homogenous equations:

$$\sum_{i=1}^{n}[\{(1+\alpha^2)\rho A{\omega_n}^2 + \rho I_1 {\omega_n}^2 {m_n}^2\}W_n + \{\left(\frac{4}{3h^2}\rho I_2 - \rho I_1\right){\omega_n}^2 m_n - EI_1 {m_n}^4 + (EI_1 - \frac{4}{3h^2}EI_2){m_n}^3\}\Theta_n] = 0 \tag{3.53a}$$

$$\sum_{i=1}^{n}[\left\{EI_1 - \frac{4}{3h^2}EI_2)m_n{}^3 + \left(\frac{4}{3h^2}\rho I_2 - \rho I_1\right)\omega_n{}^2 m_n\right\}W_n + \{\left(\rho I_1 + \frac{16}{9h^4}\rho I_3 - \frac{8}{3h^2}\rho I_2\right)\omega_n{}^2 + \left(\frac{8}{3h^2}EI_2 - EI_1 - \frac{16}{9h^4}EI_3\right)m_n{}^2 + (\frac{8}{h^2}GI_1 + \frac{16}{h^4}GI_2 - GA)\}\Theta_n] = 0 \quad (3.53b)$$

The system of equations shown represents a linear homogenous system. Based on linear algebra, the determinant of such a system is equal to zero which yields a quadratic equation. Finding the answer of such a system is the frequency.

### 3.2.2 Results and Verification

To numerically validate the model and results presented with benchmark, frequency is to be non-dimensional using the relationship in the following format: $\hat{\omega} = \omega L^2\sqrt{\rho A/EI}$

in Table 1, results from the proposed model are presented in the following table for a range of slenderness ratios ($L/h$).

Table 2. Different frequencies for different length ratios

| $L/h$ | 10 | 20 | 50 |
|---|---|---|---|
| Present | 9.3679 | 9.7359 | 9.8478 |

Table 2 indicates an influence of different slenderness ratios over the natural frequency values, expressing that as the slenderness ratio increases, the difference between the two results diminishes.

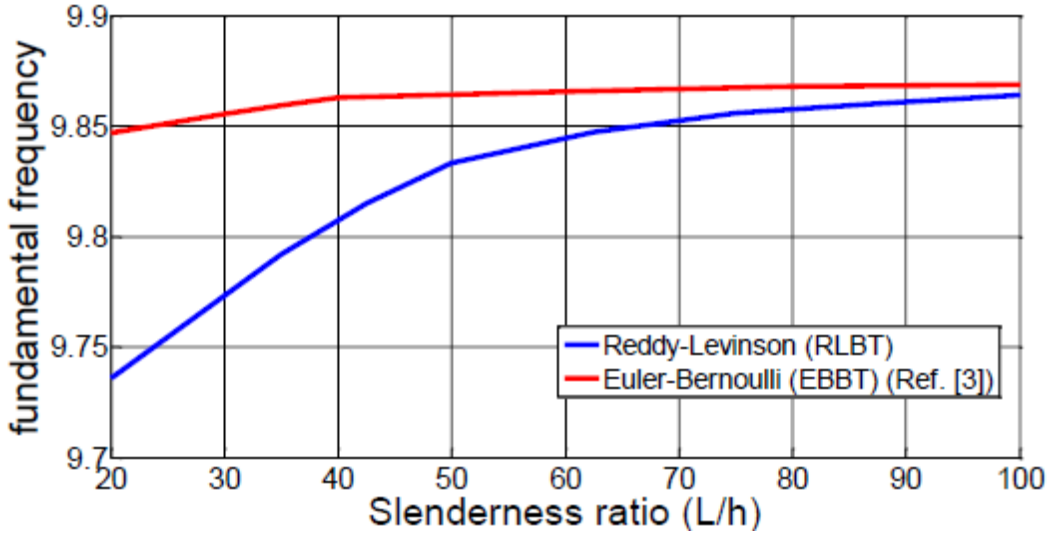


Figure 18. Comparison between EBBT and RLBT for different values of slenderness ratio

An important point to study is the behavior of the system for different values of slenderness ratio. Slenderness ratio is the ratio of the beam length to the beam thickness. Based on figure 18, thinner beams produce more intense oscillations of the beam. In this figure, results for both Euler-Bernoulli (EBBT) and Reddy-Levinson (RLBT) are illustrated and compared. It is observable that for both EBBT and RLBT, increasing the slenderness ratio results in more severe oscillations. Differences between EBBT and RLBT are detected for small values of slenderness ratios. In detail, when considering a thick beam, RLBT yields smaller and quite gentle oscillations in comparison to the EBBT. Briefly, based on RLBT, oscillations of a system are more sensitive to the slenderness ratios than EBBT.

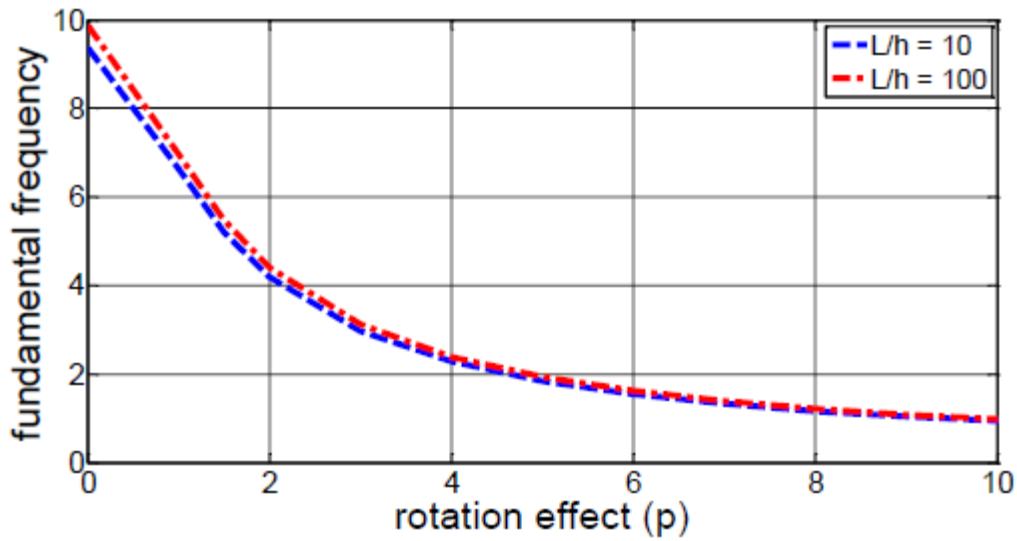


Figure 19. Impression of coupled rotation over fundamental frequency for thin and thick RLBT beams

Observations from the figure 19 demonstrate decrement of oscillations with respect to high values of the rotation parameter ($\alpha$). In other words, the rotation of the beam around a fixed axis (representing the gyroscope mount axis) decreases the vibrations. Another finding discloses the fact that, for both thin beams (big slenderness ratios) and thick beams (small slenderness ratios), the same pattern in oscillatory response is detected.

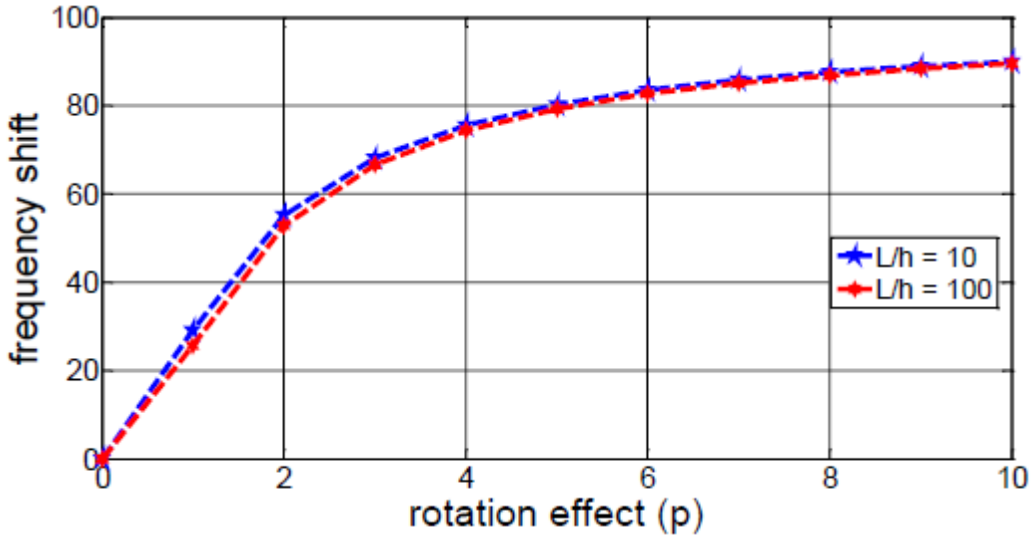


Figure 20. Frequency shift based on rotation effects for thin and thick RLBT beams

This figure is plotted to indicate the effect of rotation in terms of frequency shift. In other words, the percentage of frequency mutation due to rotation effects helps us to understand the intensity of rotation impacts. As shown in the figure, regardless of the slenderness ratio, the rotation effect can alternate the oscillatory response up to 90%. This figure illustrates the impacts of a coupled displacement field and rotations on the dynamic behavior of electro-mechanical systems.

### 3.2.3 Conclusion

Following the analysis of vibratory response of beam elements, shearing effects resulting from thick beams is an influential factor. So, in this section, oscillatory response of a rotating Reddy-Levinson beam is studied based on the coupled displacement field theory. This theory was first introduced by Babaei and Yang to consider the simultaneous effects of translation and rotation of electromechanical systems for the purpose of precise and better design and analysis. Current results compared with benchmark findings indicate

a good level of accuracy for the current model. Findings disclose that rotation decreases vibration frequency and for very large values of rotation, vibrations tend to diminish. This finding is valid for any range of slenderness ratio. The only distinction referring to slenderness ratio takes place at very insignificant rotation velocities. Thus, it has been found that highly-rotating systems essentially behave independently of the slenderness ratio. Eventually, rotation effects in terms of coupled displacement field theory can mitigate and suppress vibrations; which can be a key point in design of energy harvester. In other words, rotations lead to less extractable energy but a more durable energy harvester device from a longevity perspective. Further investigation is required to address the effect of rotations over increasing frequency bandwidth, which can be attractive from all aspects including device durability, vibration suppression and most energy harness-able.

### 3.3 Deriving System of Coupled Electromechanical Integral-Partial Differential Equations

In this section, using coordinate-dependent variational method, mechanical equation of motion with electrical coupling and electrical circuit equation will be obtained for the cantilever beam undergoing temperature fluctuations. Such system of equations pertains to the cantilever beam covered with piezoelectric layers at the top and bottom surfaces which is connected to the electric circuit with resistance load.

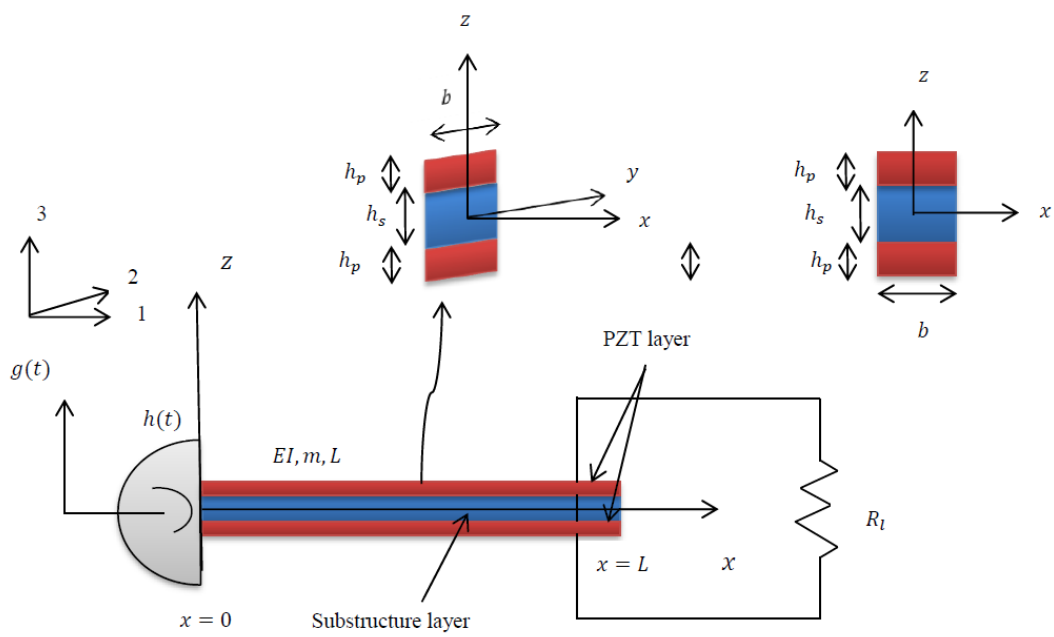


Figure 21. Cantilever beam with piezoelectric layers at the top and bottom

Geometric properties of the cantilever are shown in Figure 21. To consider non-conservative work induced to the system, extended Hamilton's principle is in use. Based on the plane-stress assumptions for liner isotropic elements following the Hooke's law, constitutive relations of substrate and piezoelectric layers can be stated as following [35]:

$$T_1{}^s = E_s S_1 \tag{3.54}$$

$T_1{}^s$ is stress, $E_s$ represents elastic modulus and $S_1$ is strain of substrate layer. The above equation and most of the following equations except the novelties of this paper are derived from the reference paper [35]. Based on piezoelectric constitutive equations stress-strain and electric field relations are:

$$T_1{}^p = E_p(S_1 - d_{31}E_3) \tag{3.55}$$

$$\varepsilon_{33}{}^s = \varepsilon_{33}{}^T - d_{31}{}^2 E_p \tag{3.56}$$

$$D_3 = d_{31}T_1{}^p + \varepsilon_{33}{}^T E_3 \tag{3.57}$$

${T_1}^p$,$E_p$ are stress at piezoelectric layers and elastic modulus at constant electric field of piezoelectric. $d_{31}$ is piezoelectric coupling coefficient. $E_3$ is electric field in $z$-direction. ${\varepsilon_{33}}^s$ and ${\varepsilon_{33}}^T$ show permittivity at constant strain and stress. $D_3$ is electric displacement which acts only in $z$-difrection, respectively. Two types of damping mechanisms, internal and external, are considered in this study. Internal damping is modeled as Kelvin-Voigt damping also named as strain-rate damping [35]:

$$T_d = c_s \dot{S}_1 \tag{3.58}$$

$T_d$ is stress due to strain-rate damping and $c_s$ illustrates viscoelastic damping coefficient due to structural viscoelasticity. Dot sign indicates differentiation in temporal domain. Both internal and external damping satisfy proportional damping criteria. For the proposed cantilever beam model, the kinetic energy ($U_k$) due to base excitations is [35]:

$$U_k = \frac{1}{2}\int_0^L \rho A(\dot{w}_{rel}(x,t) + \dot{w}_b(x,t))^2\, dx \tag{3.59}$$

$\rho$ is density and $A$ denotes cross section area of the beam. Strain energy generated due to deflections ($U_s$) is comprised of energy of substrate and energy of piezoelectric layers integrated over volume fractions ($V_s, V_p$):

$$U_s = U_{s-1} + U_{s-2} = \frac{1}{2}\int_{V_s} {T_1}^s S_1 dV_s + \frac{1}{2}\int_{V_p} {T_1}^p S_1 dV_p = \tag{3.60}$$

$$\frac{1}{2}\int_{V_s} E_s {S_1}^2 dV_s + \frac{1}{2}\int_{V_p} E_p({S_1}^2 - S_1 d_{31} E_3) dV_p$$

similar to the preceding sections, temperature shifts exerted to the system show up in the form of energy term which is due to the thermal stress:

$$U_T = \frac{1}{2}\int_{V_s} T^{th}(w_{rel,x})^2\, dV_s \tag{3.61}$$

thermal stress ($T^{th}$) can be reputed as:

$$T^{th} = -E_s \alpha_s \Delta T \tag{3.62}$$

$\alpha$ is the thermal expansion coefficient of substrate layer. Electrical energy ($W_e$) is [35]:

$$W_e = \frac{1}{2}\int_{V_p} D_3 E_3 dV_p \tag{3.63}$$

using following auxiliary relations, Eq. (3.63) can be written in the following format [35]:

$$E_3 = -{}^{v(t)}\!/_{(2h_p)} \tag{3.64}$$

$$D_3 = d_{31} E_p S_1 - \varepsilon_{33}{}^s \frac{v(t)}{2h_p} \tag{3.65}$$

$$C_p = \frac{\varepsilon_{33}{}^s bL}{h_p} \tag{3.66}$$

$$v(t) = R_l \dot{q}_3(t) \tag{3.67}$$

$$W_e = \frac{1}{2}\int_{V_p} -d_{31} E_p z w_{rel,xx} (\frac{-v(t)}{2h_p}) dV_p + \frac{1}{2}\int_{V_p} \varepsilon_{33}{}^s (\frac{-v(t)}{2h_p})^2 dV_p \tag{3.68}$$

in which $v(t)$ is voltage across the resistive load and $q_3(t)$ is electric charge. External virtual work ($W_{nc}$) resulting from damping and dissipating resistive load of electrical circuit is [35]:

$$W_{nc} = -\frac{d}{dt}\int_0^L \frac{1}{2} c_a \, (w_{rel} + w_b)^2 dx - \frac{d}{dt}\int_{V_s} \frac{1}{2} T_s S_1 \, dV_s - \frac{d}{dt}(\frac{1}{2} R_l q_3{}^2(t)) \tag{3.69}$$

based on the extended Hamilton's variational principle, variations of energy terms' Lagrangian ($L = U_k - U_s - U_{th} + W_e + W_{nc}$) is zero in a short time interval ($\int_{t_1}^{t_2} \delta L dt = 0$). To this end, variations of energy terms are to be obtained:

$$\delta U_k = \int_0^L \rho A \, (\dot{w}_{rel}(x,t) + \dot{w}_b(x,t)) \delta \dot{w}_{rel} dx \tag{3.70}$$

$$\delta U_{s-1} = E_s I_s w_{rel,xx} \delta w_{rel,x}\Big|_0^L - E_s I_s w_{rel,xxx} \delta w_{rel}\Big|_0^L + \int_0^L E_s I_s w_{rel,xxxx}\, \delta w_{rel} dx \tag{3.71}$$

$$\delta U_{s-2} = 2 I_p E_p w_{rel,xx} \delta w_{rel,x}\Big|_0^L - 2 E_p I_p w_{rel,xxx} \delta w_{rel}\Big|_0^L + \int_0^L 2 E_p I_p w_{rel,xxxx}\, \delta w_{rel} dx + -Q_p E_p \frac{d_{31}}{2h_p} v(t)[H(x) - H(x - L)]\delta w_{rel,x}\Big|_0^L + Q_p E_p \frac{d_{31}}{2h_p} v(t)[\delta(x) - \delta(x-L)]\delta w_{rel}\Big|_0^L - \int_0^L Q_p E_p \frac{d_{31}}{2h_p} v(t)\left[\acute{\delta}(x) - \acute{\delta}(x-L)\right] \delta w_{rel} dx - \int_0^L Q_p E_p \frac{d_{31}}{2h_p} w_{rel,xx} \delta \dot{v}(t) dx \tag{3.72}$$

$$\delta U_{th} = -E_s A_s \alpha \Delta T \delta w_{rel,x}\Big|_0^L + \int_0^L E_s A_s \alpha \Delta T w_{rel,xx} \delta w_{rel} dx \tag{3.73}$$

$$\delta W_e = = -Q_p E_p \frac{d_{31}}{2h_p} v(t)[H(x) - H(x-L)]\delta w_{rel,x}\Big|_0^L + Q_p E_p \frac{d_{31}}{2h_p} v(t)[\delta(x) - \delta(x-L)]\delta w_{rel}\Big|_0^L - \int_0^L Q_p E_p \frac{d_{31}}{2h_p} v(t)\left[\acute{\delta}(x) - \acute{\delta}(x-L)\right] \delta w_{rel} dx - \int_0^L Q_p E_p \frac{d_{31}}{2h_p} w_{rel,xx} \delta \dot{v}(t) dx + \int_{V_p} \varepsilon_{33}{}^s \frac{v(t)}{(2h_p)^2} \delta v(t) dV_p \tag{3.74}$$

$$\delta W_{nc} = -\int_0^L c_a(\dot{w}_{rel} + \dot{w}_b)\delta w_{rel} dx - \int_0^L c_s I\, \dot{w}_{rel,xxxx} \delta w_{rel} dx - \frac{\dot{v}(t)}{R_l} \delta v \tag{3.75}$$

in these equations $I_s$, $I_p$ are second moment of inertia of substrate and piezoelectric layers. $H(x)$ is Heaviside (unit step) function to model concentrated coverage of electrodes in $x$-direction. $\delta(x)$ is Dirac delta function. $Q_p$ is the first moment of inertia of piezoelectric layers. $c_a$ denotes viscous air damping coefficient.

$$I_s = \int_{A_s} z^2 dA_s = \frac{1}{12} b {h_s}^3 \tag{3.76}$$

$$Q_p = \int_{A_p} z dA_p = \frac{1}{2} b h_p (h_p + h_s) \tag{3.77}$$

$$I_p = \int_{A_p} z^2 dA_p = \frac{1}{3} b h_p ({h_p}^2 + \frac{3}{2} h_p h_s + \frac{3}{4} {h_s}^2) \tag{3.78}$$

$$EI = E_s I_s + 2E_p I_p \tag{3.79}$$

$EI$ is the total flexural rigidity of cantilever beam in bending. After some mathematical operations, system of coupled electromechanical partial integral-differential equations of the thermally stressed piezoelectric beam is:

$$\rho A \ddot{w}_{rel} + EI w_{rel,xxxx} + E_s A_s \alpha_s \Delta T w_{rel,xx} + c_a \dot{w}_{rel} + c_s I \dot{w}_{rel,xxxx} - \Gamma_2 v(t)[\acute{\delta}(x) - \acute{\delta}(x - L)] = -\rho A \ddot{w}_b - c_a \ddot{w}_b \tag{3.80}$$

$$\int_0^L \Gamma_2 \dot{w}_{rel,xx} dx + \frac{C_p}{2} \dot{v} = -\frac{v}{R_l} \tag{3.81}$$

where, $\Gamma_2$ is:

$$\Gamma_2 = \frac{E_p Q_p d_{31}}{h_p} \tag{3.82}$$

boundary conditions of the thermally stressed cantilever energy harvester are:

$$x = 0, \tag{3.83}$$

$$w_{rel} = w_{rel,x} = 0$$

$$x = L,$$

$$w_{rel,xx} = w_{rel,xxx} = 0$$

### 3.3.1 Analytical-Numerical Solution Approach Based on Modal Decomposition Method

Based on modal decomposition, relative vibratory motion of the distributed-parameter system can be expressed by convergent expansion series [35]:

$$w_{rel}(x,t) = \sum_{n=1}^{\infty} \phi_n(x)\,\eta_n(t) \tag{3.84}$$

$\phi_n(x)$ is mass-normalized eigenfunction and modal coordinate of the system in $n$th vibration mode. $\phi_n(x)$ can be obtained from the corresponding undamped cantilever system with free vibration and stress-free conditions:

$$\phi_n(x) = \frac{1}{\sqrt{\rho AL}}\left(\cosh\lambda_n x - \cos\lambda_n x - \frac{\cosh\lambda_n L + \cos\lambda_n L}{\sinh\lambda_n L + \sin\lambda_n L}(\sinh\lambda_n x - \sin\lambda_n x)\right) \tag{3.85}$$

$\lambda_n L$ is the root of the following transcendental equation:

$$1 + \cos\lambda_n L \cosh\lambda_n L = 0 \tag{3.86}$$

substituting Eq. (3.83) into Eq. (3.79), and multiplying by $\phi_m(x)$, and utilizing orthogonality of eigenfunctions, Eq. (3.79) can be re-written as:

$$\ddot{\eta}_n(t) + \left(\frac{c_s I}{EI}{\omega_n}^2 + \frac{c_a}{\rho A}\right)\dot{\eta}_n(t) + \left({\omega_n}^2 + {M_n}^{th}\right)\eta_n(t) = \chi_n v(t) + \rho A \gamma_n Y_0 {\omega_e}^2 e^{j\omega_e t} \tag{3.87}$$

Where:

$$D_n = \int_0^L \phi_{n,xx}(x)\phi_n(x)dx \tag{3.88}$$

$$\gamma_n = \int_0^L \phi_n(x)dx \tag{3.89}$$

$$\chi_n = \Gamma_2 \phi_{n,x}\Big|_L \tag{3.90}$$

$$M_n{}^{th} = E_s A_s \alpha_s \Delta T D_n \tag{3.91}$$

it is also important to note that according to the findings of section 3.1, $\omega_n{}^2 + M_n{}^{th}$ is identical to $\omega_n{}^2$. The excitations are supposed to be simple harmonic excitation: $w_b = Y_0 e^{j\omega_e t}$. Since the model is linear and based on the principle of superposition, output voltage can also be assumed as a harmonic function with amplitude $V_0$ [35]:

$$v(t) = V_0 e^{j\omega_e t} \tag{3.92}$$

substituting Eqs. (3.92) and (3.84) into Eq. (32) yields the following equation:

$$\dot{v}(t) + \frac{1}{\tau_c} v(t) = -\sum_{n=1}^{\infty} \Theta_n \dot{\eta}_n(t) \tag{3.93}$$

$$\tau_c = \frac{C_p R_l}{2} \tag{3.94}$$

$$\Theta_n = \frac{2\Gamma_2}{C_p} \phi_{n,x}\Big|_L \tag{3.95}$$

in energy harvesting systems, steady-state response of the vibratory part is of main concern. Thus, particular answer part of Eq. (3.86) is to be obtained in the following form:

$$\eta_n(t) = \frac{\rho A \gamma_n Y_0 \omega_e{}^2 + \chi_n V_0}{\omega_{n-th}{}^2 - \omega_e{}^2 + j2\zeta_n \omega_n \omega_e} e^{j\omega_e t} \tag{3.96}$$

in Eq. (3.96), thermally-stressed natural frequency obtained informer section is replaced with natural frequency term. Also $\zeta_n$ is modal damping term [35]:

$$\zeta_n = \frac{c_a}{2\rho A \omega_n} + \frac{c_s I}{2EI} \omega_n \tag{3.97}$$

now, substitution of Eq. (3.97) into Eq. (3.87) results output voltage across the resistive load:

$$v(t) = \frac{\sum_{n=1}^{\infty} \frac{-j\Theta_n \rho A Y_0 \gamma_n {\omega_e}^3}{{\omega_{n-th}}^2 - {\omega_e}^2 + j2\zeta_n \omega_n \omega_e}}{\frac{1}{\tau_c} + j\omega_e + \sum_{n=1}^{\infty} \frac{j\Theta_n \chi_n \omega_e}{{\omega_{n-th}}^2 - {\omega_e}^2 + j2\zeta_n \omega_n \omega_e}} e^{j\omega_e t} \tag{3.98}$$

besides to the output voltage, shunted vibration response can be found using Eq. (3.98), (3.84) and (3.85):

$$w_{rel}(x,t) = \sum_{n=1}^{\infty} \frac{1}{\sqrt{\rho A L}} (\cosh \lambda_n x - \cos \lambda_n x - \frac{\cosh \lambda_n L + \cos \lambda_n L}{\sinh \lambda_n L + \sin \lambda_n L} (\sinh \lambda_n x - \sin \lambda_n x)) \frac{\rho A \gamma_n Y_0 {\omega_e}^2 + \chi_n \frac{\sum_{n=1}^{\infty} \frac{-j\Theta_n \rho A Y_0 \gamma_n {\omega_e}^3}{{\omega_{n-th}}^2 - {\omega_e}^2 + j2\zeta_n \omega_n \omega_e}}{\frac{1}{\tau_c} + j\omega_e + \sum_{n=1}^{\infty} \frac{j\Theta_n \chi_n \omega_e}{{\omega_{n-th}}^2 - {\omega_e}^2 + j2\zeta_n \omega_n \omega_e}}}{{\omega_{n-th}}^2 - {\omega_e}^2 + j2\zeta_n \omega_n \omega_e} e^{j\omega_e t} \tag{3.99}$$

### 3.3.2 Results and Discussion

In this section parametric study of steady-state response of the proposed electromechanical system is to be elucidated. Piezoelectric systems under an input (mechanical excitation), operate with both transient and steady-state responses. Since energy scavenging takes place in long time span, steady-state response is the desired one for analysis. Geometrical parameters of the harvester piezoelectric beam are presented in the former tables of current chapter.

Table 3. Geometric and mechanical properties of beam [35]

| | |
|---|---|
| Beam length | $L = 100mm$ |
| Beam width | $b = 20mm$ |
| Substrate layer thickness | $h_s = 5\mu m$ |
| PZT layer thickness | $h_p = 4\mu m$ |
| PZT modulus of elasticity | $E_p = 66\ GPa$ |
| PZT mass density | $\rho = 7800 \frac{kg}{m^3}$ |
| PZT coupling coefficient | $d_{31} = -190 \frac{pm}{V}$ |
| PZT permittivity at constant strain | ${\varepsilon_{33}}^s = 15.93 \frac{nF}{m}$ |

Temperature shift range is supposed to be big enough to be enforceable in further applications besides to the RFID tag communication systems. Reference temperature (ambient temperature) is supposed to be: $T_{ref} = 20^{o}C$. Using the method of modal decomposition, distributed-parameter model is considered as infinite lumped-parameter models with infinite degrees of freedom (DOF). On the other hand, it is proved in benchmark that matching of driving frequency with natural frequencies results in maximum (utmost) values in output voltage. Furthermore, such remarkable peak values pertain to initial natural frequencies. As a result, excitation frequency is considered to cover the first three vibration modes of the mechanical part. Since, effect of various resistive load values over output voltage and shunted vibration response are widely explained in benchmark, we take a representative value of $R_l = 10^6\Omega$ for current analysis. As a standard scale to figure out responses of a system, electromechanical frequency response function (FRF) is provided. Damping ratio is considered following values which are obtained experimentally by Erturk and Inman [35]:

Table 4. Proportional damping values for first three modes of vibration [35]

| $\zeta_1$ | $\zeta_1$ | $\zeta_1$ |
|---|---|---|
| 0.010 | 0.013 | 0.033 |

Output voltage frequency response function (V-FRF): mostly, in coupled electromechanical systems voltage FRF is described as modulus of output voltage to the base acceleration ratio [35].

$$\frac{v(t)}{\ddot{g}(t)} = \frac{\sum_{n=1}^{\infty} \frac{-j\Theta_n \rho A \gamma_n \omega_e}{{\omega_{n-th}}^2 - {\omega_e}^2 + j2\zeta_n \omega_n \omega_e}}{\frac{1}{\tau_c} + j\omega_e + \sum_{n=1}^{\infty} \frac{j\Theta_n \chi_n \omega_e}{{\omega_{n-th}}^2 - {\omega_e}^2 + j2\zeta_n \omega_n \omega_e}} \tag{3.100}$$

to give a better description, $\phi_n(x)$ is normalized with respect to mass of the system. However, thermal stress effect is independent of mass/inertia and bending stiffness of the system. Consequently, to calculate values of this factor, MATLAB is employed. Using MATLAB, voltage-FRF (V-FRF) of current model is obtained and demonstrated as follows:

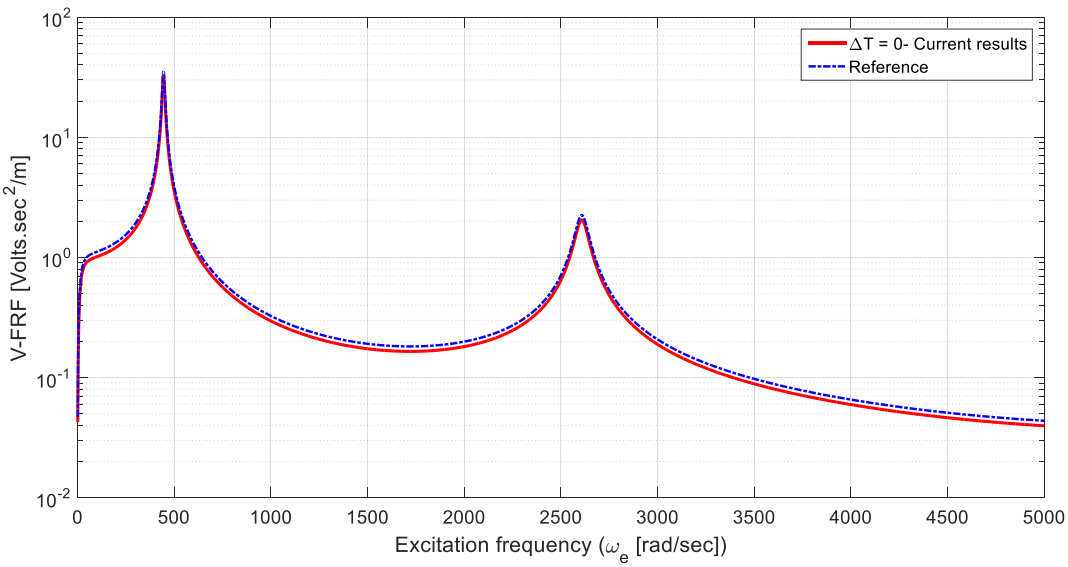


Figure 22. Verification of current results

In Figure 22, the current model is compared with the experimentation result reported in the benchmark to verify current results accuracy. Obviously, deleting thermal stress effects ($\Delta T = 0$), the results should be identical to the case reported in benchmark. The red line represents the current model whenever the temperature fluctuations are zero. This red line is in a good level of agreement with the blue line which certifies the accuracy of the current model.

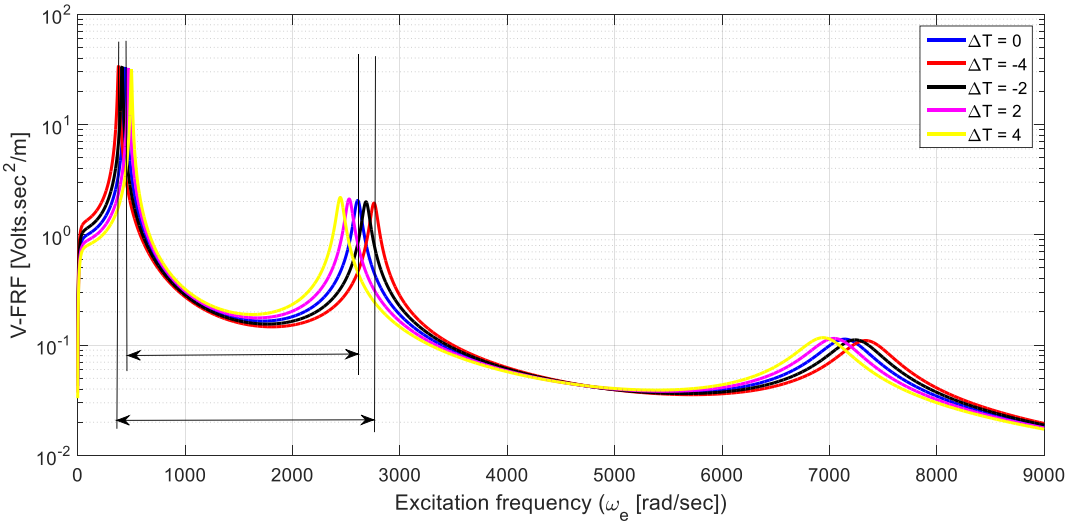


Figure 23. Voltage frequency response function (V-FRF)

Figure 23 is plotted for five different temperature shifts. It can be interpreted that with temperature increment ($\Delta T = -2, -4$), first V-FRF crest (taking place at $\omega_e \rightarrow \omega_1$) is tilted to the left. In other words, increasing temperature leads to the occurrence of the first maximum value of V-FRF in smaller frequency. Conversely, such thermal manipulation drives occurrence of second and third summits in a bit bigger frequency. Since it is complicated to find extreme/tip values with calculation treatment, approximate MATLAB tool named as "Data Cursor" is adopted. It can be deduced that the maximum value of the obtainable voltages is not manipulated by temperature fluctuations. However, the effective frequency bandwidth has changed. According to the observations mentioned, temperature increments result in widened bandwidth which can be highly appealing and helpful. As for the shunted vibration frequency response function ($W_{rel}$-FRF), relative motion transmissibility function of the energy harvester is of concern which can be gained by finding ratio of shunted relative tip displacement to input excitation. $W_{rel}$-FRF provides

information addressing shunted vibration response due to the electrical coupling. This FRF is accompanied by impression of thermal stress as well [35].

$$\frac{w_{rel}(x,t)}{g(t)} = \sum_{n=1}^{\infty} \frac{1}{\sqrt{\rho AL}} (\cosh \lambda_n x - \cos \lambda_n x - \frac{\cosh \lambda_n L + \cos \lambda_n L}{\sinh \lambda_n L + \sin \lambda_n L} (\sinh \lambda_n x - \sin \lambda_n x)) \frac{\rho A \gamma_n Y_0 {\omega_e}^2 + \chi_n \frac{\sum_{n=1}^{\infty} \frac{-j\Theta_n \rho A \gamma_n {\omega_e}^3}{{\omega_{n-th}}^2 - {\omega_e}^2 + j2\zeta_n \omega_n \omega_e}}{\frac{1}{\tau_c} + j\omega_e + \sum_{n=1}^{\infty} \frac{j\Theta_n \chi_n \omega_e}{{\omega_{n-th}}^2 - {\omega_e}^2 + j2\zeta_n \omega_n \omega_e}}}{{\omega_{n-th}}^2 - {\omega_e}^2 + j2\zeta_n \omega_n \omega_e} \tag{3.101}$$

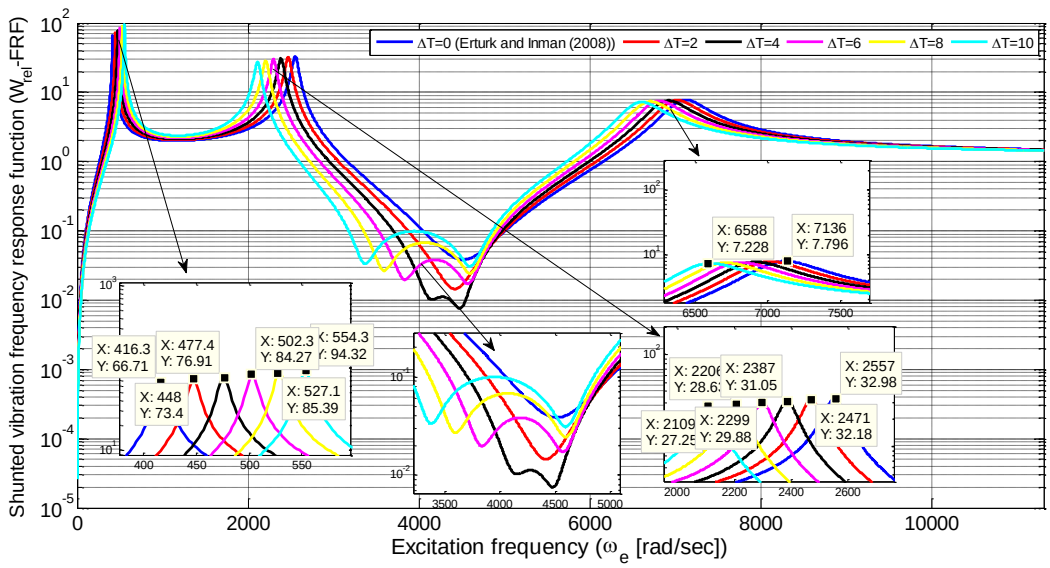


Figure 24. Shunted vibration frequency response function (Wrel-FRF)

Shunted vibration FRF is plotted in Figure 24 for five sampling temperature shifts. Results of mechanical FRF are rectified with those available in the benchmark. Several findings can be achieved from this figure. Firstly, temperature fluctuations gradually deform minimal value which happens between second and third excitation modes ($\omega_e = \omega_2$ and $\omega_e = \omega_3$). In details, for zero temperature fluctuations or quite small values of $\Delta T$, there is only one minima point. Contrarily, As highlighted in the box for $\Delta T \geq 4$ double

consecutive minima points emerge. Mechanical FRF profile passing from the first minima to the second one reveals a concave-wise curve. Besides, comparing different concave curves in this interval ascertains the fact that greater temperature shifts end up in approximately identical minima points. However, for mild values of temperature shift, former minima is less extreme than the latter one corresponding to bigger frequency value. Moreover, temperature increments lead to less minima point(s). Next observation addresses the aberration of mechanical FRF in two different manners. Temperature growth drags the first (major) crest point to the right while second and third climax points are inclined to the left. Minima point(s) deviate to the left. Increasing temperature yields concave curves for all three excitation modes. For the first excitation mode, temperature fluctuations cause severe and intense variations of mechanical FRF. However, such mutations are mild and gentle for the second and specifically for the third excitation mode. In contrast to the electrical FRF, there are not any double-successive summits when excitation frequency is identical to the first natural frequency.

# CHAPTER 4. ANALYTICAL NUMERICAL ANALYSIS OF OSCILLATOR-SPRING SUBSYSTEM INTEGRATION

## 4.1 Reinforced Piezoelectric Vibration Energy Harvester Using Cantilever-Spring-Oscillator System - Pure Mechanical Analysis

In this section of the dissertation, an improved model for energy harvesters will be presented and proposed. As discussed earlier, efficacy of a piezoelectric vibration-based energy harvester (PVEH) is assessable according to three items: 1- maximum amount of extractable voltage (or power), 2- effective frequency bandwidth, and 3- transmissibility function of the oscillator. The former two cases are usually more attractive and integral to the scholars and designers. Lack of match (synchrony) between the excitation (driving) frequency and the natural frequency of the cantilever beam is one of the main challenges and issues with PVEH. Such a drawback leads to trifle extractable power and inefficiency of the harvester module. To remedy such disadvantage, tuning masses has been widely utilized with PVEH. Such a tip mass (end mass, attached mass, tuning mass) is usually constrained to lateral displacement of the cantilever beam at the free end (tip). With such constraint, although the maximum voltage is enhanced it yields to fleet and ephemeral oscillations. The shortened duration of oscillations results in fugacious chance to harness the electric power. In order to further improve the efficacy of the harvester in terms of maximum extractable power and more importantly to obviate the fleet (transient) response challenge, the conventional cantilever-tuning mass system is supposed to be replaced with a cantilever-spring-oscillator system and instead of constraining the tuning mass to the tip of the beam, the augmented inertia will be hung by means of a spring and move as an oscillator. Such modification results in a more perplexing system with three differential equations rather than two, increases the degrees of freedom from three to four and the

generalized modal coordinates from two to three. As compensation for such added complexity, the new system will render one more eigenvalue smaller than the conventional first eigenvalue (1.8759). Correspondingly, one more resonance will be generated. Such new behavior of the harvester system ends up in significantly wider effective frequency bandwidth and strikingly more amount of power extractable in a given bandwidth. This way, the PVEH system will be notably and efficiently improved and developed. To model such reinforced PVEH; first, mechanical-domain modeling is required. This means to study the cantilever-spring-oscillator system from advanced vibrations and dynamics viewpoint to eventually derive the governing equations of motion, which provides valuable information about the vibratory response of the system including: frequency shifts, and mode shapes, and transmissibility functions.

## 4.2 Governing Equations of Motion, Boundary Conditions and Kinematics of Cantilever-Oscillator-Spring

Schematic configuration of the elastically restrained oscillator and cantilever beam system is presented in Figure 32. Oscillator with mass $m_0$ is attached to the cantilever via a linear spring with constant of $k_s$.

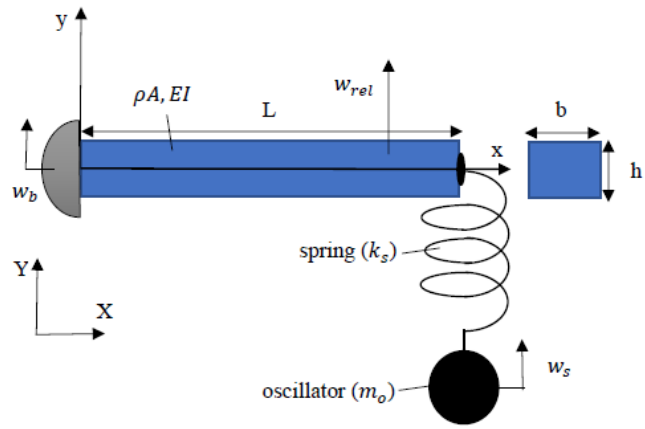


Figure 25. Schematic of cantilever-oscillator-spring system

$\rho$ is beam density, $A$ is the cross-section area, $E$ represents Young's modulus, $I$ is second moment of inertia, beam has length of $L$, thickness of $h$, width of $b$; $x - y$ represents the Lagrangian cartesian coordinates, $X - Y$ is the fixed Eulerian cartesian coordinates. $w_b(x,t)$ is the base excitation in case of forced vibrations, and $w_{rel}(x,t)$ and $w_s(t)$ represent relative lateral displacement of beam and oscillator with respect to the Lagrangian coordinates, respectively. According to Euler-Bernoulli beam models; displacement fields are defined as following [35]:

$$\mathrm{u_x(x,z,t)} = -\mathrm{y}\frac{\partial \mathrm{w}_{rel}}{\partial \mathrm{x}}(\mathrm{x,t}) \tag{4.1a}$$

$$\mathrm{u_y(x,z,t)} = \mathrm{w}_{rel}(x,t) \tag{4.1b}$$

$$\mathrm{u_z(x,z,t)} = 0 \tag{4.1c}$$

4.3 Variational Terms and Extended Hamilton's Principle

According to the modified couple stress theory, variations of strain energy terms due to deformation ($U_{s-1}$), spring ($U_{s-2}$) and kinetic energy terms ($U_k$) are as follows [35]:

$$\delta U_{s-1} = (EI + Gl^2A)\frac{\partial^2 w_{rel}}{\partial x^2}\delta\frac{\partial w_{rel}}{\partial x}\Big|_0^L - (EI + Gl^2A)\frac{\partial^3 w_{rel}}{\partial x^3}\delta w_{rel}|_0^L + \int_0^L (EI + Gl^2A)\frac{\partial^4 w_{rel}}{\partial x^4}\delta w_{rel}dx \tag{4.2a}$$

$$\delta U_{s-2} = k_s w_s \delta w_s \tag{4.2b}$$

$$\delta U_k = \int_o^L \rho A\big(\ddot{w}_{rel}(x,t) + \ddot{w}_b(x,t)\big)\delta w_{rel}dx + m_s\big(\ddot{w}_{rel}(L,t) + \ddot{w}_b(L,t) + \ddot{w}_s(t)\big)\delta w_s + m_s\big(\ddot{w}_{rel}(L,t) + \ddot{w}_s(t)\big)\delta w_{rel} + \int_o^L m_s\ddot{w}_b(x,t)\delta(x-L)\delta w_{rel}dx \tag{4.2c}$$

variations of nonconservative dissipating terms ($W_{nc}$) are:

$$\delta W_{nc} = -\int_0^L c_a(\dot{w}_{rel} + \dot{w}_b)\delta w_{rel}dx - \int_0^L c_s I\frac{\partial^4 \dot{w}_{rel}}{\partial x^4}\delta w_{rel}dx \tag{4.3}$$

where, $G$ represents rigidity modulus of beam, $l$ is the material length scale parameter, and $\delta$ is the Dirac delta function. $c_a$ is viscous air damping coefficient, and $c_s$ represents equivalent coefficient of strain rate damping (Kelvin-Voigt damping). Using the Extended Hamilton's variational approach, governing system of equations are as follows:

$$\rho A\ddot{w}_{rel}(x,t) + (EI + Gl^2A)\frac{\partial^4 w_{rel}}{\partial x^4} + c_s I\frac{\partial^4 \dot{w}_{rel}}{\partial x^4} + c_a\dot{w}_{rel} = -\big(\rho A + m_s\delta(x-L)\big)\ddot{w}_b(x,t) - c_a\dot{w}_b \tag{4.4a}$$

$$m_s\big(\ddot{w}_{rel}(L,t) + \ddot{w}_b(L,t) + \ddot{w}_s(t)\big) + k_s w_s = 0 \tag{4.4b}$$

corresponding boundary condition are shown in the following:

$$w_{rel}(0,t) = 0 \tag{4.5a}$$

$$\frac{\partial}{\partial x}w_{rel}(0,t) = 0 \tag{4.5b}$$

$$\frac{\partial^2}{\partial x^2}w_{rel}(0,t) = 0 \tag{4.5c}$$

$$(EI + Gl^2A)\frac{\partial^3}{\partial x^3}w_{rel}(0,t) - m_s\left(\ddot{w}_{rel}(L,t) + \ddot{w}_s(t)\right) = 0 \tag{4.5d}$$

## 4.4 Solution Procedure

### 4.4.1 Free Vibrations: Natural Frequency, Mode Shape Functions

Finding resonant frequencies of the system is imperative for any further analysis. In this regard, equating all damping terms as well as forcing term to zero, and using the method of separation of variables ($w_{rel} = \varphi_n(x)e^{j\omega_n t}$, $\varphi_n(x)$ is eigenfunctions, $j$ is unit imaginary number, $\omega_n$ represents beam natural frequency, and $t$ is time variable), Eq. (4.4) is in the following form:

$$(EI + Gl^2A)\frac{\partial^4\varphi_n(x)}{\partial x^4} - \rho A\varphi_n(x){\omega_n}^2 = 0 \tag{4.6a}$$

$$\ddot{w}_s(t) + {\omega_{n-o}}^2 w(t) = {\omega_n}^2\varphi_n(L)e^{-j\omega_n t} \tag{4.6b}$$

where, $\omega_{n-o}$ represents natural frequency of the oscillator ($\omega_{n-o} = \sqrt{{k_s}/{m_0}}$). General solution to the Eq. (4.6a) is a combination of trigonometric and hyperbolic functions with eigenvalue $\lambda_n$ (${\lambda_n}^4 = {\rho A{\omega_n}^2}/{(EI + Gl^2A)}$).

$$\varphi_n(x) = A_1\cosh(\lambda_n x) + A_2\cos(\lambda_n x) + A_3\sinh(\lambda_n x) + A_4\sin(\lambda_n x) \tag{4.7}$$

corresponding boundary conditions to the undamped, free vibration case is as following:

$$\varphi_n(0) = 0 \tag{4.8a}$$

$$\frac{\partial}{\partial x}\varphi_n(0) = 0 \tag{4.8b}$$

$$\frac{\partial^2}{\partial x^2}\varphi_n(L) = 0 \tag{4.8c}$$

$$(EI + Gl^2A)\frac{\partial^3}{\partial x^3}\varphi_n(L) - m_s\left(-{\omega_n}^2\varphi_n(L) + \ddot{w}_s(t)\right) = 0 \tag{4.8d}$$

Obviously, the shear force boundary condition is dependent on the motions and inertia of the oscillator. So, solving Eq. (4.6b) is the proceeding step. Considering beating conditions ($w_s(0) = \dot{w}_s(0) = 0$), proposed solution is:

$$w_s(t) = \frac{{\omega_n}^2}{{\omega_{n-o}}^2 - {\omega_n}^2}\varphi_n(L) \tag{4.9}$$

inserting Eq. (4.9) into Eq. (4.8d) and applying the boundary conditions of Eq. (4.8) into the general solution in Eq. (4.7), after some mathematical operations one obtains the following nonlinear transcendental equation:

$$(EI + GAl^2){\lambda_n}^3(1 + \cosh(\lambda_n L)\cos(\lambda_n L)) + \frac{{\omega_{n-o}}^2{\omega_n}^2 m_0}{{\omega_{n-o}}^2 - {\omega_n}^2}(\sinh(\lambda_n L)\cos(\lambda_n L) - \cosh(\lambda_n L)\sin(\lambda_n L)) = 0 \tag{4.10}$$

It is very important to note the differences between the obtained characteristic equation and that of the reference systems (cantilever-oscillator or a single cantilever). In the reference system, a rigid support is assumed instead of the spring support with changeable stiffness and as mentioned in several research efforts, such a characteristic equation is simply the first part of Eq. 4.10 ($1 + \cosh(\lambda_n L)\cos(\lambda_n L)$). So, including an elastic support renders a more complicated transcendental characteristic equation. Introducing mass ratio ($r_m = \frac{m_0}{\rho AL}$) and stiffness ratio ($r_s = \frac{k_s}{(EI/L^3)}$), and ignoring nonclassical effects as having either $EI$ or $EI + GAl^2$ as the coefficient of $1 + \cosh(\lambda_n L)\cos(\lambda_n L)$ does not alter function graph remarkably; Eq. (4.10) can be re-written in the following shape:

$$f(\lambda_n L) = (r_s - r_m(\lambda_n L)^4)(1 + \cosh(\lambda_n L)\cos(\lambda_n L)) + \tag{4.11}$$

$$(r_s r_m((\lambda_n L))(\sinh(\lambda_n L)\cos(\lambda_n L) - \cosh(\lambda_n L)\sin(\lambda_n L))$$

Eq. (4.11) as a nonlinear transcendental equation does not have a closed-form (exact) solution. Consequently, numerical solvers are proposed. Among root-finding algorithms available, VPASOLVE is an efficient solver included within MATLAB software package. However, similar to most of the numerical solvers, VPASOLVE precision entirely depends on the value of the initial guess. To reach the most feasible precise numerical values of the eigenvalues of Eq. (4.11), plotting the nonlinear transcendental equation is helpful.

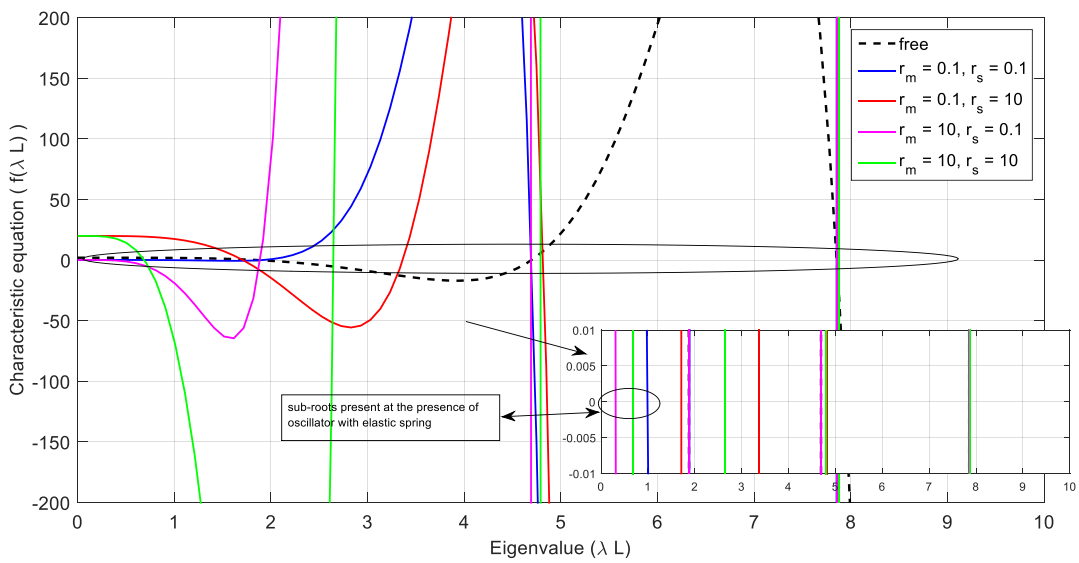


Figure 26. Characteristic equations' graphs for different values of mass ratio and stiffness ratio

Based on the figure presented, it is interesting to note that adding an oscillator which is attached to the free end of the beam via a spring results in roots smaller than 1.875104. 1.875104 is the first eigenvalue of a clamped free beam in sole. This conveys

that if the oscillator is attached via a spring support with elasticity, the restoring force in the spring accompanied with the mass of the oscillator yields another root (eigenvalue) smaller than 1.875104. Second root of cantilever-oscillator-spring system is almost overlapped with the first root of the reference system ($r_s \to \infty$). This key point can be highly important through the analysis of such integrated multi-systems. Accordingly, eigenvalues of the nonlinear transcendental equation are numerically obtainable. In the following, dimensionless undamped natural frequency of the considered system is defined based on both classical and modified couple stress theories, respectively.

$$\Omega_n = \omega_n L^2 \sqrt{\rho A/EI} = (\lambda_n L)^2, \;\; \omega_n = \sqrt{EI/\rho A}\;\; {\lambda_n}^2 \tag{4.12a}$$

$$\Omega_{n-MCST} = \sqrt{(EI + GAl^2)/EI}\,(\lambda_n L)^2, \;\; \omega_{n-MCST} = \sqrt{(EI + GAl^2)/\rho A}\;\; {\lambda_n}^2 \tag{4.12b}$$

Despite the transition from Eq. (4.10) to Eq. (4.11) in which nonclassical effects were ignored, such effects emerge stronger within the definition of natural frequencies. So, in Eq. (4.12b), $GAl^2$ is weighted. Correspondingly, mass-normalized mode shape functions (eigenfunction) are expressible in the following format:

$$\varphi_n(x) = \frac{1}{\sqrt{\rho AL}}(\cosh(\lambda_n x) - \cos(\lambda_n x) - \left(\frac{\cosh(\lambda_n L)+\cos(\lambda_n L)}{\sinh(\lambda_n L)+\sin(\lambda_n L)}\right)(\sinh(\lambda_n x) + \sin(\lambda_n x))) \tag{4.13}$$

### 4.4.2 Forced Vibrations: Harmonic Base Excitations

To analyze the multisystem performance under forced vibrations, harmonic excitations are considered. Harmonic base excitations ($w_b = Y_0 e^{j\omega_e t}$), with excitation frequency and amplitude of $\omega_e$, $Y_0$ triggers the system to oscillate. Mechanical frequency

response functions along with temporal modal response of the system are under scrutiny. Using Galerkin modal decomposition, displacement function is assumed as [35]:

$$w_{rel}(x,t) = \sum_{n=1}^{\infty} \varphi_n(x)\, \eta_n(t) \tag{4.14}$$

due to proportional damping criteria, $\varphi_n(x)$ is the same mode shape functions of the undamped free system. $\eta_n(t)$ is the modal coordinate of the beam at the $n'th$ mode. After discretizing the governing equations of motion of the beam and multiplying by $\varphi_m(x)$, and using the orthogonality in integration over beam length $L$; one obtains the following relationship:

$$\int_0^L \rho A\, \varphi_n(x)^2 dx = B_n \cong 1 \tag{4.15a}$$

$$\int_0^L (EI + Gl^2A)\varphi_n(x) \frac{d^4}{dx^4} \varphi_n(x)\, dx = B_n {\omega_{n-MCST}}^2 \tag{4.15b}$$

duplicating same process for the Eq. (4.14a) and using Eqs. (4.15); following time-domain ordinary differential equation is obtained (Eq. 4.16b is extracted from reference [35]):

$$B_n\big(\ddot{\eta}_n(t) + 2\omega_n\zeta_n\dot{\eta}_n(t) + {\omega_{n-MCST}}^2\eta_n(t)\big) = (\rho A\gamma_n + m_0\acute{\gamma}_n)Y_0{\omega_e}^2 e^{j\omega_e t} \tag{4.16a}$$

$$\zeta_n = \frac{c_a}{2\rho A\omega_{n-MCST}} + \frac{c_s I\omega_{n-MCST}}{2EI} \tag{4.16b}$$

$$\gamma_n = \int_0^L \varphi_n\,(x)dx \tag{4.16c}$$

$$\acute{\gamma}_n = \int_0^L \varphi_n\,(x)\delta(x-L)dx \tag{4.16d}$$

$\zeta_n$ is the mechanical damping ratio including both Kelvin-Voigt and air viscous damping. According to the beating conditions, steady-state temporal modal response of the system is the only solution of Eq. (4.16a) which is expressed as:

$$\eta_n(t) = \frac{(\rho A\gamma_n + m_0\acute{\gamma}_n)Y_0{\omega_e}^2}{B_n({\omega_{n-MCST}}^2 - {\omega_e}^2 + j2\omega_n\omega_{n-MCST}\zeta_n)} e^{j\omega_e t} \tag{4.17}$$

4.5 Results and Discussion

In this section, numerical results pertaining to the natural frequency, modal response, and mechanical frequency response functions (FRFs) are brought and elaborated. Geometrical, and mechanical properties utilized in reference [35], is used in this study which is summarized in the following table:

Table 5. Geometrical, and mechanical parameters of the cantilever-oscillator-spring [35]

| | | |
|---|---|---|
| $L = 100mm$ , beam length | $\rho = 7165\, kg/m^3$ , beam density | $\zeta_2 = 0.013$, damping ratio of 2nd mode |
| $b = 20mm$ , beam width | $E = 100GPa$, Young's modulus | $\zeta_3 = 0.033$, damping ratio of 3rd mode |
| $L = 0.5mm$ , beam thickness | $G = 41GPa$ , shear modulus | |
| $l = 15\mu m$ , non-classical parameter | $\zeta_1 = 0.010$ , damping ratio of 1st mode | |

According to the plots of the characteristic equation, it sounds necessary to find eigenvalues and frequencies of the system of cantilever-oscillator-spring, specifically new roots (eigenvalues) are present that are not accompanied with a simple cantilever or cantilever-oscillator systems.

### 4.5.1 New Eigenvalues and Restoring Force of the Spring

To study the effects of the subsystem integrated to the cantilever system, 4 extreme cases of the oscillator mass and spring stiffness values are considered. Then, the first three frequencies of the new multi-system are found numerically and according to the path explained above. Such values are compared against the reference system of a cantilever.

Table 6. First eigenvalue and dimensionless resonant frequency of cantilever-oscillator-spring system

| $(r_m, r_s)$ | $\lambda_1 L$ | Overshoot (%) compared with 1.875104 | $\Omega_1$ | $\Omega_{1-MCST}$ |
|---|---|---|---|---|
| (0.01,0.01) | 0.999097 | 46.7178 | 0.998196 | 1.000403 |
| (0.01,100) | 1.856765 | 0.9780 | 3.455203 | 3.447578 |
| (10,0.01) | 0.177680 | 90.5243 | 0.031570 | 0.031640 |
| (10,100) | 0.730603 | 61.0366 | 0.533782 | 0.5349626 |

Table 7 is provided to numerically evaluate the effects of restoring force of the spring and the following effects of oscillator inertia over fundamental natural frequency of the proposed multisystem. Four representative cases of: light oscillator-soft spring ($r_m = 0.01, r_s = 0.01$); light oscillator-stiff spring ($r_m = 0.01, r_s = 100$); heavy oscillator-soft spring ($r_m = 10, r_s = 0.01$); heavy oscillator-stiff spring ($r_m = 10, r_s = 100$) are shown in the table. Results show that if the oscillator is hung with a soft spring, the first eigenvalue (fundamental natural frequency) of the cantilever-spring-oscillator is significantly far away from the reference one (pure cantilever) (1.875104). Remarkably, increasing the mass of the oscillator, attempts to further deviate from the reference one. On the other hand, perusing spring constant effects reveals an attractive tendency of the

first eigenvalue towards the reference one, meaning that stiffer spring is inclined to suppress and counteract the inertial effects of the oscillator.

Table 7. Second eigenvalue and dimensionless resonant frequency of cantilever-oscillator-spring system

| $(r_m, r_s)$ | $\lambda_2 L$ | Overshoot (%) compared with 4.694091 | $\Omega_2$ | $\Omega_{2-MCST}$ |
|---|---|---|---|---|
| (0.01,0.01) | 1.876751 | 60.0189 | 3.522196 | 3.529985 |
| (0.01,100) | 4.647680 | 0.9887 | 21.60093 | 21.64870 |
| (10,0.01) | 1.876618 | 60.0217 | 3.521698 | 3.529487 |
| (10,100) | 3.655735 | 22.1205 | 13.36440 | 13.39396 |

Table 8 is duplicated in a similar path for the second vibration mode. Comparatively to the first mode gradations, light oscillator-stiff spring has almost same second eigenvalue ($\lambda_2 L$) of rigidly-hung oscillator ($r_s = \infty$). With the strong restoring forces ($r_s = 100$) oscillator inertial effect is tangible only if the mass ratio is strikingly high ($r_m = 10$). Conversely, with weak restoring forces ($r_s = 0.01$) inertial effects of the oscillator significantly deduces the second eigenvalue. Interestingly, inertial effect drags the second eigenvalue towards the first eigenvalue of the rigidly-hung oscillator ($\lambda_2 L \rightarrow \lambda_1 L$). Eventually, if stiff spring is used with heavy oscillator; moderate variations are observable as restoring forces tend to behave like the reference system, but inertial effects are inclined to deviate from the reference system.

Table 8. Third eigenvalue and dimensionless resonant frequency of cantilever-oscillator-spring system

| $(r_m, r_s)$ | $\lambda_3 L$ | Overshoot (%) compared with 7.854757 | $\Omega_3$ | $\Omega_{3-MCST}$ |
|---|---|---|---|---|
| (0.01,0.01) | 4.694188 | 40.2376 | 22.035401 | 22.084133 |

| | | | | |
|---|---|---|---|---|
| (0.01,100) | 7.747153 | 1.3699 | 60.018382 | 60.151116 |
| (10,0.01) | 4.694187 | 40.2376 | 22.035399 | 22.084131 |
| (10,100) | 5.623066 | 28.4120 | 31.618871 | 31.688798 |

Table 9 pertains to the third vibration mode. Similar patterns to the first and second vibration mode are inferable. Main differences between the first three modes include: the most notable deviation refers to the heavy oscillator with weak spring. In this case, oscillator has sensible relative motions so impacts the beams behavior substantially. Clearly, the least sensible effects of oscillator inertia occur with stiff or hard spring with the least overshoot. Finally, it is also good to note that dimensionless frequency of classical theory and Modified Couple Stress theory (MCST) have almost 0.22% shifts.

### 4.5.2 Effect of Mass and Stiffness Ratios over Natural Frequencies

By detecting the emerging minimal frequency values, it sounds necessary to study the effect of the oscillator mass and spring stiffness over the frequency values for a specific range of continuous values.

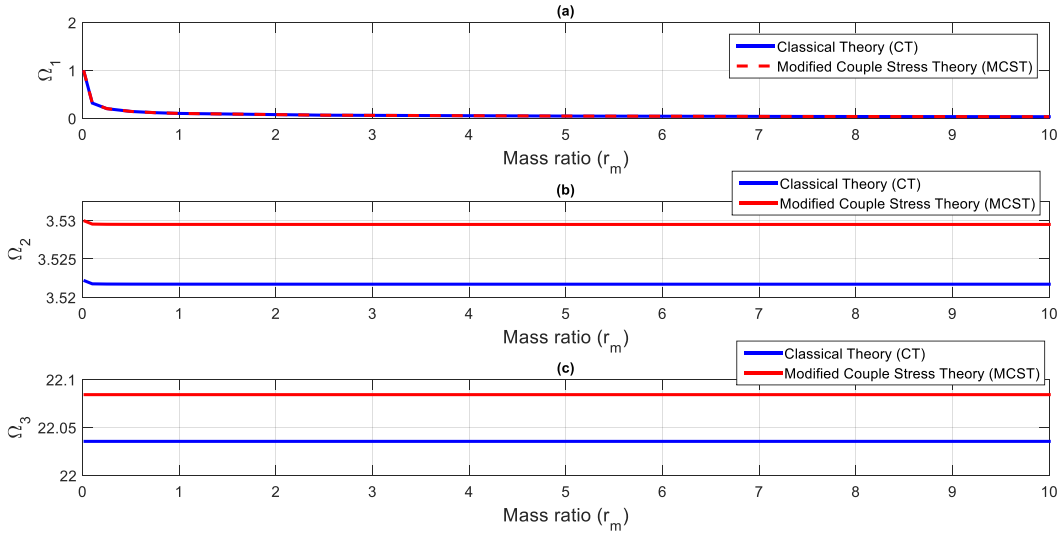


Figure 27. Variations of dimensionless frequencies versus mass ratio with soft spring (r_s=0.01; a. first mode, b. second mode, c. third mode)

This figure demonstrates variations of dimensionless frequency of the first three modes with respect to mass ratio in case of soft spring. Obviously, in the first mode, increasing the mass ratio (increasing the mass of the oscillator) decreases the frequency. In the second mode, such a decrement is barely sensible, while in the third mode, mass ratio almost does not alter the frequency. Even for the first mode with more tangible variations, frequency decrements take place at the very small values of mass ratio only.

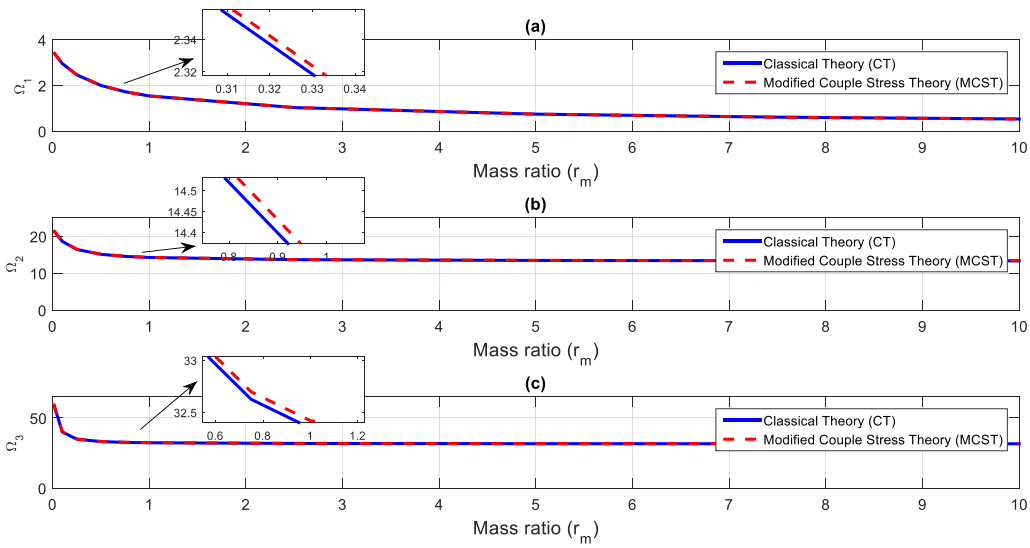


Figure 28. Variations of dimensionless frequencies versus mass ratio with stiff spring (r_s=100; a. first mode, b. second mode, c. third mode)

Figure 28 is plotted to show the variations of the first three frequency modes with respect to mass ratio in case of stiff (hard) spring. It is evident that despite the case of soft spring, oscillator mass suppresses frequencies significantly as it increases. In other words, mass ratio effects over frequencies is more perceptible if the spring is stiffer. Besides the impression of spring stiffness, the heavier the oscillator the smaller the natural frequencies.

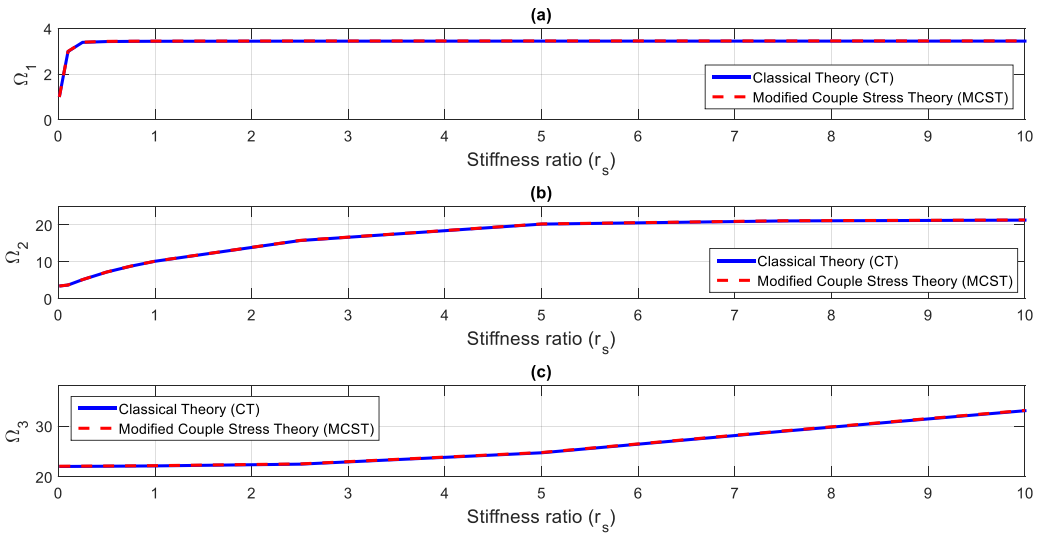


Figure 29. Variations of dimensionless frequencies versus stiffness ratio with light oscillator ($r_m$=0.01; a. first mode, b. second mode, c. third mode)

To peruse the effect of the spring stiffness constant over natural frequency, figure 29 is presented. In this figure, light-mass oscillator ($r_m = 0.01$) is assumed. It is evident that all three mode's frequencies increase with increment in the stiffness. It means that stiffer spring yields bigger resonant frequencies.

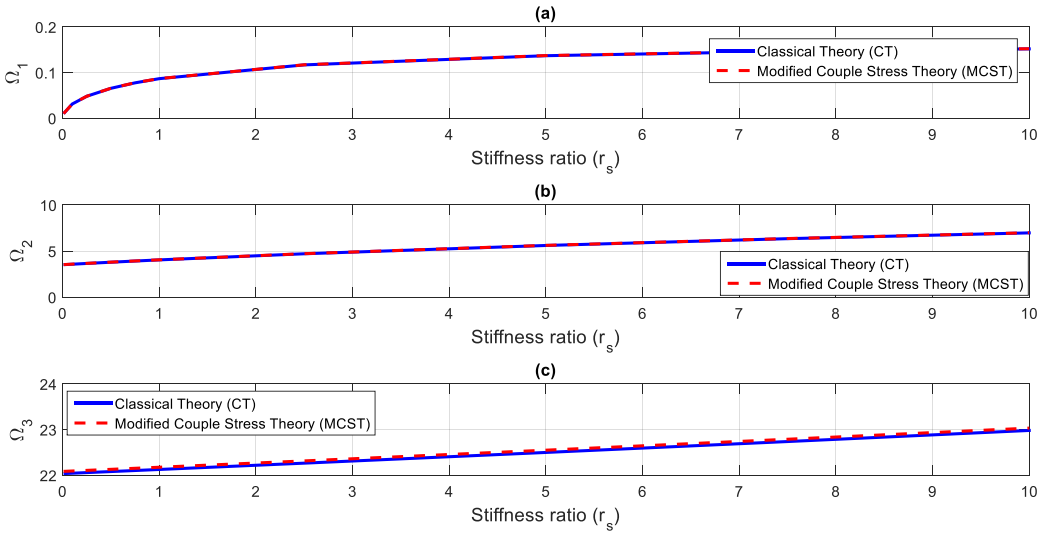


Figure 30. Variations of dimensionless frequencies versus stiffness ratio with heavy oscillator ($r_m$ =10; a. first mode, b. second mode, c. third mode)

Figure 30 illustrates variations of frequencies with respect to stiffness ratio in case of heavy-mass oscillator. A similar profile to the case of light-mass oscillator is repeated confirming that stiffer spring ends up in increments in frequencies.

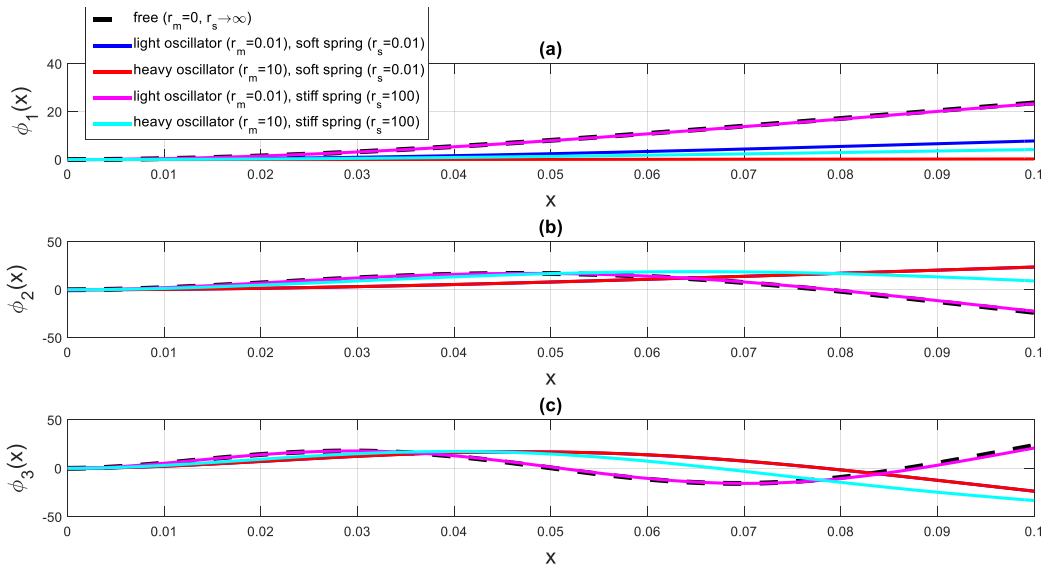


Figure 31. Mode shape functions of reference system and extreme cases of mass and stiffness ratios (a. mode one; b. mode two; c. mode three)

Mode shape functions are plotted to signify the effect of new resonant frequency generated due to the inertial effects of the oscillator accompanied with stiffness effects (restoring force) of the spring. It is evident that mode shape functions of all three first modes are the most diverse than the reference system (also mentioned as free in the figure legend) if oscillator is heavy. Besides, to focus on small-scaled systems, results of the modified couple stress theory are presented only.

### 4.5.3 Mechanical Frequency Response of Beam Vibration

In this section relative tip motion frequency response function (FRF) also known as the relative motion transmissibility function, is presented and elaborated. Relative motion transmissibility function is the ratio of vibration amplitudes at the free end (tip of the beam) to the amplitude of the base displacement.

$$\frac{w_{rel}}{Y_0 e^{j\omega_e t}} = \sum_{n=1}^{\infty} \varphi_n(L)\left[\frac{(\rho A\gamma_n + m_0\acute{\gamma}_n)\omega_e{}^2}{B_n(\omega_{n-MCST}{}^2 - \omega_e{}^2 + j2\omega_n\omega_{n-MCST}\zeta_n)}\right] \tag{4.18}$$

Relative motion transmissibility (tip motion FRF) is of particular interest, specifically for the cantilever energy harvesters or vibration isolators. With such mechanical FRF, valuable information about the level of tip displacement of a harvester or isolator is demonstrated.

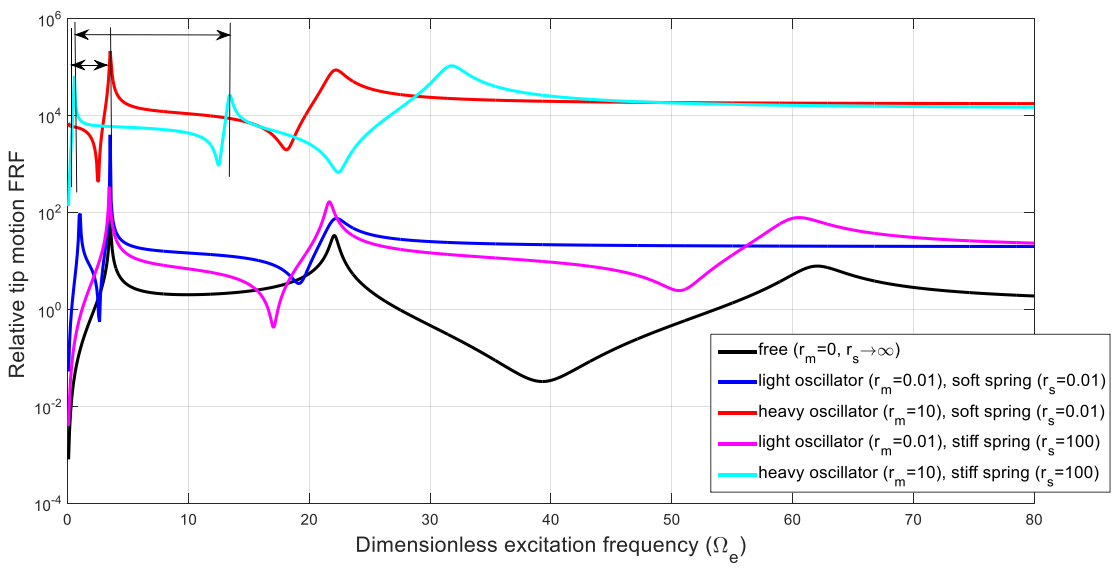


Figure 32. Relative tip motion FRF versus dimensionless excitation frequency (reference system and extreme cases of mass and stiffness ratios)

In Figure 32, the modulus of relative tip motion FRF against dimensionless excitation frequency is plotted for the four extreme cases as well as the reference case ($r_s \to \infty$, or $r_m = 0$). According to this plot, vibration amplitudes at the tip (free end) is increased substantially with heavy oscillator ($r_m = 10$). While, spring stiffness constant does not manipulate oscillation amplitudes, restoring spring force drags the FRF towards the reference case ($r_m = 0\ or\ r_s \to \infty$). It means that a weak (soft) spring yields in striking

shortened frequency bandwidth as in red and blue lines. Such finding is also sensible by comparison between red line and cyan line, where both pertain to identical mass ratios but different restoring forces. Red line refers to the soft spring and has significantly shorter bandwidth between the first and second resonant frequencies than cyan with hard (stiff) spring between the first and second resonant frequencies. Concisely, vibration amplitudes are mutable with only mass ratios and frequency bandwidth is highly dependent on the amount of restoring forces. In details, dominant inertial effects (heavy oscillator) generate a minimal resonant frequency close to zero, while the second resonant frequency is overlaid on the first resonant frequency of the reference case. Finally, it is understandable that the inertial effects strongly impact the oscillation amplitudes, but frequency bandwidth is varying based on both inertial effects and spring stiffness in correlation. It is also good to note that with heavy oscillator and soft spring, system's behavior is the most significantly diverse than the reference system's behavior, and with the light oscillator and stiff spring, system's behavior is most remarkably similar to the behavior of reference system. Such findings can be crucial for the design of energy harvesters or vibration controllers. For example; in the case of energy harvesters, increasing the relative tip motion is of interest, while decreasing the frequency bandwidth is not desired. So, a trade-off should be considered with heavy oscillator and stiff spring. However, according to the desires of each application, spring stiffness constant and oscillator mass should be adopted quantitatively and in single case-study rather than qualitative elaboration which was provided in this study.

## 4.6 Conclusion

Energy harvesters at small scales have high resonance frequencies which are hard to reach for the external source frequency. Thus, devising novel models to extenuate the harvesters' resonance frequency is beneficial. For the first time, the effects of an augmented generalized coordinate over the vibratory response of a cantilever-oscillator-spring system are scrutinized. In this chapter, it is elaborated that for such a multisystem with applications in energy harvesters integrable with RFID components, vibration controllers, or M-NEMS sensors; replacing a rigid support with an elastic support via a spring will shift systems response drastically. Such mutation is very important as the resonance frequency is generatable at smaller values which strikingly increases the efficiency of the harvesters. The corresponding new nonlinear transcendental characteristic equation is numerically solved using the MATLAB root-solver algorithm. Due to the relative motions of the oscillator with respect to the cantilever, small newly-generated frequencies between zero and the first natural frequency of the cantilever system (reference system) are detected. Through our scrutiny, we figured out that increasing the stiffness of the spring results in a response similar to the response of the reference system which is valid for all three vibration modes. Contrarily, inertial effects derived from the oscillations of the lumped oscillator are prone to substantially deviate system response by means of dragging the minimal (new) frequency to the left and far from the first frequency of the reference system. For the case of forced vibrations with harmonic base excitations, relative tip motion FRF (transmissibility function) is obtained. Results demonstrate that significant inertial effects resulted from a heavier oscillator, alter system's response and yield big amplitudes and strikingly increased transmissibility. On the other hand, spring

stiffness cannot neutralize the inertial effects regarding the vibration amplitudes and transmissibility. However, such parameters can stretch the FRF diagram profile, meaning that stiffer springs result in wider bandwidth. The new system, with values of oscillator inertia and spring restoring force, leads to the generation of minimal frequencies which can be at the vicinity of the first frequency of the reference system. In any case, such newly-generated frequency yields widened bandwidth and one more resonance particularly at the small excitations. In short, it is inferable that depending on the specific desires of each application, oscillator mass and spring stiffness can be greatly conducive as the design parameters, and to alter systems response as demanded. Findings of current chapter are summarized in the following:

1- The cantilever system joined with oscillator-spring leads to the generation of new characteristic equations and eigenvalues. This means the opportunity for an augmented resonance particularly at low frequencies, which can be helpful as the external excitations are mostly small and generation of more resonances in a given bandwidth.

2- The increment in mass ratio (inertial effects of the oscillator), causes intensified oscillation amplitudes, but the impact over the bandwidth is suppressed by rigidity level.

3- The increment in rigidity of the support (spring constant) ends up in wider bandwidth and stretched profile of transmissibility FRF. Spring constant is the more dominant influential factor rather than inertia in terms of bandwidth mutations and gradations.

4- To design more efficient energy harvesters, vibration controllers, M-NEMS sensors, quantitative analysis is required over qualitative analysis. This means that for a

cantilever energy harvester system integrated with a spring-mass system at the tip, stiffness and mass ratios are the design parameters providing plenty of maneuverability which needs to be studied for each specific value of such parameters.

5- To tune an energy harvester, such a proposed system overcomes the lack of coincidence and overlap between the excitation and natural frequencies since the location of the resonant frequencies can be significantly manipulated and altered by means of different values of oscillator mass and spring constant.

Finally, it is noteworthy to mention that further analysis and study is required to find the optimal values of the design parameters (oscillator mass, and spring stiffness) to design the most optimized piezoelectric vibration-based energy harvester. Such topics will be studied and presented in the following chapter.

# CHAPTER 5. OPTIMIZATION OF THE ENERGY HARVESTER

## 5.1 Introduction and Background

As mentioned in the preceding chapter, there is a growing trend in the generation of electrical energy from mechanical vibrations particularly from piezoelectricity. Current piezoelectric vibration-based energy harvesters (PVEH) are under significant attention to improve and develop them for more applicable usage. Current PVEHs usually have two big issues which decrease efficacy: the matching between the excitation (driving) frequency and the effective (operational) frequency bandwidth. It is widely explained in the former chapters that as long as the excitation or driving frequency coming from an external source is not aligned with the resonance frequency of the harvester substrate, the outcome energy is insignificant. So, it is vital to match the mentioned frequencies. Mostly, the excitation frequency is not adaptable and there is no control over it. Besides, in small-size energy harvesters, due to the size reduction the resonance frequency of the system is notably high. With all that mentioned, it sounds reasonable to alter the resonance frequency of the substrate to match the frequency coming from the external source. To do so, the integration of spring-mass subsystem with the main substrate (cantilever) is proposed. Another important point is to widen the effective frequency bandwidth. This leads to capturing and harvesting more energy since the wider bandwidth encompasses more resonance. It was discussed how the integration of such a subsystem alters the vibratory response of the harvesters from a dynamic aspect. In this chapter, such integration will be studied in detail from an electrical energy aspect. Besides, the optimum values of the oscillator mass and spring stiffness constant will be found using the optimization algorithms. Such optimal design parameters lead to the maximum amount of harvestable

power as well as the maximum widened effective frequency bandwidth. In other words, in this chapter, besides the effects of the subsystem integration over the harvester's performance and efficacy, the proposed model of the PVEH is optimized. Such optimization of the PVEH renders the best performance possible and enhances and reinforces the performance. Based on the literature review presented in the former chapters, several research efforts have been accomplished to optimize the tuning mass to maximize the harvestable energy as well as widening the effective frequency bandwidth. According to the literature review presented, there is no published technical essay considering optimizing the efficacy of energy harvesters with a spring-mass system integrated with the cantilever. In detail, it is established to provide a relative motion and oscillation for the tuning mass (oscillator) by means of a spring. This is feasible by replacing the rigid support with an elastic support with restoring force capability. Such augmentation increases the degrees of freedom and the number of governing equations. Moreover, the boundary condition is strikingly changed which raises the expectations for different resonance frequencies. In this response, in this chapter, the proposed model of the cantilever-oscillator-spring is modeled accounting the electrical circuit equations. Some of the mechanical and kinematics are similar to the former chapter, but for purpose of integrity they are duplicated in this chapter as well.

## 5.2 Mathematical Modeling

Schematic configuration of a cantilever energy harvester integrated with oscillator-spring system at the tip end is shown in the following figure which includes the piezoelectric layers highlighted in black at the top and bottom surfaces:

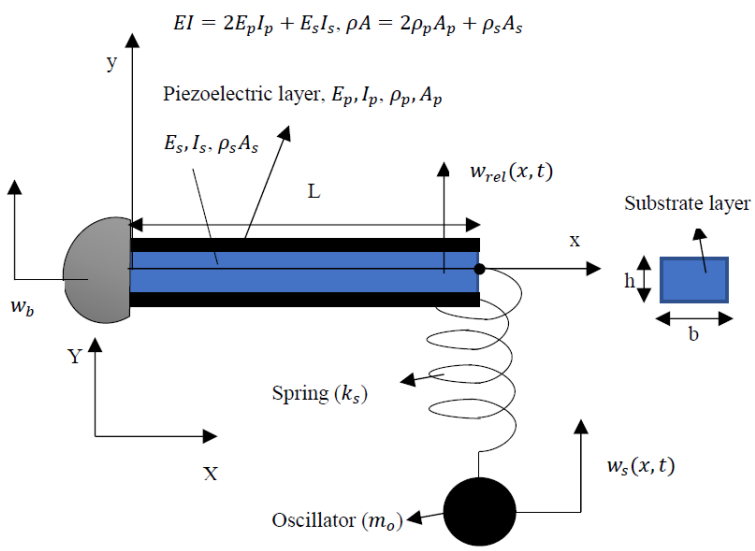


Figure 33. Schematic of the cantilever-spring-mass energy harvester

$\rho_s, \rho_p$ are substrate and piezoelectric layers density, $A_s, A_p$ show substrate and piezoelectric layers cross section areas, $E_s, E_p$ represent substrate and piezoelectric layers Young's modulus, $I_s, I_p$ are substrate and piezoelectric layers second moment of inertia, beam has length of $L$, thickness of $h$, width of $b$; $x - y$ represents the Lagrangian cartesian coordinates, $X - Y$ is the fixed Eulerian cartesian coordinates. $w_b(x,t)$ is the base excitation, and $w_{rel}(x,t)$ and $w_s(t)$ represent relative lateral displacement of beam and oscillator with respect to the Lagrangian coordinates, respectively. According to the Euler-Bernoulli beam models; displacement fields are defined as follows [35]:

$$\mathrm{u_x(x,z,t)} = -\mathrm{y}\frac{\partial \mathrm{w}_{rel}}{\partial \mathrm{x}}(\mathrm{x,t}) \tag{5.1a}$$

$$\mathrm{u_y(x,z,t)} = \mathrm{w}_{rel}(x,t) \tag{5.1b}$$

$$\mathrm{u_z(x,z,t)} = 0 \tag{5.1c}$$

to consider non-conservative work induced in the system, extended Hamilton's principle will be utilized. Based on plane-stress assumptions for liner isotropic elements following

Hooke's law, constitutive relations of substrate and piezoelectric layers can be expressed as follows [35]:

$$T_1{}^s = E_s S_1 \tag{5.2}$$

$T_1{}^s$ is stress, $S_1$ is strain of substrate layer. Based on the piezoelectric constitutive equations stress-strain and electric field relations are [35]:

$$T_1{}^p = E_p(S_1 - d_{31}E_3) \tag{5.3a}$$

$$\varepsilon_{33}{}^s = \varepsilon_{33}{}^T - d_{31}{}^2 E_p \tag{5.3b}$$

$$D_3 = d_{31}T_1{}^p + \varepsilon_{33}{}^T E_3 \tag{5.3c}$$

$T_1{}^p$ is stress at piezoelectric layers. $d_{31}$ is piezoelectric coupling coefficient. $E_3$ is electric field in $y$-direction. $\varepsilon_{33}{}^s$ and $\varepsilon_{33}{}^T$ represent permittivity at constant strain and stress. $D_3$ is electric displacement which acts only in $z$-difrection, respectively. Two types of damping mechanisms, internal and external, are considered in this study. Internal damping is modeled as Kelvin-Voigt damping also named as strain-rate damping:

$$T_d = c_s \dot{S}_1 \tag{5.4}$$

$T_d$ is stress due to strain-rate damping and $c_s$ illustrates viscoelastic damping coefficient due to structural viscoelasticity. Dot sign indicates differentiation in temporal domain. Both internal and external damping satisfy proportional damping criteria. For the proposed cantilever beam model, the kinetic energy ($U_k$) due to base excitations is:

$$U_k = \frac{1}{2}\int_0^L \rho A(\dot{w}_{rel}(x,t) + \dot{w}_b(x,t))^2\, dx + \frac{1}{2}m_o(\dot{w}_{rel}(L,t) + \dot{w}_b(L,t) + \dot{w}_s(t))^2 \tag{5.5}$$

strain energy generated due to deflections ($U_s$) is comprised of energy of the substrate and energy of the piezoelectric layers integrated over volume fractions ($V_s, V_p$):

$$U_s = \delta U_{s-1} + \delta U_{s-2} = \frac{1}{2}\int_{V_s} {T_1}^s S_1 dV_s + \frac{1}{2}\int_{V_p} {T_1}^p S_1 dV_p = \tag{5.6}$$

$$\frac{1}{2}\int_{V_s} E_s {S_1}^2 dV_s + \frac{1}{2}\int_{V_p} E_p({S_1}^2 - S_1 d_{31} E_3) dV_p$$

electrical energy ($W_e$) is [35]:

$$W_e = \frac{1}{2}\int_{V_p} D_3 E_3 dV_p \tag{5.7}$$

following auxiliary relations are used to re-write the electrical section of the equation [35]:

$$\mathrm{E_3} = -{\mathrm{v(t)}}/{(2\mathrm{h_p})} \tag{5.8}$$

$$\mathrm{D_3} = \mathrm{d_{31}E_pS_1} - {\varepsilon_{33}}^{\mathrm{s}}\frac{\mathrm{v(t)}}{2\mathrm{h_p}} \tag{5.9}$$

$$\mathrm{C_p} = \frac{{\varepsilon_{33}}^{\mathrm{s}}\mathrm{bL}}{\mathrm{h_p}} \tag{5.10}$$

$$v(t) = R_l \dot{q}_3(t) \tag{5.11}$$

$$W_e = \frac{1}{2}\int_{V_p} -d_{31}E_p z w_{rel,xx}(\frac{-v(t)}{2h_p})dV_p + \frac{1}{2}\int_{V_p} {\varepsilon_{33}}^s(\frac{-v(t)}{2h_p})^2 dV_p \tag{5.12}$$

in which $v(t)$ is the voltage across the resistive load and $q_3(t)$ is the electric charge. External virtual work ($W_{nc}$) resulting from damping and dissipating resistive load of electrical circuit is [35]:

$$W_{nc} = -\frac{d}{dt}\int_0^L \frac{1}{2} c_a\,(w_{rel} + w_b)^2 dx - \frac{d}{dt}\int_{V_s} \frac{1}{2} T_s S_1\, dV_s - \frac{d}{dt}(\frac{1}{2} R_l {q_3}^2(t)) \tag{5.13}$$

based on the Hamilton's variational principle, variations of systems' Lagrangian ( $L = U_k - U_s - U_{th} + W_e + W_{nc}$) is zero in a short time interval ($\int_{t_1}^{t_2} \delta L dt = 0$). To apply such a concept, variations of energy terms are to be obtained:

$$\delta U_k = \int_0^L \rho A \left(\dot{w}_{rel}(x,t) + \dot{w}_b(x,t)\right)\delta\dot{w}_{rel}(x,t)dx + m_o\left(\dot{w}_{rel}(L,t) + \dot{w}_b(L,t) + \dot{w}_s(t)\right)\delta\dot{w}_s(t) + \int_0^L m_o \left(\dot{w}_{rel}(x,t) + \dot{w}_b(x,t) + \dot{w}_s(t)\right)\delta(x-L)\delta\dot{w}_{rel}(x,t)dx \tag{5.14}$$

$$\delta U_{s-1} = E_s I_s w_{rel,xx}\delta w_{rel,x}\Big|_0^L - E_s I_s w_{rel,xxx}\delta w_{rel}\Big|_0^L + \int_0^L E_s I_s w_{rel,xxxx}\,\delta w_{rel}dx \tag{5.15}$$

$$\delta U_{s-2} = 2I_p E_p w_{rel,xx}\delta w_{rel,x}\Big|_0^L - 2E_p I_p w_{rel,xxx}\delta w_{rel}\Big|_0^L + \int_0^L 2E_p I_p w_{rel,xxxx}\,\delta w_{rel}dx + -Q_p E_p \frac{d_{31}}{2h_p} v(t)[H(x) - H(x-L)]\delta w_{rel,x}\Big|_0^L + Q_p E_p \frac{d_{31}}{2h_p} v(t)[\delta(x) - \delta(x-L)]\delta w_{rel}\Big|_0^L - \int_0^L Q_p E_p \frac{d_{31}}{2h_p} v(t)\left[\acute{\delta}(x) - \acute{\delta}(x-L)\right]\delta w_{rel}dx - \int_0^L Q_p E_p \frac{d_{31}}{2h_p} w_{rel,xx}\delta\dot{v}(t)dx \tag{5.16}$$

$$\delta U_{ss} = k_s w_s \delta w_s \tag{5.17}$$

$$\delta W_e = -Q_p E_p \frac{d_{31}}{2h_p} v(t)[H(x) - H(x-L)]\delta w_{rel,x}\Big|_0^L + Q_p E_p \frac{d_{31}}{2h_p} v(t)[\delta(x) - \delta(x-L)]\delta w_{rel}\Big|_0^L - \int_0^L Q_p E_p \frac{d_{31}}{2h_p} v(t)\left[\acute{\delta}(x) - \acute{\delta}(x-L)\right]\delta w_{rel}dx - \int_0^L Q_p E_p \frac{d_{31}}{2h_p} w_{rel,xx}\delta\dot{v}(t)dx + \int_{V_p} \varepsilon_{33}{}^s \frac{v(t)}{(2h_p)^2}\delta v(t)dV_p \tag{5.18}$$

$$\delta W_{nc} = -\int_0^L c_a(\dot{w}_{rel} + \dot{w}_b)\delta w_{rel}dx - \int_0^L c_s I\,\dot{w}_{rel,xxxx}\delta w_{rel}dx - \frac{\dot{v}(t)}{R_l}\delta v \tag{5.19}$$

in the above-mentioned equations $I_s$, $I_p$ are second moment of inertia of the substrate and the piezoelectric layers. $H(x)$ is Heaviside (unit step) function to model concentrated coverage of electrodes in $x$-direction. $\delta(x)$ is Dirac delta function. $Q_p$ is the first moment of inertia of the piezoelectric layers. $c_a$ and $c_a$ denote the viscous air damping and the structural strain rate (Kelvin-Voigt) damping coefficients.

$$I_s = \int_{A_s} z^2 dA_s = \frac{1}{12} b {h_s}^3 \tag{5.20}$$

$$Q_p = \int_{A_p} z dA_p = \frac{1}{2} b h_p (h_p + h_s) \tag{5.21}$$

$$I_p = \int_{A_p} z^2 dA_p = \frac{1}{3} b h_p ({h_p}^2 + \frac{3}{2} h_p h_s + \frac{3}{4} {h_s}^2) \tag{5.22}$$

$$EI = E_s I_s + 2E_p I_p \tag{5.23}$$

$EI$ is the total flexural rigidity (bending stiffness) of the cantilever beam in bending. After some mathematical operations, the system of coupled electromechanical partial integro-differential equations of the cantilever-oscillator-spring piezoelectric beam is derived:

$$\rho A \ddot{w}_{rel}(x,t) + EI w_{rel,xxxx}(x,t) + c_a \dot{w}_{rel}(x,t) + c_s I \dot{w}_{rel,xxxx}(x,t) - \Gamma_2 v(t)[\acute{\delta}(x) - \acute{\delta}(x-L)] = -\rho A \ddot{w}_b(x,t) - c_a \ddot{w}_b(x,t) - m_o \delta(x-L) \ddot{w}_b(t) \tag{5.24a}$$

$$\int_0^L \Gamma_2 \dot{w}_{rel,xx}(x,t) dx + \frac{C_p}{2} \dot{v}(t) = -\frac{v(t)}{R_l} \tag{5.24b}$$

$$m_o(\ddot{w}_{rel}(L,t) + \ddot{w}_s(t) + \ddot{w}_b(L,t)) + k_s w_s(t) = 0 \tag{5.24c}$$

where, $\Gamma_2$ is:

$$\Gamma_2 = \frac{E_p Q_p d_{31}}{h_p} \tag{5.25}$$

corresponding boundary conditions of the modeled system is:

$$w_{rel}(0,t) = 0 \tag{5.26a}$$

$$w_{rel,x}(0,t) = 0 \tag{5.26b}$$

$$w_{rel,xx}(L,t) = 0 \tag{5.26c}$$

$$EIw_{rel,xxx}(L,t) - m_o\left(\ddot{w}_{rel}(L,t) + \ddot{w}_s(t)\right) = 0 \tag{5.26d}$$

5.3 Analytical Solution Approach Based on Galerkin's Modal Decomposition Method

Using the modal Galerkin's decomposition, relative vibratory motion of the distributed-parameter system can be expressed by converging expansion series of temporal and spatial functions [35]:

$$w_{rel}(x,t) = \sum_{n=1}^{\infty} \phi_n(x)\,\eta_n(t) \tag{5.27}$$

$\phi_n(x)$ is the mass-normalized eigenfunction corresponding to the free vibration case and $\eta_n(t)$ is the modal coordinate of the system in $n$th vibration mode. To find the eigenfunctions and the eigenvalues, spatial part can be assumed as an exponential function $\eta_n(t) = e^{j\omega_n t}$ (however to find the time-domain response, $\eta_n(t)$ needs to be determined). $j$ is the unit imaginary number, $\omega_n$ is the natural frequency of the system, and $t$ is the time variable. The undamped free vibration system is simply obtainable and the boundary conditions are identical to the main system:

$$\rho A\ddot{w}_{rel}(x,t) + EIw_{rel,xxxx}(x,t) = 0 \tag{5.28a}$$

$$m_o(\ddot{w}_{rel}(L,t) + \ddot{w}_s(t)) + k_s w_s(t) = 0 \tag{5.28b}$$

$$w_{rel}(0,t) = 0 \tag{5.29a}$$

$$w_{rel,x}(0,t) = 0 \tag{5.29b}$$

$$w_{rel,xx}(L,t) = 0 \tag{5.29c}$$

$$EIw_{rel,xxx}(L,t) - m_o\left(\ddot{w}_{rel}(L,t) + \ddot{w}_s(t)\right) = 0 \tag{5.29d}$$

general proposed solution for $\phi_n(x)$ is a linear combination of trigonometric and hyperbolic functions:

$$\phi_n(x) = \frac{1}{\sqrt{\rho AL}}\left(cosh\,\lambda_n\,x - cos\,\lambda_n\,x - \frac{cosh\,\lambda_n L + cos\,\lambda_n L}{sinh\,\lambda_n L + sin\,\lambda_n L}\left(sinh\,\lambda_n x - sin\,\lambda_n x\right)\right) \tag{5.30}$$

the equation of the oscillator should be solved first.

$$\ddot{w}_s(t) + {\omega_{no}}^2 w_s(t) - {\omega_n}^2 \phi_n(L) e^{j\omega t} = 0 \tag{5.31}$$

where $\omega_{no}$ represents the natural frequency of the oscillator ($\omega_{no} = \sqrt{k_s/m_o}$). The particular solution (transient response) for oscillations of the oscillator is:

$$w_s(t) = \frac{{\omega_n}^2}{{\omega_{no}}^2 - {\omega_n}^2}\phi_n(L) e^{j\omega t} \tag{5.32}$$

applying the natural boundary conditions of a clamped-free beam to Eq. (5.30), the transcendental characteristic equation is derived with $\lambda_n L$ as the roots (eigenvalues):

$$\left(\frac{m_o L^3}{\rho AL}{\lambda_n}^4 - \frac{k_s L^3}{EIL}\right)\left(1 + cos(\lambda_n\,L)\,cosh(\lambda_n\,L)\right) - \lambda_n\left(\frac{m_o}{\rho AL}\right)\left(\frac{k_s L^3}{EI}\right)\left(sinh(\lambda_n L)\,cos(\lambda_n L) - cosh(\lambda_n L)\,sin(\lambda_n L)\right) = 0 \tag{5.33}$$

introducing the mass ratio ($r_m = \frac{m_o}{\rho AL}$) and the stiffness ratio ($r_s = \frac{k_s}{(EI/L^3)}$) parameters, one can re-write the transcendental nonlinear characteristic equation in the following format:

$$r_s r_m(\lambda_n L)\left(sinh(\lambda_n L)\,cos(\lambda_n L) - cosh(\lambda_n L)\,sin(\lambda_n L)\right) - \left(r_s - r_m(\lambda_n L)^4\right)\left(1 + cos(\lambda_n\,L)\,cosh(\lambda_n\,L)\right) = 0 \tag{5.34}$$

Eq. (5.40) as a nonlinear transcendental equation does not have a closed-form (exact) solution. Consequently, numerical solvers are proposed. Among root-finding algorithms available, VPASOLVE is an efficient solver included within MATLAB software package. It is reported how to solve the mentioned characteristic nonlinear equation in the former chapter and to avoid duplication, next steps are to be mentioned here. After finding the eigenvalues of the system, one can find the time-domain response using Galerkin's approach. Substitution Eq. (5.27) into Eq. (5.24a), multiplying both sides by $\phi_m(x)$ and integrating over the length of the beam along with benefiting the orthogonality of eigenfunctions, partial differential equation can be converted into time-domain ordinary differential equation:

$$\ddot{\eta}_n(t) + \left(\frac{c_s I}{EI}\omega_n{}^2 + \frac{c_a}{\rho A}\right)\dot{\eta}_n(t) + \omega_n{}^2\,\eta_n(t) = (\chi_n v(t) + (\rho A\gamma_n + m_o\gamma_n{}^o)\omega_e{}^2 Y_0 e^{j\omega_e t})/B_n \tag{5.35}$$

where,

$$B_n = \int_0^L \phi_{n,xx}(x)\phi_n(x)dx \tag{5.36a}$$

$$\gamma_n = \int_0^L \phi_n(x)dx \tag{5.36b}$$

$$\gamma_n = \phi_n(L) \tag{5.36c}$$

$$\chi_n = \Gamma_2\phi_{n,x}\big|_L \tag{5.36d}$$

the excitation is assumed to be harmonic ($w_b(t) = Y_0 e^{j\omega_e t}$) and, since the model is linear and based on the principle of superposition, output voltage can also be assumed as a harmonic function of identical argument with amplitude of $V_0$ [35]:

$$v(t) = V_0 e^{j\omega_e t} \tag{5.37}$$

substituting Eqs. (5.35) and (5.34) into Eq. (5.32) yields the following:

$$\dot{v}(t) + \frac{1}{\tau_c} v(t) = -\sum_{n=1}^{\infty} \Theta_n \, \dot{\eta}_n(t) \tag{5.38a}$$

$$\tau_c = \frac{C_p R_l}{2} \tag{5.38b}$$

$$\Theta_n = \frac{2\Gamma_2}{C_p} \phi_{n,x}\big|_L \tag{5.38c}$$

in energy harvesting systems, steady-state response of the vibratory part is of primary concern. Thus, particular answer part of the Eq. (5.35) is to be obtained:

$$\eta_n(t) = \frac{(\rho A \gamma_n + m_o {\gamma_n}^o) Y_0 {\omega_e}^2 + \chi_n V_0}{B_n({\omega_n}^2 - {\omega_e}^2 + j2\zeta_n \omega_n \omega_e)} e^{j\omega_e t} \tag{5.39}$$

in Eq. (5.39), $\zeta_n$ is modal damping term [35]:

$$\zeta_n = \frac{c_a}{2\rho A \omega_n} + \frac{c_s I}{2EI} \omega_n \tag{5.40}$$

now, substitution Eq. (39) into Eq. (38a) results the output voltage across the resistive load:

$$v(t) = \frac{\sum_{n=1}^{\infty} \frac{-j\Theta_n (\rho A \gamma_n + m_o {\gamma_n}^o) {\omega_e}^3 Y_0}{B_n({\omega_n}^2 - {\omega_e}^2 + j2\zeta_n \omega_n \omega_e)}}{\frac{1}{\tau_c} + j\omega_e + \sum_{n=1}^{\infty} \frac{j\Theta_n \chi_n \omega_e}{B_n({\omega_n}^2 - {\omega_e}^2 + j2\zeta_n \omega_n \omega_e)}} e^{j\omega_e t} \tag{5.41}$$

besides to the output voltage, shunted vibration response of the cantilever can be found as follows:

$$w_{rel}(x,t) = \sum_{n=1}^{\infty} \frac{1}{\sqrt{\rho AL}} \Big( \cosh \lambda_n x - \cos \lambda_n x - \frac{\cosh \lambda_n L + \cos \lambda_n L}{\sinh \lambda_n L + \sin \lambda_n L} (\sinh \lambda_n x - \sin \lambda_n x) \Big) \frac{(\rho A \gamma_n + m_o {\gamma_n}^o) Y_0 {\omega_e}^2 + \chi_n \frac{\sum_{n=1}^{\infty} \frac{-j\Theta_n (\rho A \gamma_n + m_o {\gamma_n}^o) \gamma_n {\omega_e}^3}{B_n({\omega_n}^2 - {\omega_e}^2 + j2\zeta_n \omega_n \omega_e)}}{\frac{1}{\tau_c} + j\omega_e + \sum_{n=1}^{\infty} \frac{j\Theta_n \chi_n \omega_e}{B_n({\omega_n}^2 - {\omega_e}^2 + j2\zeta_n \omega_n \omega_e)}}}{B_n({\omega_n}^2 - {\omega_e}^2 + j2\zeta_n \omega_n \omega_e)} e^{j\omega_e t} \tag{5.42}$$

## 5.4 Results and Discussion

In this section parametric study of the steady-state response of the electromechanical system is to be elucidated. Piezoelectric systems under an input (mechanical excitation), operate with both transient and steady-state responses. Since energy scavenging takes place in long-time span, steady-state response is the desired one for analysis. The properties of the harvester piezoelectric beam are presented in the following table.

Table 9. geometric and mechanical properties of beam [35]

| | |
|---|---|
| Beam length | $L = 100mm$ |
| Beam width | $b = 20mm$ |
| Substrate layer thickness | $h_s = 5\mu m$ |
| PZT layer thickness | $h_p = 4\mu m$ |
| PZT modulus of elasticity | $E_p = 66\ GPa$ |
| PZT mass density | $\rho = 7800\frac{kg}{m^3}$ |
| PZT coupling coefficient | $d_{31} = -190\frac{pm}{V}$ |
| PZT permittivity at constant strain | ${\varepsilon_{33}}^s = 15.93\frac{nF}{m}$ |

It is proved in the benchmark that synchrony of the driving frequency with the natural frequencies results in leap in the output voltage. Furthermore, such remarkable upheavals pertain to the first three vibration modes. As a result, excitation frequency range is considered to cover the first three vibration modes of the mechanical part. Since, the effect of various resistive load values over the output voltage and the shunted vibration response are widely explained in the benchmark, we take a representative value of $R_l = 10^6\Omega$ for current analysis. As a standard scale to figure out the responses of a system, eletromechanical frequency response function (FRF) is provided. Damping ratio is

considered as following values which are obtained experimentally by Erturk and Inman [35]:

Table 10. Proportional damping values for first three modes of vibration [35]

| $\zeta_1$ | $\zeta_1$ | $\zeta_1$ |
|---|---|---|
| 0.010 | 0.013 | 0.033 |

Mostly, in coupled electromechanical systems voltage FRF is described as the modulus of the output voltage to the base acceleration.

$$\frac{v(t)}{\ddot{g}(t)} = \frac{\sum_{n=1}^{\infty} \frac{-j\Theta_n(\rho A\gamma_n + m_o{\gamma_n}^o)\omega_e}{B_n({\omega_n}^2 - {\omega_e}^2 + j2\zeta_n\omega_n\omega_e)}}{\frac{1}{\tau_c} + j\omega_e + \sum_{n=1}^{\infty} \frac{j\Theta_n\chi_n\omega_e}{B_n({\omega_n}^2 - {\omega_e}^2 + j2\zeta_n\omega_n\omega_e)}} \tag{5.43}$$

accessing the voltage function, the power frequency response function is simply obtainable:

$$\frac{p(t)}{\ddot{g}(t)} = \left(\frac{\sum_{n=1}^{\infty} \frac{-j\Theta_n(\rho A\gamma_n + m_o{\gamma_n}^o)\omega_e}{B_n({\omega_n}^2 - {\omega_e}^2 + j2\zeta_n\omega_n\omega_e)}}{\frac{1}{\tau_c} + j\omega_e + \sum_{n=1}^{\infty} \frac{j\Theta_n\chi_n\omega_e}{B_n({\omega_n}^2 - {\omega_e}^2 + j2\zeta_n\omega_n\omega_e)}}\right)^2 / R_l \tag{5.44}$$

## 5.5 Optimizing the Energy Harvester via Soft Computing Techniques

After proposing a new type of piezoelectric vibration-based energy harvesters (PVEH) based on the model of cantilever-oscillator-spring system, variational concepts of advanced continuous vibrations and dynamics were employed to derive the governing differential equations and the corresponding boundary conditions. It was observed that the new type of elastic boundary condition at the tip end of the cantilever appoints a relative motion for the oscillator. This means that there are three distinct relative motions (oscillations) with respect to the Eulerian coordinates. Three distinct degrees of freedom

(DOF) of such proposed model encompass: the base motion, the cantilever motion, and the oscillator motion. Degrees of freedom (DOF) in terms of vibrations though is one order more. Since the system deals with mechanical oscillations and the resulting electric charge; a total of four DOF are to be considered in variational approach. It was well-described and studied that the adoption of spring which results in the distinct and relative motion of the oscillator, ends up in three coupled integral-partial differential equations. Two of the mentioned equations are titled mechanical equations with electrical coupling and the electrical equation is usually called the electrical equation with mechanical coupling. Moreover, the oscillation of the oscillator significantly changes the shearing boundary condition. Such impact is derived from the inertial effect of the oscillator when the system is in vibration and oscillation. Due to such mutation, the corresponding characteristic equation is a much more complicated transcendental nonlinear equation than the equation of the conventional system. After solving the mentioned equation using VPASOLVE algorithm in MATLAB, it was observed that for a wide range of the oscillator mass and the spring constant; the first eigenvalue is remarkably dragged to the left and close to the origin. For the conventional system (cantilever), the first eigenvalue is at the vicinity of 1.8749. The generation of such a minimal eigenvalue is strikingly beneficial for the PVEH particularly at small scales. For micro-electro-mechanical-systems (MEMS) energy harvesters, it is well-studied and reported in the literature that the first resonance is a large value meaning that resonance takes place at high frequencies. Such an increment in frequency value is usually due to the shrinkage in the system's dimensions. On the other hand, the excitation (driving) frequency as the external frequency and generated at the background, is mostly limited to a few hundreds of hertz. To compensate such a drawback

and incommensurateness, it is essential to alter systems vibrational characteristics and devise more efficient PVEH. In this response, the cantilever-oscillator-spring system is modeled in this dissertation. Eventually, tuning of PVEH is crucially important and vital. As far as the PVEH is not well-tuned the harvestable amount of electric energy is trivial. Such energy harvesting systems are inefficient and practically unapplicable to the industrial level implementations. Tuning of a PVEH mostly alludes to two distinct features of the harvester: the oscillator mass and stiffness constant of the spring. Tuning such factors leads to development and improvement in two vital features of the harvester: reinforcing the maximum amount of the harvested energy particularly throughout initial resonances as well as widening the effective (operational) frequency bandwidth. As mentioned earlier, optimizing PVEH from maximum harvested energy and maximum operational (effective) frequency bandwidth aspects, is vitally essential to improve and develop the PVEH efficiency.

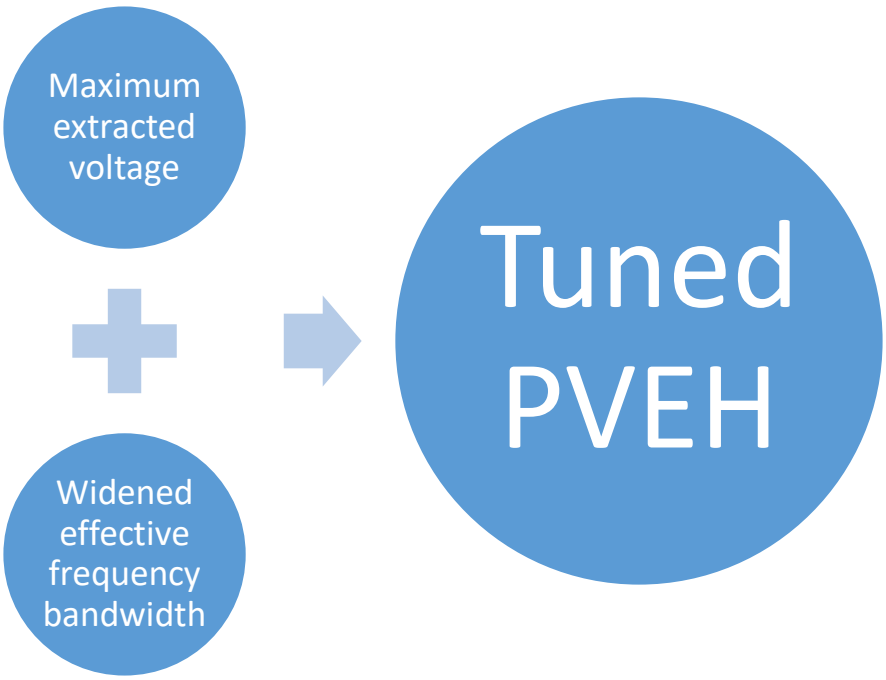


Figure 34. Tuned PVEH perspective

The well-tuned piezoelectric vibration-based energy harvester (PVEH) should be able to render the most feasible amount of electric power (or voltage), and the most widened effective (operational) frequency bandwidth (EFBW). The mentioned qualifications mostly are important spanning through the first few resonances. The reason for this is: most vibrating elements oscillate at the vicinity of the initial vibration modes. Higher vibration modes require very strong and specific motivations and excitements which is mostly rare in the physical realistic world. At the end it is good to note that such a tuning problem falls in the optimization category:

Maximum Electric Voltage: It is expressed in the preceding chapter that the maximum amount of electric voltage of a harvester system (PVEH) takes place at the first resonance. This fact is certainly conditional to the harmonic type of base excitations. In other words, harmonic type of excitation is assumed to motivate the harvester to oscillate

and vibrate. Comprehensive analysis of the electric frequency response function (FRF) is submitted in the former chapter and only the conclusion is used in this episode. Obviously, any continuous vibration system has infinite numbers of degrees of freedom (DOF) and consequently infinite numbers of resonances. However, in analyzing the electric FRF only the first few resonances are of importance. This is because in the higher vibration modes, the extractable amount of electric voltage is diminished. So, it suffices to mainly focus on the first vibration mode (or the few initial modes) in terms of mechanical and electrical analysis. Obviously, the desired situation and performance of any harvester is to extract and harness (scavenge) as much electric voltage (power) as viable and feasible. This means it is desired to maximize the performance of the PVEH so that the tuned and maximized system renders the most electric power.

Widened Effective (Operational) Frequency Bandwidth (EFBW): Another feature to assess the performance of any PVEH is the operational frequency bandwidth. Besides the maximum extractable voltage amount, the frequency bandwidth that the harvester operates is also of major vitality. There are several PVEHs that have great potential to convert mechanical energy into big huge amount of electrical energy; but, the operating frequency bandwidth is not wide enough to cover acceptable frequency range and span. So, widening the EFBW of a PVEH directly determines the system's success and operation.

In conclusion, the goal is to tune the PVEH in terms of maximizing the resonance voltage and widening the effective and operational frequency bandwidth. Basically and as mentioned earlier, such problems are maximization optimization problems. For any optimization problem, design parameters are to be well-addressed, clearly specified and

customized according to the current demands. For particular and specific values of design parameters, the objective function yields the optimal value. Such specific and particular design parameter values are titled the optimal parameters and the value of the desired function is entitled the optimal value. For minimization optimization problems the objective function is interchangeably called the cost (loss) function. In contrast, in maximization cases, the mentioned function is titled as the utility or fitness function. In short; in this part of the current chapter, two separate optimization case studies are delivered:

### 5.5.1 Optimizing the Extractable Voltage Amount at the First Resonance:

The closed-form solution found previously for the proposed PVEH, is a hard-to-assess function. The process of finding the voltage (electric) frequency response function (FRF) includes the following steps: first, the roots of the nonlinear transcendental characteristic equation are to be found. Since the equation is transcendental one, it does not have any exact solutions and numerical methods are adopted inevitably. Among such methods, the VPASOLVE algorithm requires decent initial guesses. To estimate such suitable guesses, the characteristic equation is plotted and visualized. In this section the human being inference and deduction is required to make an initial guess. After finding the roots which are indeed the system's eigenvalues, several coefficients are to be found and substituted in the voltage FRF. The mentioned integral coefficients are mostly expensive in terms of computational time and resource power as they are based on multi-functions of hyperbolic and trigonometric functions. There are two major issues in this whole process. First of all, the process is not automated. It means there is not any

programming script which can accomplish disparate steps in a single run. The very first step (finding the roots/eigenvalues) cannot be rendered by a computer or programming algorithm. As mentioned, this step needs an operator's insight and visualizing inferences. In other words, the analyzer (human being operator) needs to deduce and infer the eigenvalue initial guesses. The second issue refers to the huge number, and highly complicated computations which requires fast and strong processor and power resources with super powerful compiling capabilities. In other words, the derived voltage function is a hard-to-evaluate function since it is computationally expensive. On the other side, to find the optimal values of mass and spring constant an optimization algorithm should be applied and implemented. Such an optimizer mostly launches with an initial population of guesses titled as the candidate solutions. Such candidate solutions will undergo particular operations (e.g., in the case of genetic algorithm; genetic operations like: mutation, crossover, etc.). The result will be a set of solutions titled offspring population which genetically have superior features. This process will be iterated several times until a satisfactory level of solutions are obtained or there is no further convergence available. In each iteration, the objective function will be evaluated. Depending on the complexity of the problem, such objective functions will be evaluated hundreds, thousands, or even millions of times. Function evaluation requires a strong processor and compiler. Particularly if the function is too complicated, the optimization computational time costs will be unaffordable. In the first part of this section, it is already well detailed how and why the electric frequency response function (FRF) is a hard-to-assess function with non-automated (algorithmic) steps as well as the computational unaffordable costs. Due to the mentioned issues, it sounds necessary to find a decent regressor (estimator) which plays

the role of a function approximator. In other words, it is implied that the closed-form voltage FRF cannot be utilized in function evaluation in the optimization process. Consequently, it is indispensable to approximate the function using regression algorithms and execute the genetic algorithm with such an estimator. Such function approximator should be capable of finding the patterns in the electric FRF and render decent approximations. To do so, neural networks (or any machine learning regression algorithms) can be adopted. On the other hand, fuzzy logic is a superior method as it can utilize human reasoning for taking decisions, fuzzy logic can handle nonlinearity and uncertainty well. Consolidation and integration of fuzzy logic and neural networks is formed in ANFIS (adaptive-neuro-fuzzy-inference-system) toolbox in MATLAB. The proposed neural network fuzzy inference model captures the mass of the oscillator, and stiffness of the spring; and yields an approximation for the electric (in this case the voltage) value. Consolidation of the fuzzy logic, neural networks, and the genetic algorithm; forms a soft computing approach for the case studies in this chapter. After finding the optimal values of the design parameters (the oscillator mass and the spring constant) by means of the soft computing algorithms; the analytical methods (presented in former chapters and sections) will be implemented to verify the correctness and soundness of the soft computing method (the fuzzy logic, the neural network, and the genetic algorithm). So that several random values for the design parameters will be adopted arbitrarily. Voltage FRF will be then compared between the random parameter values and the optimal values. Such a comparison can validate the correctness of the designed soft computing algorithms.

Adaptive-Neuro-Fuzzy-Inference-System (ANFIS): as for explaining ANFIS shortly, one needs to first consider the fuzzy logic (FL) or fuzzy inference system (FIS).

FL mainly pertains to the multivalued logic. Fuzzy boundaries have a distinct and bold difference than classical logics. Fuzzy boundaries are not crisp, unlike the classical boundaries with clearly defined crisp set. Another feature of FL alludes to the fact that fuzzy sets are basically established based on the linguistic variables and words rather than numbers and numeric entities. Computations and reasoning based on linguistic variables are inherently less precise than numbers; though, such type of operation for decision taking is close to human intuition. Moreover, linguistic-based decisional operations exploit the tolerance for imprecision and lower the computational and solution costs subsequently. Fuzzy rules are mainly formed according to the simple if-then rules. An ever-growing trend pertains to the application of fuzzy logic in combination with genetic algorithm and neuro-computing. As mentioned earlier in this chapter, such a subtle combination is titled soft computing. On contrary to hard computing, soft computing accommodates the imprecision in the real world, exploits the tolerance and error for imprecision, captures and takes into account the uncertainty and nonlinearity, provides robustness, decreases the time computations and costs, and renders partial truth to gain tractability. It is expected the soft computing will play a remarkably important role in the design of futuristic systems with strikingly high machine IQ (MIQ). One of the major benefits rendered by neuro-fuzzy systems is to balance a tradeoff between precision and significance. Fuzzy logic as a black box simply maps an input space to an output space. Such a black box is better than most of the artificial intelligence algorithms since it is faster and cheaper, conceptually it is easy to understand for human beings since it is an intuitive approach, deals with uncertainty and error tolerance, can model nonlinearity, or functions with high complexity. All if-then rules in FL take the role of mapping inputs to outputs. Fuzzy rules are executed in parallel.

Within the structure of a fuzzy system, we have fuzzy sets with fuzzy boundaries and can contain elements with partial degree of membership. Another constituent of FL is the membership functions (MFs). A MF defines how each point in the input space is mapped to a membership value or degree of membership between zero and one. There are eight built-in MFs in MATLAB. However, it is feasible to devise a new MF from scratch. In the design of any MF, it is valuable to consider some factors including the: convenience, efficiency, simplicity, and speed or computational time. Two linear built-in MFs include: the trapezoidal and triangular functions. These are the fastest MFs with lower precision and simple structure. On the other hand, we have nonlinear MFs like: Gaussian, Gaussian2, Generalized Bell shaped, sigmoidal, double sigmoidal, polynomial sigmoidal. Fuzzy operations mainly include fuzzy intersection or conjunction (AND), fuzzy union or disjunction (OR), and fuzzy complement (NOT). Classical operators for the motioned functions are: AND ≡ min, OR ≡ max, NOT ≡ additive complement. Fuzzy sets and operators are the subjects and verbs of fuzzy rules. If-then rules are then used to formulate the conditional statements that comprise the fuzzy logic. In FL, interpreting the if-then rules involves two steps: evaluation of the antecedent and application of the result to the consequent.

Integration of fuzzy logic with neural networks ends up in adaptive-neuro (network-based)-fuzzy-inference-system (ANFIS). ANFIS executes the FL using neural networks. In a plain language, designing a fuzzy inference system needs adoption of MFs specifying limits and statistical parameters. It means how much of a function span is overlapped with the other function. What part of a function is interfered mathematically with another function. In other words, the function curve distributions are so important. Such function

distribution can be accomplished using neural networks. Benefits of utilizing the neural networks instead of manual MF distribution may pertain to more accuracy while keeping the computational costs as low as possible. This means efficient adoption of the functions. However manual procedure requires a high level of experience. Even with high experience, the process may be a burden and time-consuming.

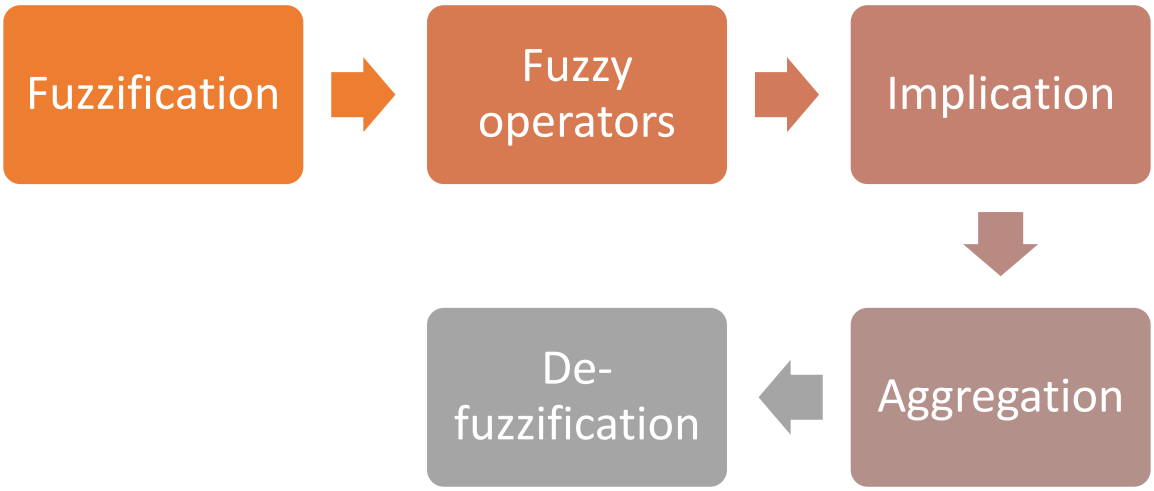


Figure 35. FIS schematic structure

In Figure 35, the schematic structure of fuzzy inference systems is provided in a single chart. The first step is the fuzzification step: in the fuzzification step; we utilize the MF to determine the degree to which the inputs belong to each appropriate fuzzy set (i.e., linguistic variables and semantic descriptions). Output of the fuzzification step is numeric value. Now, such numeric value is fed to the fuzzy rules.

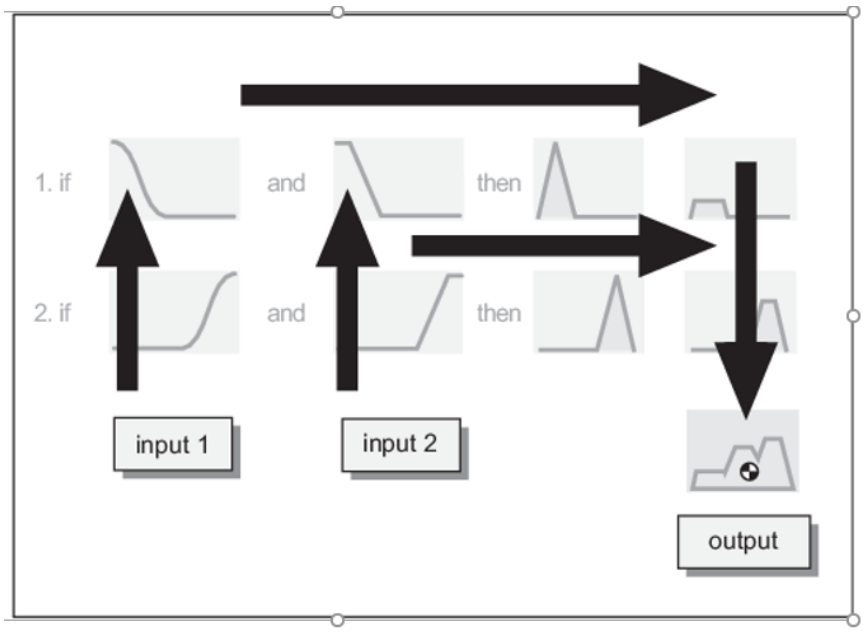


Figure 36. Fuzzy inference structure to make the aggregated output.

Fuzzy rules consist of antecedents and consequents with fuzzy operators including AND (min), OR (max), NOT (complement). Output of the fuzzy operators is to be fed to the implication step. Before the implication step, we can apply a weight to the rules to alter a specific rule effect over the others. This can be helpful when some specific rules are prior to the others and have a stronger impact. Implication: using implication the antecedents will be signified and implicated to the sequels. So, implication will be used to generate the consequents, which is a fuzzy set represented by MF. For each rule, the implication process from antecedent to consequent will take place. Input to the implication process is a single number and the output is a fuzzy set. In implication we have two built-in methods to imply the antecedents to consequent: AND (min) which truncates the output fuzzy set; and prod (product) which scales the output fuzzy set. Since we have multiple fuzzy rules in FIS, we need to integrate and incorporate all such rules into a single one. Aggregation is the process by which the fuzzy sets representing outputs of each rule will be combined into a single

fuzzy set. As long as the aggregation is a commutative process, then the order in which the rules are executed is unimportant. Three built-in methods for aggregation encompass: Max (OR), propor (probabilistic OR), sum (sum of the rule output sets). Eventually, last step is the de-fuzzification step to yield the final result. De-fuzzification: input to this step is the aggregated single fuzzy set (linguistic variables-semantic descriptions) and the output will be a numeric entity. Five built-in methods for de-fuzzification encompass: centroid, bisector, middle of maximum (the average of the maximum value of the output fuzzy set), largest of maximum, and smallest of maximum.

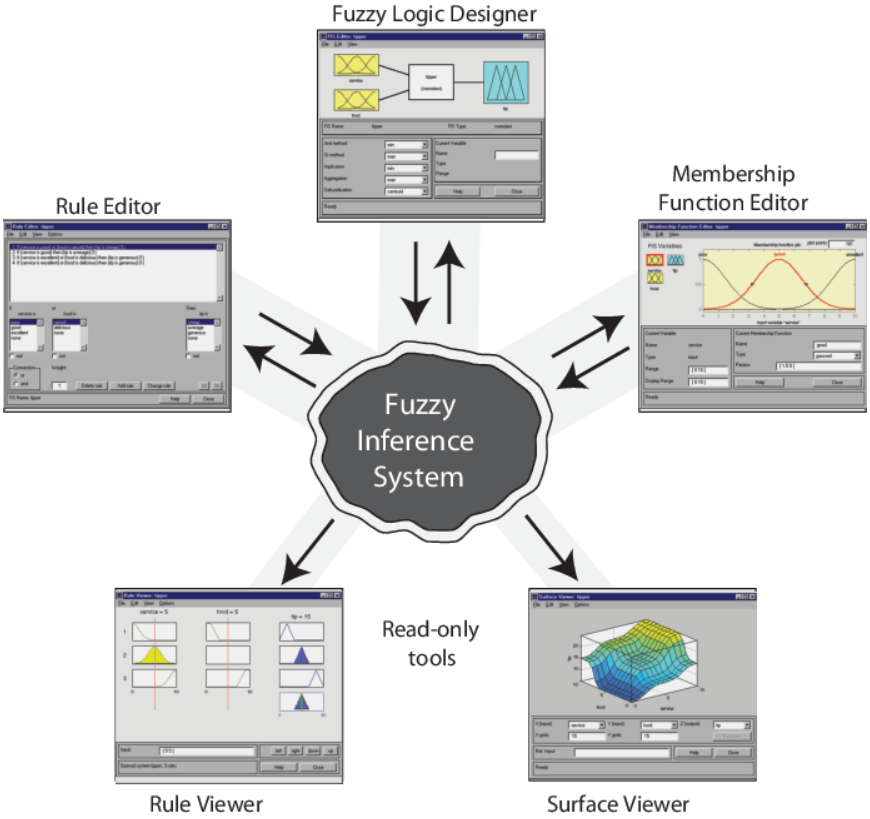


Figure 37. FIS editors and viewers in MATLAB

Figure 37 summarizes different steps in the FIS toolbox in MATLAB. In fuzzy logic designer section, one can change and modify inference settings. In the Membership function editor, one can modify input-output membership functions in terms of statistical features and the distribution. In Surface viewer the membership functions and the generated rules are observable in a graphical user interface (GUI) platform. In rule viewer, one can readily and instantly test input-output relationships. In the rule editor, one can modify or define the fuzzy rules including the if-then rules.

After providing a comprehensive explanation regarding the fuzzy inference system (FIS) structure and how it works, it is readily describable to state what adaptive-neuro-fuzzy-inference-system (ANFIS) is comprised of and how it works. Main part of the ANFIS is the FIS. ANFIS is a superior choice to FIS which is made up manually, as the neural network helps in integration and formation of the membership functions and fuzzy inference part. However, to benefit from such a privilege, one needs to provide sufficient and pre-processed dataset. So, ANFIS takes advantage of both fuzzy logic and neural networks in a single platform. The only limit to ANFIS alludes to the fact that since it is based on the Takagi-Sugeno inference logic, only systems with single output are qualified.

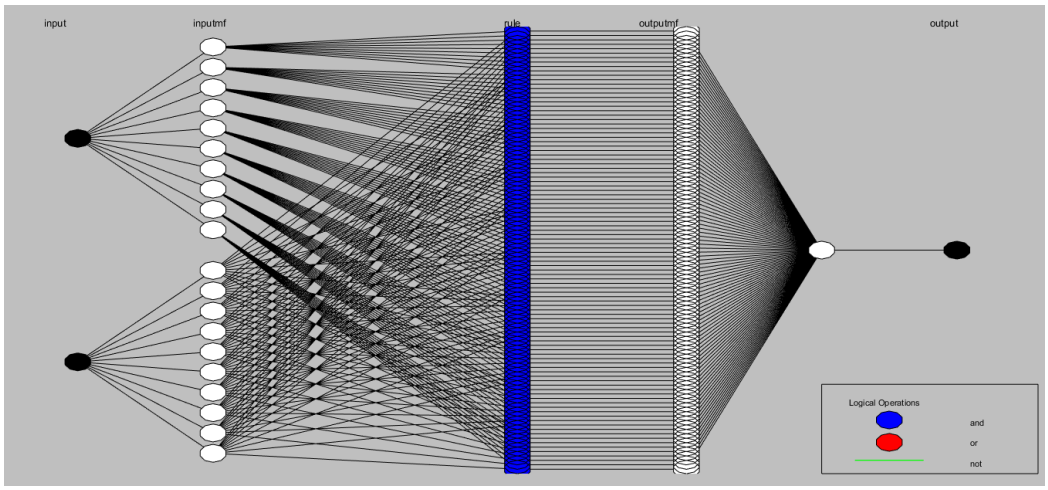


Figure 38. Schematic of the 5 layers in ANFIS

Figure 38 visually depicts the five layers implemented in an ANFIS structure. The first layer is the inputs. Such inputs depend on the number of entities describing the system input. Per each input specific number of membership functions (MFs) will be allotted. Premise (antecedence) set will be formed in this step. This step is usually titled as the fuzzification layer. In the second layer, strength fuzzy rules are generated. So, this layer is usually called the rule layer. In the third layer, the computed firing strengths are normalized. This process can be readily doable by dividing each value to the total firing strengths value. In the fourth layer, the consequence set, and the normalized value of the firing strength are taken. Values returned by this layer are de-fuzzified and fed to the last layer. In the last layer, the output of the fourth layer is aggregated, and the final output is achieved.

In this section, using the closed-form solution captured in the preceding chapter, voltage frequency response function (FRF) is to be discussed and plotted. For the two influential factors (oscillator mass, and spring stiffness coefficient); it is already stated that

the voltage FRF is altered and mutated strikingly with respect to various values of the mentioned parameters.

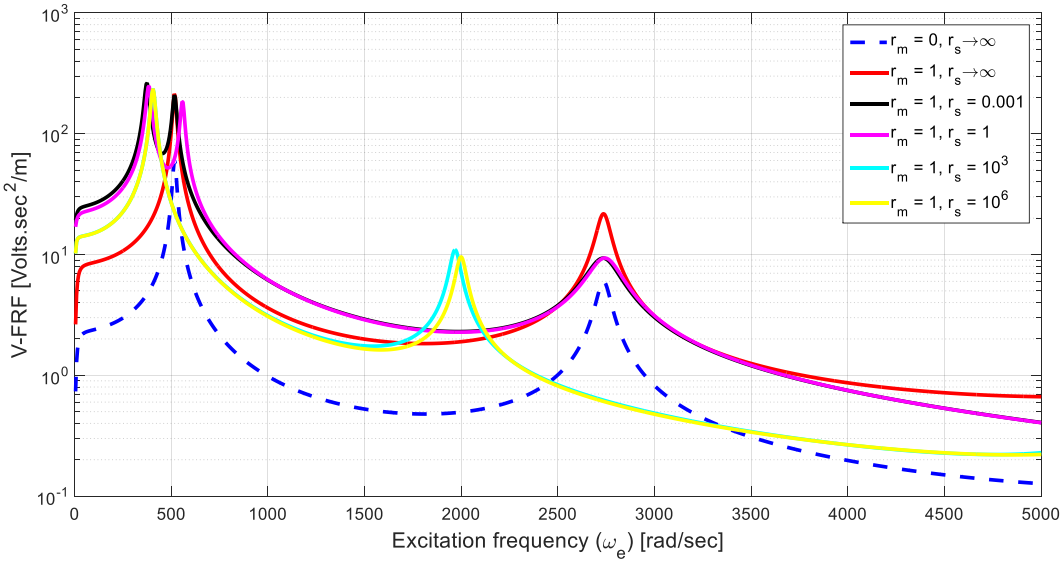


Figure 39. Voltage frequency response function with respect to excitation frequency (constant mass ratio)

As a recap from the former chapter, and to consider the effects of the restoring force effects resulting from the spring, constant value for mass ratio is adopted. It is evident that for very big values of the spring stiffness, two resonant voltages are observed. While, adopting a weaker spring (less stiff or a soft spring) with more flexibility in elongations results in three resonant voltages. Based on the figure provided, it can be concluded that number of resonant voltages is more dependent on the stiffness ratio and mass ratio implicitly alters the amount of harvestable voltage in each resonance. It is also good to note that the pure and sheer effects of the mass of the oscillator are reported in the former chapter in detail. Thus, considering the fact that for some values of the spring constant the minimal (newly-generated) resonance at the vicinity of the origin is observed; it sounds

essential to consider a wide range of spring constant along with oscillator mass to peruse the optimization problem of the proposed energy harvester.

Training ANFIS for the first resonance voltage: it is proved in the literature that the maximum voltage corresponds to the first resonance. So, only the first vibration mode is studied. Besides, to train the FIS by means of the neural network a decent dataset is required. Such dataset will be divided into three sections in which one of them will be utilized to train the FIS. Since the current case study has two inputs, a minimum of 100 datasets should suffice. It is derived from the concept that per each degree of freedom at least 10 data samples are needed. So, for a two-DOF system 10 by 10 results in 100 dataset. 231 cases (11 different values for $r_m$ and 21 different values for $r_s$) have been perused using the closed-form expressions for electrical FRFs. The first three eigenvalues along with all of the coefficients have been found for such cases.

$$r_s = [10^{-4}, 10^{-3}, 10^{-2}, 10^{-1}, 1, 10, 10^2, 10^3, 10^4, 10^5, 10^6]$$
$$r_m = [10^{-4}, 0.005, 10^{-3}, 0.005, 10^{-2}, 0.05, 10^{-1}, 0.2, 0.3, 0.4, 0.5, 0.6, 0.7, 0.8, 0.9, 1, 2.5, 5, 7.5, 10, 10^2]$$

The generated dataset (available in the appendix) of the resonance voltages is divided into train set (80%), validation (checking) set (10%), and test set (10%). Test dataset is used to evaluate the performance of the trained model on the new and previously unseen data. On the other hand, validation (checking) dataset is created to avoid overfitting of the model. It is also good to note that overfitting and underfitting mainly pertain to the complexity of the model. If the model is too simple, it will fail to predict with the train dataset, this is known as the underfitting issue. Such models are computationally cost-

effective, but practically they lack precision. Increasing the complexity of the model leads to more accurate predictions and regression performance on the train dataset. However, this will also result in more computational time and effort and slows the regressor model pace and speed. Besides the computational cost issue, highly complex models perform well with the train dataset but fail to operate correctly with the new previously unseen datasets in terms of accuracy and precision of the estimations. This is known as the overfitting issue which means the model fails to generalize with unseen data. Similarly, such too complex models are impractical and not desired. To avoid the overfitting issue by means of cross validation technique, ANFIS toolbox in MATLAB is equipped with checking (validation) dataset. In this section fuzzy inference systems (FISs) are designed and trained based on the eight built-in membership functions (MFs) available in MATLAB fuzzy toolbox.

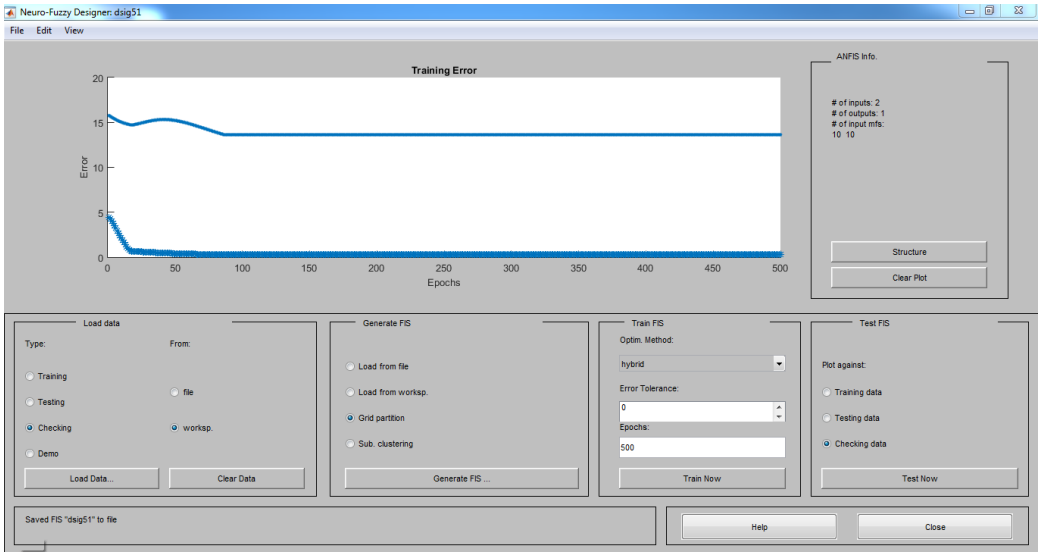


Figure 40. Neuro Fuzzy designer

The neuro fuzzy designer application in MATLAB is toolbox is shown in Figure 40. Due to the type of the input dataset distribution, it is required to pre-process the data and scale them in an effective expression range. To do so, input datasets are converted into the logarithm range to the base of 10. Features adopted to train the FIS based on the built-in MFs are summarized in Table 14:

Table 11. ANFIS training properties

| | | |
|---|---|---|
| Number of MF for $r_m$: 8 | Neural network optimization: Hybrid | Fuzzy type: Takagi Sugeno (MISO) |
| Number of MF for $r_s$: 8 | Number of Epochs: 300 | Number of Fuzzy rules: 64 |
| Type of MF: Gaussian | Error tolerance: 0 | |
| FIS Generation: Grid partitioning | Output MF type: Constant | |

Table 12 shows a brief comparison between different types of membership functions executed with 8 functions per each input (total of 64 fuzzy rules in the fuzzy set) and 300 epochs as the number of times the training dataset has been passed through the learning procedure.

Table 12. Comparison of various built-in membership functions (MFs)

| MF type | Train RME | Test RMSE | Validation RMSE |
|---|---|---|---|
| Triangular | 0.66464 | 1.2794 | 0.69288 |
| Trapezoidal | 0.50462 | 0.89916 | 1.34183 |
| G-Bell shaped | 0.14981 | 0.21771 | 0.207997 |
| Gauss | 0.34832 | 0.55443 | 0.30657 |
| Double Gauss (Gauss2) | 0.42936 | 0.67454 | 0.64669 |
| Polynomial | 4.4771 | 8.8079 | 6.9751 |
| Double sigmoid | 1.0146 | 1.9336 | 1.1787 |
| P-sigmoidal | 1.018 | 1.9495 | 1.1778 |

The table presented in the above section compares disparate membership functions in terms of accuracy in training the membership functions (MFs). Such a comparison is assessed based on the root-mean-square-error (RMSE) for train dataset, RMSE of test dataset, and RMSE of checking (validation) dataset. Obviously, it is shown that Generalized-Bell shaped (G Bell shaped) type of membership functions show the least root-mean-square-error (RMSE) for all datasets. This means that fuzzy system established based on the Generalized-Bell shaped functions have the most accuracy and precision as well as the most generalization. Generalization refers to the capability of the fuzzy system to avoid overfitting. A generalized system has the power to predict unseen data with a high level of accuracy. Such a regressor system has small test RMSE. Besides the Generalized-Bell shaped MFs, Gaussian MFs rank the second place as the best function to train an adaptive network based fuzzy system. Best here means the function with most accuracy in capturing the structure of train dataset along with the smallest RMSE for previously unseen dataset. The latter particularly alludes to the generalization feature. After choosing the type of the best membership functions, the next step is to come up with the proper number of the membership functions per degree of freedom (input). To do so, a trial-and-error procedure is adopted to pick the proper number of membership functions per input along with a decent number of epochs. Such an effort is considered to reach a high level of accuracy along with reasonable time computations to find a cost-effect fuzzy system. It means the major goals are: Accuracy and precision of the regressor (estimator, approximator) FIS, Computational costs in terms of time.

Table 13. Evaluation of Gaussian MF, 300 epochs

| Number of MFs | Number of Epochs | Train RMSE error | Test RMS error | Validation RMSE error |
|---|---|---|---|---|
| 4 by 4 | 300 | 8.1471 | 10.6965 | 7.9777 |
| 5 by 5 | 300 | 5.575 | 6.5074 | 5.8024 |
| 6 by 6 | 300 | 2.5022 | 2.8248 | 2.0664 |
| 7 by 7 | 300 | 0.71071 | 1.0824 | 0.97397 |
| 8 by 8 | 300 | 0.34832 | 0.55443 | 0.30657 |
| 9 by 9 | 300 | 0.25229 | 3.2761 | 4.016 |
| 10 by 10 | 300 | 0.22361 | 54.9307 | 21.4041 |
| 11 by 11 | 300 | 0.077939 | 182.4772 | 182.5246 |

Taking different numbers of MFs with Gaussian MF also called Gauss MF, corresponding RMSE values of the train, test, and validation datasets are found. It is observed that the number of epochs does not significantly alter the RMSE. RMSE diminishes gradually as the epoch number increases. However, the number of MFs strongly and highly impacts the performance of the FIS. So, to reach the desired accuracy level, MF numbers as the role-playing factor are to be scrutinized. In contrast, the epoch number is a minor factor which is not as important as the number of MFs. The epochs number only increases the time computations with minimal modification over the performance of the FIS. This is the main reason to keep the epoch numbers constant and mainly alter the membership function numbers.

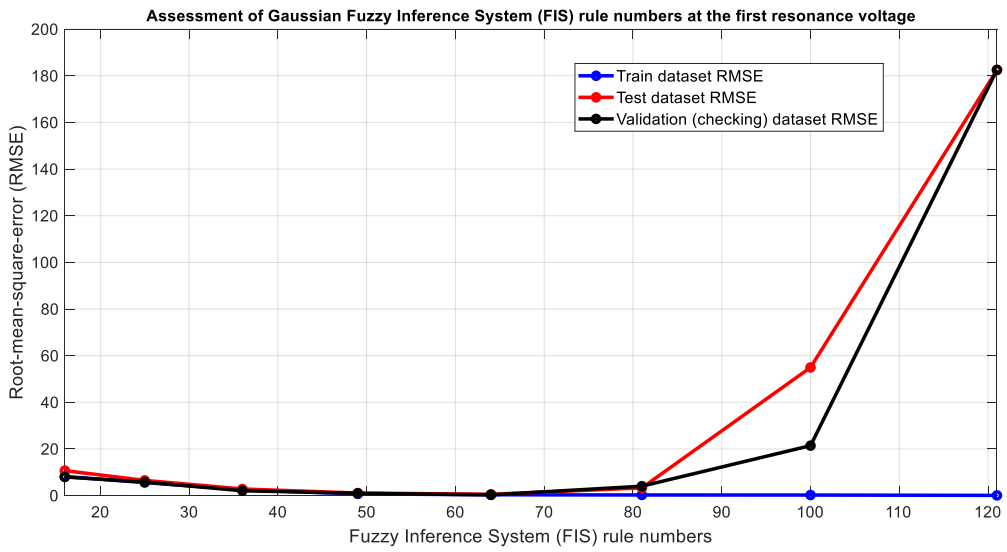


Figure 41. RMSE with respect to the Gaussian fuzzy rule numbers

To visualize the RMSE value for the trained fuzzy system using Gaussian MF with different numbers of fuzzy rules, Figure 48 is presented. It is clear that the fuzzy system with 64 rules demonstrates the least RMSE for test and validation datasets. Expectedly, the train RMSE declines with higher fuzzy rules. For example, the fuzzy system with 121 rules, has much better RMSE value for train dataset. But, the test and validation RMSEs are significantly and adversely big. This fact points to the overfitting issue. So, setting the test RMSE as the major criteria, the 64-fuzzy rule system with Gaussian MF looks the most accurate and efficient choice.

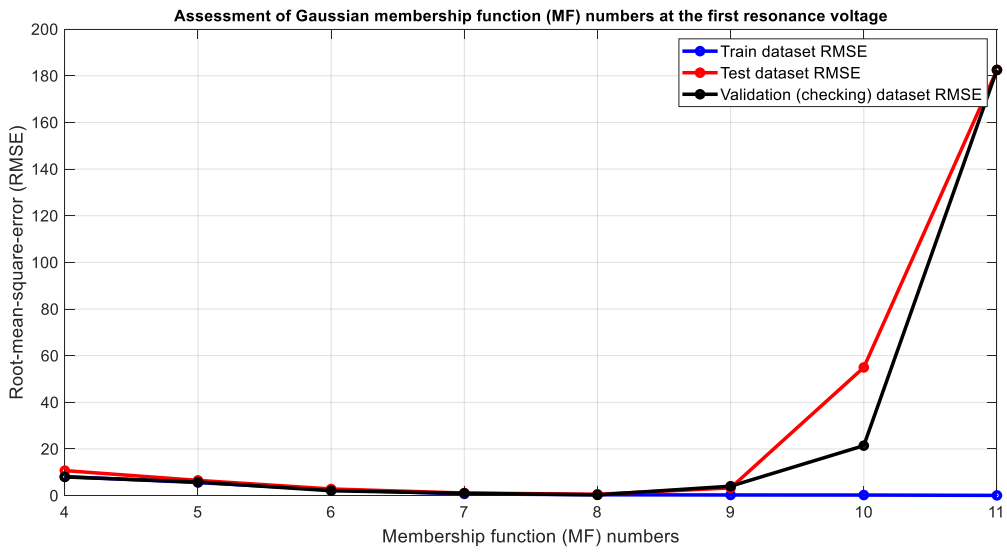


Figure 42. RMSE with respect to the Gaussian fuzzy membership function numbers

Similar results of the Gaussian type fuzzy inference systems (FIS) are shown in figure 42 with respect to the number of MFs. Expectedly, the FIS with 8 by 8 MFs yields the most accurate system with the least test and validation (checking) dataset RMSE values.

Table 14. Evaluation of Generalized-Bell shaped MF, 300 epochs

| Number of MFs | Number of Epochs | Train RMSE error | Test RMS error | Validation RMSE error |
|---|---|---|---|---|
| 4 by 4 | 300 | 3.9852 | 4.66 | 3.9007 |
| 5 by 5 | 300 | 1.4319 | 1.5073 | 1.4736 |
| 6 by 6 | 300 | 1.3714 | 1.6408 | 0.80779 |
| 7 by 7 | 300 | 0.71116 | 1.2121 | 0.83427 |
| 8 by 8 | 300 | 0.14981 | 0.21771 | 0.208 |
| 9 by 9 | 300 | 0.22531 | 0.6286 | 1.0404 |
| 10 by 10 | 300 | 0.13322 | 68.6687 | 17.8264 |
| 11 by 11 | 300 | 0.078786 | 182.4359 | 183.2008 |

The same procedure is performed here for the Generalized-Bell shaped MFs. According to the explanation provided in the above section, the number of fuzzy rules or

number of fuzzy membership functions is of primary concern. Disparate values of MFs numbers are assigned to the Generalized-Bell MF to train the fuzzy inference system.

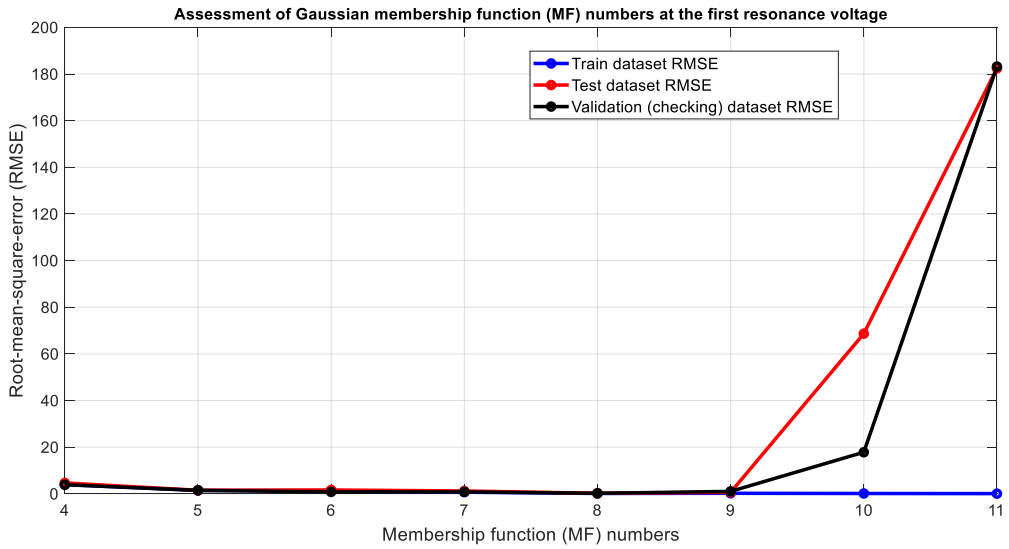


Figure 43. RMSE with respect to the Generalized-Bell shaped fuzzy rule numbers

To compare the RMSE values of the fuzzy systems trained with G Bell (Generalized-Bell shaped) MFs, figure 43 is presented. RMSE is plotted with respect to the number of MFs allotted per MF. It is good to note that identical numbers of MFs are assigned for each input. Visually, the 8 by 8 fuzzy system shows the least RMSE value.

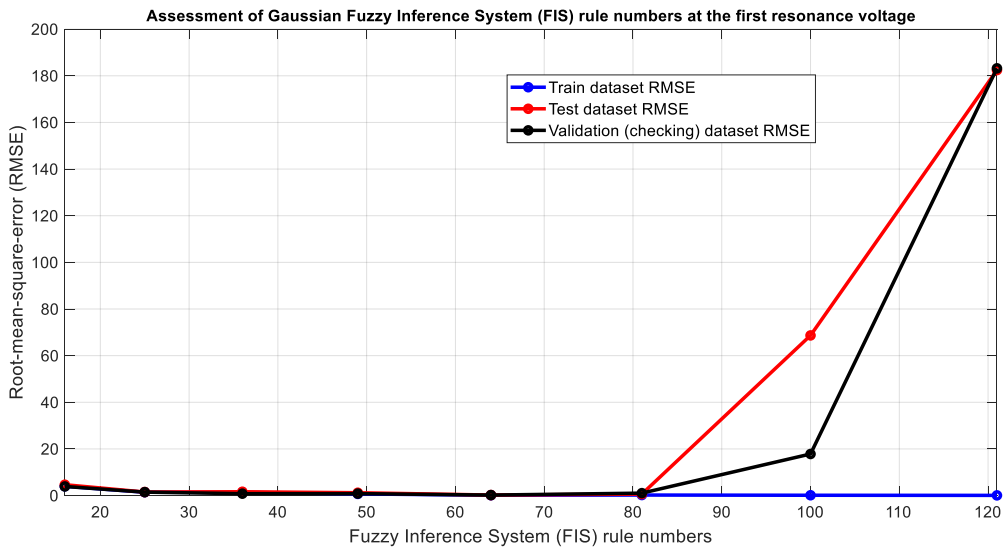


Figure 44. RMSE with respect to the Generalized-Bell shaped fuzzy membership function numbers

The same demonstration is duplicated with respect to the number of fuzzy rules. Proving findings in figure 44, the G Bell MFs with 64 fuzzy rules result in the smallest RMSE value for test and checking (validation) datasets. Now, based on the two adopted MFs, fuzzy inference system is to be designed as demonstrated in the following section:

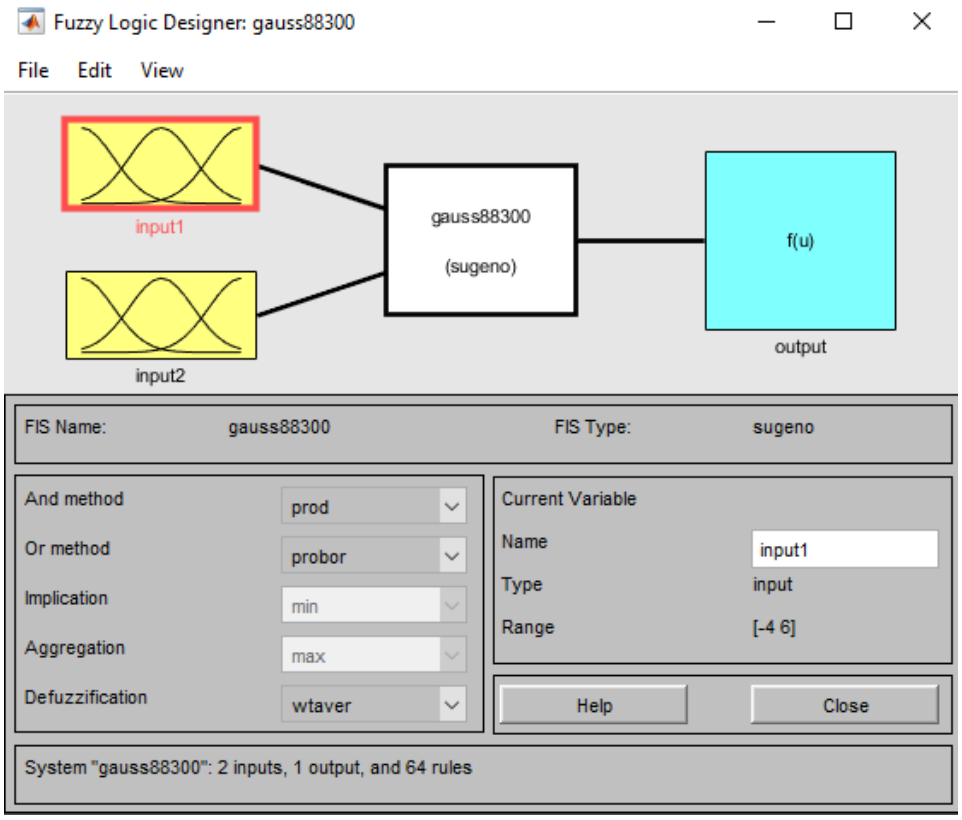


Figure 45. Fuzzy logic designer application setting

This figure represents the fuzzy logic file of the first FIS established based on the Gaussian MFs. In the 'And method', the production method is adopted ('prod'), 'Or method' is established based on the 'probor' which refers to the probability. 'implication' is formed due to the 'min' which represents the minimum value, and the 'Aggregation' is taken by means of the 'max' which means the maximum values. Aggregation step integrates and incorporates all of the fuzzy output results into a single output. Finally, in the defuzzification step, the 'wtaver' is used meaning the averaging method.

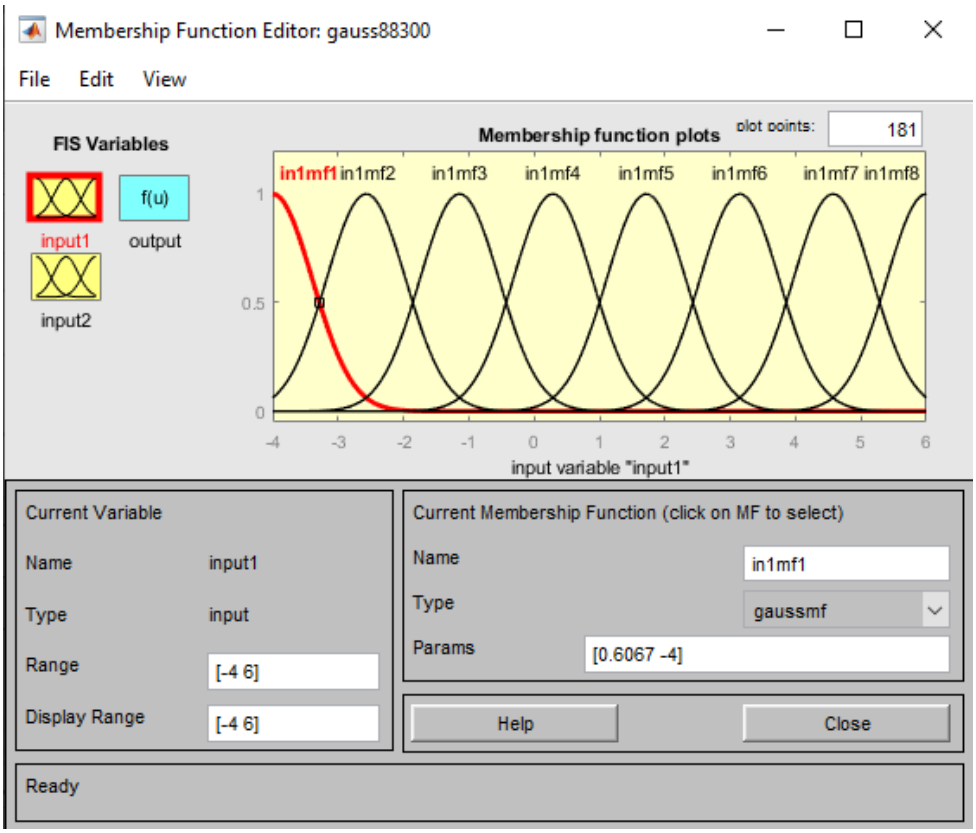


Figure 46. Fuzzy logic membership function editor – first input

In Figure 46, 8 Gaussian-type membership functions for stiffness ratio are adopted and depicted in the range of $[-4,6]$. Parameters of such functions are tuned using neural networks. Visually the MFs are uniformly and symmetrically distributed.

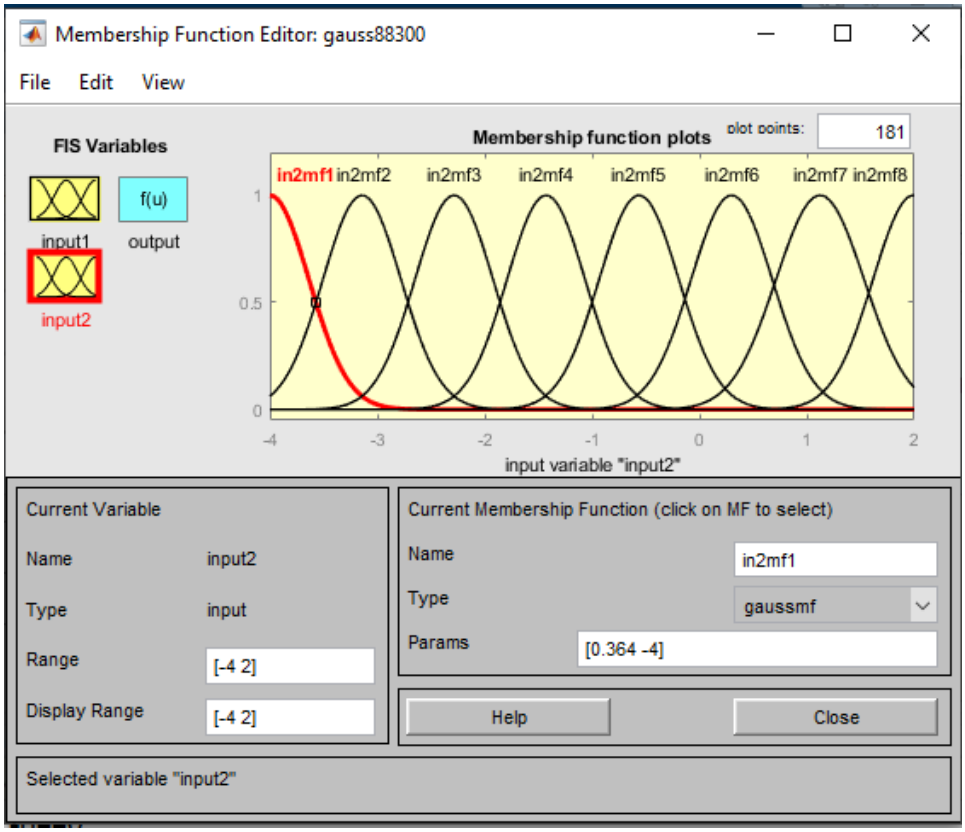


Figure 47. Fuzzy logic designer application setting – second input

In Figures 47, 8 Gaussian-type membership functions for mass ratio are chosen and depicted in the range of $[-4,2]$. Parameters of such functions are tuned using neural networks. Similar to the MFs of the stiffness ratio, a uniform distribution is observed in this case.

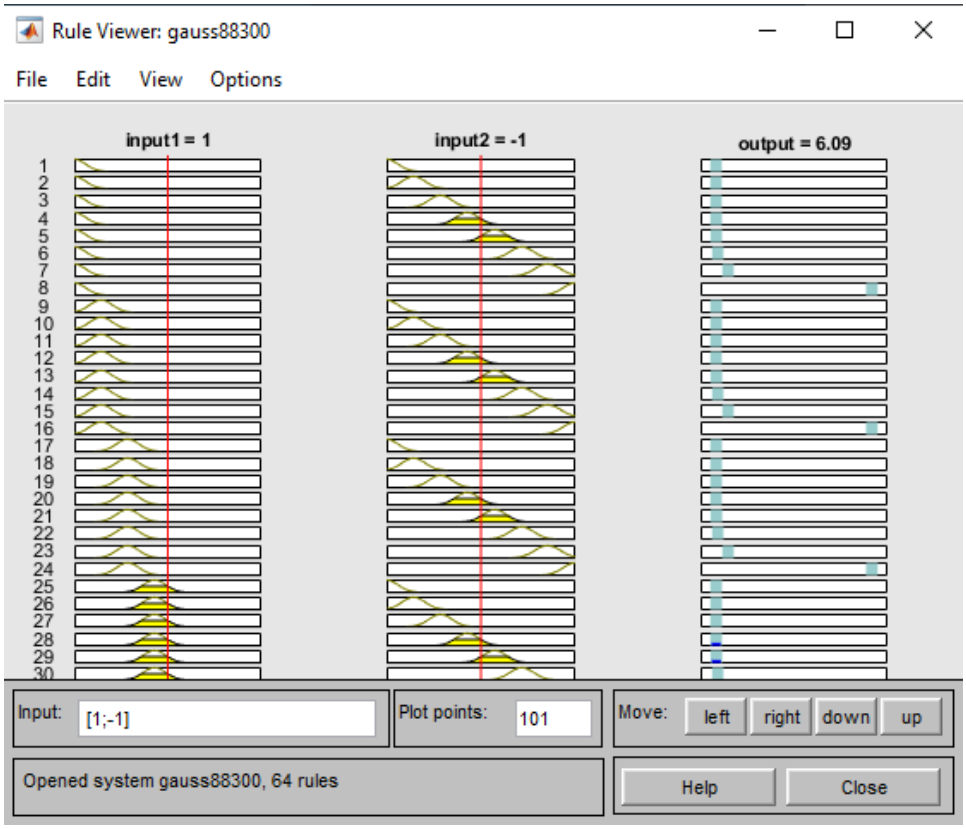


Figure 48. Fuzzy logic rule viewer

Gaussian-type membership functions of each input ($r_m$ $and$ $r_s$) generate total of 64 fuzzy rules. Corresponding fuzzy rules generated from the Gaussian type MFs are shown in figure 48. Such a rule viewer is conducive in interpreting the fuzzy inference process in a single observation. It also shows how the shape of the MFs influences the overall result of the fuzzy inference mechanism. It can be readily tested by changing the inputs to see the outcoming result.

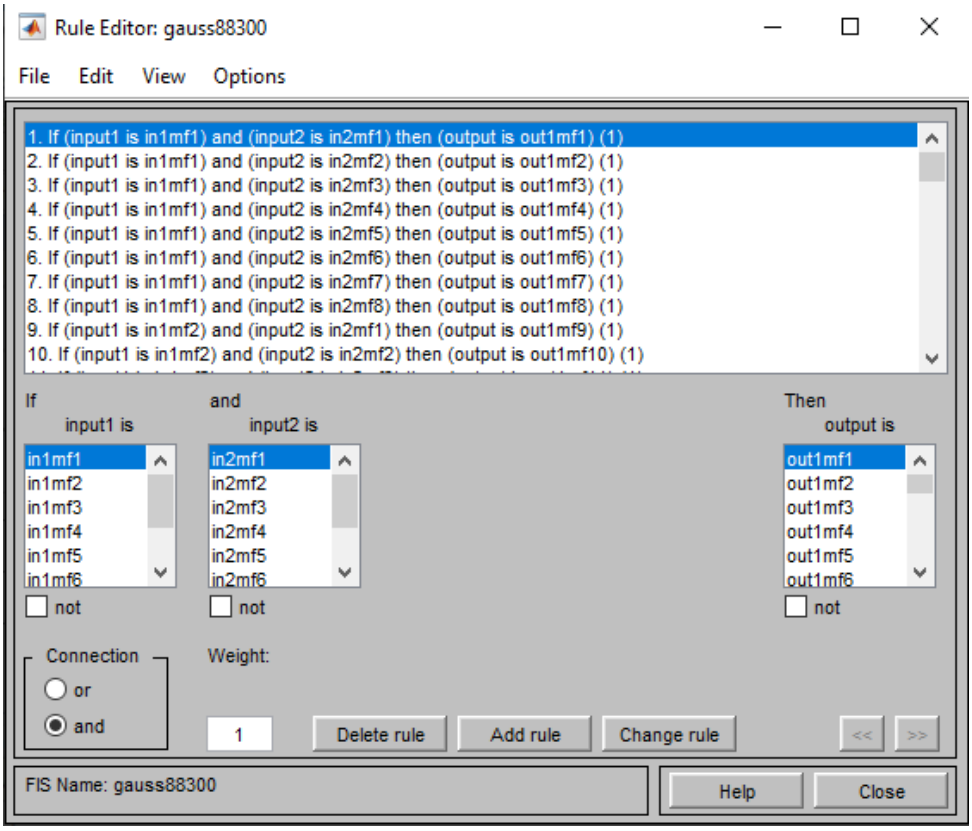


Figure 49. Fuzzy inference verbose rule editor

The verbose format of the mentioned fuzzy rules is shown in figure 49. Fuzzy rules are established based on the truncation of the fuzzy sets using the ‘AND’ (minimum) operator arranged with identical unit weight per set.

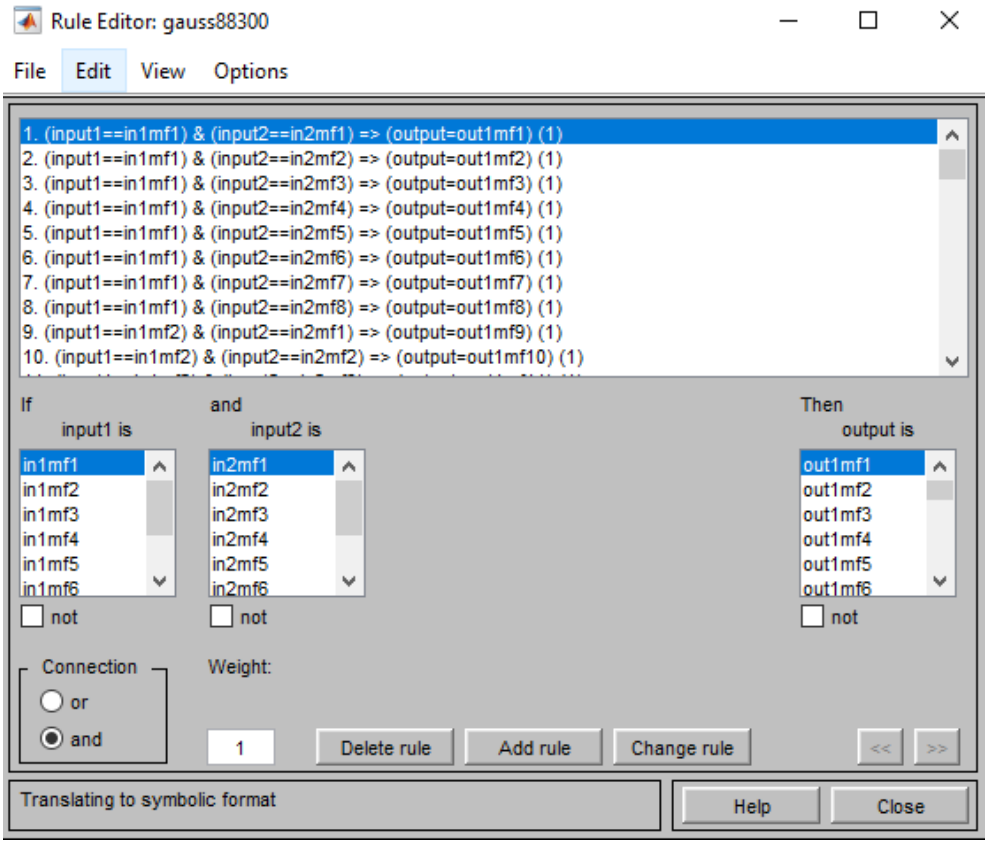


Figure 50. Fuzzy inference symbolic rule editor

This picture shows the fuzzy rules in the symbolic format. The rule editor is shown by symbols in this figure. The relation between inputs, the weights, and the connection type are all shown.

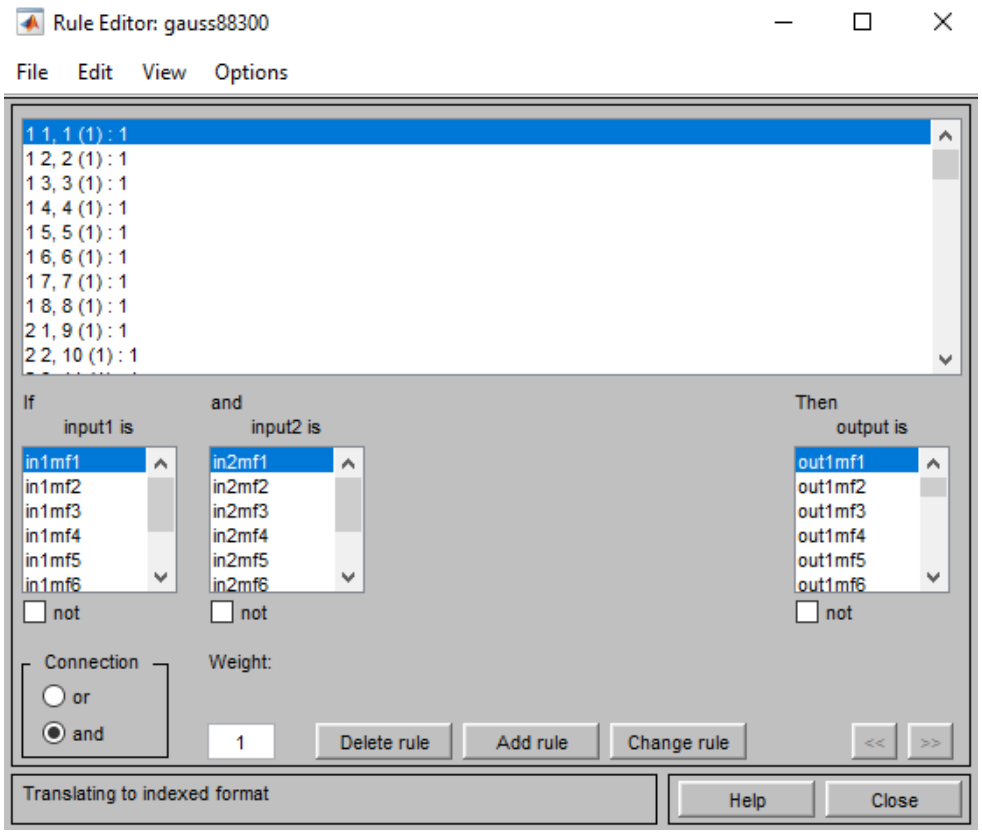


Figure 51. Fuzzy inference indexed rule editor

Rule editor in indexed format is represented in figure 51. The three above figures show the same thing in different expression languages and formats.

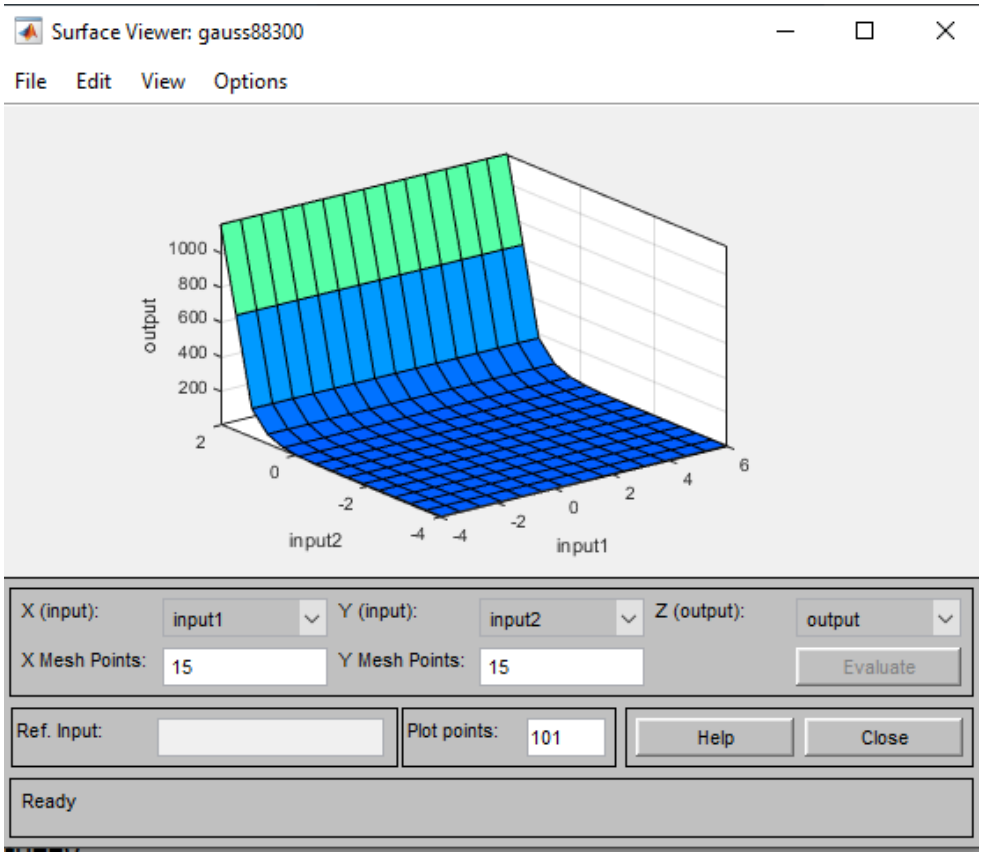


Figure 52. Fuzzy inference surface viewer

This figure shows the graphical demonstration of the rules using the graphical user interface (GUI) available in MATLAB. This figure is shown in three dimensions to depict the corresponding rule curves with respect to the inputs (mass ratio and stiffness ratio). Now in the following section, similar steps in training the fuzzy inference system based on the G-Bell (Generalized-Bell) shaped membership functions are presented.

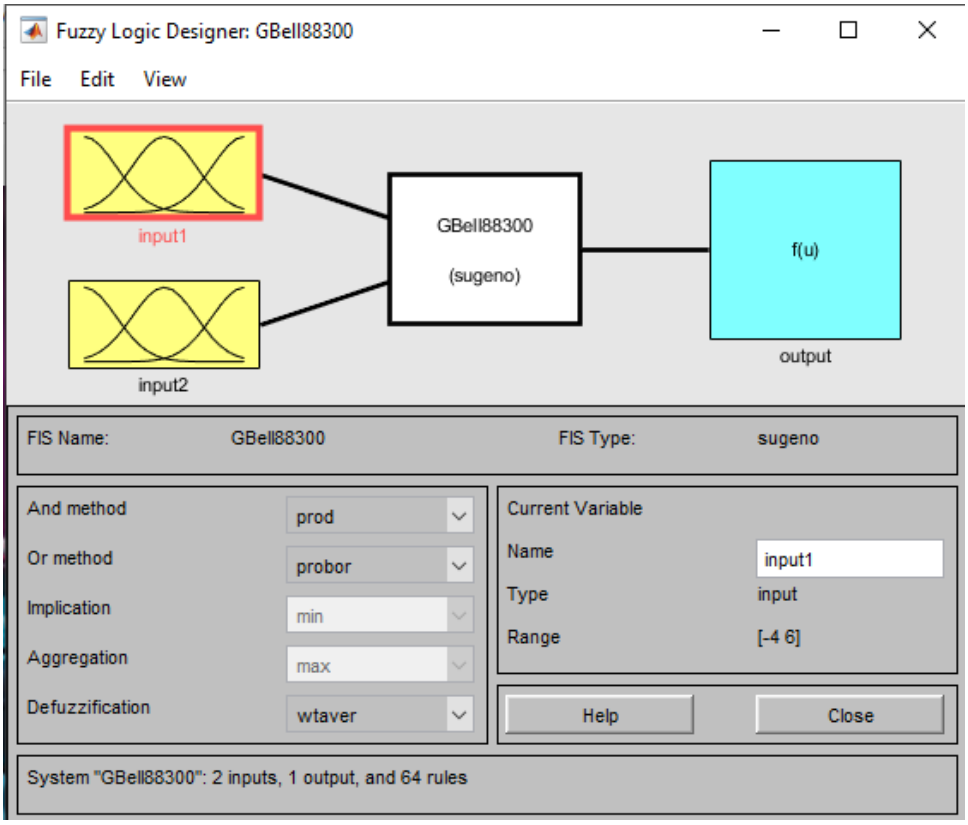


Figure 53. Fuzzy logic designer application setting

Besides the implementation of Gaussian MFs, a second fuzzy inference system is to be designed based on the Generalized-Bell shaped MFs. Thus, in the fuzzy logic designer application in MATLAB, the G-Bell shaped (Generalized-Bell shaped) membership functions (MFs) are being utilized for both of the inputs to train the reasoning fuzzy inference system (FIS) using neural network. In the 'And method' the 'prod' option is used showing the production, 'Or method' is established based on the 'probor' which represents the probability. 'implication' is founded according to the 'min' representing the minimum value, and the 'Aggregation' is formed using 'max' meaning the maximum values. The aggregation step integrates and consolidates all of the fuzzy output results into

a single output. Finally, for defuzzification, the ‘wtaver’ is used meaning the averaging method.

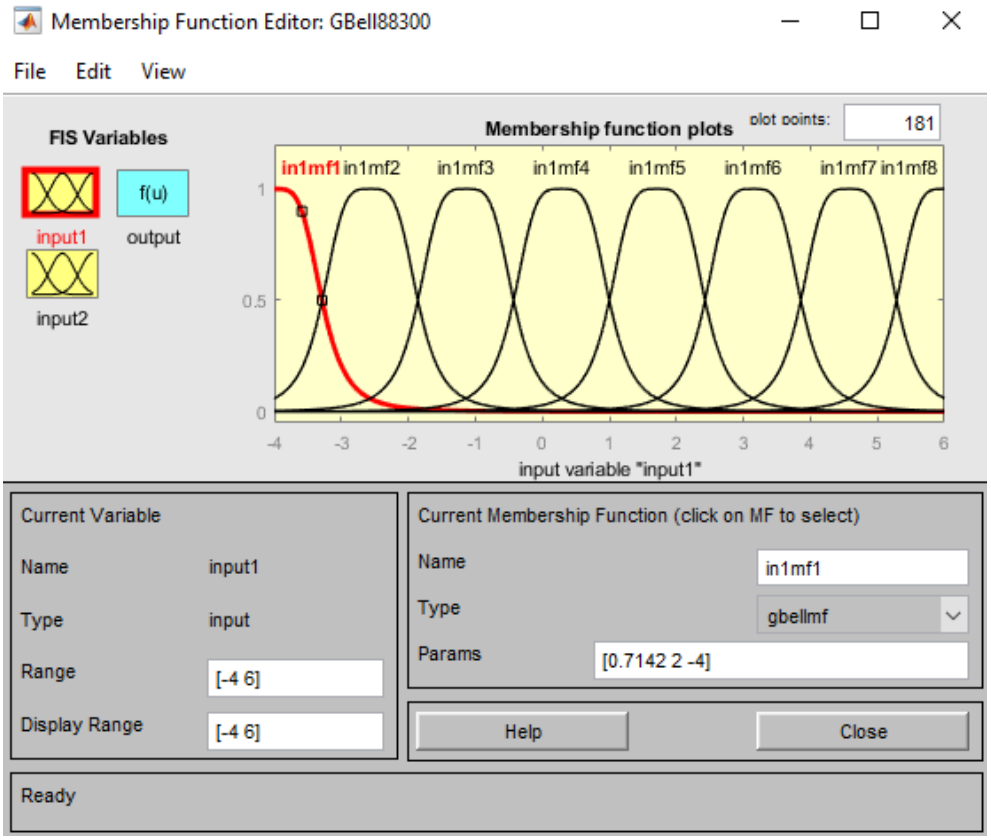


Figure 54. Fuzzy logic membership function editor – first input

In this section, 8 Generalized-Bell shaped membership functions are used to distribute the first input functions in the range of $[-4,6]$. The mentioned first input pertains to the stiffness ratio.

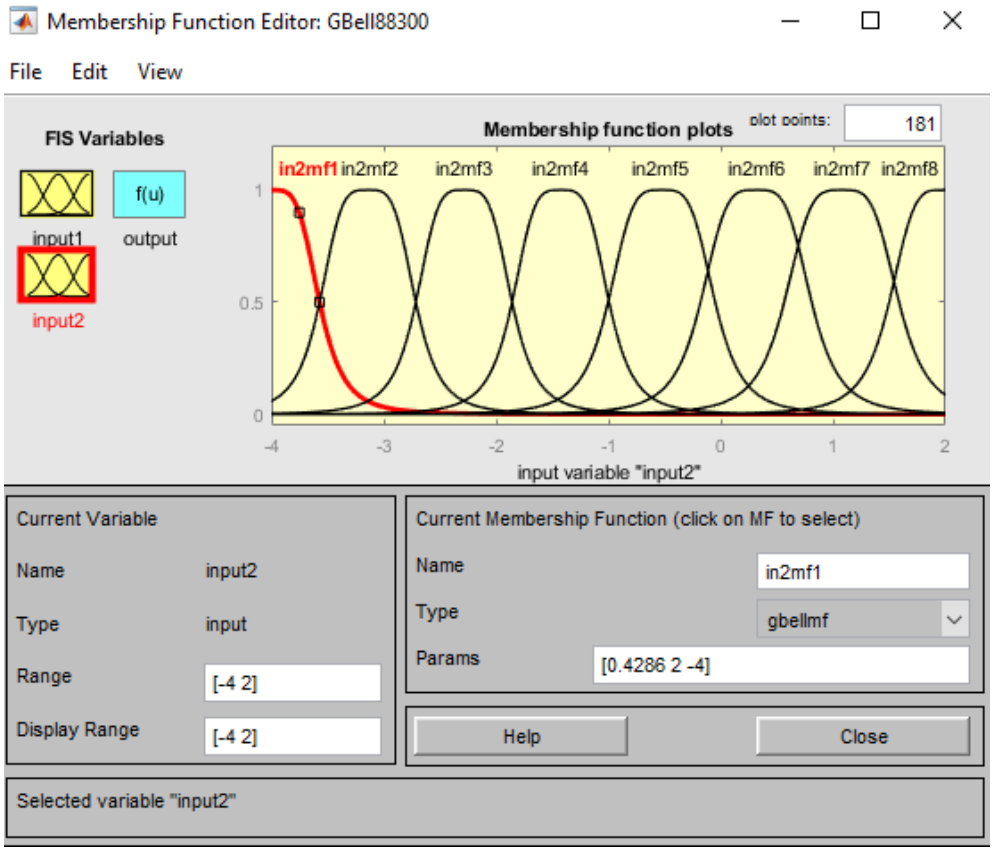


Figure 55. Fuzzy logic membership function editor – second input

Functions determining the degrees of membership of the second input (mass ratio) are shown in figure 55. Distribution range is $[-4,2]$. The functions plot shows the Generalized-Bell features with a smooth acme (summit) per each function.

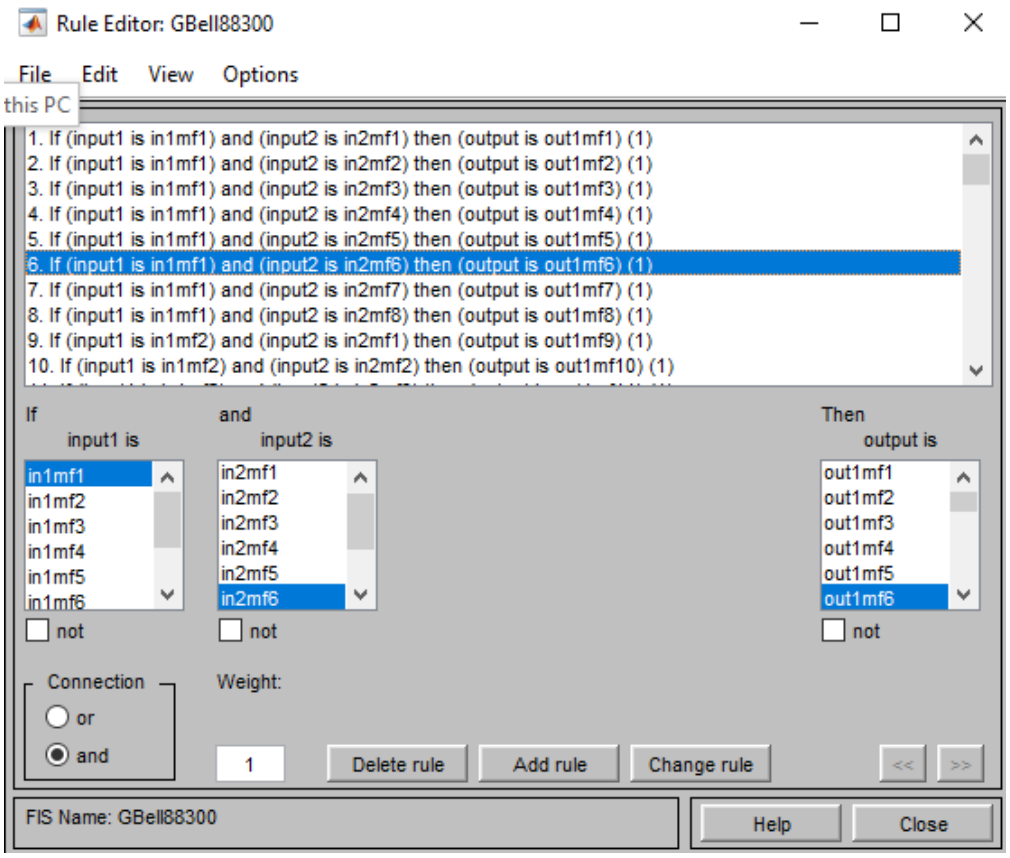


Figure 56. Fuzzy inference verbose rule editor

Rule editor is provided in figure 56 to show the fuzzy rules of the system in the verbose format. Fuzzy sets are connected to each other using the ‘and’ method, with unit identical weight of 1 per each entity.

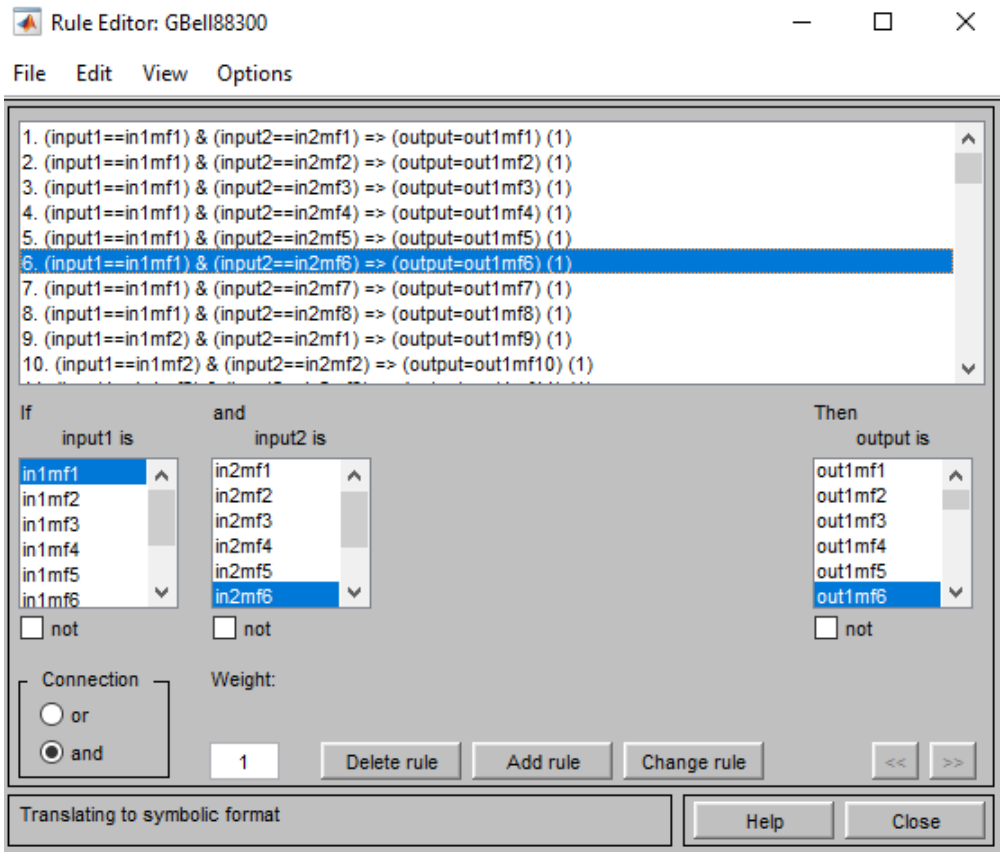


Figure 57. Fuzzy inference symbolic rule editor

Figure 57 represents the fuzzy rules generated via the Generalized-Bell shaped MFs in the symbolic format. It is actually the same rules expressed in symbols than verbose.

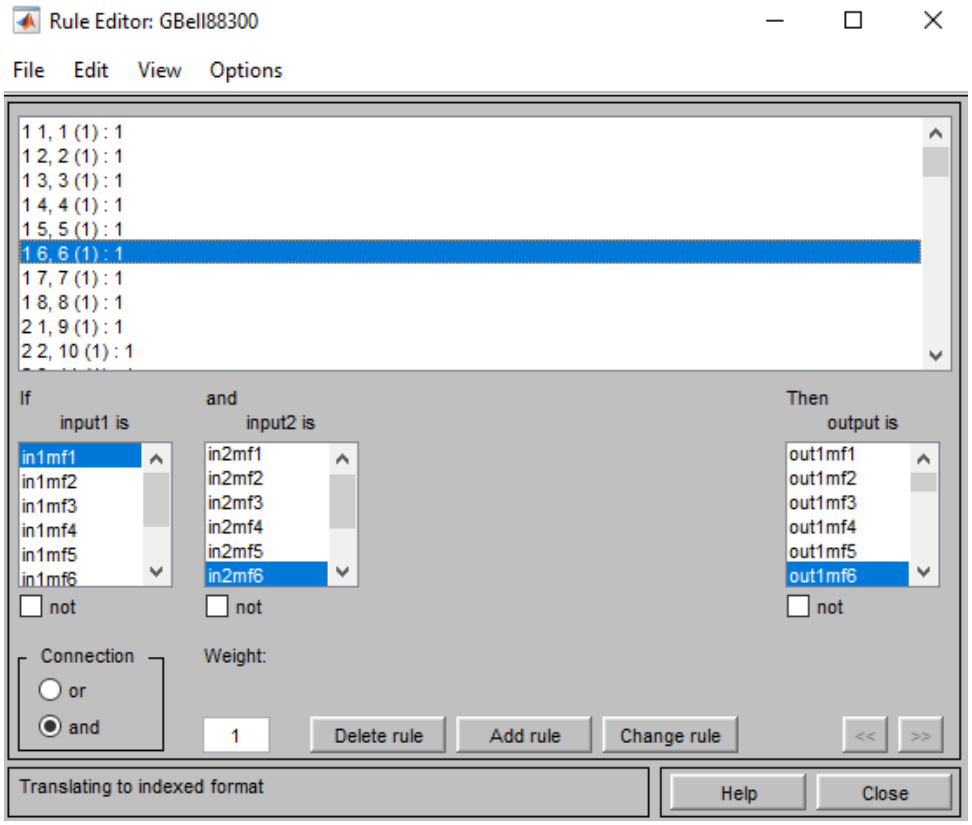


Figure 58. Fuzzy inference indexed rule editor

Eventually, the mentioned fuzzy rules in the indexed format are shown in figure 58. With this figure, all three types of fuzzy rules expression are provided and presented.

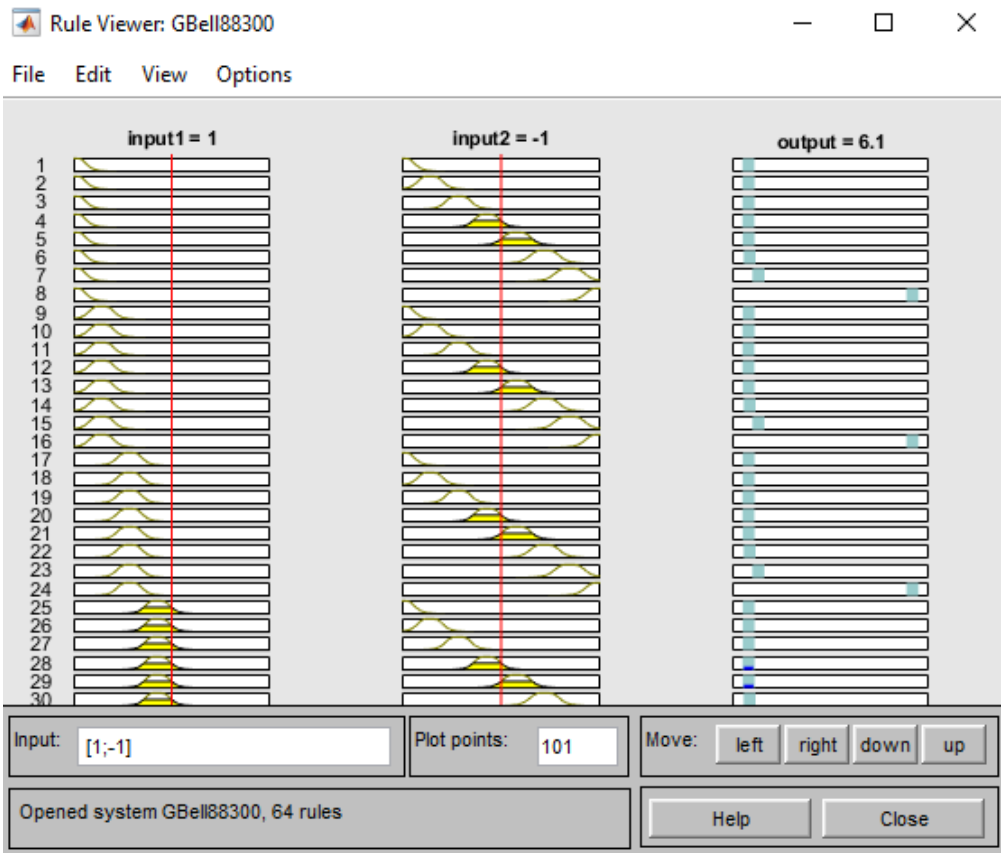


Figure 59. Fuzzy logic rule viewer

Rule viewer is presented in figure 59 to enable designer to interpret the fuzzy inference process at once. From this figure, it is also inferable to deduce how certain shape of membership functions influences the overall result. This means how the reasoning is justified and formed in the fuzzy rules.

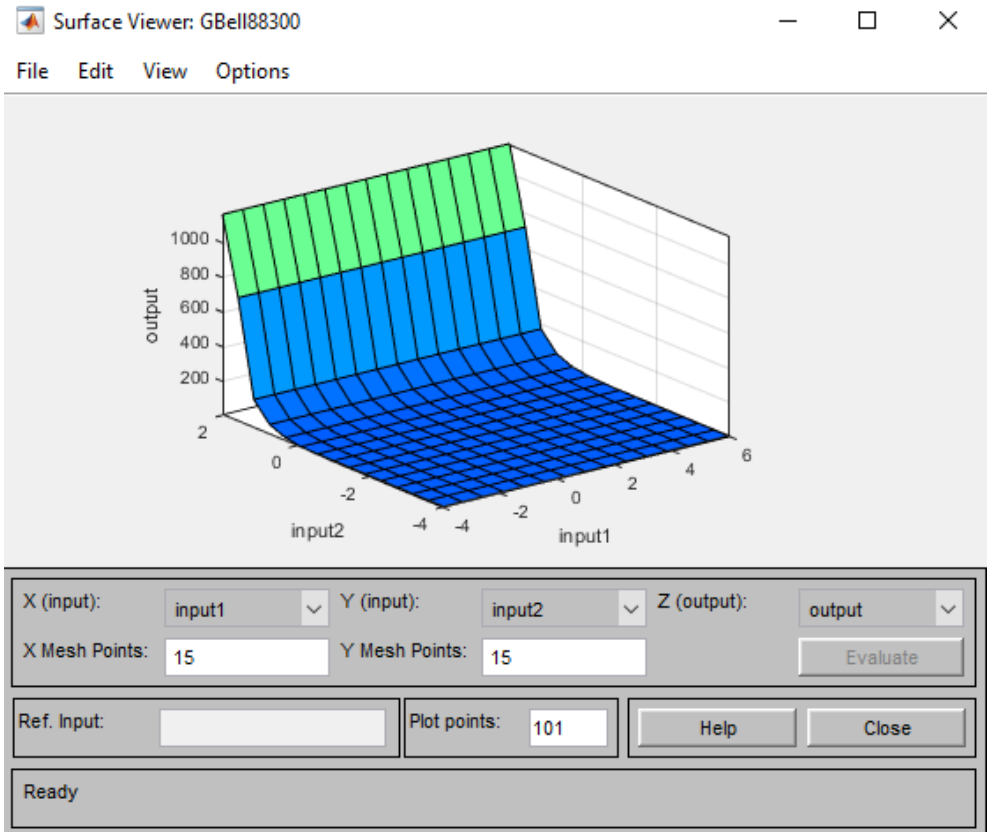


Figure 60. Fuzzy inference surface viewer

Finally, to represent the 3-dimensional (3-D) configuration of the fuzzy rules, surface viewer is provided. The inputs are located on the horizontal axes and the output is shown on the vertical axis.

By training and designing the fuzzy inference systems (FISs) using the neural networks, the function approximator (regression-estimator model) can be fed to the genetic optimization algorithm to find the optimal values for the inputs to yield the maximum resonance voltage with respect to the specific values of the mass and stiffness ratios. Such specific values are called the optimal design parameters.

Genetic optimization algorithms: Genetic optimization (GA) algorithm is a population-based, global optimization method. It is a metaheuristic approach inspired by

the process of natural selection which belongs to the bigger class named evolutionary algorithms. GA starts with randomly generated solutions called candidate solution. GA then evaluates each individual in a generation, meaning that GA finds the fitness of each individual with respect to the objective function. Now, GA sorts the individuals in a generation according to the level of fitness. It means that more fit individuals are listed at the top. Now, picking a finite number of more fit individuals, and applying genetic operations (mutation, selection, cross-over, …) results in a new generation called offspring. Such offspring (genome) generation is even more fit than the selected individuals at the former population (parent's generation). Among different types of genetic operations, mutation applies a kind of jump with the hope of finding further optima in the whole domain, but cross-over tries to exploit the current individual to see if it can make it better in the smaller sub-domain. Such iterative process goes on and terminates until a satisfactory level of fitness is obtained or a maximum number of offspring is generated. As outlined in the above section, solutions need to be selected based on a well-defined procedure. In genetic algorithms there are several selection methods proposed for selecting and choosing among the potential optimal solutions. Selection is indeed the stage of a genetic algorithm in which individual genomes (offspring) are chosen from a population for later breeding (using the crossover operation). Genetic selection works based on the following methods: the evaluation of each individual with fitness values is being revealed. Such values are then normalized. Normalization means dividing the fitness value of each individual by the sum of all fitness values, so that the sum of all resulting fitness values equals unity. Accumulated normalized fitness values are to be computed in the next step. The accumulated fitness value of an individual is the sum of its own fitness

value plus the fitness values of all the previous individuals; the accumulated fitness of the last individual should be unity, otherwise something is wrong with the normalization step. A random number *R* between 0 and 1 is adopted in an arbitrarily fashion. The selected individual is the first one whose accumulated normalized value is greater than or equal to *R*. For many problems the above algorithm might be computationally demanding. A simpler and faster alternative uses the so-called stochastic (random) acceptance. If this procedure is repeated until there are enough selected individuals, this selection method is called fitness proportionate selection or roulette wheel selection. If instead of a single pointer spun multiple times, there are multiple, equally spaced pointers on a wheel that is spun once, it is called stochastic universal sampling or random sampling. Repeatedly selecting the best individual of a randomly arbitrarily chosen subset is titled as the tournament selection. Taking the best half, third or another proportion of the individuals is called the truncation selection. There are other selection algorithms that do not take into account all individuals for selection, but only those with a fitness value that is higher than a given arbitrary constant are considered. Other algorithms select from a restricted pool where only a certain percentage of the individuals are allowed and picked, based on fitness value. Retaining the best individuals in a generation unchanged in the next generation is called elitism or elitist selection. It is a successful (slight) variant of the general process of constructing a new population. Roulette wheel: In the roulette wheel the probability of choosing an individual for breeding of the next generation is proportional to its fitness, the better the fitness is, the higher chance for that individual to be chosen. Choosing individuals can be depicted as spinning a roulette that has as many pockets as there are individuals in the current generation, with sizes depending on their probability. The

probability of choosing an individual pertains to the size of the generation and where the fitness belongs. In this approach, one single individual can be adopted several times. Stochastic universal sampling (random): it is a technique for selecting potentially useful solutions for recombination. It was introduced by James Baker. In this method there is no bias or partiality in choosing a specific individual. After choosing several numbers randomly, a single random value is used to sample all of the chosen solutions at an evenly spaced interval of numbers. Such a concept of randomness provides weaker numbers in terms of fitness and the chance to be adopted. In optimization problems, determining the design parameters range is a first step. It is supposed for the spring constant to stay in the interval of $r_s = [0.1, 100]$ and the oscillator mass to fall in the interval of $r_s = [0.01, 2]$.

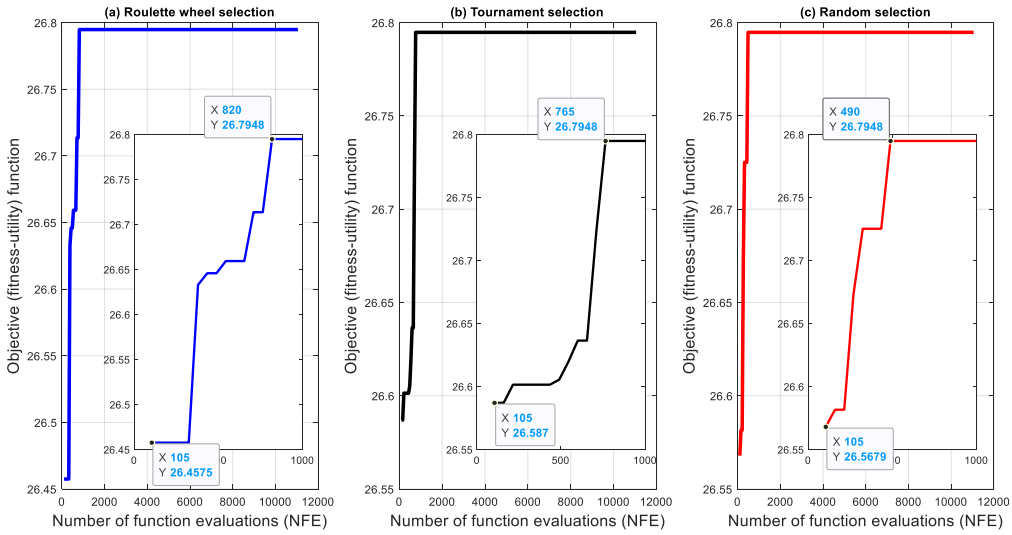


Figure 61. Objective function (resonance voltage) optimizing track – Gaussian FIS

This figure demonstrates the evolutionary path of the genetic algorithm in finding the optimal solution for the resonance voltage. Three different types of selection approaches (roulette wheel, tournament, and random) are applied within the genetic

operations. Since the desired case is to maximize the electric voltage at the vibrational resonance, the objective function is a fitness (utility) function in terms of maximization problem. For this case, the genetic algorithm is being fed up by the Gaussian type of MFs.

Table 15. Optimization algorithm properties and information

| GA Selection type | Optimal $r_m$ | Optimal $r_s$ | Initial solution | Optimal solution | Total NFE |
|---|---|---|---|---|---|
| Roulette wheel | 100 | 2 | (105,26.4575) | (820,26.7948) | 11050 |
| Tournament | 100 | 2 | (105,26.587) | (765,26.7948) | 11050 |
| Random | 100 | 2 | (105,26.5679) | (490,26.7948,) | 11050 |
| population | 50 | | | | |
| iteration | 200 | | | | |
| FIS | Gaussian | | | | |

Evolutions and operations of the adopted selection approaches integrated with the genetic algorithm are summarized in Table 16. According to this table and Figure 68, the optimal value for the oscillator mass is: $r_m = 2$ and that of the spring constant is: $r_s = 100$. The genetic algorithm has accomplished 11050 numbers of function evaluations (NFEs). The algorithm initiated with 50 candidate solutions which also conveys the number of populations in each generation. The maximum number of iterations per evolution is set at 200. Random selection reaches the optimal solution in the least computational effort and is the most cost-effective selection method. Roulette wheel initiates with the weakest candidate solutions and reaches the optimal solution in the most computationally expensive effort. In other words, the mentioned selection approach showed the weakest behavior. Tournament selection launches with the best initial solution and performs better than the roulette wheel. However, the random selection method renders the most cost-effective performance as it reaches the optimal solution in

remarkably shorter computations. In short, the random selection method reaches the optimal solution with the least evolutionary path jumps and genetic mutations.

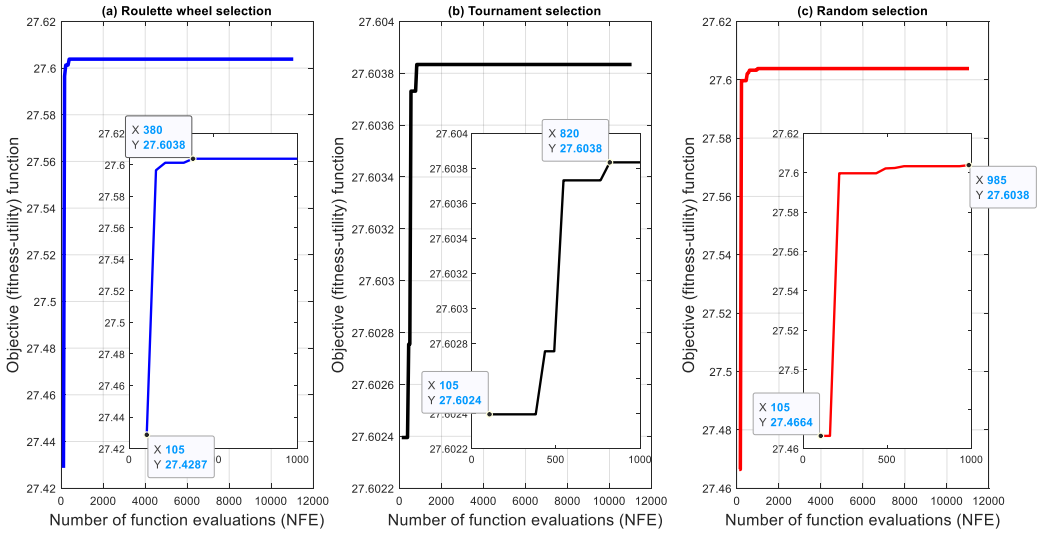


Figure 62. Objective function (resonance voltage) optimizing track – Generalized-Bell FIS

Table 16. Optimization algorithm properties and information

| GA Selection type | Optimal $r_m$ | Optimal $r_s$ | Initial solution | Optimal solution | Total NFE |
|---|---|---|---|---|---|
| Roulette wheel | 100 | 2 | (105,27.4287) | (380,27.6038) | 11050 |
| Tournament | 100 | 2 | (105,27.6024) | (820,27.6038) | 11050 |
| Random | 100 | 2 | (105,27.4664) | (985,27.6038) | 11050 |
| population | 50 | | | | |
| iteration | 200 | | | | |
| FIS | Generalized-Bell shaped | | | | |

Evolutions of the mentioned selection approaches integrated with the fuzzy system of Generalized-Bell shaped (G-bell) MFs is illustrated in figure 62 with information summaries in Table 19. Accordingly, the obtained optimal values for the oscillator mass are: $r_m = 2$ and that of the spring constant is: $r_s = 100$. This means that using either

Gaussian MFs or Generalized-Bell shaped MFs, identical results are observed. The only difference pertains to the estimated value for the maximum value of the utility (fitness) function. The genetic algorithm has accomplished 11050 function evaluations. The algorithm initiated with 50 candidate solutions in each generation with a maximum of 200 iterations per evolution. In comparison, roulette wheel reaches the optimal solution in a strikingly faster evolutionary path. All three selection approaches are initiated with almost identical initial (candidate) solutions but they track different evolutionary paths to reach the optimal solution. Tournaments and random selections trace more computations and require computationally expensive paths to reach the optimal solution. As a final comment, it is noted that, since the nature of the genetic algorithm as a population-based evolutionary global optimization method is established based on stochastic adoption of solutions, different performance of the algorithm is expected in each set of running and the comparison between roulette wheel, tournament, and random selection methods are valid only for this current run. Eventually, to ensure the correctness of the proposed genetic algorithms, several values of the mass and stiffness ratios are adopted and tested.

Table 17. Evaluation of the proposed optimization algorithm using 'readfis' for various values of inputs (design) values

| $r_s$ | $r_m$ | Maximum voltage | Percentage (%) |
|---|---|---|---|
| 1E+10 | 0 | 4.847469 | 49.47116 |
| 0.01 | 0.01 | 3.344365 | 3.12311 |
| 100 | 0.01 | 3.342263 | 3.05829 |
| 0.01 | 1 | 15.77137 | 386.3084 |
| 1 | 1 | 14.64587 | 351.6036 |
| 100 | 1 | 13.61919 | 319.9463 |
| 100 | 2 | 24.38628 | 651.9481 |

Based on Table 18, the proposed genetic optimization algorithm ends up in the maximum (optimal) value of the utility function. Such results verify the correctness of the method adopted. Moreover, adopting two different types of fuzzy inference systems (one based on the Gaussian MFs and the other based on the G-Bell shaped MFs); same result is obtained for the design parameters. Such nominated optimal values will be used in the closed-form solution to find the electrical frequency response function (FRF). Using the nominated optimal values, one needs to plot the nonlinear transcendental characteristic equation to estimate the initial guesses. Such initial guesses will be utilized in the VPASOLVE algorithm to numerically solve the mentioned equation and to find the eigenvalues.

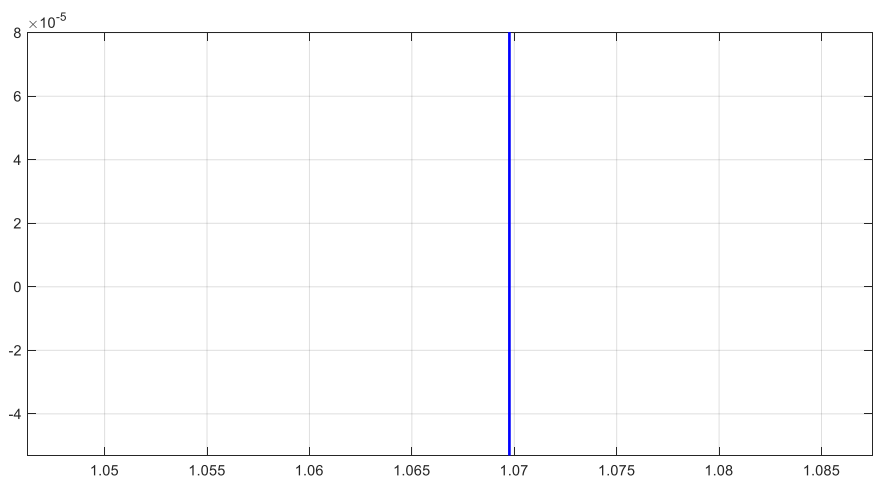


Figure 63. Plotting the characteristic equation at the vicinity of the first eigenvalue

This figure shows the nonlinear characteristic equation at the vicinity of the first eigenvalue. The mentioned eigenvalue seems to be a number close to 1.07.

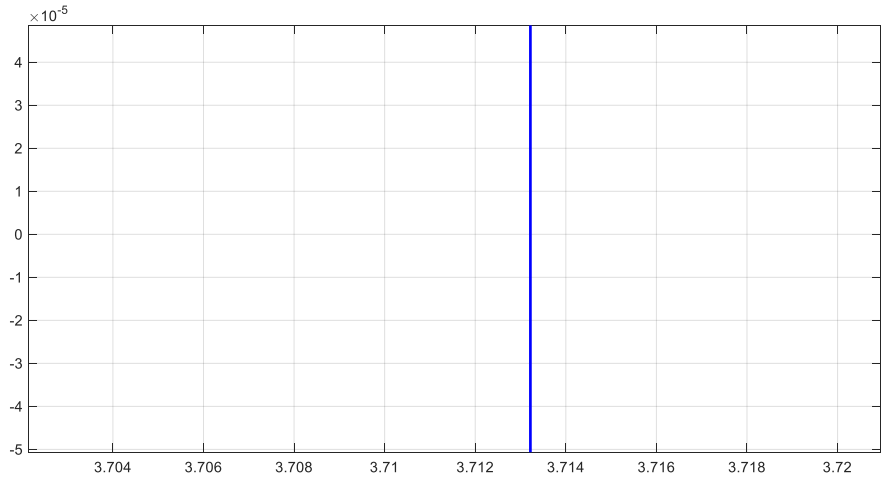


Figure 64. Plotting the characteristic equation at the vicinity of the second eigenvalue

The second eigenvalue (root) of the cantilever-oscillator-spring system looks to be at the vicinity of 3.713.

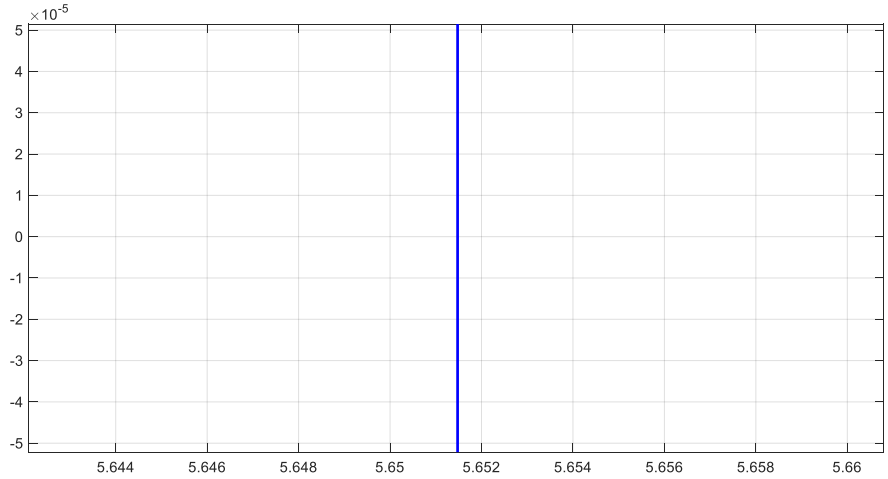


Figure 65. Plotting the characteristic equation at the vicinity of the third eigenvalue

The third eigenvalue of the mentioned system appears at the vicinity of 5.65. Such plots are helpful in estimating the initial guesses for the VPASOLVE algorithm to find the numerically solved eigenvalues of the system. Providing such initial guesses found by

plotting the characteristic equation, VPASOLVE numerically solves the mentioned equation for the first three roots as summarized in the following table:

Table 18. Numerically-solved eigenvalues by means of VPASOLVE

| $r_s$ | $r_m$ | $\lambda_1 L$ | $\lambda_2 L$ | $\lambda_3 L$ |
|---|---|---|---|---|
| 100 | 2 | 1.069820232696740 0384678732708611 | 3.713273412667149 6406982206795232 | 5.651559108089050 9527882164100682 |

To further evaluate and assess the correctness of whole soft computing procedure (the adaptive-network based fuzzy inference system (ANFIS) and the genetic algorithm); the optimal values found through the ANFIS, and genetic algorithm are used to find the voltage frequency response function (FRF) via the analytical and closed-form solution.

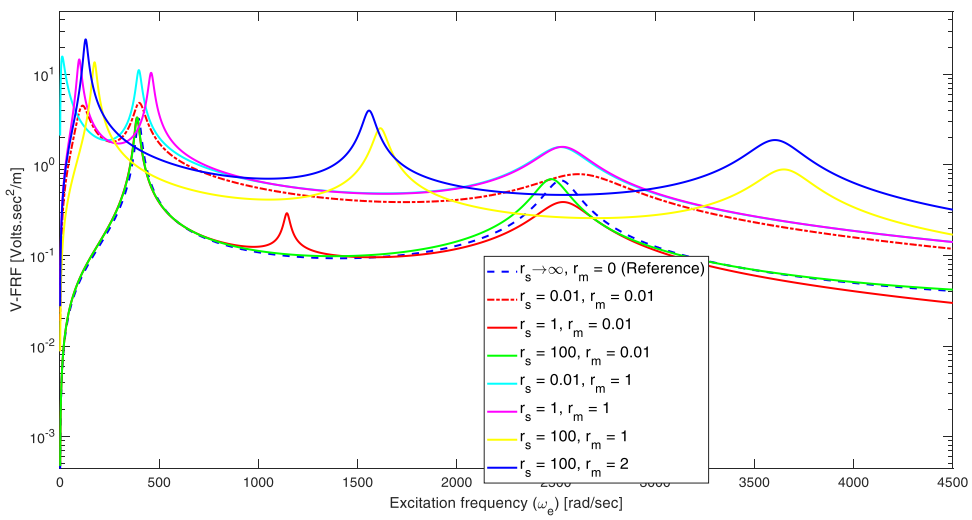


Figure 66. Voltage frequency response function (FRF)

Voltage frequency response function (V-FRF) is demonstrated in figure 66 to compare with eight random cases with arbitrary values of mass and stiffness ratios. It is noteworthy to mention again that Such findings are depicted using the closed-form solution for electrical FRFs. It is verified that the optimal piezoelectric vibration-based

energy harvester (PVEH) including the stiffness or spring constant of 0.01 times the flexural rigidity (bending stiffness) of the cantilever and an oscillator 2 times the mass of the cantilever; yields the maximum (optimal) voltage at the first resonance. Such findings improve the accuracy of the trained neuro fuzzy inference system and the genetic algorithm (soft computing algorithm). Furthermore, the resonant voltage at the second and the third vibration modes are also the biggest for the optimal case. This means that optimizing the PVEH with respect to the first vibrational mode automatically tunes and optimizes the system for the second and the third resonances as well. Finally, the corresponding operational frequency bandwidth is widened (considering the first and third modes). It is good to note that the latter two points (maximum voltages at the second and third resonances along with the widened effective frequency bandwidth) are studied separately in the following sections of the current chapter.

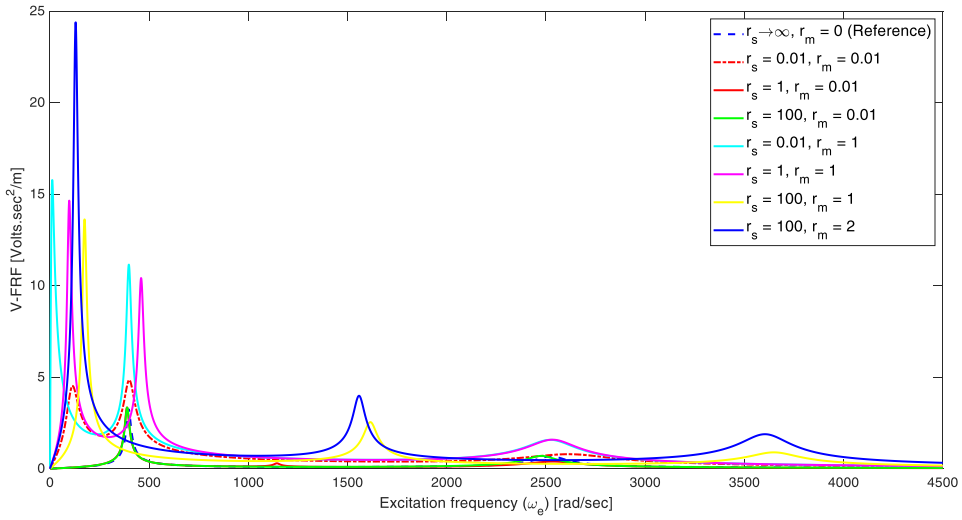


Figure 67. Voltage frequency response function (FRF)

This figure shows the same results (voltage FRF) with respect to the standard scale. In the former figure, the logarithmic scale was adopted. The current figure shows the same

results as mentioned in the above part showing that the harvester system with mass ratio of 2 and stiffness ratio of 0.01 leads to the most harvestable energy.

### 5.5.2 Optimizing the Effective (Operational) Frequency Bandwidth (EFBW)

As mentioned in the above sections of current chapter, the efficiency and success of a piezoelectric vibration-based energy harvester (PVEH) is mostly based on two items: the maximum amount of extractable voltage and the frequency bandwidth in which the harvester covers. The former one is studied comprehensively in terms of optimization, and the optimal values of the oscillator mass and spring constant are determined. In this section, the same procedure will be accomplished to determine the optimized PVEH in terms of effective (operational) frequency bandwidth. The optimal system will cover the most frequency bandwidth possible between the minimal resonance frequency and the third frequency. It is also noteworthy that the minimal resonance frequency is the one which is generated due to the oscillations of the oscillator at the tip end. Such oscillations differ from the cantilever's modal behavior and strikingly alter such modal and vibrational behavior. Another important note is the third frequency which occurs at the conventional system's second resonance. In response to the ambiguity why the third resonance is preferred to the second one for assessing the frequency bandwidth; one would interpret the first two resonances take place at a close vicinity. Which means they are closely located next to each other. In detail, the newly generated resonance at small values and close to the origin, is resulted from the integration of the oscillator subsystem. Such integration mutates the cantilever's vibratory modes. As the new resonance is very close to the other following resonance, the operational bandwidth seems to be fair if considered between the

first (new) resonance and the third one. After defining the preliminaries of the current chapter, the main goal of this section is to widen the operational frequency bandwidth as much as possible. There is a wide range of oscillator mass and spring constant values to alter the mentioned factor. In other words, the major contribution of this section is to find the optimal oscillator mass and spring stiffness, so that the effective frequency bandwidth is widened the most, which results in development and improvement in PVEH applications. To do so, a maximization optimization problem has to be solved. As a short recap, due to the non-automated process of voltage and mechanical frequency response functions (FRFs) evaluations along with high computational costs (in terms of curse of high time computations); training a decent regressor (estimator, function approximator) model looks necessary. The designed estimator will be utilized in function evaluation step in the genetic algorithm to find the optimal parameters. Eventually, the nominated parameters will be used in the closed-from solution to evaluate the correctness of the soft computing process. More elaboration and explanation in this response is thoroughly discussed in the resonance voltage optimization part.

Training ANFIS for the first and the third resonance frequencies: due to the nature of the ANFIS, two separate fuzzy inference systems (FISs) are to be designed, in which one estimates the first resonance frequency value and the other one predicts the third resonance frequency value. This mainly pertains to the ANFIS reasoning structure which is established based on the Takagi-Sugeno inference system. The mentioned system can accept multiple or single inputs but yields only single outputs. So, the ANFIS supports only the MISO or SISO. Moreover, design parameters are the inputs. Such specific values are to be found and titled as the optimal values rendering the optimal and developed energy

harvester. Same input dataset used in the previous section are considered here. 231 cases (11 different values for $r_m$ and 21 different values for $r_s$) have been taken as the input dataset range. The output is obtained using the closed-form solution available in the mechanical FRF representing the resonance frequencies. Thus, the first three eigenvalues along with all of the coefficients have been found for such cases.

$$r_s = [10^{-4}, 10^{-3}, 10^{-2}, 10^{-1}, 1, 10, 10^2, 10^3, 10^4, 10^5, 10^6]$$

$$r_m = [10^{-4}, 0.005, 10^{-3}, 0.005, 10^{-2}, 0.05, 10^{-1}, 0.2, 0.3, 0.4, 0.5, 0.6, 0.7, 0.8, 0.9, 1, 2.5, 5, 7.5, 10, 10^2]$$

Similar to the former section of current chapter, the generated dataset of voltage resonances is divided into train dataset (80%), validation (checking) dataset (10%), and test dataset (10%). Although a comprehensive explanation about the ANFIS and data pre-processing is mentioned in the former section, it is good to note some of major points in short. Train dataset is expectedly used to train the model and capture the structure for the purpose of prediction and estimation. Test dataset is considered to evaluate the performance of the fuzzy inference system (FIS) which is trained using neural networks. This dataset is previously unseen to the model and assesses the model performance in terms of prediction capability. On the other side, checking (validation) dataset is supposed to be employed to avoid overfitting in the model. Too complicated models are usually capable of predicting the new dataset properly. However, the algorithm will be slow (due to the time computations) and more importantly the algorithm will most likely fail to generalize and exhibit a decent performance with respect to the new unseen dataset. A thorough explanation is elaborated in this response in the following section. Similar to the

previous section, the raw dataset including the oscillator mass and the spring constant (as the inputs) and the resonance frequencies (as the output); need to be pre-processed before being employed in the training section. Similarly, taking the logarithm of the input dataset to the base of 10, the dataset is ready to be uploaded.

In the following section, all eight built-in MFs are adopted to train fuzzy inference systems as regressor for the first resonance and the third resonance values. Similarly, the criteria to choose the most accurate membership function (MF) is the root-mean-square-error (RMSE) of the train, test, and validation (checking) dataset. In the tables, the root-mean-square-error (RMSE) are reported per each FIS and the corresponding training dataset errors, test dataset errors, and the validation dataset errors are also reported. Such comparison makes the decision-making process easier to take the best MF to use in the design of the FIS, and later to choose the proper number of membership functions as well. Best here refers to the most accurate MF with the least test RMSE and trained RMSE, respectively.

Table 19. Membership function type evaluation for the first resonance

| MF type | Train error | Test error | Validation error |
|---|---|---|---|
| Triangular | 0.0068735 | 0.13659 | 0.096411 |
| Trapezoidal | 0.010127 | 0.13489 | 0.10126 |
| Bell | 0.0069811 | 0.13598 | 0.092355 |
| Gaussian | 0.0068203 | 0.13632 | 0.092211 |
| Gaussian2 | 0.0094394 | 0.13704 | 0.098782 |
| Polynomial | 0.037733 | 0.12612 | 0.11003 |
| Polynomial-sigmoid | 0.0011285 | 0.14043 | 0.09739 |
| Double sigmoid | 0.011307 | 0.14044 | 0.097398 |
| Epochs | 300 | | |
| Number of MFs | 7 by 7 | | |

Complicated and nonlinear MF usually start with better initial guesses. While the simple and linear MF (e.g., trapezoid and triangular) usually initiate with weak start offs (big RMSE) and as a result require more epochs and computational efforts. According to the different root-mean-square-error (RMSE) for train, test, and validation datasets; it is evident that Gauss, polynomial, trapezoidal, and bell type of membership functions show the best performance in capturing the structure of the dataset and ending in the least test error. Since, as for all the mentioned MFs, the resulting RMSE is small number, all of the mentioned MF stay in the acceptable region to be adopted to train the network. Although, the value of RMSE for test dataset looks more important in adopting the proper MF, other RMSE values (RMSE for train and validation datasets) can be handy and conducive in cases where, the test RMSE values are close to each other. In other words, since the test RMSE values for the mentioned MFs are highly close to each other, we rely on the values of the train and validation RMSE values as the alternative priority and criteria. Doing so, Gaussian MF looks the best function with the best RMSE values for overall train, test, and validation dataset root-mean-square-errors (RMSEs).

Table 20. Membership function type evaluation for the third resonance

| MF type | Train error | Test error | Validation error |
|---|---|---|---|
| Triangular | 0.0097362 | 0.16244 | 0.031308 |
| Trapezoidal | 0.012658 | 0.16402 | 0.024406 |
| Bell | 0.0085471 | 0.15886 | 0.022625 |
| Gaussian | 0.008666 | 0.15791 | 0.018515 |
| Gaussian2 | 0.0088859 | 0.16234 | 0.014357 |
| Polynomial | 0.014318 | 0.16453 | 0.025687 |
| Polynomial-sigmoid | 0.0088589 | 0.16211 | 0.014197 |
| Double-sigmoid | 0.00888698 | 0.16211 | 0.014218 |
| Epochs | 300 | | |
| Number of MFs | 7 by 7 | | |

A similar assessment process is accomplished to choose the best operational membership function (MF) for training the neural networks and fuzzy inference sets to estimate the third resonance frequency. To recall from the previous sections, the third resonance alludes to the second resonance of the conventional system. In Table 23, eight (8) different types of the built-in membership functions (MFs) are trained in a seven (7) by even (7) membership function sets for each case and 300 epochs. Error tolerance is set to 0. By comparison, bell, and Gaussian MFs reveal the smallest RMSE corresponding to the test dataset. Taking advantage of the RMSE for train and validation datasets, Gaussian MF yields the best MF with least root-mean-square-error overall. In other words, the fuzzy system established based on the Gaussian functions has the most accuracy as well as the most generalization which enables the system to avoid overfitting. Such a system shows the best performance with previously unseen and new dataset.

Table 21. Gaussian membership function number evaluation for first resonance

| Number of MFs | Number of FIS rules | Train RMSE error | Test RMS error | Validation RMSE error |
|---|---|---|---|---|
| 4 by 4 | 16 | 0.020586 | 0.13979 | 0.098779 |
| 5 by 5 | 25 | 0.012186 | 0.14225 | 0.13314 |
| 6 by 6 | 36 | 0.0051999 | 0.14459 | 0.11353 |
| 7 by 7 | 49 | 0.0068761 | 0.13632 | 0.092211 |
| 8 by 8 | 64 | 0.0030542 | 0.14326 | 0.088407 |
| 9 by 9 | 81 | 0.00313 | 0.42387 | 0.44046 |
| 10 by 10 | 100 | 0.0005196 | 0.18506 | 0.38915 |
| 11 by 11 | 121 | 0.00043178 | 0.27641 | 0.61551 |

After choosing the most accurate type of MF to train the fuzzy inference system; number of membership functions (MFs) per each input, and the corresponding number of generated fuzzy rules for the entire fuzzy inference system are to be determined. It is good to note, since the adaptive-neural-fuzzy-inference-system (ANFIS) was established based

on the Takagi Sugeno system, it accepts only the MISO (multi input single output). As a result, two different types of ANFIS systems are designed, one for the minimal (first) resonance prediction, and the other one for estimating the third resonance. Identical numbers of the MFs are considered for each input. The ANFIS system is designed for various numbers of the MF revealing the corresponding RMSE for train, test, and validation datasets. 64-fuzzy-rule system looks the best one as it has the smallest overall RMSE values. The only close performance pertains to the 49-fuzzy-rule system which has better test RMSE but slightly bigger train and validation RMSE values.

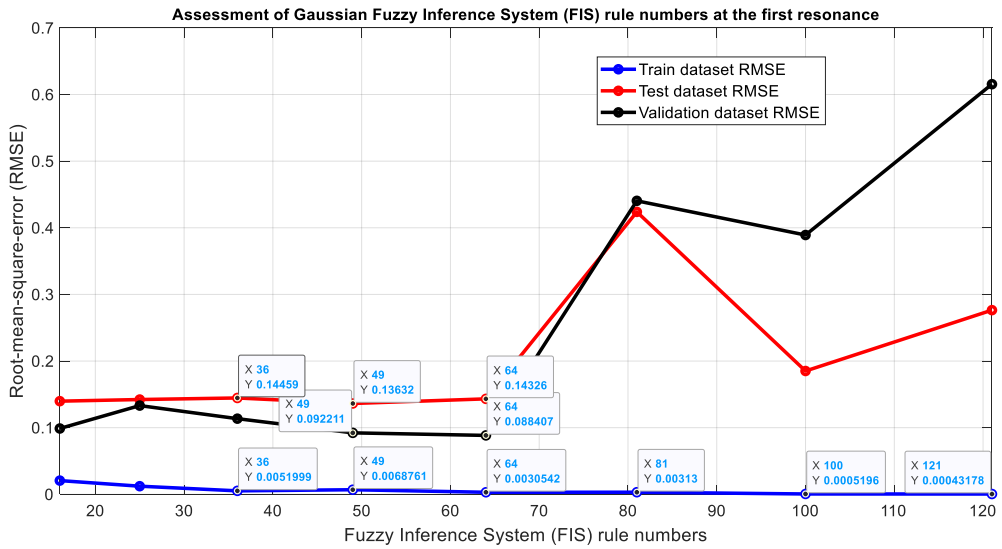


Figure 68. RMSE with respect to the Gaussian fuzzy rule numbers

Results of the above table are plotted to demonstrate the trained RMSE, test RMSE, and validation RMSE with respect to the fuzzy rule numbers. The fuzzy system with 64 rules exhibits the most precise performance as mentioned in the above section.

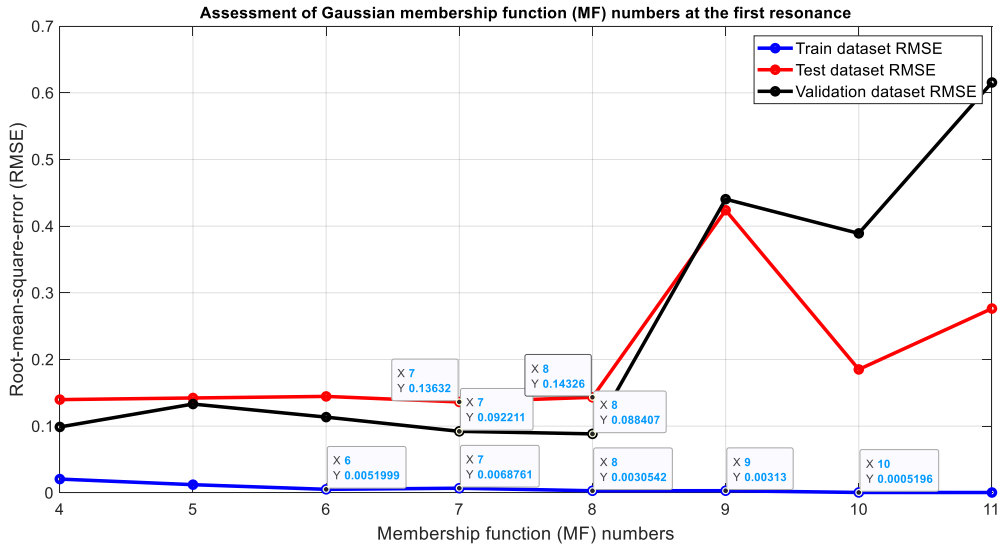


Figure 69. RMSE with respect to the Gaussian fuzzy MF numbers

Results of the above table are plotted to demonstrate the train RMSE, test RMSE, and validation RMSE with respect to the fuzzy rule numbers. The fuzzy system with eight by eight (8 by 8) architecture exhibits the most precise performance. The interesting finding refers to the RMSE decrement with the ten by ten (10 by 10) fuzzy system. However, such a fuzzy system does not perform as accurately as the fuzzy system of eight by eight (8 by 8) rule sets.

Table 22. Gaussian membership function number evaluation for third resonance

| Number of MFs | Number of FIS rules | Train RMSE error | Test RMS error | Validation RMSE error |
|---|---|---|---|---|
| 4 by 4 | 16 | 0.028322 | 0.15453 | 0.032258 |
| 5 by 5 | 25 | 0.0314667 | 0.16453 | 0.027144 |
| 6 by 6 | 36 | 0.012834 | 0.15349 | 0.020544 |
| 7 by 7 | 49 | 0.008666 | 0.15791 | 0.018515 |
| 8 by 8 | 64 | 0.0084171 | 0.21796 | 0.16123 |
| 9 by 9 | 81 | 0.00042842 | 0.38683 | 0.30777 |
| 10 by 10 | 100 | 0.00045149 | 0.57157 | 1.0133 |
| 11 by 11 | 121 | 0.00025684 | 1.0601 | 1.0177 |

Table 23 is provided to compare different numbers of MFs and the corresponding generated fuzzy rules for the third resonance. Starting from a five by five (5 by 5) fuzzy system and increasing up to eleven by eleven (11 by 11) fuzzy system; the 49-fuzzy-rule system generated from a seven by seven (7 by 7) system performs the most accurately due to the least overall train, test, and validation RMSE values.

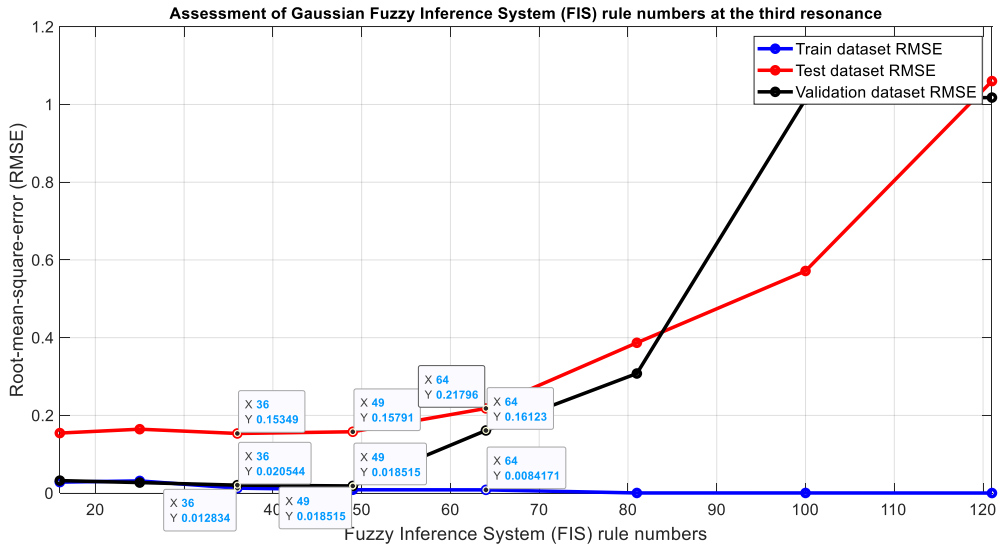


Figure 70. RMSE with respect to the Gaussian fuzzy rule numbers

To visualize the third resonance RMSE values for train, test, and validation datasets; the following figure is presented. It is observable that the 49-fuzzy-rule system performs with the least RMSE values.

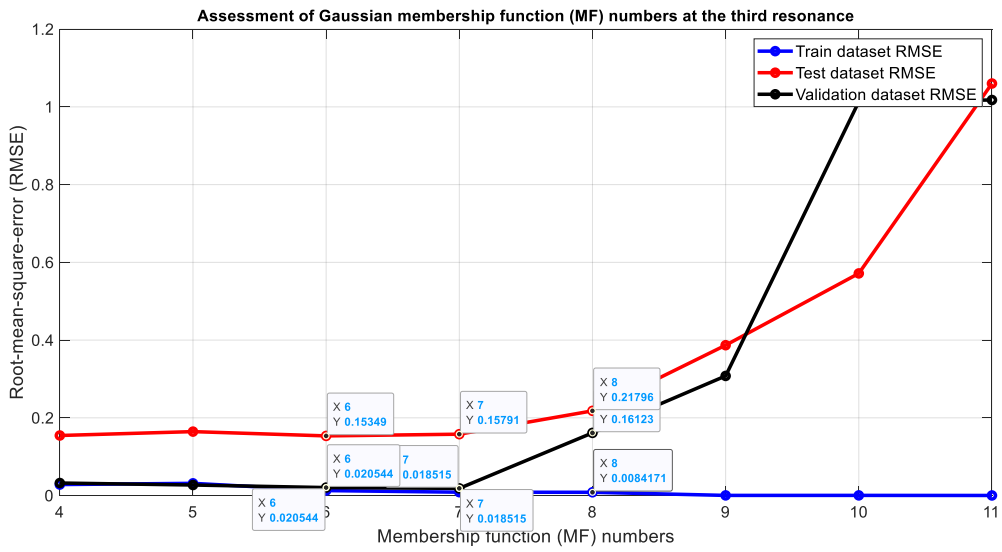


Figure 71. RMSE with respect to the Gaussian fuzzy MF numbers

To demonstrate the RMSE values with respect to the MF numbers, figure 71 is presented. Similarly, the seven by seven (7 by 7) fuzzy system operates the most accurately with the least root-mean-square-error. As the proper number and type of the MFs are adopted throughout the assessment procedure, it is required to train the fuzzy inference system (FIS) accordingly. Consequently, in the following section all the details and steps in establishing the FIs are pictured and elaborated.

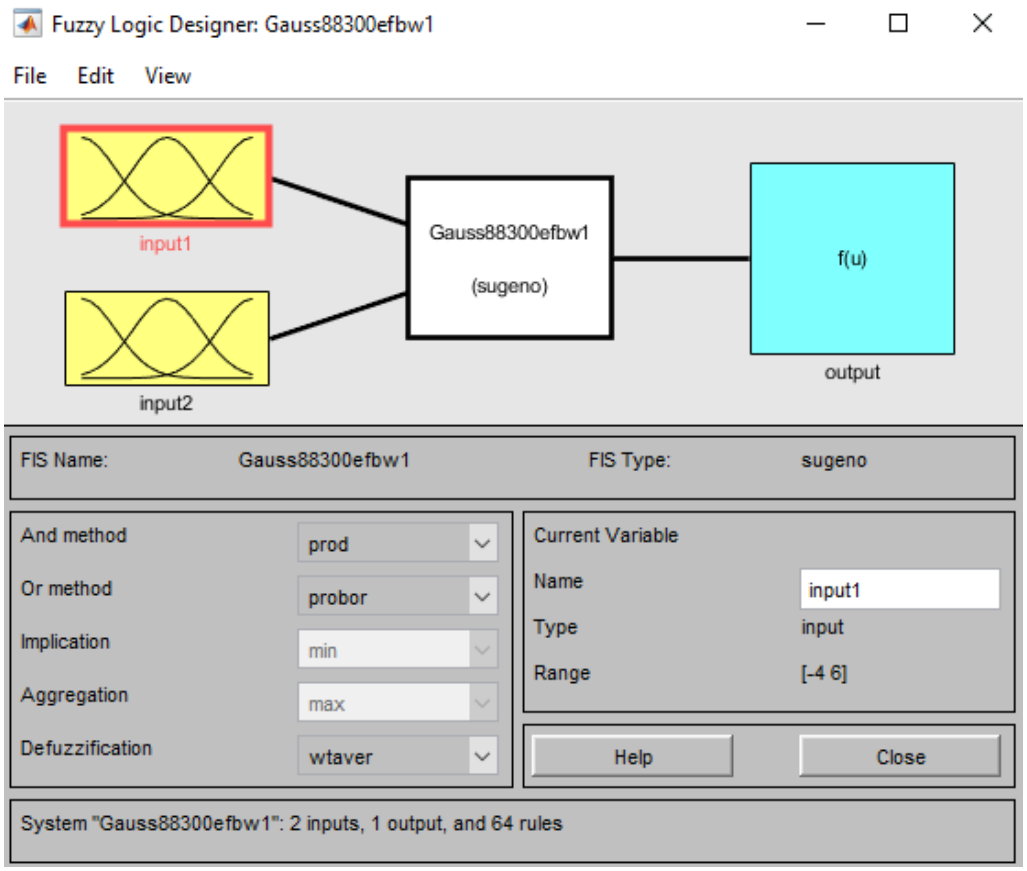


Figure 72. Fuzzy logic designer application setting

Figure 72 shows the fuzzy inference system (FIS) architecture trained using neural networks for the first (minimal) resonance. Since there are two inputs (the mass and the stiffness ratios), along with a single output (minimal resonance frequency) and the system is a MISO, Takagi Sugeno type of fuzzy systems is adopted. Production ('pord') is adopted as for the 'And' method. Probably ('propor') is chosen for the 'Or' method. Finally, defuzzification is established based on the 'wtaver' (averaging).

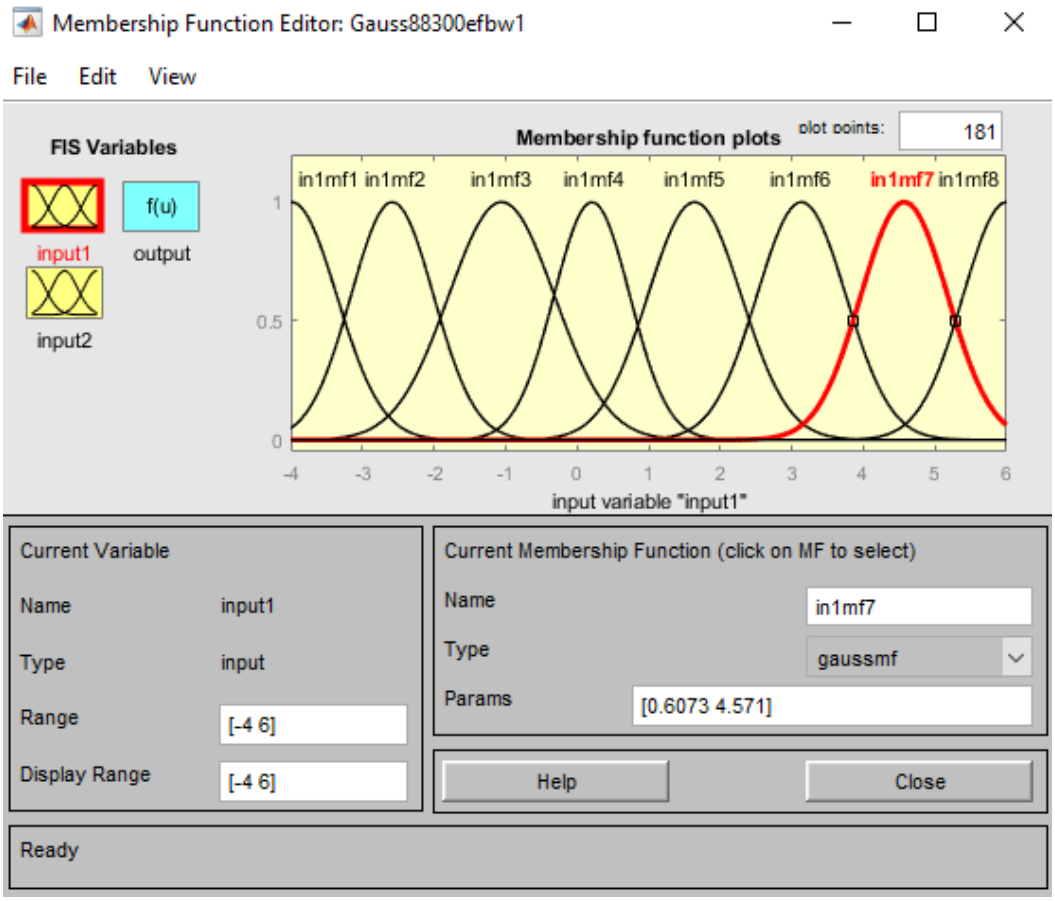


Figure 73. Fuzzy logic membership function editor – first input

This figure shows the membership function (MF) distributions for the stiffness ratio. The eight (8) Gaussian type MFs are distributed in the interval of $[-4, 6]$. Statistical information of the chosen values is available in the 'Params' section.

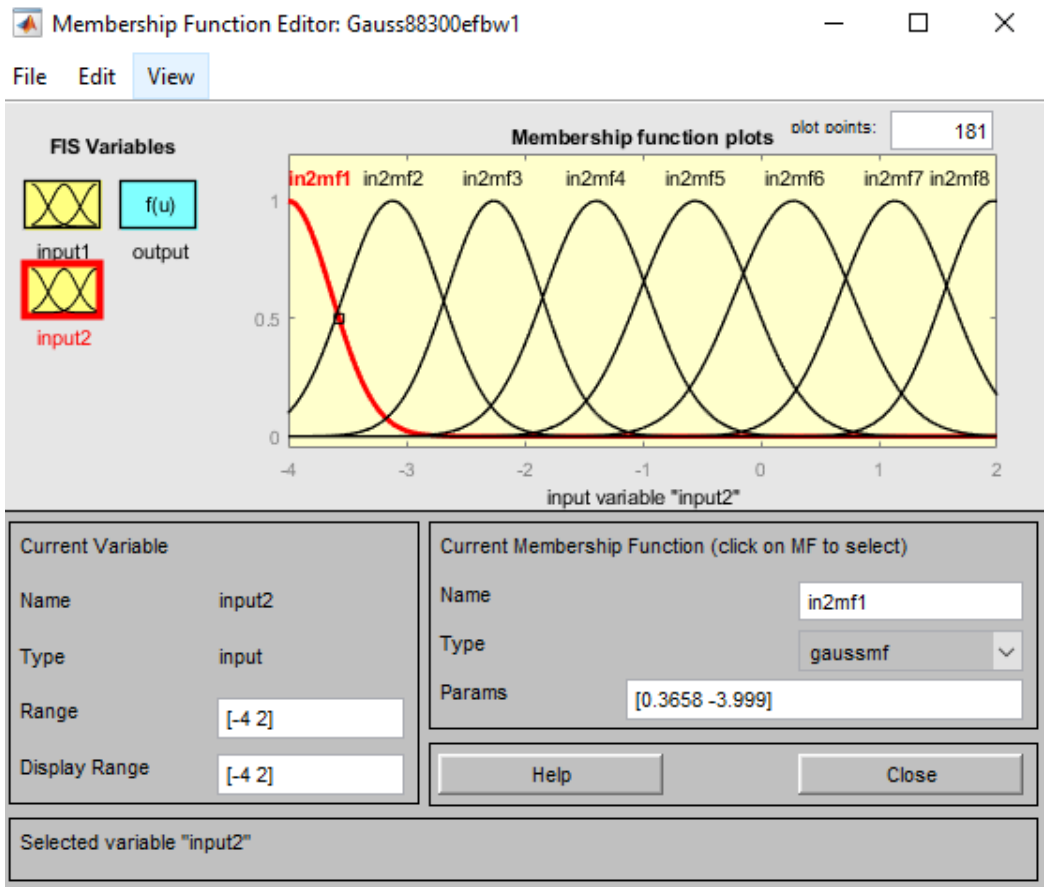


Figure 74. Fuzzy logic membership function editor – second input

A similar image is provided for the mass ratio as the second input to the MISO inference system. The only difference refers to the interval in which in this case it is: $[-4, 2]$ as well as the statistical values.

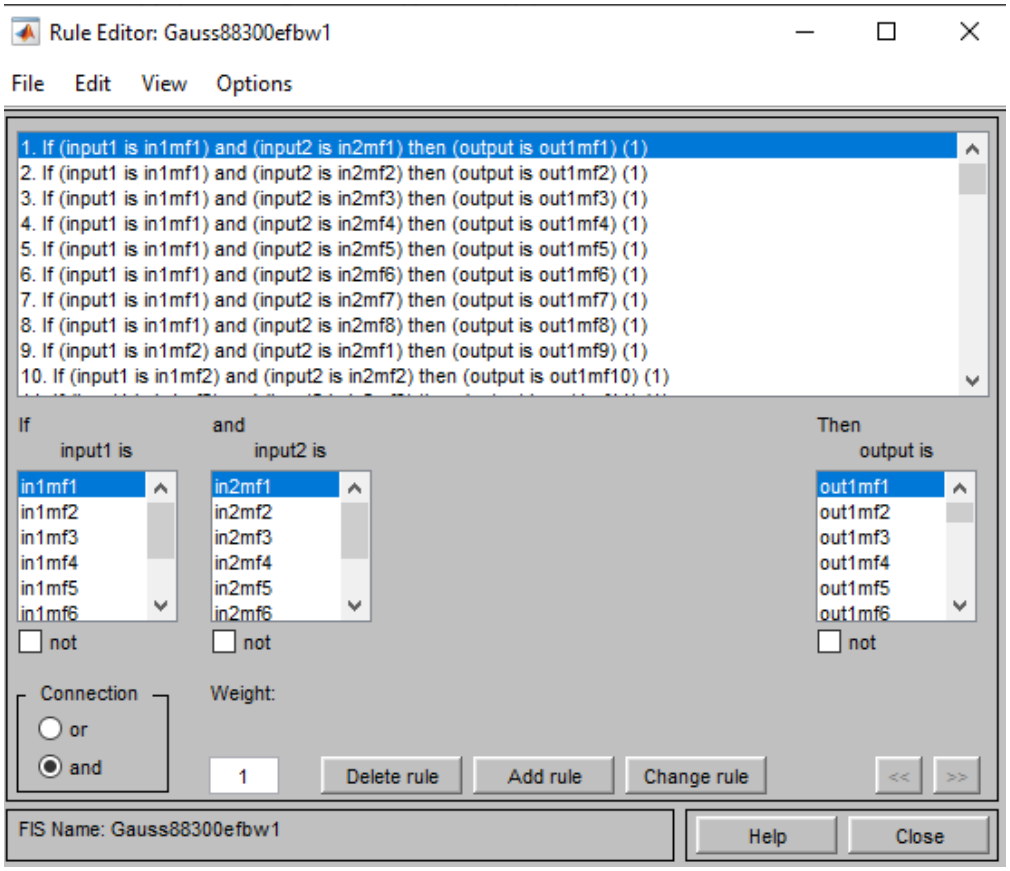


Figure 75. Fuzzy logic verbose rule viewer

Rules of the trained FIS are depicted in figure 75. A total of 64 rules are generated from the 8 by 8 fuzzy structure. The rules are connected with each other by 'and' connection method and with unit weight per rule.

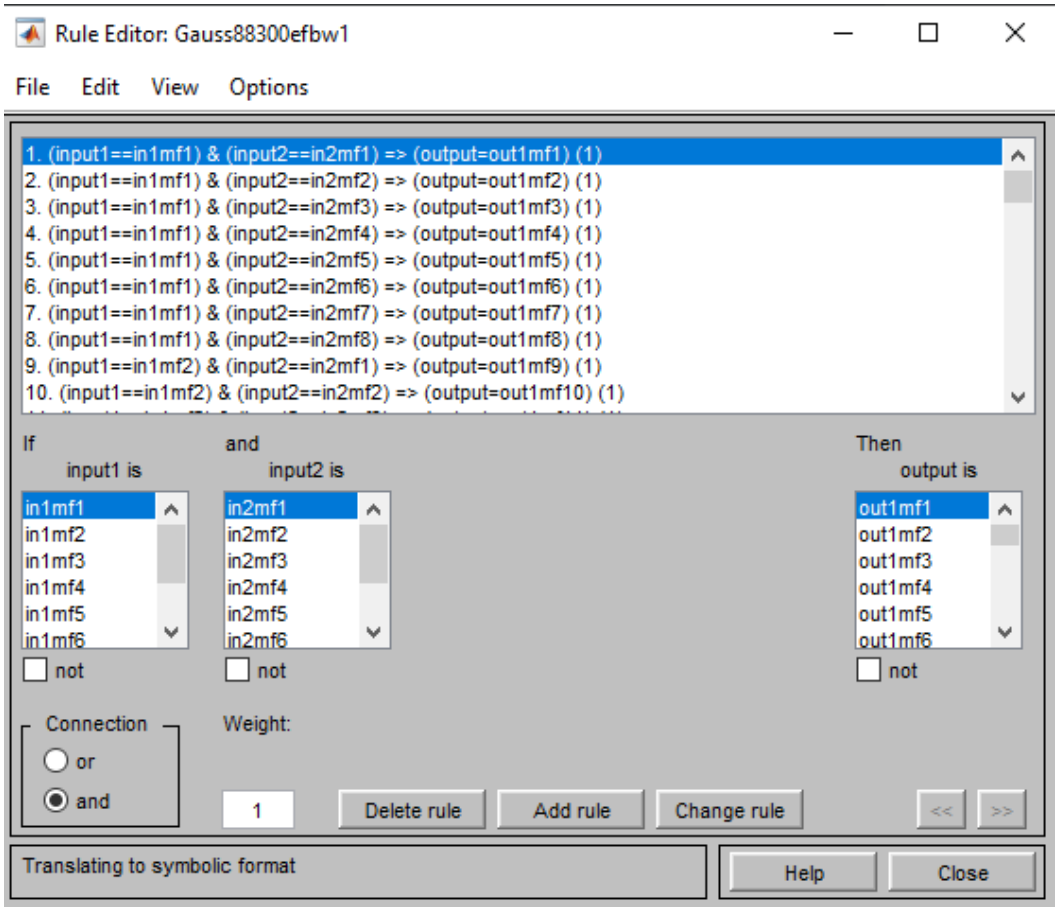


Figure 76. Fuzzy inference symbolic rule editor

Rule editor in symbolic format is represented in figure 76. Connection type is based on the ‘and’ or minimum type. Unit identical weight is also considered per each fuzzy rule.

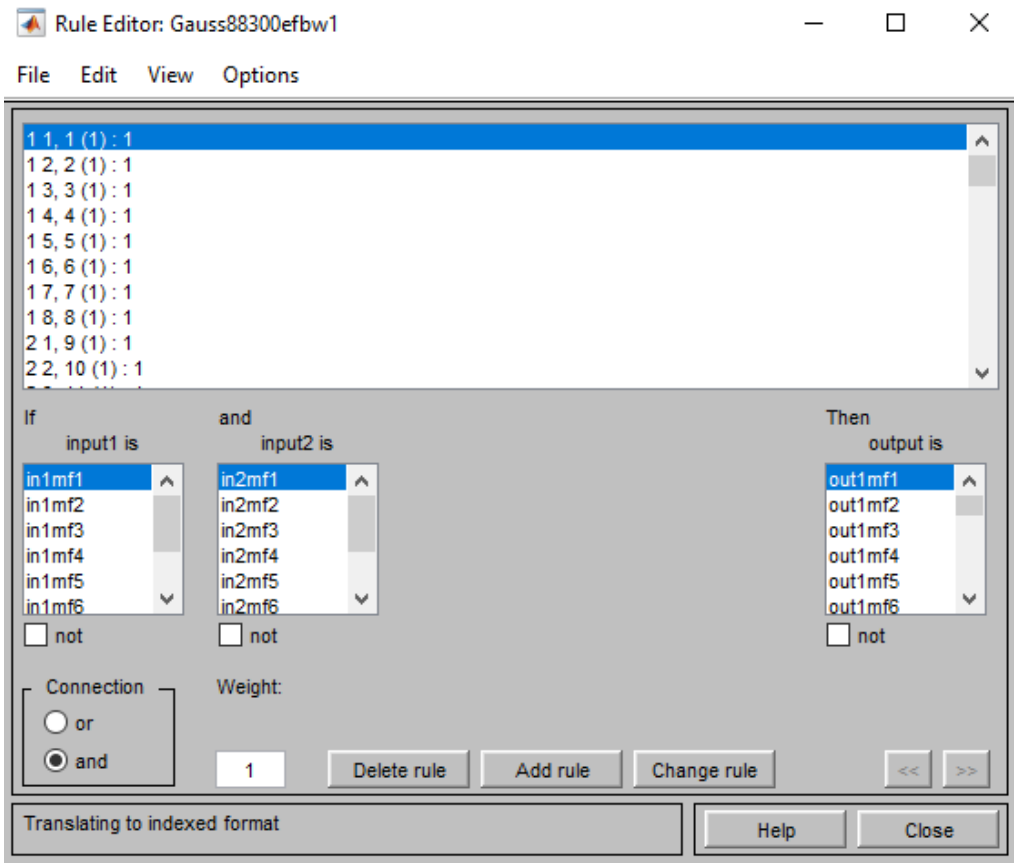


Figure 77. Fuzzy inference indexed rule editor

Fuzzy rules are depicted in the indexed format in figure 77. The three recent figures all represent the same concept in different formats. Connection types are obvious in the application. One can readily apply specific inputs and observe the outcome output in a single trial.

Figure 78. Fuzzy inference rule viewer

Figure 78 illustrates the rule viewer separating the two inputs and the resulting output. Such a rule viewer illustrates the inference process of the designed fuzzy inference systems (FIS). In the viewer, it is feasible to adjust each of the input values and observe the resulting output per each fuzzy rule. Such output is the aggregated output fuzzy set and the defuzzied value(s).

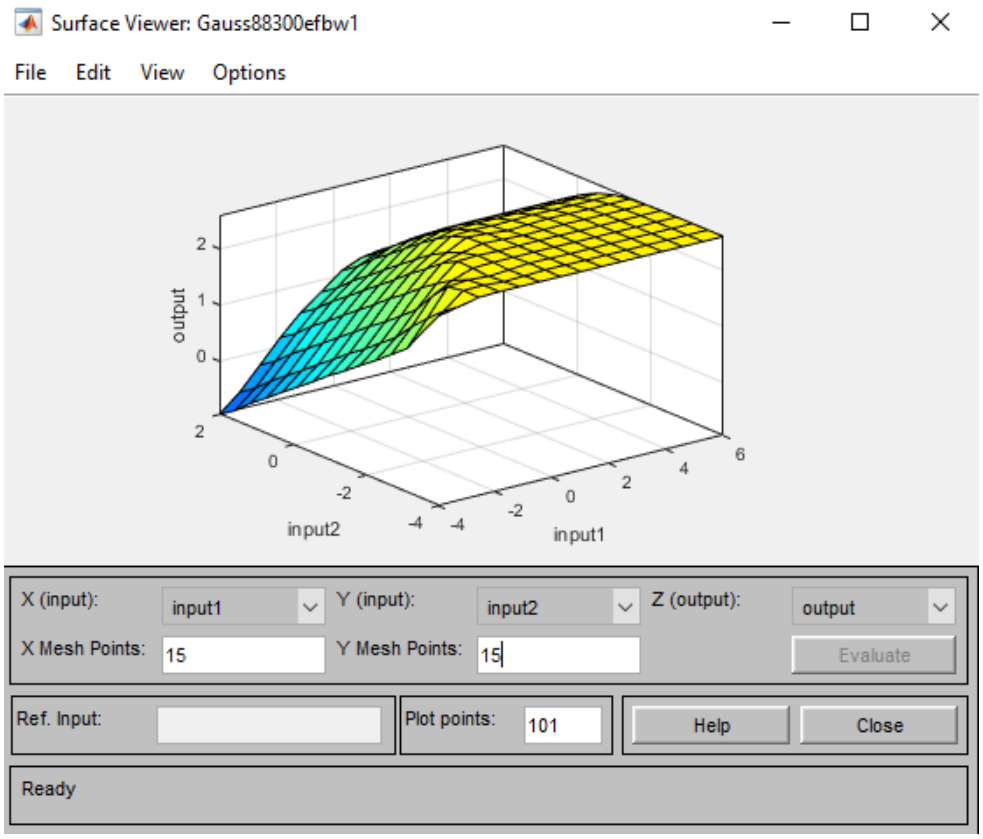


Figure 79. Fuzzy inference surface viewer

Surface viewer of the rules is also demonstrated in figure 79. This is a 3-dimenstional (3-D) plot showing the dependency of the first resonance to the inputs on the stiffness coefficient and the oscillator mass.

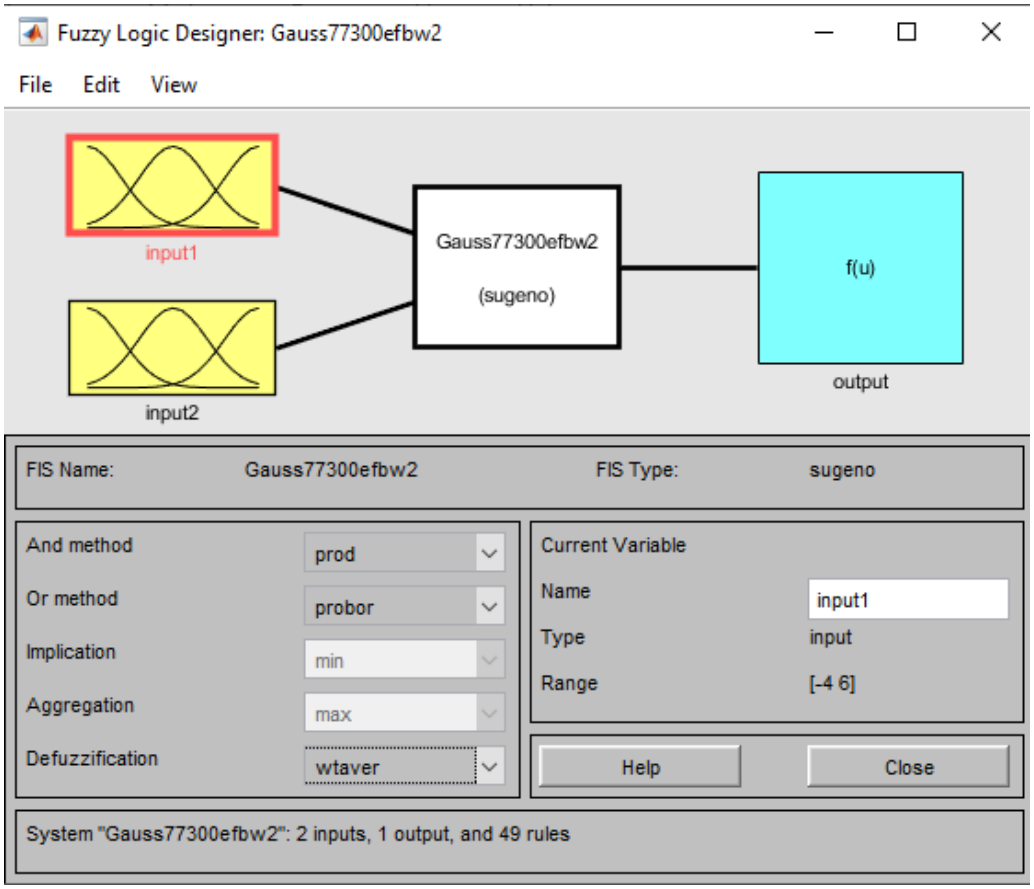


Figure 80. Fuzzy logic designer application setting – third resonance

Fuzzy inference system (FIS) architecture is plotted in figure 80 for the third resonance. ‘And’ method is established based on the ‘prod’ meaning the production of the entities, ‘Or’ method is designated to ‘probor’ alluring to the probabilistic computations, and ‘Defuzzification’ is formed according to the ‘wtaver’ pertaining to the averaged values of the output fuzzy sets.

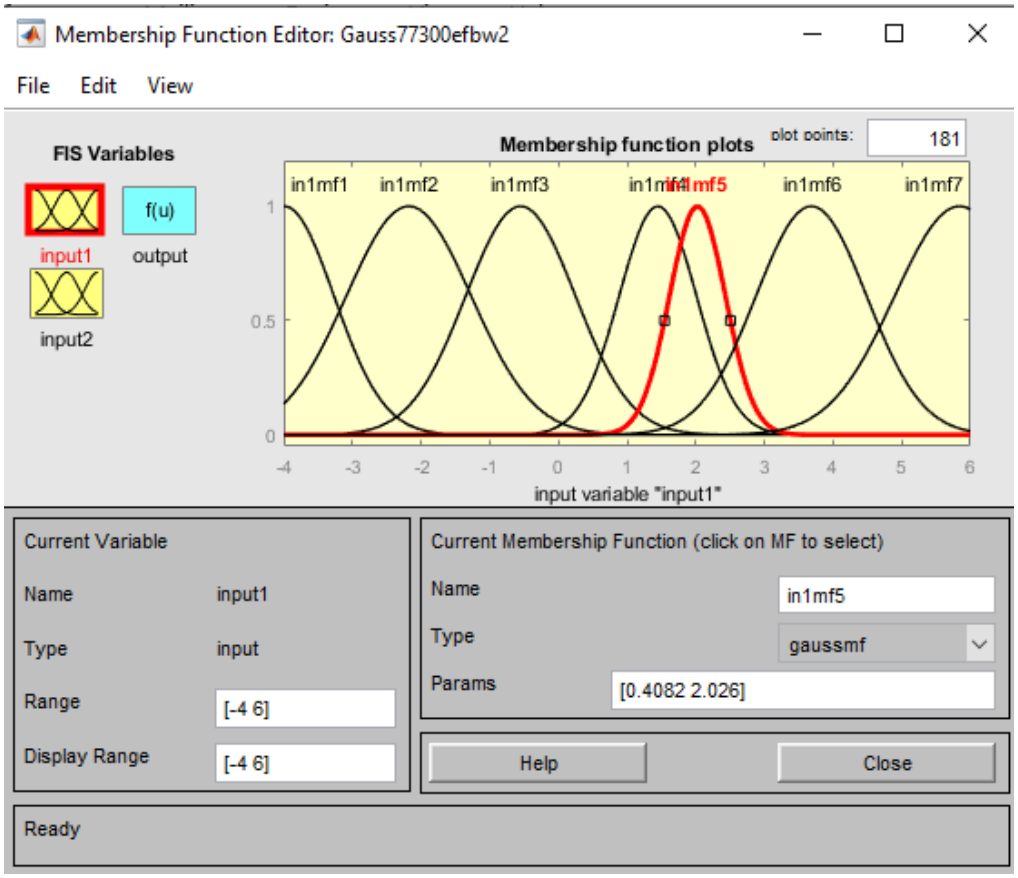


Figure 81. Fuzzy logic membership function editor – third resonance

Seven fuzzy membership functions (MFs) of the built-in Gaussian type are utilized for modeling the first input (stiffness ratio). The mentioned fuzzy MFs are distributed from -4 to 6. Functions are distributed in a non-symmetric fashion.

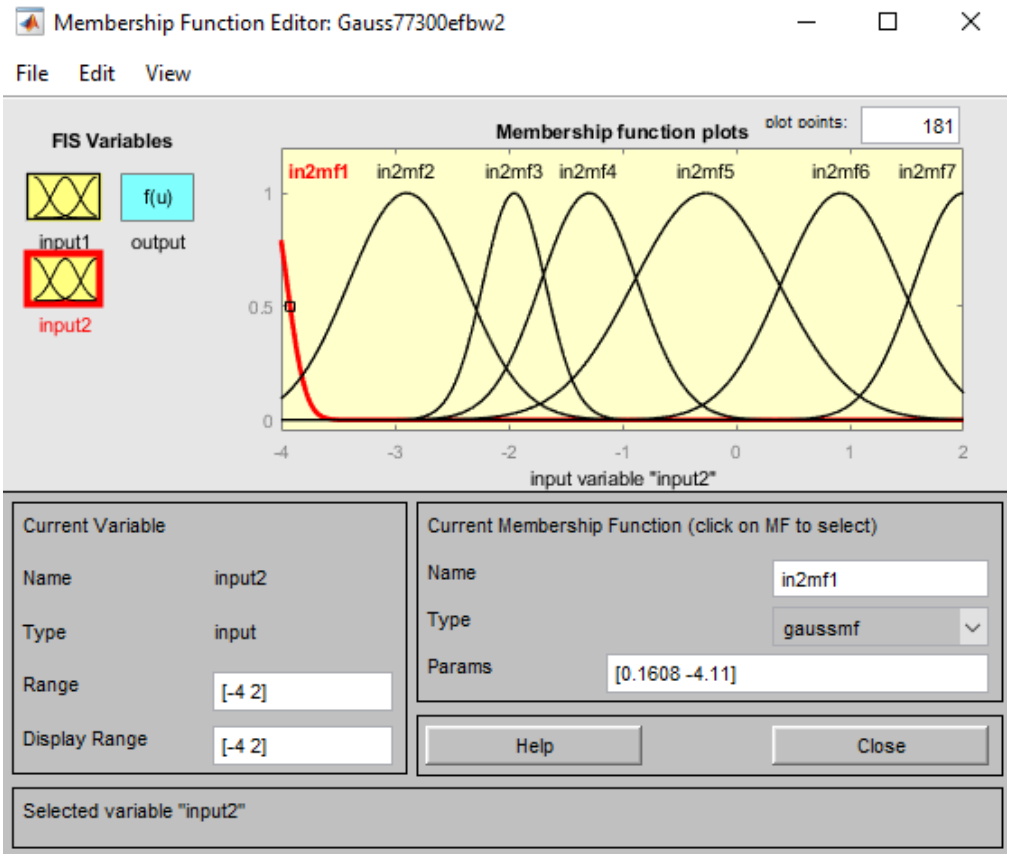


Figure 82. Fuzzy logic membership function editor – third resonance

Seven Gaussian MFs for the second input (mass ratio) are scattered from -4 to 2 to capture and model the third resonance. Similar to the stiffness ratio MFs, function distributions are not symmetric in this case.

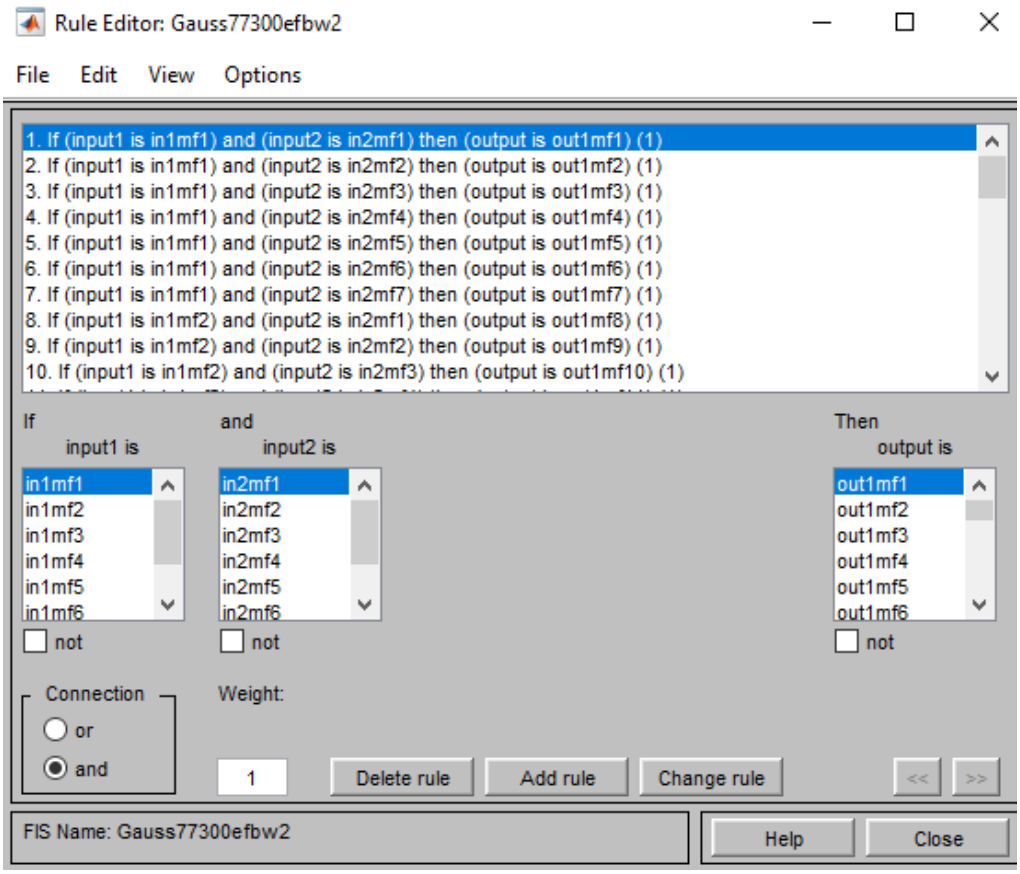


Figure 83. Fuzzy inference verbose rule editor

Regarding the third resonance, adopting 7 by 7 Gaussian MFs, total of 49 fuzzy rules are generated with ‘and’ connection approach and the unit identical weight per each. This figure is in the verbose format.

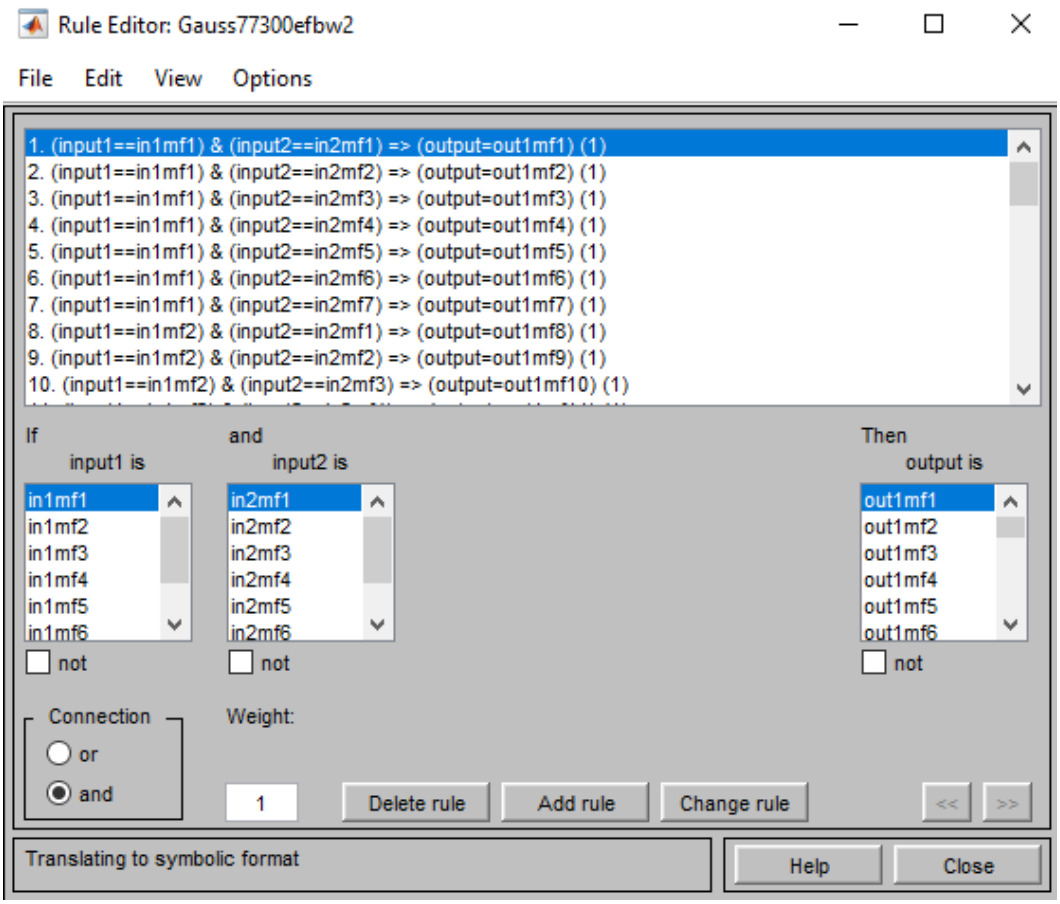


Figure 84. Fuzzy inference indexed rule editor

Fuzzy rules of the second inference system for estimating the third resonance frequency are depicted here, in the symbolic format.

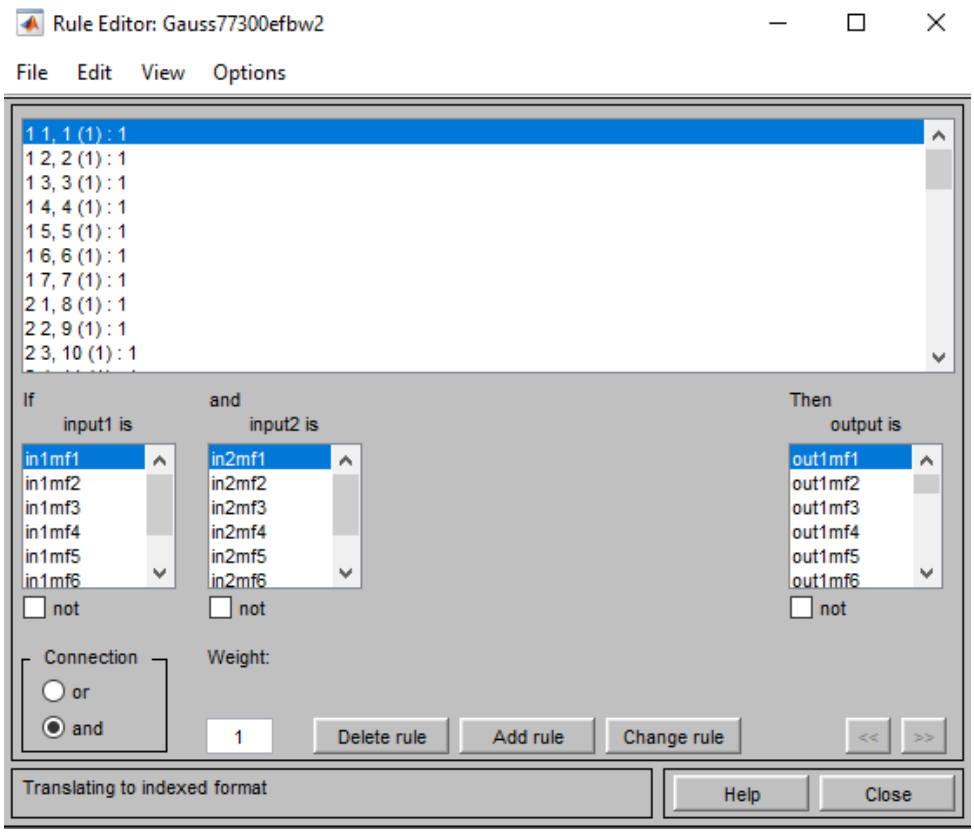


Figure 85. Fuzzy inference symbolic rule editor

The mentioned rules are shown in the indexed fashion in figure 85. As a brief note, all the three figures (Figures 90, 91, and 92) represent the fuzzy rules in different fashions. One can easily connect the particular type of input one to input two, and then observe the resulting output as the consequence.

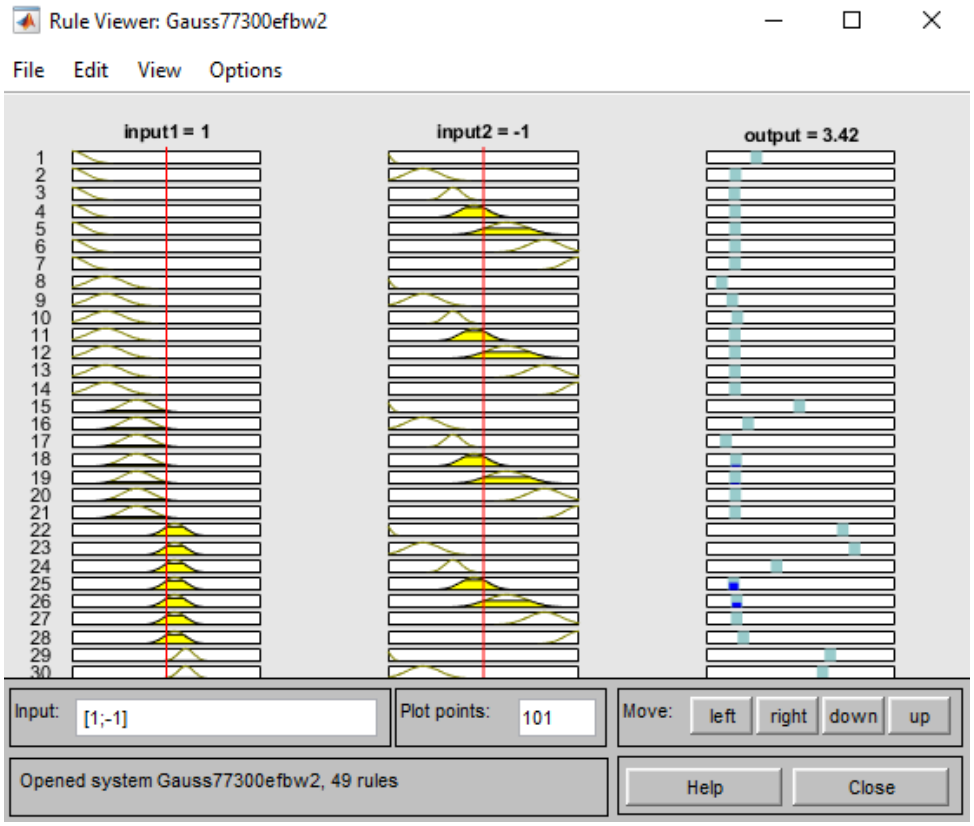


Figure 86. Fuzzy inference rule viewer

To view the inference process of the trained fuzzy inference system (FIS) for the third resonance, figure 86 is presented. Specifying numeric values for the inputs, the defuzzified values for the third resonance as is obtainable.

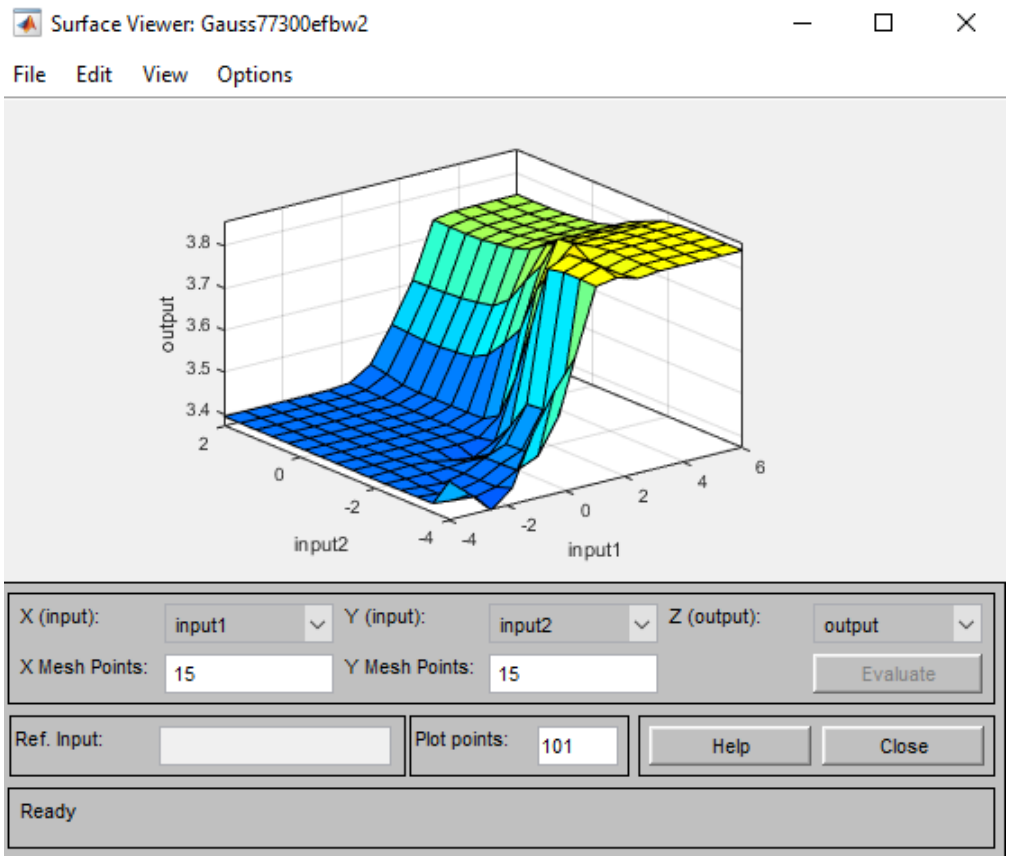


Figure 87. Fuzzy inference surface viewer

3-D plot of the fuzzy rules pertaining to the third resonance is illustrated in figure 87. Input1 pertains to the spring constant value, input2 refers to the oscillator's mass value, and the output yields the corresponding value for the third resonance.

By training and designing the fuzzy inference system using neural networks, the function approximator (regression model) can be fed up to the genetic optimization algorithm to find the optimal values for the inputs to yield the maximum effective (operational) frequency bandwidth between the minimal (first) resonance and the third resonance. As a recap the reason for considering such a frequency bandwidth from the minimal resonance rather than the second resonance is due to the fact that such a minimal resonance does not take place in all of the design parameter values, and this way the impact

of the new system configuration over the effective bandwidth is highlighted. Determining the design parameters range is a first step in optimization design problems. It is supposed for the spring constant to stay in the interval of $r_s = [0.01, 1]$ and the oscillator mass to fall in the interval of $r_s = [0.01, 2.5]$. Since a comprehensive explanation regarding the genetic optimization algorithm is presented in the proceeding section of current chapter, directly the results of the soft computing algorithm are presented here:

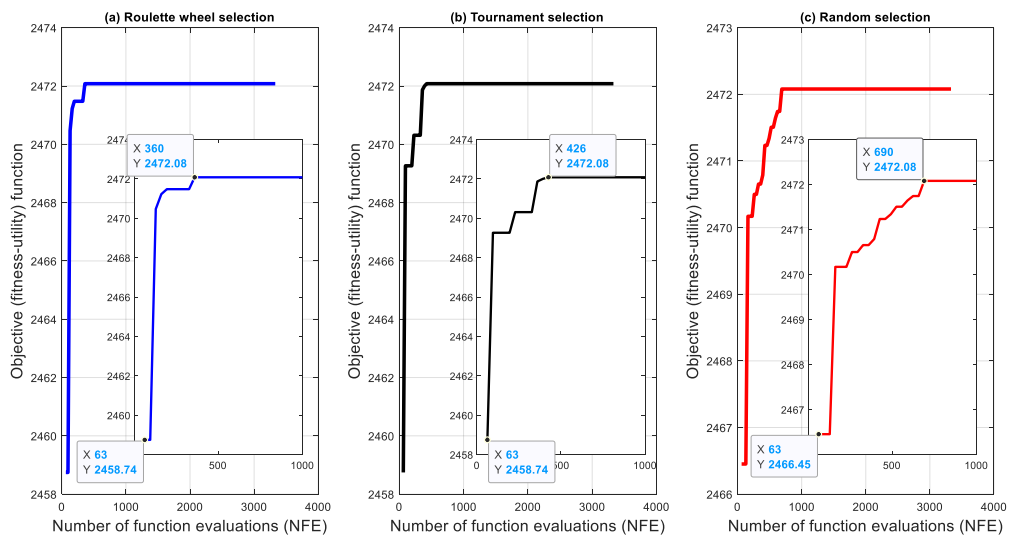


Figure 88. Objective function (operational frequency bandwidth) optimizing track

This figure demonstrates the evolutionary path of the genetic algorithm in finding the optimal solution for the effective frequency bandwidth. Three different types of selection approaches (roulette wheel, tournament, and random) are applied within the genetic operations. Since the desired case is to widen the effective frequency bandwidth, the objective functions are indeed fitness (utility) functions in terms of maximization problem.

Table 23. Optimization algorithm properties and information

| GA Selection type | Optimal $r_m$ | Optimal $r_s$ | Initial solution | Optimal solution | Total NFE |
|---|---|---|---|---|---|
| Roulette wheel | 0.01 | 2.5 | (63,2458.74) | (360,2472.08) | 3330 |
| Tournament | 0.01 | 2.5 | (63,2458.74) | (426,2472.08) | 3330 |
| Random | 0.01 | 2.5 | (63,2466.45) | (690,2472.08) | 3330 |
| population | 100 | | | | |
| iteration | 30 | | | | |
| FIS | Generalized-Bell shaped and Triangular | | | | |

Evolutions and operations of the adopted selection approaches integrated with the genetic algorithm are summarized in figure 88. According to the mentioned table and figure, optimal value for the oscillator mass is: $r_m = 2.5$ and that of the spring constant is: $r_s = 0.01$. The genetic algorithm is executed for 3330 number of function evaluations (NFEs). The algorithm initiated with 30 candidate solutions which also conveys the number of populations in each generation. The maximum number of iterations per evolution is set to 100. Roulette wheel reaches the optimal solution in the least computational effort and is the most cost-effective selection method. Random selection initiates with a better initial solution but evolves with more computations. The tournament launches with the same initial guess as the roulette wheel but requires more computational time than the others to find the optimal solutions. In short, the roulette wheel catches the optimal solution in the most cost-effective evolutionary path. As the final note, it is evident that roulette wheel shows more efficiency as it evolves with less genetic jumps (evolutions), tournament operates with medium genetic operational jumps and random traces a more complicated evolutionary track with several genetic operations. At the end it is noteworthy that such a comparison between different types of the selection methods is valid only for current results. It means that due to the nature of the genetic algorithm,

running the algorithm yields different evolutionary paths according to the selection types in each time it is run. After finding the optimal solution via soft computing algorithms which is combination of the fuzzy logic, neural networks, and the genetic algorithm; it is intended to assess the performance of the whole soft computing algorithm. To do so, the optimal design parameter values will be picked for the analytical solution which is found as a closed-form expression in the prior chapters. So, for specific mass and stiffness ratios (optimal values), the voltage frequency response function (FRF) is to be obtained and compared against several randomly-chosen case studies. Such a comparison is expected to certify the fact that the effective frequency bandwidth of the optimal solution is the most widened. To find the voltage FRF, the following steps are to be accomplished: Using the nominated optimal values, one needs to plot the nonlinear transcendental characteristic equation to estimate the initial guesses. Such initial guesses will be utilized in the VPASOLVE algorithm to numerically solve the mentioned nonlinear transcendental characteristic equation and to find the eigenvalues.

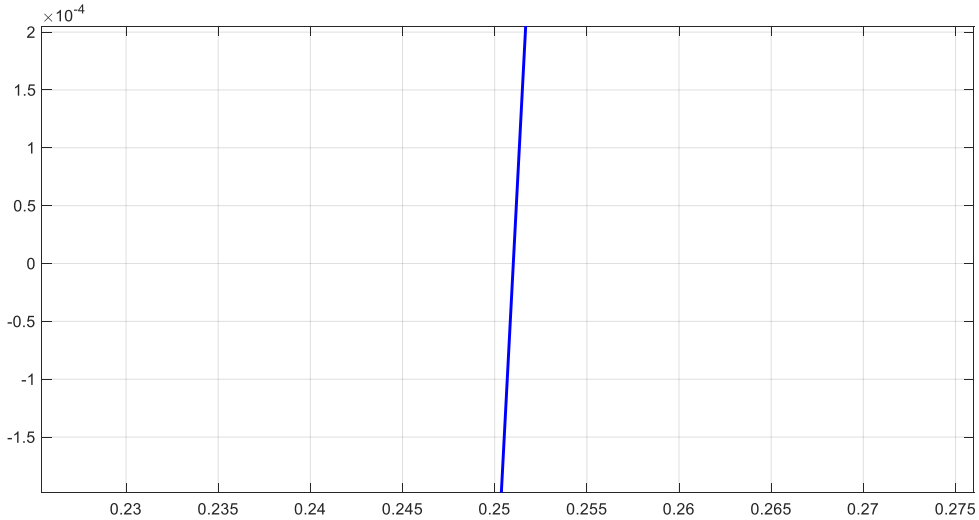


Figure 89. Plotting the characteristic equation at the vicinity of the first eigenvalue

Zooming in the neighborhood of the first eigenvalue, the first root should stay at the vicinity of $\lambda_1 L = 0.25$.

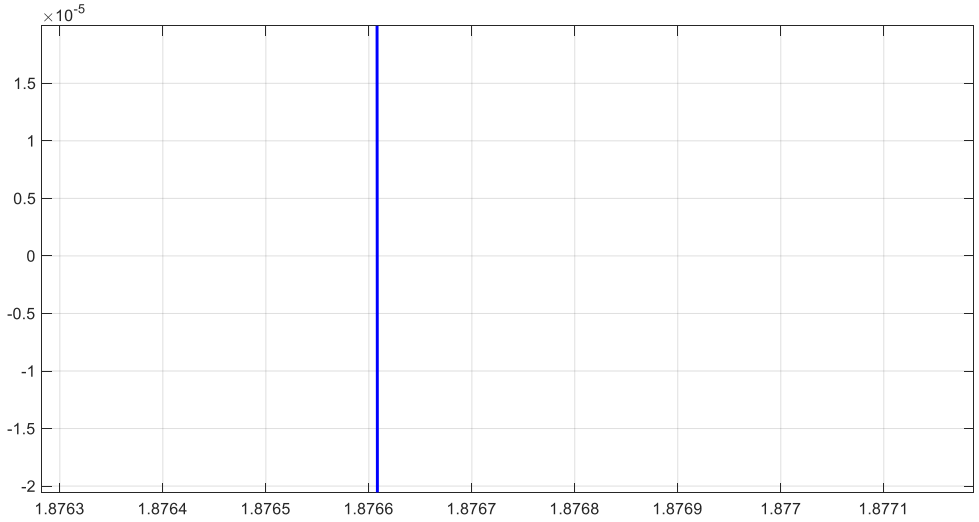


Figure 90. Plotting the characteristic equation at the vicinity of the second eigenvalue

Neighborhood of the second root of the characteristic equation is shown in Figure 97. Second root initial guess sounds to fit $\lambda_2 L = 1.8766$.

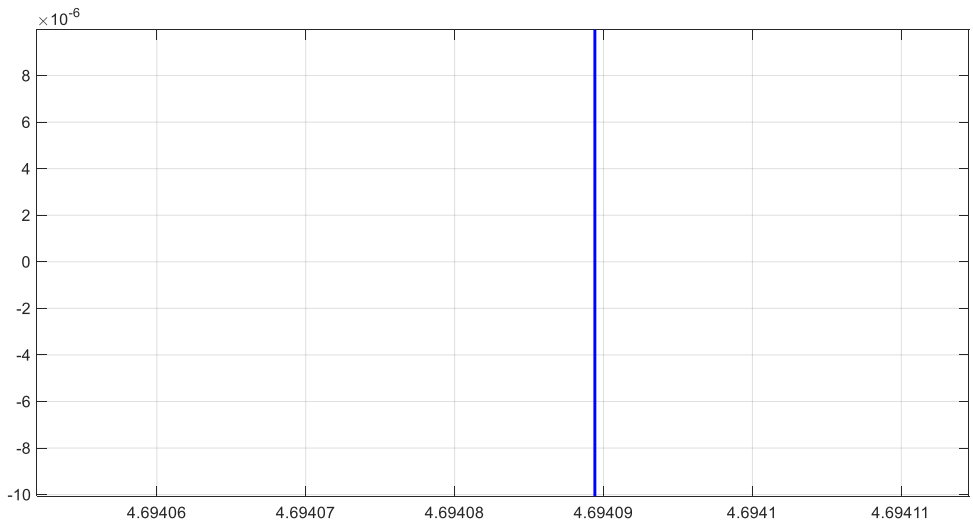


Figure 91. Plotting the characteristic equation at the vicinity of the third eigenvalue

This figure is plotted to estimate the third eigenvalue of the cantilever-oscillator-spring system. Visually, $\lambda_3 L = 4.69409$ appears to be a decent guess.

Feeding such estimations to the VPASOLVE, following values are obtained as the eigenvalues of the system:

Table 24. Numerically-solved eigenvalues using VPASOLVE

| $r_s$ | $r_m$ | $\lambda_1 L$ | $\lambda_2 L$ | $\lambda_3 L$ |
|---|---|---|---|---|
| 0.01 | 2.5 | 0.251277483823365 | 1.87661935315381 | 1.87661935315381 |

It is good to recall that the obtained values are solved using a numerical root-solving algorithm. So, such values are approximate solutions as the nonlinear transcendental equations do not have an exact (closed form) solution. To evaluate the adaptive-network based fuzzy inference system (ANFIS) and the genetic algorithm; the optimal values found

through the ANFIS, and genetic algorithm are used to find the voltage frequency response function (FRF) by means of the closed-form solution found in the preceding chapters.

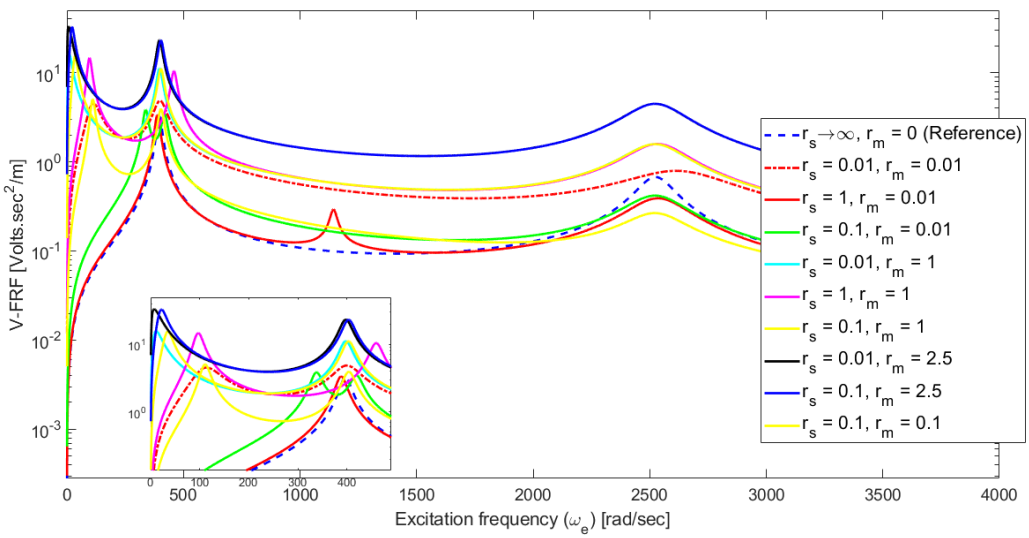


Figure 92. Voltage frequency response function (FRF)

Figure 92 depicts the voltage FRF for 9 case studies along with the reference case (pure cantilever). Oscillator mass and spring constants are chosen randomly. It is evident that the effective (operational) frequency bandwidth of the optimal solution is wider than any other case. In other words, this figure approves the authenticity and correctness of the ANFIS system consolidated with the genetic algorithm. Besides to the verification of the ANFIS-genetic algorithm, findings reveal that the weak (soft) spring and the heavy oscillator contribute to the most widened energy harvester which is the desired factor in designing the piezoelectric vibration-based energy harvesters (PVEHs). In the figure, the black line with optimal values of: $r_m = 2.5, r_s = 0.01$ operates with the most widened effective frequency bandwidth in comparison to the 8 cases studies. Similar to the former

section, voltage frequency response function (FRF) is found using the analytical-numerical method.

## 5.6 Conclusion

Harvested electric energy from conventional PVEH is mostly at small orders making the application of such devices less frequent. Another issue with the mentioned systems is the inefficient operating (effective) frequency bandwidth. To compensate for such issues, several models have been proposed. As mentioned in the literature review chapter of this dissertation, amongst the most common methods are using the tuning masses and dynamic magnifiers. In order to further develop PVEHs, integration of multiple subsystems is proposed and modeled in this project for the first time. In this chapter, the proposed model of piezoelectric vibration-based energy harvester (PVEH) is optimized with respect to the optimal and decent values of mass of the oscillator and stiffness of the spring, so that the maximum harvestable electric energy and the operational frequency bandwidth are both optimized. As a short recap, the proposed model of the energy harvester encompasses cantilever structure integrated with oscillator-spring subsystem at the tip end. Using the extended Hamilton's principle, electromechanical equations of motion of the beam, electric circuit, and oscillator motion are obtained. Due to the new boundary condition resulting from the restricted tip motion of the beam, new resonance frequency is observed which is directly dependent on the values of the oscillator mass and the spring constant. The mentioned motion restriction is resultant of the restoring effects of the spring. To optimize the energy harvester module by genetic algorithm, harvestable voltage at the first vibration mode, and the operational frequency bandwidth between the first and the third resonances; are considered as the utility (fitness) function

with oscillator mass and spring constant as the design parameters. Although closed-from expression for the voltage frequency response function (FRF) is obtained, optimization algorithm requires an estimator to evaluate the utility function values at each iteration. This is because: the voltage FRF comprises parameters that need to be found in a non-automated process (i.e., guessing the initial guess for eigenvalues cannot be automated). Moreover, the mentioned function is hard-to-evaluate function and computationally expensive. As a result, adaptive-neuro-fuzzy-inference-system (ANFIS), is utilized as a regressor to estimate the function values and perform as a function approximator. Such estimated values are utilized in genetic optimization and these entire inter-connected algorithms form the soft computing technique. To train the regressor model, 231 case studies are accomplished using the analytical-numerical voltage function. Two well-tuned and adjusted fuzzy inference systems (FISs) are designed using trial and error and by adopting different types and numbers of MFs. Such MFs per each input (oscillator mass and spring constant) and the corresponding fuzzy rules are adopted with respect to the regressor model precision and complexity. Gaussian and Generalized-Bell shaped MFs perform the most precisely than other types of the built-in functions. Both fuzzy inference architectures use 64 fuzzy rules which is based on the Takagi-Sugeno fuzzy type. Takagi-Sugeno type of fuzzy inference system is adopted as multiple (two) inputs and a single output form current regression architecture. In the design procedure, conjunction-type operators (AND) are used with identical unit weight for each of the 64 fuzzy rules. Such regressor model is integrated with the genetic algorithm initiating with 50 candidate solutions selected randomly and 200 iterations per evolution loop. The other genetic optimization algorithm initiates with 50 candidate solutions and 100 iterations per

evolution loop. The former algorithm is designed for maximizing the voltage resonance and the later algorithm is devised for optimizing the effective frequency bandwidth. Three different types of selection methods: roulette wheel, tournament, and random are adopted and compared against each other. All selection approaches yield the same optimal design parameter values (for the voltage resonance: $r_s = 100, r_m = 2$, and for the effective frequency bandwidth: $r_s = 0.01, r_m = 2.5$). At the end, to verify soundness of the devised soft computing techniques, voltage FRF of the optimal case is manually found using the analytical-numerical closed-form FRF and compared with 8 random cases of mass and stiffness ratios. Besides, several values of the design parameters which are close to the optimal values are passed through the 'readfis' function in MATLAB for the purpose of comparison. It is shown that the optimal design parameters result in the maximum harvestable voltage and maximum value of the widened operational frequency bandwidth, approving the authenticity of the soft computing processes. Such a comprehensive study reveals the successful integration of a mechanical oscillatory subsystem with cantilever piezoelectric energy harvester to improve and develop the energy harvesters. Moreover, such a reinforced model is optimized via adoption of Takagi-Sugeno type of fuzzy logic, neural networks, and genetic algorithms to render the maximum amount of the energy particularly at the first resonance, along with the mostly widened effective frequency bandwidth. It was also observed that the optimal case not only shows the maximum amount of harvestable electric voltage at the first vibration mode, but also captures the most energy in the following modes comparatively. In short, the optimal harvester systems both excel in harvesting more energy as well as widening the effective frequency bandwidth, meaning that the system with maximum harvestable voltage also has a widened effective frequency

bandwidth, and the system with the most widened frequency bandwidth also harvests great amount of energy. To choose among the mentioned systems, designers may prioritize maximum harvestable energy or effective frequency bandwidth to the other. Such a compensation looks fair. As the final benefit of the proposed PVEH, generation of the minimal resonance at small frequencies is notable. In the literature it is reported that reaching to the resonance frequencies of the vibrating structure (cantilever) is mostly hard and unaffordable. This issue will be intensified adversely if the size of the PVEH is scaled down. In small-scale PVEH (MEMS PVEH), resonance frequency of the system is mostly bigger than the macro-scale PVEH, which makes their applicability lesser. In the proposed model of PVEH, the minimal resonance is generated around very small numbers. Such a resonance prior to the other resonances avoids the issue of resonance mismatch. In short, in the proposed PVEH model: the maximum amount of the harvestable energy as well as widened effective frequency bandwidth, are reinforced; the mentioned parameters are optimizable; and the resonance generated at small values makes their applicability accessible.

# CHAPTER 6. ADAPTIVE PIEZOELECTRIC VIBRATION-BASED ENERGY HARVESTER (PVEH)

## 6.1 Introduction and Background to Adaptive PVEH

In the preceding chapters, analytical-numerical procedure for analyzing the new type of piezoelectric vibration-based energy harvester (PVEH) is studied. The new model consists of a cantilever system with an oscillator attached to the free (tip) end via a spring. It was shown that the relative motion of the oscillator mass significantly changes the vibrational and dynamical characteristics of the cantilever-oscillator-spring system in terms of resonance frequency and vibration modes and mode shape functions. It is exclusively studied how the inertial effects of the oscillator manipulate resonance frequencies and new resonances emerge. It is also highlighted that generation of such minimal frequencies is of primary importance to energy harvesters, especially at small scales. In the former chapter, optimization of the proposed energy harvester is carried out. It is shown that PVEHs are not efficient unless at least two major cases are covered and accommodated technically: the maximum amount of extractable energy and the effective (operational) frequency bandwidth (EFBW). It is also mentioned that the proposed cantilever-oscillator-spring energy harvester system has a major and primary superiority to other systems due to the design parameters (oscillator mass and spring constant). Such design parameters play a vital role in the performance of the harvester as they readily mutate the system's vibrational behavior. Accordingly, two separate optimization case studies were delivered in the former chapter to: optimize the maximum amount of electric voltage at the first vibration mode and optimize the systems effective frequency bandwidth in terms of widening the bandwidth. Such widened bandwidth leads to covering wider and

broader operational bandwidth. Finally, the optimal design parameters were inserted into the analytical solution to compare and evaluate the soft computing approach used beforehand. After addressing such critical points in designing the new piezoelectric vibration-based energy harvester (PVEH), another case study sounds essential to further elaborate the benefits of such novel energy harvester system.

In other words, in continuance of devising the efficient PVEH, it sounds helpful and crucial to design an adaptive system. Such an adaptive system means devising a system which adapts and adjusts itself to the available sources (excitation frequencies) in the background. Since it is proved and scrutinized that the proposed model is able to be altered remarkably, one can exploit such a trait in adapting the PVEH to reach harmony with external source. Such an adaptation and adjustment lead to resonance and wider effective frequency bandwidth and as a result in efficient PVEH for all scales (micro, meso, and macro scales). For the adaptive PVEH, the design and implementation process are reversed in comparison to the optimization processes. It means that, in adaptive PVEH, we intend to drag the system's resonance frequency to the excitation (driving) frequency which is available in the external source. To do so, we need to rely on the main parameters of the system (spring constant and the oscillator mass). As a result, the first resonance frequency is the input to the adaptive PVEH design problem, and the output is going to be either the spring constant or the oscillator mass. The reason for choosing only the first resonance is stated in detail in the former chapters. As a brief and concise recall, it is due to the importance and accessibility of the first vibration mode than the higher modes. So; in this chapter, unlike the former chapter it is assumed the system needs to adjust itself to the surroundings and enhance its performance by such adaptation. In this chapter, we deal

with a reverse engineering problem. Since the main goal is to design an adaptive energy harvester which adjusts either: the spring constant, or the oscillator mass; the excitation frequency is the input. In other words, in the ideal adaptive system, the excitation frequency is captured as the input and the systems' characteristics (in this case the oscillator mass or the spring constant) are adjusted so that the resonance frequency of the energy harvester will match the excitation (driving) frequency. To accomplish such an adaptation, fuzzy inference regression system is taken. Since a comprehensive explanation about the mentioned regressor is elaborated in the former chapters, further description is skipped. The fuzzy inference model is expected to run with a single input (excitation or resonance frequency) and yield a single output (spring constant or oscillator mass). So, the regression model is single input-single output (SISO). It may be asked why not to design a model of single input-multiple output (SIMO) which can provide an estimation for spring stiffness (constant) and oscillator mass simultaneously? The answer to this question falls in the capability of fuzzy inference models. Designing a SIMO fuzzy model is definitively more complicated than a SISO or MISO model. The fuzzy models are basically established based on either Takagi-Sugeno or Mamdani reasonings. Mamdani is capable of training models with multiple outputs (SIMO or MIMO); although, the accuracy and the computational costs are not as efficient as the single output cases. It means that better and more accurate fuzzy systems take place with single output cases. As for Takagi-Sugeno, the fuzzy reasoning is only capable of training single outputs. ANFIS toolbox is established based on the Takagi-Sugeno. So, only single output systems are available to be trained and designed. Considering all the mentioned points, it sounds a better decision to keep one of the outputs (spring constant or oscillator mass) constant and vary the other

one, while the fuzzy system is provided with excitation frequency as the input or given data. Eventually, the fuzzy system will reveal the suitable value of one of the system features (spring constant or oscillator mass).

## 6.2 Training the Fuzzy Inference System for the Adaptive PVEH

It is already mentioned that fuzzy inference system will be built based on ANFIS toolbox in MATLAB. Eight built-in membership functions (MFs) are available in the toolbox. As a brief overview of the steps required to build and design a FIS, the following figure is provided:

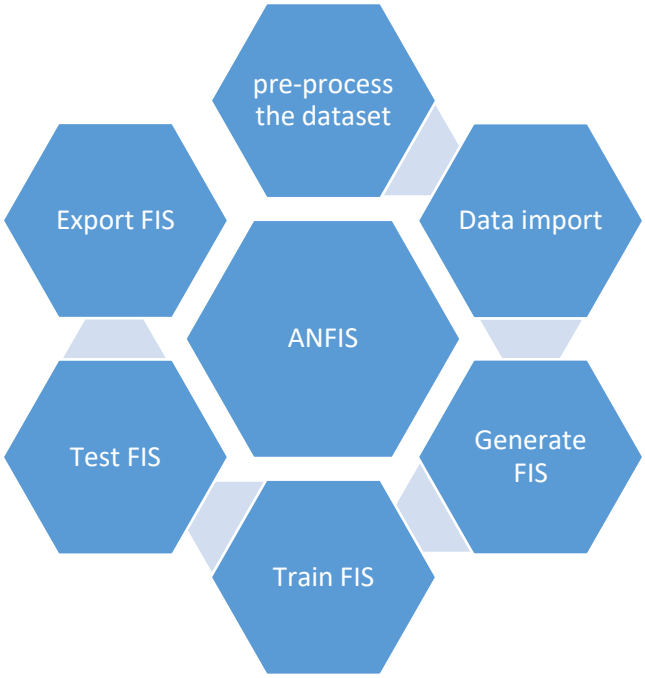


Figure 93. ANFIS toolbox chart in MATLAB

Pre-process and gather the dataset: in this section, the excitation frequency dataset will be provided as the desired input, and the corresponding oscillator mass or spring

constant will be estimated accordingly. The given dataset should be probed first, particularly in terms of distribution range. Since the distribution range accompanies normal values and excessive variants or other statistical features do not exist; it is not required to apply any operations over the dataset. As another important fact, the resource of gathering such an input dataset is to be disclosed. Since the analytical method elaborated in the previous chapters provides the closed-form solution to the electric frequency response function (FRF), we can find the required dataset. Two different case studies of: fixed spring constant and varying oscillator mass, and fixed oscillator mass and varying spring stiffness; are to be studied. For the fixed oscillator mass, the mass ratio is taken as: $r_m = 1$, and the spring stiffness ratio has the distribution range of: $r_s = [0.0001, 100]$, starting from the weakest (the softest) spring up to the hardest (the stiffest) spring. As for the varying oscillator mass and fixed spring constant, the stiffness of the spring is supposed to be 0.1 times of the flexural rigidity (bending stiffness) of the cantilever beam, and the oscillator mass falls in the range of: $r_m = [0.0001, 100]$. For each case study, the analytical solution is adopted to find the resonance frequency of the system:

Table 25. Resonance frequency of the cantilever-spring-oscillator system found analytically ($r_m = 1$)

| Case study number | $r_s$ | Frequency (Hz) (1/sec) |
|---|---|---|
| 1 | 0.0001 | 0.179089998 |
| 2 | 0.0005 | 0.400430715 |
| 3 | 0.001 | 0.566247364 |
| 4 | 0.005 | 1.265324214 |
| 5 | 0.01 | 1.787950058 |
| 6 | 0.02 | 2.524343638 |
| 7 | 0.03 | 3.086551165 |
| 8 | 0.04 | 3.558143927 |
| 9 | 0.05 | 3.971553985 |

| | | |
|---|---|---|
| 10 | 0.06 | 4.343445122 |
| 11 | 0.07 | 4.68373457 |
| 12 | 0.08 | 4.998895866 |
| 13 | 0.09 | 5.293433902 |
| 14 | 0.1 | 5.570634804 |
| 15 | 0.2 | 7.751334436 |
| 16 | 0.3 | 9.343543454 |
| 17 | 0.4 | 10.62194885 |
| 18 | 0.5 | 11.69543259 |
| 19 | 0.6 | 12.62110079 |
| 20 | 0.7 | 13.43361765 |
| 21 | 0.8 | 14.15603533 |
| 22 | 0.9 | 14.80467272 |
| 23 | 1 | 15.39161865 |
| 24 | 1.5 | 17.66662197 |
| 25 | 2 | 19.23772152 |
| 26 | 2.5 | 20.39276512 |
| 27 | 3 | 21.27840485 |
| 28 | 3.5 | 21.97894735 |
| 29 | 4 | 22.54671195 |
| 30 | 4.5 | 23.01599073 |
| 31 | 5 | 23.41022203 |
| 32 | 5.5 | 23.74597357 |
| 33 | 6 | 23.41022203 |
| 34 | 6.5 | 24.28712083 |
| 35 | 7 | 24.50827869 |
| 36 | 7.5 | 24.70401645 |
| 37 | 8 | 24.8784587 |
| 38 | 8.5 | 25.03488657 |
| 39 | 9 | 25.17594234 |
| 40 | 9.5 | 25.30377725 |
| 41 | 10 | 25.42016026 |
| 42 | 20 | 26.59155626 |
| 43 | 30 | 27.00974933 |
| 44 | 40 | 27.22427744 |
| 45 | 50 | 27.35475877 |
| 46 | 60 | 27.44248717 |
| 47 | 70 | 27.50551488 |
| 48 | 80 | 27.55298564 |
| 49 | 90 | 27.59002613 |
| 50 | 100 | 27.61973348 |

Table 26. Resonance frequency of the cantilever-spring-oscillator system found analytically ($r_s = 0.1$)

| Case study number | $r_m$ | Frequency (Hz) (1/sec) |
|---|---|---|
| 1 | 0.0001 | 62.95661845 |
| 2 | 0.0005 | 62.90236023 |
| 3 | 0.001 | 62.82622369 |
| 4 | 0.005 | 61.48766825 |
| 5 | 0.01 | 53.56161113 |
| 6 | 0.02 | 39.01624036 |
| 7 | 0.03 | 31.99216342 |
| 8 | 0.04 | 27.75201867 |
| 9 | 0.05 | 24.84406746 |
| 10 | 0.06 | 22.6918416 |
| 11 | 0.07 | 21.01639125 |
| 12 | 0.08 | 19.66434189 |
| 13 | 0.09 | 18.54351324 |
| 14 | 0.1 | 17.59474376 |
| 15 | 0.2 | 12.44992528 |
| 16 | 0.3 | 10.16753468 |
| 17 | 0.4 | 8.806283698 |
| 18 | 0.5 | 7.877079207 |
| 19 | 0.6 | 7.191058778 |
| 20 | 0.7 | 6.657825723 |
| 21 | 0.8 | 6.227964854 |
| 22 | 0.9 | 5.871883375 |
| 23 | 1 | 5.570634804 |
| 24 | 1.5 | 4.548592545 |
| 25 | 2 | 3.939277918 |
| 26 | 2.5 | 3.523440786 |
| 27 | 3 | 3.216473106 |
| 28 | 3.5 | 2.977892923 |
| 29 | 4 | 2.785576013 |
| 30 | 4.5 | 2.62627523 |
| 31 | 5 | 2.491510258 |
| 32 | 5.5 | 2.375567134 |
| 33 | 6 | 2.274436608 |
| 34 | 6.5 | 2.185211454 |
| 35 | 7 | 2.10572529 |
| 36 | 7.5 | 2.034326281 |
| 37 | 8 | 1.969729969 |
| 38 | 8.5 | 1.910920483 |
| 39 | 9 | 1.857082393 |
| 40 | 9.5 | 1.807552568 |

| | | |
|---|---|---|
| 41 | 10 | 1.761785454 |
| 42 | 20 | 1.245778089 |
| 43 | 30 | 1.017175631 |
| 44 | 40 | 0.880900837 |
| 45 | 50 | 0.787902144 |
| 46 | 60 | 0.719253257 |
| 47 | 70 | 0.665899316 |
| 48 | 80 | 0.62289191 |
| 49 | 90 | 0.587268225 |
| 50 | 100 | 0.557131633 |

A total of 100 case studies are shown in Tables 25 and 27. For each one, the following procedure is accomplished:

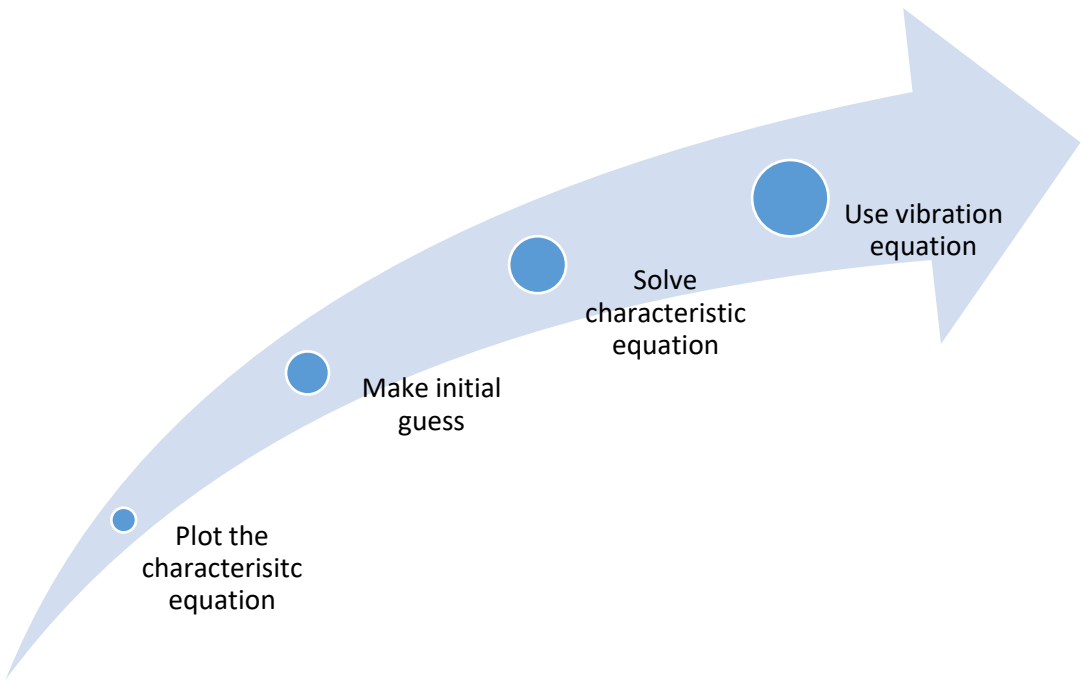


Figure 94. Analytical-numerical voltage FRF procedure

In the first step, the nonlinear transcendental characteristic equation is plotted. Second, the initial guess of the root(s) is deduced to be applied in the numerical solver. In the third step, initial guess is provided as input to the numerical solver (VPASOLVE) to

find the real root(s). Finally, the root is applied into the vibration equation ($\lambda_n L = \omega_n L\sqrt{\rho A/EI}\,, fr_n = \omega_n/2\pi$) to find the resonance frequency of the system in angular version (rad/sec) or in linear version (in Hz). Now, the dataset is to be utilized inversely. It means that the gathered and obtained frequency dataset will be the input and the spring constant (or mass of the oscillator) will be used as the output.

Data import: in this section, the 50 datasets are divided into train (80%), test (10%), and validation (checking) (10%) datasets. Most of the dataset is used to train the fuzzy regressor inference system using the neural network. A small portion is required to test and assess the performance of the regressor (function approximator). Eventually, another small portion is implemented in fuzzy toolbox to avoid overfitting. Such dataset is titled checking or validation dataset.

Generate Fuzzy Inference System (FIS): in this step, the fuzzy inference system (FIS) will be implemented and designed using the dataset provided and imported. To design an FIS, there are eight built-in membership functions (MFs) available in the toolbox. There is another option to design MFs from scratch and by writing the code at the editor platform window. It was tried to design specific and non-general MF but none of them have the accuracy and high performance of the pre-built (built-in) MFs available in the toolbox. In order to choose the best MF, there are two main points to be considered. First of all, the function should be accurate and precise enough. It means the ability to capture the structure in the dataset and predict the outcomes in a high level of acceptance and precision. To assess such trait, root-mean-square-error (RMSE) is a great and handy criterion. So, in the following section different types of MFs are adopted to generate the

FIS and the corresponding RMSE per each dataset (train, test, and checking) are recorded. To add MFs, eight disparate types of MFs are available:

Table 27. Disparate types of built-in membership functions (MFs)

| | |
|---|---|
| Triangular | Double Gaussian |
| trapezoidal | Polynomial |
| Generalized Bell shaped | Double sigmoid |
| Gaussian | Polynomial sigmoid |

It is also good to note that each input of the system is to be assigned with specific MFs. FIs can be imported from files, workspace, or can be generated via subtractive clustering or grid partitioning.

Train the fuzzy inference system (FIS): in this section, the generated fuzzy inference system is optimized and trained. Two different types of optimization algorithms are available: the hybrid versus the back-propagation methods. Moreover, the number of epochs, and the error tolerance needs to be specified in this section.

Test the fuzzy inference system (FIS): after training the FIS, the performance needs to be assessed and tested against the previously unseen dataset (test dataset). The corresponding plots for testing against the: train dataset, test dataset, and the validation dataset; will be shown in the plot box. Such plots disclose the error versus accurateness of the generated FIS.

Export to the workspace: the generated FIS can now be exported to the workspace or saved as a fuzzy file with ‘.fis’ extension. In the following tables, root-mean-square-error (RMSE) for eight different types of the built-in MFs along with disparate numbers and various design parameters are provided:

Table 28. Triangular MF evaluation with respect to RMSE

| MF numbers | Epochs | RMSE-train | RMSE-test | RMSE-validation |
|---|---|---|---|---|
| 5 | 300 | 0.28728 | 0.30494 | 0.48043 |
| 6 | 300 | 0.22991 | 0.16021 | 0.47199 |
| 7 | 300 | 0.1952 | 0.092573 | 0.46825 |
| 8 | 300 | 0.17379 | 0.078632 | 0.43309 |
| 9 | 300 | 0.14307 | 0.083305 | 0.43642 |
| 10 | 300 | 0.1052 | 0.079339 | 0.44039 |
| 11 | 300 | 0.079556 | 0.099031 | 0.42106 |
| 12 | 300 | 0.059876 | 0.047074 | 0.38766 |

Using triangular type of membership functions, adopting more than 6 functions leads to small test RMSE and the best one alludes to 12 numbers. It is also good to note that if the number of epochs is not mentioned, it is set as 300, and main criteria for decent performance is obtaining $RMSE < 0.1$ in all cases.

Table 29. Trapezoidal MF evaluation with respect to RMSE

| MF numbers | Epochs | RMSE-train | RMSE-test | RMSE-validation |
|---|---|---|---|---|
| 5 | 300 | 0.4081 | 0.23318 | 0.54155 |
| 6 | 300 | 0.33277 | 0.16359 | 0.48856 |
| 7 | 300 | 0.26852 | 0.14876 | 0.48785 |
| 8 | 300 | 0.23697 | 0.14094 | 0.46779 |
| 9 | 300 | 0.19566 | 0.15741 | 0.46259 |
| 10 | 300 | 0.14812 | 0.13553 | 0.47246 |
| 11 | 300 | 0.1065 | 0.12603 | 0.45548 |
| 12 | 300 | 0.068137 | 0.11128 | 0.45448 |

Trapezoidal membership functions exhibit the best performance with 12 numbers. Adopting more MFs leads to overfitting expectedly. A small number of MFs end up in regressors with week precision.

Table 30. GeneralizedBell shaped (G-bell) MF evaluation with respect to RMSE

| MF numbers | Epochs | RMSE-train | RMSE-test | RMSE-validation |
|---|---|---|---|---|
| 5 | 300 | 0.29771 | 0.20215 | 0.20729 |
| 6 | 300 | 0.26453 | 0.1725 | 0.13977 |
| 7 | 300 | 0.22972 | 0.11632 | 0.10527 |
| 8 | 300 | 0.20958 | 0.081313 | 0.47481 |
| 8 | 300 | 0.20958 | 0.081313 | 0.47481 |
| 9 | 300 | 0.12152 | 0.059204 | 0.096509 |
| 10 | 300 | 0.11679 | 0.03397 | 0.11041 |
| 11 | 300 | 0.11481 | 0.019829 | 0.13647 |
| 12 | 300 | 0.11316 | 0.01628 | 0.66331 |
| 13 | 300 | 0.11188 | 0.020892 | 0.52034 |
| 13 | 300 | 0.11188 | 0.020892 | 0.52034 |
| 14 | 300 | 0.11083 | 0.0089137 | 0.5565 |
| 14 | 300 | 0.11083 | 0.0089137 | 0.5565 |
| 14 | 500 | 0.100160 | 0.011729 | 0.32424 |
| 15 | 300 | 0.10983 | 0.015019 | 0.78242 |
| 16 | 300 | 0.1086 | 0.012102 | 0.13304 |
| 16 | 500 | 0.007247 | 0.011306 | 0.099889 |
| 16 | 1000 | 0.0062894 | 0.011063 | 0.12126 |

Table 31. Gaussian MF evaluation with respect to RMSE

| MF numbers | Epochs | RMSE-train | RMSE-test | RMSE-validation |
|---|---|---|---|---|
| 5 | 300 | 0.35989 | 0.27335 | 0.28226 |
| 6 | 300 | 0.32196 | 0.23625 | 0.2216 |
| 7 | 300 | 0.29191 | 0.20686 | 0.13546 |
| 8 | 300 | 0.25816 | 0.17533 | 0.4682 |
| 9 | 300 | 0.14459 | 0.1261 | 0.16817 |
| 10 | 300 | 0.1373 | 0.10629 | 0.47266 |
| 11 | 300 | 0.1314 | 0.086961 | 0.013093 |
| 12 | 300 | 0.12677 | 0.068266 | 1.4865 |

Generalized-Bell shaped membership functions with numbers more than 8 exhibit decent performance in terms of the root-mean-square-error. The best performance pertains to the 14 numbers of the MF and 300 epochs.

Adopting Gaussian membership functions, numbers more than 11 exhibit decent RMSE and a suitable choice. Gaussian type of membership functions is among the well-known type of functions in most of the case studies. This trait pertains to the mathematical properties of the mentioned function which enables the curve to capture features and patterns in a dataset efficiently.

Table 32. Gaussian2 (double Gaussian) MF evaluation with respect to RMSE

| MF numbers | Epochs | RMSE-train | RMSE-test | RMSE-validation |
|---|---|---|---|---|
| 5 | 300 | 0.38231 | 0.30089 | 0.34652 |
| 6 | 300 | 0.33874 | 0.25132 | 0.3177 |
| 7 | 300 | 0.30598 | 0.20527 | 0.26177 |
| 8 | 300 | 0.27476 | 0.17321 | 0.92836 |
| 9 | 300 | 0.19422 | 0.16473 | 0.21536 |
| 10 | 300 | 0.15875 | 0.14802 | 0.17772 |
| 11 | 300 | 0.10623 | 0.04385 | 0.72062 |
| 12 | 300 | 0.12689 | 0.080923 | 0.2049 |

Choosing double gaussian membership functions and 300 epochs, numbers more than 11 lead to decent performance. Adopting fewer number of membership functions ends up in less accurate systems and underfitting issues emerge.

Using polynomial membership functions, it sounds that more numbers are required as the only decent performance is observed at 11 numbers ($RMSE < 0.1$). Polynomial type of the membership functions requires mor computational efforts to capture the structure.

Table 33. Polynomial MF evaluation with respect to RMSE

| MF numbers | Epochs | RMSE-train | RMSE-test | RMSE-validation |
|---|---|---|---|---|
| 5 | 300 | 0.47863 | 0.41728 | 0.50848 |
| 6 | 300 | 0.44353 | 0.38673 | 0.36892 |
| 7 | 300 | 0.43844 | 0.31482 | 0.29768 |
| 8 | 300 | 0.44451 | 0.37251 | 0.42007 |
| 9 | 300 | 0.37075 | 0.27882 | 0.17246 |
| 10 | 300 | 0.29154 | 0.25305 | 0.31898 |
| 11 | 300 | 0.24237 | 0.094843 | 0.75068 |
| 12 | 300 | 0.23606 | 0.12205 | 0.2889 |

Table 34. Double sigmoid MF evaluation with respect to RMSE

| MF numbers | Epochs | RMSE-train | RMSE-test | RMSE-validation |
|---|---|---|---|---|
| 5 | 300 | 0.27299 | 0.19035 | 0.31572 |
| 6 | 300 | 0.2451 | 0.17625 | 0.12893 |
| 7 | 300 | 0.22931 | 0.15414 | 0.09776 |
| 8 | 300 | 0.18463 | 0.1192 | 1.7933 |
| 9 | 300 | 0.13249 | 0.08558 | 0.13321 |
| 10 | 300 | 0.12228 | 0.036821 | 3.5956 |
| 11 | 300 | 0.12228 | 0.036821 | 3.5956 |
| 12 | 300 | 0.1191 | 0.024707 | 0.42674 |

Adopting double sigmoidal membership functions, decent performance is observed for all numbers greater than 8. This type of function reaches a good level of accuracy in prediction at a fair number of the adopted functions.

Finally, choosing polynomial sigmoidal membership functions leads to decent error for numbers bigger than 8. The mentioned type of the functions work based on the features of both polynomial and sigmoid functions. Such a combination may lead to high complication of the system.

Table 35. Polynomial-sigmoid MF evaluation with respect to RMSE

| MF numbers | Epochs | RMSE-train | RMSE-test | RMSE-validation |
|---|---|---|---|---|
| 5 | 300 | 0.27749 | 0.17839 | 0.19521 |
| 6 | 300 | 0.2556 | 0.17307 | 0.1575 |
| 7 | 300 | 0.22025 | 0.13292 | 0.23212 |
| 8 | 300 | 0.18857 | 0.12695 | 1.6113 |
| 9 | 300 | 0.13238 | 0.085323 | 0.13309 |
| 10 | 300 | 0.12228 | 0.36825 | 3.5957 |
| 11 | 300 | 0.1191 | 0.024704 | 0.42674 |
| 12 | 300 | 0.11803 | 0.038741 | 0.17486 |

Comparatively, among all of the best performances in various types of MFs, the Generalized-Bell shaped type of the MF with 14 number of the membership functions (MF) and 300 epochs exhibits the best performance for the first adaptive case study (constant spring stiffness ratio and varying oscillator mass). Obviously, the RMSE of the test dataset is the smallest observed (0.0089137). This point is also important to note that there are other observations with smaller train RMSE, but the main criteria pertain to the test RMSE. Another interesting point refers to the increment in epochs' number. Interestingly, for the same membership function type and numbers; the system with higher epochs not only does not show better performance (smaller test RMSE) but results in bigger RMSE. So, it can be deduced that increment in the number of the epochs can also lead to overfitting which is similar to the increment in the number of the membership functions. Finally, it is remarkable that the main factor in choosing the best FIS is type and number of the membership functions (MFs) and number of the epochs does not affect the outcome as rigorously as the other mentioned factors.

The same procedure is duplicated in this section for the adaptive PVEH with constant oscillator mass and varying spring constant. At the end, based on the comparison of

different types of membership function, the most efficient MF will be captured and adopted to train and design the fuzzy inference system (FIS).

Table 36. Generalized-Bell shaped (G-bell) MF evaluation with respect to RMSE

| MF numbers | Epochs | RMSE-train | RMSE-test | RMSE-validation |
|---|---|---|---|---|
| 5 | 300 | 0.079942 | 0.049829 | 0.39412 |
| 6 | 300 | 0.05219 | 0.036407 | 0.32394 |
| 7 | 300 | 0.032601 | 0.024662 | 0.29147 |
| 8 | 300 | 0.021161 | 0.020835 | 0.28185 |
| 9 | 300 | 0.015933 | 0.014576 | 0.28063 |
| 10 | 300 | 0.013784 | 0.019614 | 0.2931 |
| 11 | 300 | 0.014069 | 0.012833 | 0.29699 |
| 12 | 300 | 0.011974 | 0.019372 | 0.31464 |
| 13 | 300 | 0.011258 | 0.029184 | 0.34296 |
| 13 | 500 | 0.011065 | 0.030419 | 0.34122 |
| 13 | 1000 | 0.01097 | 0.031101 | 0.34379 |
| 14 | 300 | 0.011149 | 0.17639 | 0.33641 |
| 15 | 300 | 0.011286 | 0.04445 | 0.35088 |
| 16 | 300 | 0.01094 | 0.13359 | 0.52904 |
| 17 | 300 | 0.10737 | 0.72623 | 0.72568 |

Table 37. Triangular MF evaluation with respect to RMSE

| MF numbers | Epochs | RMSE-train | RMSE-test | RMSE-validation |
|---|---|---|---|---|
| 10 | 300 | 0.029176 | 0.055093 | 0.37996 |
| 11 | 300 | 0.023862 | 0.0078375 | 0.37664 |
| 12 | 300 | 0.024351 | 0.015246 | 0.37925 |
| 13 | 300 | 0.019334 | 0.0034548 | 0.37642 |
| 14 | 300 | 0.021222 | 0.10405 | 0.27776 |
| 15 | 300 | 0.023136 | 0.0075291 | 0.37386 |
| 16 | 300 | 0.023468 | 0.022956 | 0.37376 |
| 17 | 300 | 0.023987 | 0.05463 | 0.42311 |

Adopting Generalized-Bell shaped type of membership functions, 11 numbers with 300 epochs end up in the most decent performance. It is noteworthy to imply that due to the

capability of this membership function type, several numbers can be a good fit. As a recap, the main focus on RMSE is the test dataset RMSE.

Using triangular membership functions, numbers with 11, 13, and 15; exhibit the most accurate performance (all with $RMSE < 0.01$).

Table 38. Trapezoidal MF evaluation with respect to RMSE

| MF numbers | Epochs | RMSE-train | RMSE-test | RMSE-validation |
|---|---|---|---|---|
| 10 | 300 | 0.042128 | 0.081579 | 0.37716 |
| 11 | 300 | 0.053648 | 0.13356 | 0.40617 |
| 12 | 300 | 0.054752 | 0.087603 | 0.42197 |
| 13 | 300 | 0.047144 | 0.1548 | 0.56812 |
| 14 | 300 | 0.037949 | 0.09475 | 0.42634 |
| 15 | 300 | 0.015715 | 0.3092 | 0.41747 |
| 16 | 300 | 0.021737 | 0.051579 | 0.47294 |
| 17 | 300 | 0.040746 | 0.099037 | 0.46435 |

Adopting trapezoidal membership functions, 16 numbers of the mentioned function lead to the most accuracy. Less numbers lead to less precise systems.

Table 39. Gaussian MF evaluation with respect to RMSE

| MF numbers | Epochs | RMSE-train | RMSE-test | RMSE-validation |
|---|---|---|---|---|
| 10 | 300 | 0.021225 | 0.018942 | 0.28139 |
| 11 | 300 | 0.018996 | 0.013215 | 0.27946 |
| 12 | 300 | 0.01656 | 0.014828 | 0.028476 |
| 13 | 300 | 0.013277 | 0.019451 | 0.30863 |
| 14 | 300 | 0.01221 | 0.085886 | 0.30778 |
| 15 | 300 | 0.012117 | 0.016727 | 0.31674 |
| 16 | 300 | 0.011422 | 0.21719 | 0.78383 |
| 17 | 300 | 0.011434 | 0.33009 | 0.53152 |

Gaussian type of membership functions with 11 numbers ends up in the best performance. However, other acceptable operations last for numbers between10 up to 15. For more than 16 numbers of the MFs, RMSE values for the test dataset exceeds the acceptable level.

Table 40. Gaussian2 (double Gaussian) MF evaluation with respect to RMSE

| MF numbers | Epochs | RMSE-train | RMSE-test | RMSE-validation |
|---|---|---|---|---|
| 10 | 300 | 0.019132 | 0.043057 | 0.38605 |
| 11 | 300 | 0.017696 | 0.27653 | 0.40823 |
| 12 | 300 | 0.016972 | 0.09719 | 0.41353 |
| 13 | 300 | 0.01578 | 0.077128 | 0.44166 |
| 14 | 300 | 0.013639 | 0.11888 | 0.42545 |
| 15 | 300 | 0.011346 | 0.2797 | 0.42343 |
| 16 | 300 | 0.011219 | 0.03109 | 0.47835 |
| 17 | 300 | 0.011081 | 0.096906 | 0.4692 |

Adopting double gaussian membership functions, the 16 numbers case leads to the best performance. Unlike some other cases in which the RMSE gradation reveals a sort of uniform and expectable pattern, in this case the RMSE mutation is totally unpredictable. It means that decent observations have been viewed at numbers: 10, 12, 13, 16 and 17.

Table 41. Polynomial MF evaluation with respect to RMSE

| MF numbers | Epochs | RMSE-train | RMSE-test | RMSE-validation |
|---|---|---|---|---|
| 10 | 300 | 0.071592 | 0.011366 | 0.41315 |
| 11 | 300 | 0.062095 | 0.14915 | 0.44551 |
| 12 | 300 | 0.046813 | 0.19312 | 0.45833 |
| 13 | 300 | 0.058323 | 0.30478 | 1.3772 |
| 14 | 300 | 0.079277 | 0.10419 | 0.48765 |
| 15 | 300 | 0.078054 | 1.6378 | 0.52186 |
| 16 | 300 | 0.047565 | 0.069815 | 0.4997 |
| 17 | 300 | 0.058325 | 0.10909 | 0.48834 |

Following the note mentioned in the above section, polynomial membership functions show undetectable performance and only the case-by-case comparison yields in best decision. Doing so, numbers of 10 and 16 are the best adoptions.

Table 42. Double sigmoid MF evaluation with respect to RMSE

| MF numbers | Epochs | RMSE-train | RMSE-test | RMSE-validation |
|---|---|---|---|---|
| 10 | 300 | 0.037029 | 0.037273 | 0.33847 |
| 11 | 300 | 0.023222 | 0.12083 | 0.35476 |
| 12 | 300 | 0.018269 | 0.064844 | 0.37969 |
| 13 | 300 | 0.016975 | 0.064097 | 0.87895 |
| 14 | 300 | 0.014602 | 0.34084 | 0.40528 |
| 15 | 300 | 0.015007 | 0.14025 | 0.4064 |
| 16 | 300 | 0.015461 | 0.038661 | 0.46667 |
| 17 | 300 | 0.016146 | 0.11045 | 0.4572 |

In double sigmoid, numbers of: 10, 16 are the best followed by numbers: 12, and 13.

Table 43. Polynomial MF evaluation with respect to RMSE

| MF numbers | Epochs | RMSE-train | RMSE-test | RMSE-validation |
|---|---|---|---|---|
| 10 | 300 | 0.03703 | 0.037272 | 0.33847 |
| 11 | 300 | 0.023224 | 0.12083 | 0.35476 |
| 12 | 300 | 0.018271 | 0.064843 | 0.37969 |
| 13 | 300 | 0.016976 | 0.064098 | 0.87893 |
| 14 | 300 | 0.0146 | 0.34064 | 0.40528 |
| 15 | 300 | 0.015002 | 0.14025 | 0.4064 |
| 16 | 300 | 0.015459 | 0.03865 | 0.46665 |
| 17 | 300 | 0.016198 | 0.1001 | 0.45697 |

Finally, for the polynomial-sigmoidal membership functions, numbers of 10 and 16 reveal the most decent performance. The interesting finding refers to the similar performance of the polynomial, polynomial sigmoidal, and double sigmoidal membership functions. At the end, it is also noteworthy the epochs number is mostly kept constant unless the number

is explicitly stated. This is mainly because the increment in the number of epochs results in significantly high computational costs. In other words, the regressor takes strikingly longer time to make a prediction. While, the improvement in terms of the accuracy and precision of the estimator system is barely increased and reinforced. In contrary; increment in the number of the membership functions (MFs), strongly and highly improves the regressor models performance. It means that the number of membership functions is a prior item than the number of epochs in designing the most efficient fuzzy inference regressor system. Consequently, most of the times epochs number is kept a constant number and most observations and trial and error procedure is rendered with respect to the number of the membership functions as the more influential factor. For the adaptive PVEH with constant oscillator mass and varying spring stiffness; there is a very similar performance among triangular membership functions with 15 numbers and the Generalized-Bell shaped with 11 numbers. By considering other RMSEs (train and validation), the triangular is adopted as the best membership function to train the FIS. It is good to note that adoption of the best membership functions is totally selective and optional. Another finding is the power of the linear type of curves to perform better than most of other nonlinear curves. This is a good note implying the fact that nonlinearity and complexity of a membership function does not necessarily promise the best performance in terms of precision and cost effectiveness.

## 6.3 Designing the Fuzzy Inference System (FIS)

By adopting the most efficient and proper membership functions, a fuzzy inference system will be designed based on the same procedure shown in the former chapter.

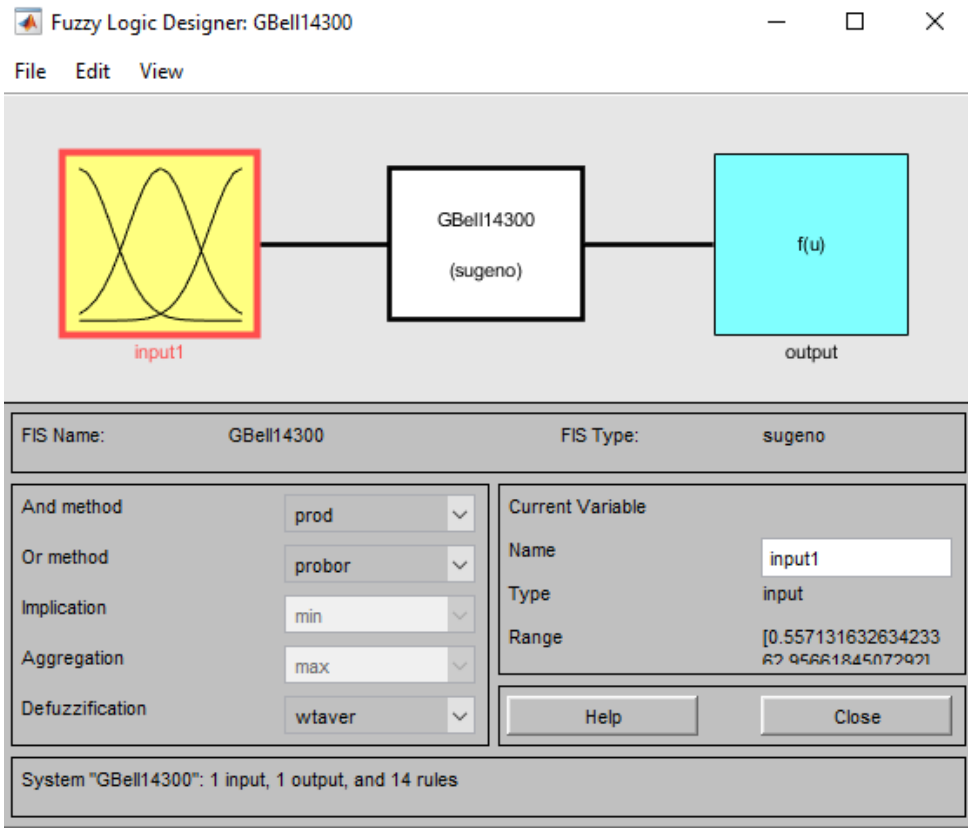


Figure 95. Fuzzy logic designer application setting

This figure represents the fuzzy logic designer toolbox. Since the fuzzy logic system is designed using ANFIS, such a toolbox reveals the features of the designed inference system. Obviously, the system is SISO (single input single output). ‘And’ method is based on production, ’OR’ method is established based on probabilistic. Implication step is based on the minimum and aggregation is based on the maximum. Finally, the defuzzification is set for weighted averaging.

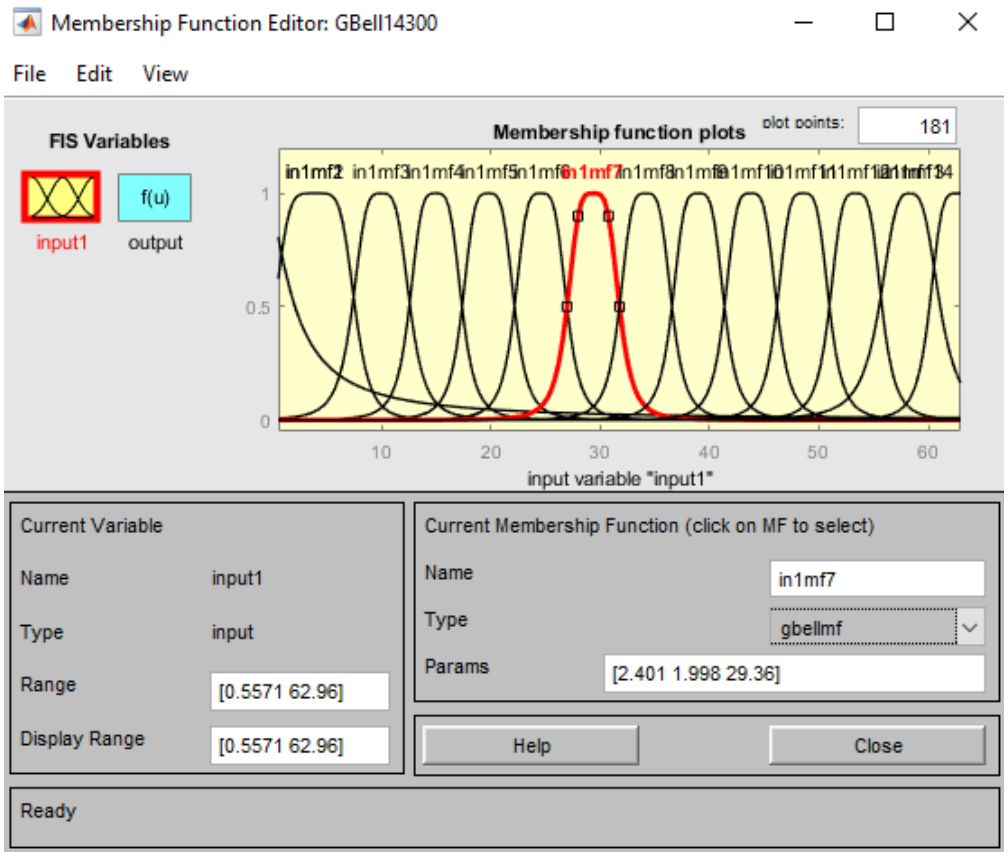


Figure 96. Fuzzy logic membership function editor

This figure shows the membership function plots for 14 numbers of Generalized-Bell shaped functions distributed from 0.5571 to 62.96. Statistical information of each function is available in the 'Params' box which emerges by clicking the function.

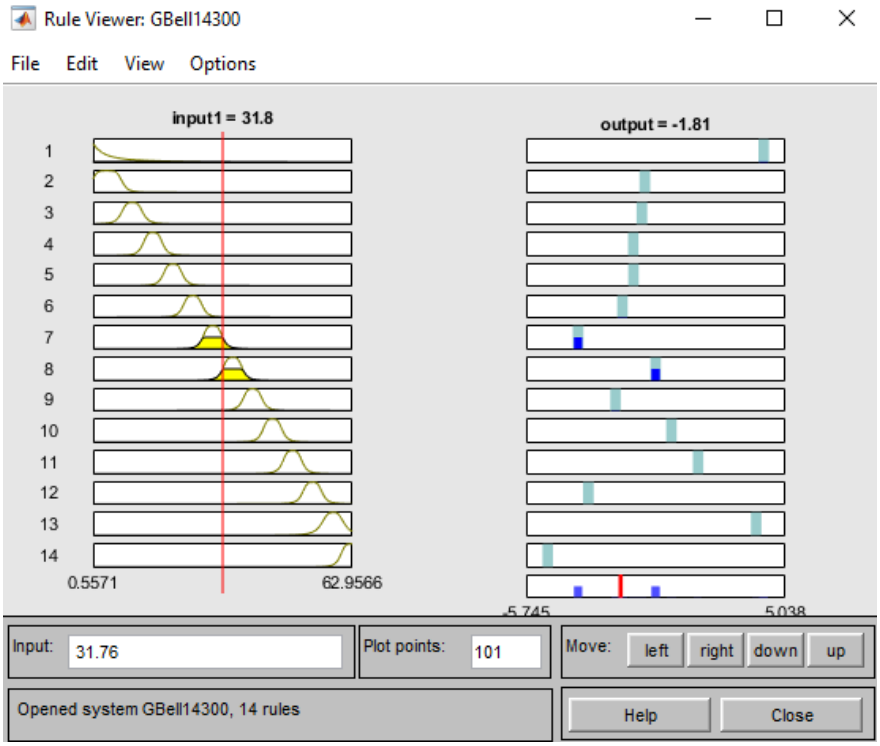


Figure 97. Fuzzy inference rule viewer

In this figure the rule viewer plot is represented. It is good to note that since there is a single input to the system, the number of fuzzy rules is identical to the number of fuzzy membership functions.

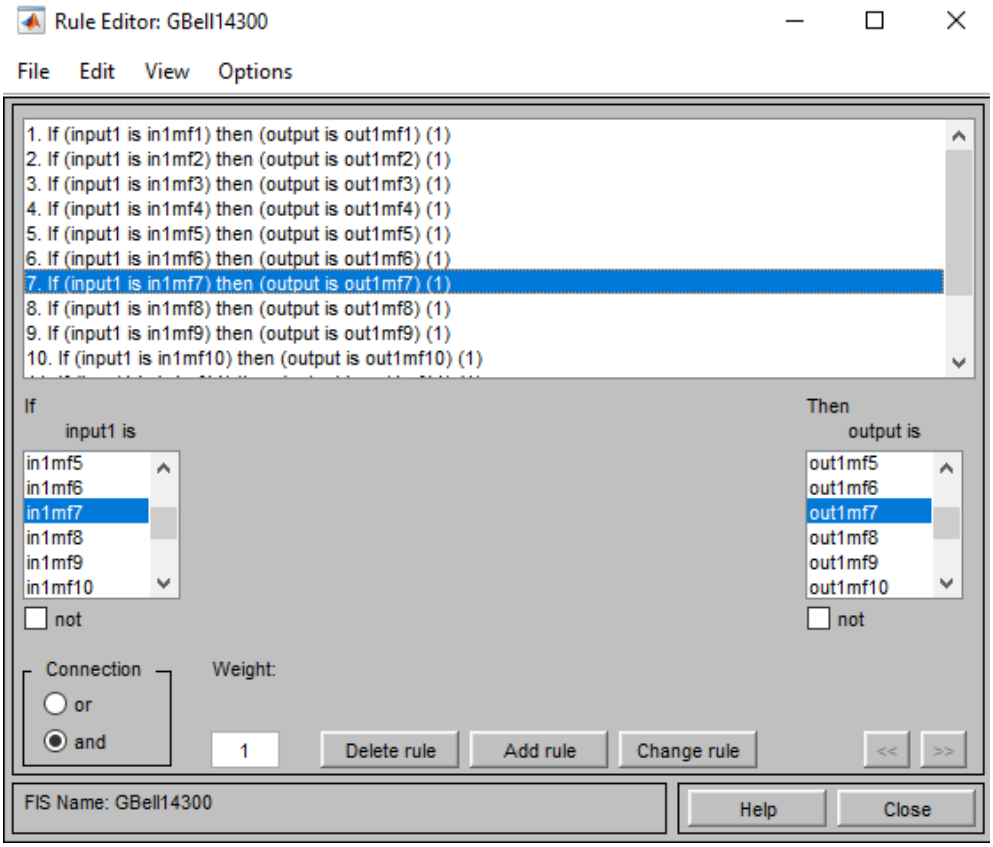


Figure 98. Fuzzy inference verbose rule viewer

Rule editor is presented in figure 98 in verbose format. All of the connections are based on the ‘and’ method with unit identical weight.

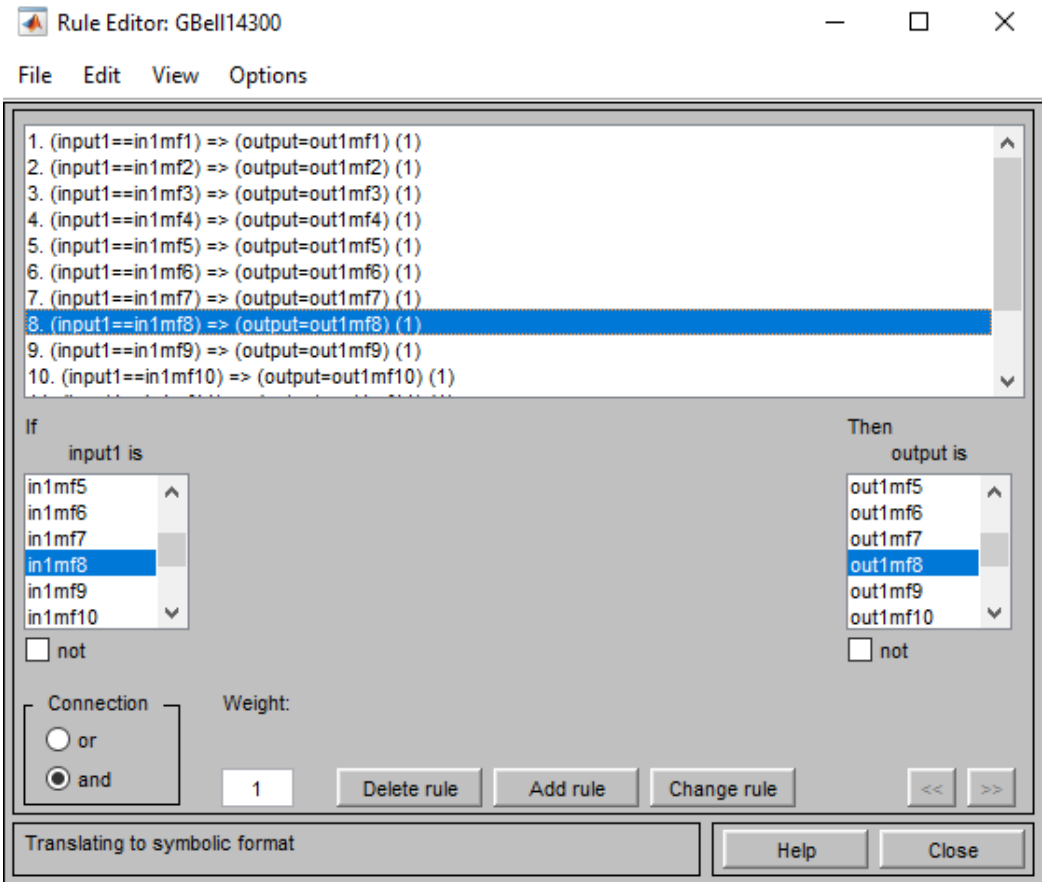


Figure 99. Fuzzy inference symbolic rule viewer

Fuzzy rules in symbolic format are shown in figure 99. Another feature of the rule editor is enabling the designer to alter the rules as desired. Designer can delete as specific rule, add rule(s), or even change an existing rule per desired.

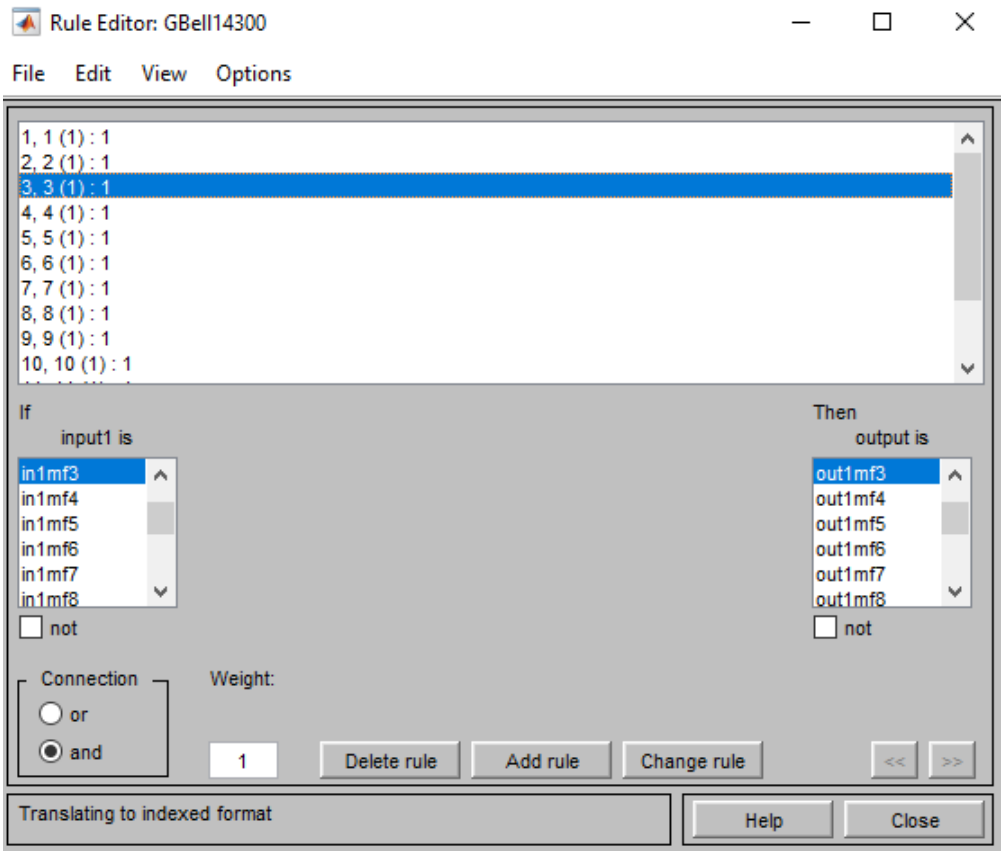


Figure 100. Fuzzy inference indexed rule viewer

Fuzzy rules for the adaptive PVEH with constant spring stiffness ration and varying oscillator mass are shown here. The format is indexed. Rule editor enables one to easily infer the relationship between the input(s) and the corresponding rule. In a SISO fuzzy system, such inference is straightforward.

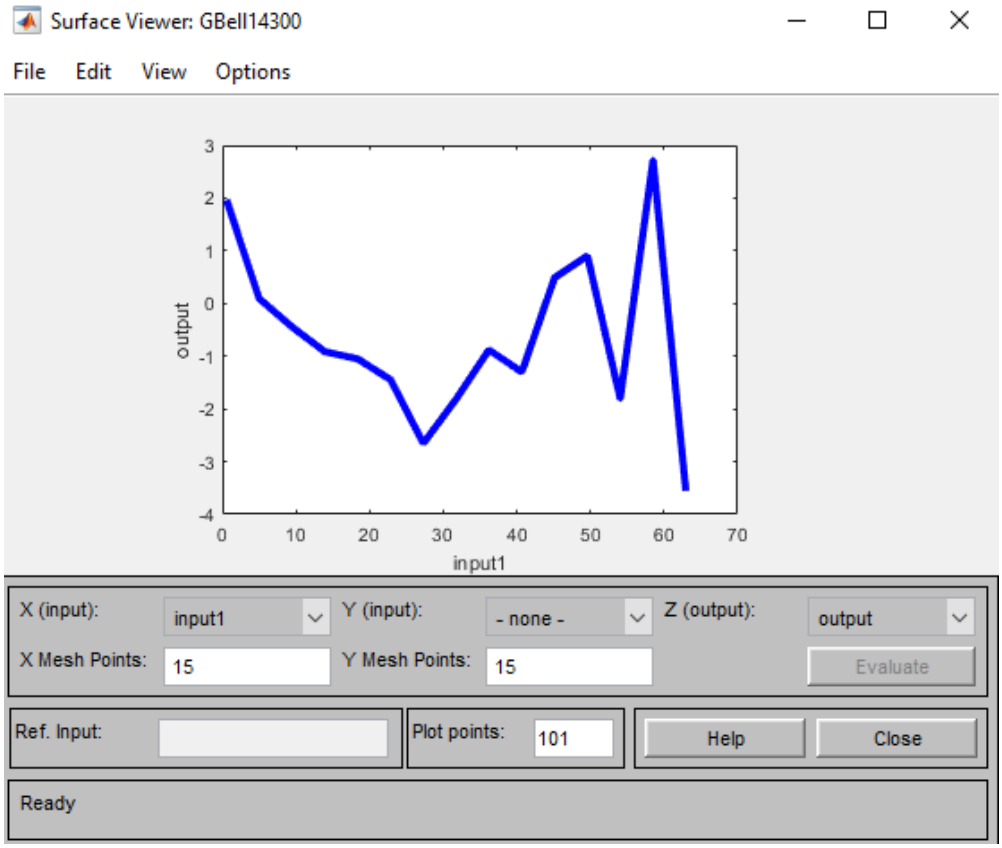


Figure 101. Fuzzy inference surface viewer

Finally, the rules surface viewer is shown here. Since there is a single input to the system, the rules surface viewer is a two-dimensional (2-D) plot demonstrating the relationship between the input and the resulting output.

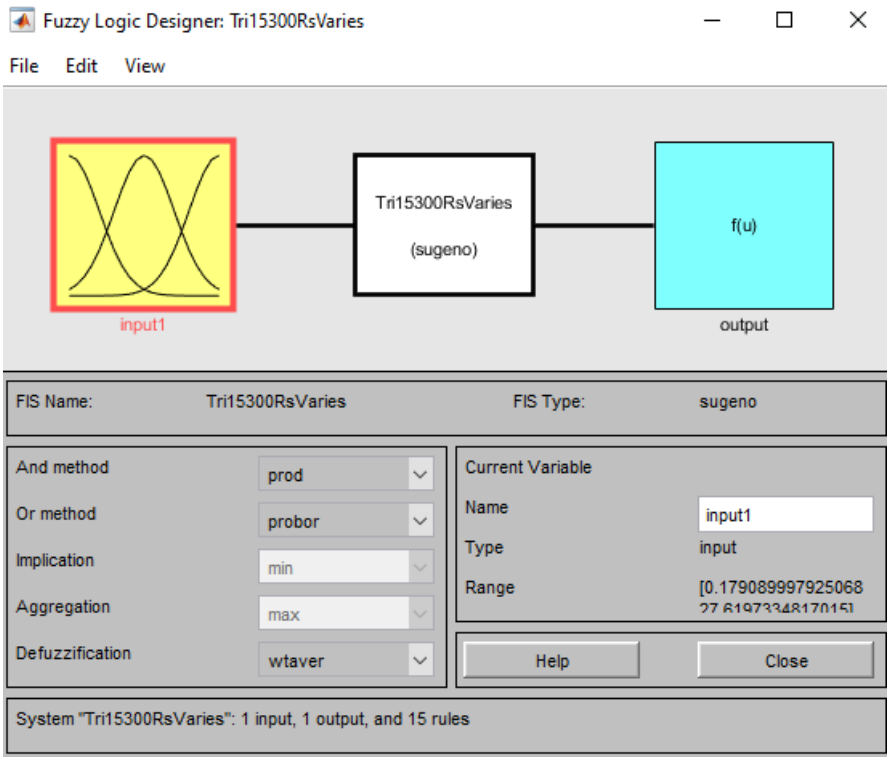


Figure 102. Fuzzy logic designer application setting

As for the fuzzy inference system of the adaptive PVEH with constant oscillator mass and varying stiffness spring; the fuzzy logic toolbox window is depicted here. The same adjustments are applied automatically here as well as in the former case study.

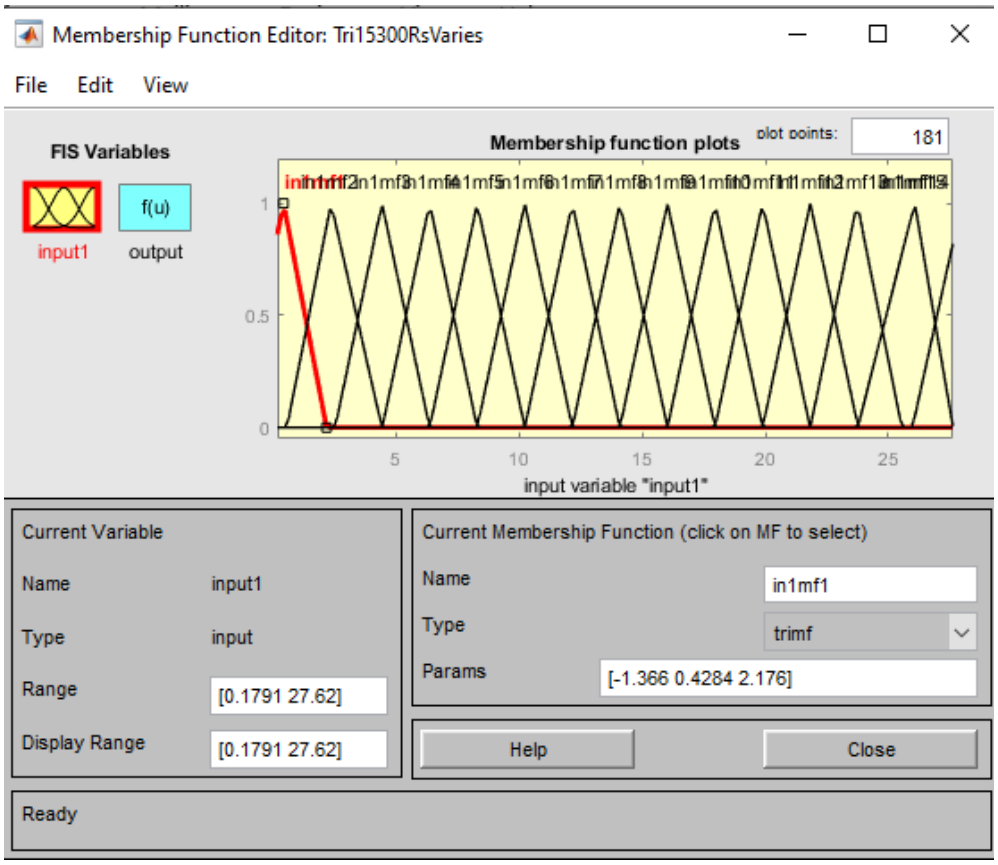


Figure 103. Fuzzy logic membership function editor

Triangular membership functions with linear curves and 15 numbers of functions are shown in this figure. The functions are distributed from 0.1791 to 27.62.

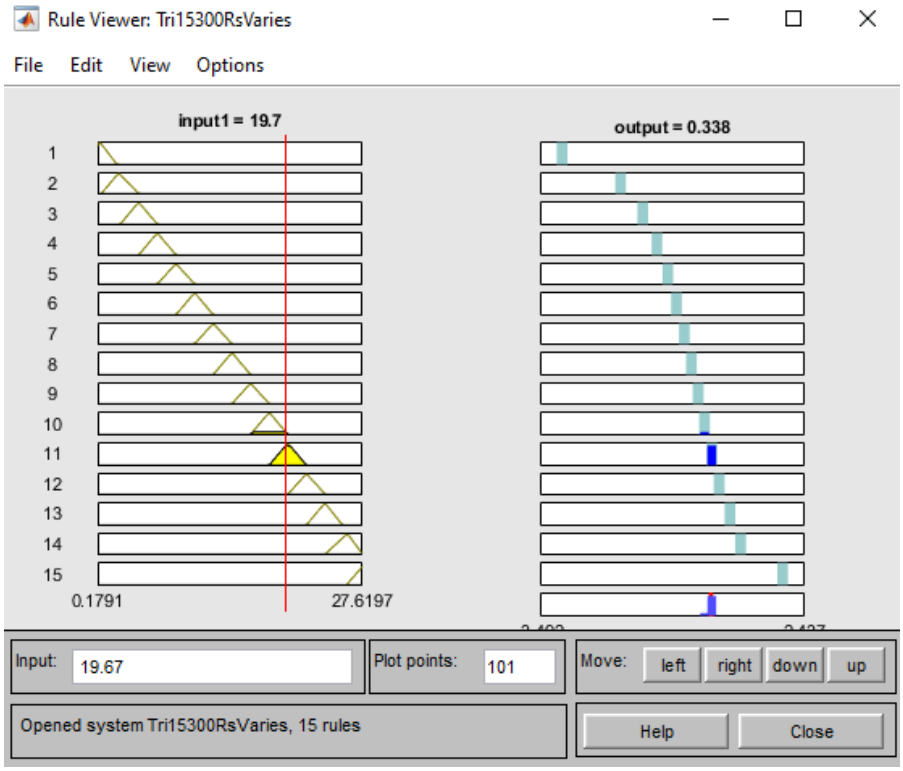


Figure 104. Fuzzy logic rule viewer

Fifteen triangular membership functions yield 15 fuzzy rules which is because of the single number of inputs, otherwise number of the fuzzy rules is more than the number of fuzzy membership functions. Such fuzzy rules are shown in the rule viewer in figure 104.

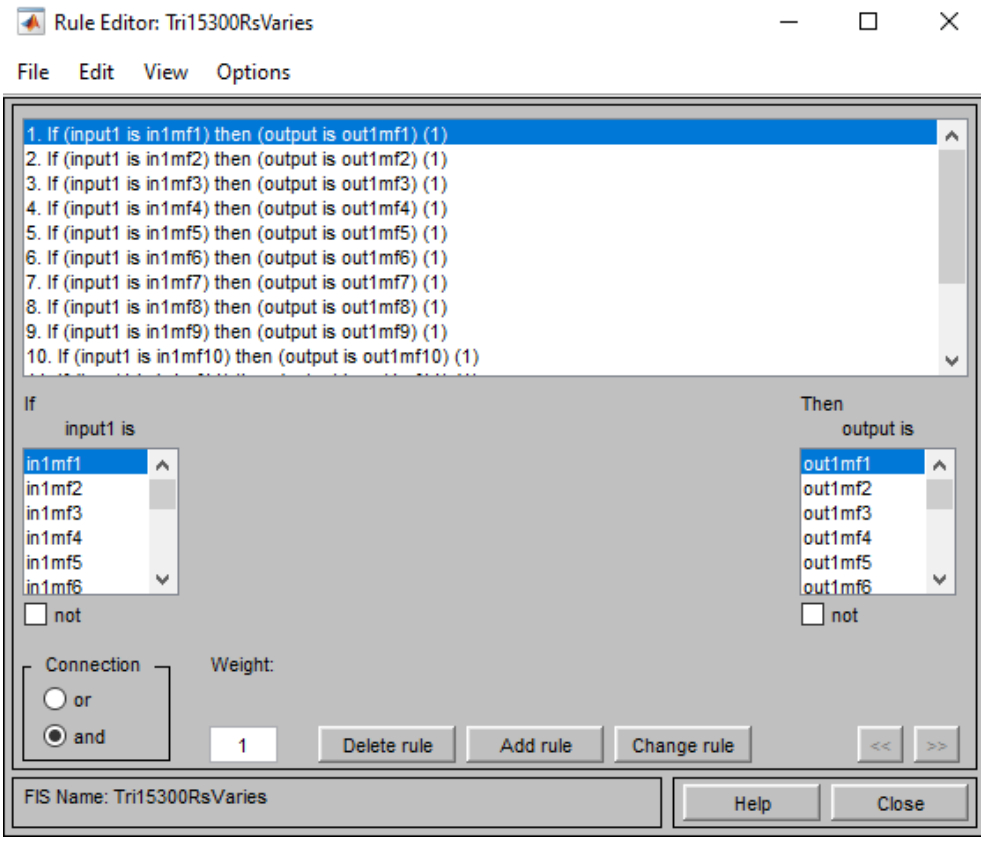


Figure 105. Fuzzy inference verbose rule editor

The mentioned fuzzy rules in verbose format are shown in figure 105. The connection type between the inputs and outputs are based on the ‘and’ method with identical unit weight.

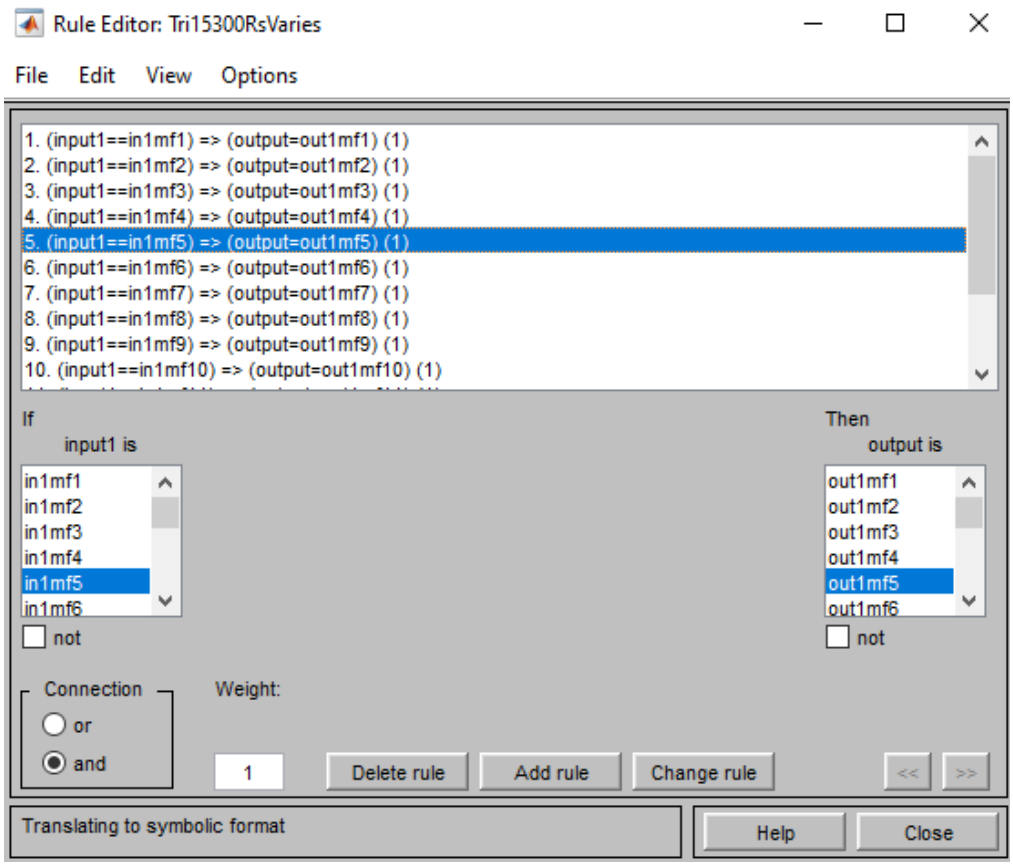


Figure 106. Fuzzy inference symbolic rule editor

The abovementioned fuzzy rules in symbolic format are illustrated in figure 106. The connection between the input and the resulting output is accessible to the rule viewer.

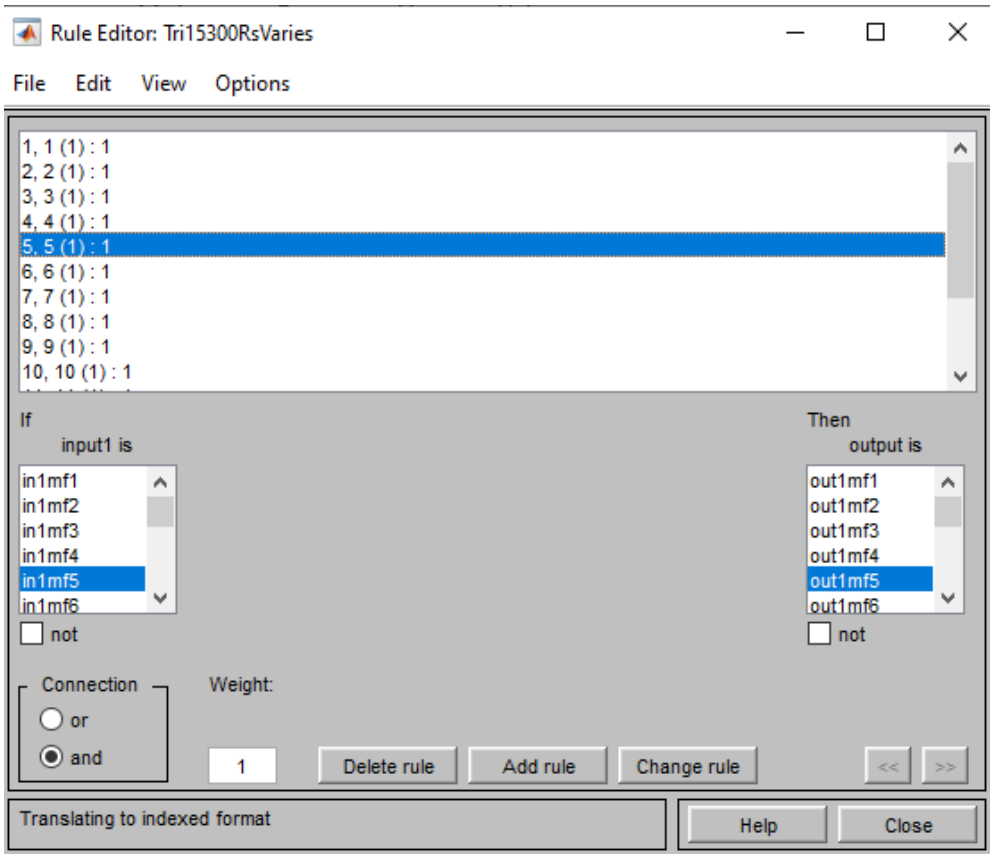


Figure 107. Fuzzy inference indexed rule editor

Eventually, the indexed format of the mentioned fuzzy rules is shown in figure 107. Based on the intuition of the designer, specific rule(s) can be deleted, added or changed in via the rule editor. However, such a mutation requires a high level of insight of the fuzzy inference system along with features of the dataset available.

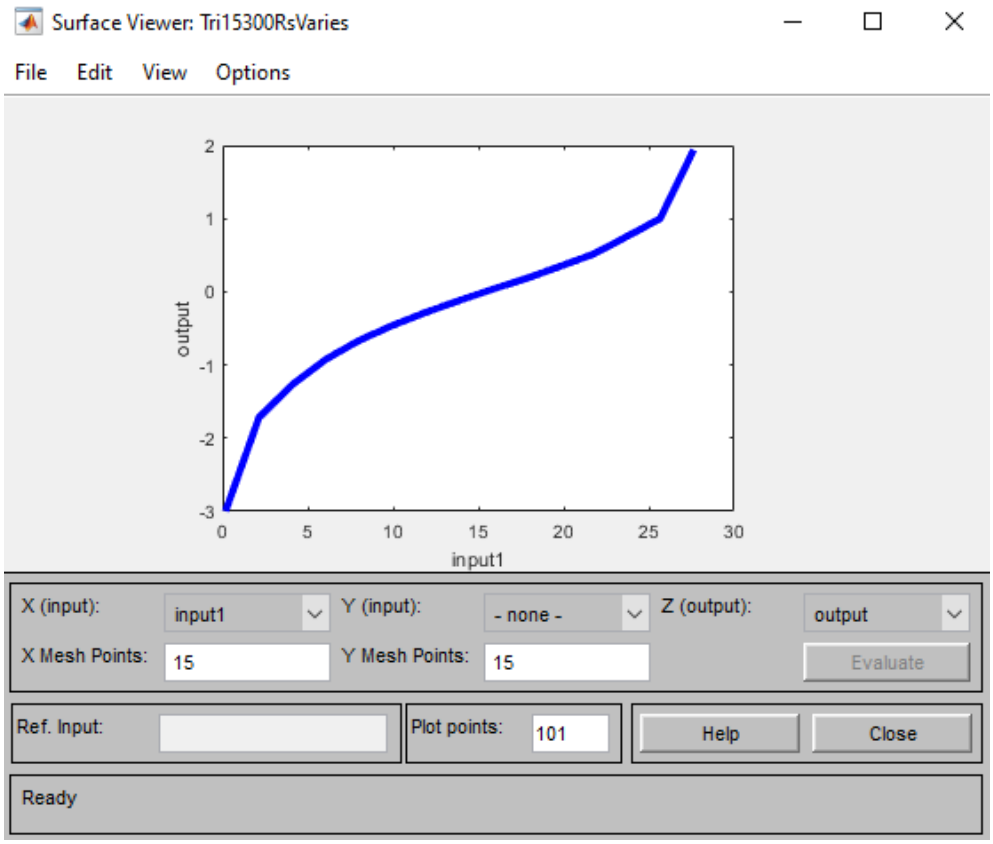


Figure 108. Fuzzy inference surface viewer

The surface viewer image is represented here to show the 2-D illustration of the triangular fuzzy rules designated to predict the spring stiffness as the output of the system.

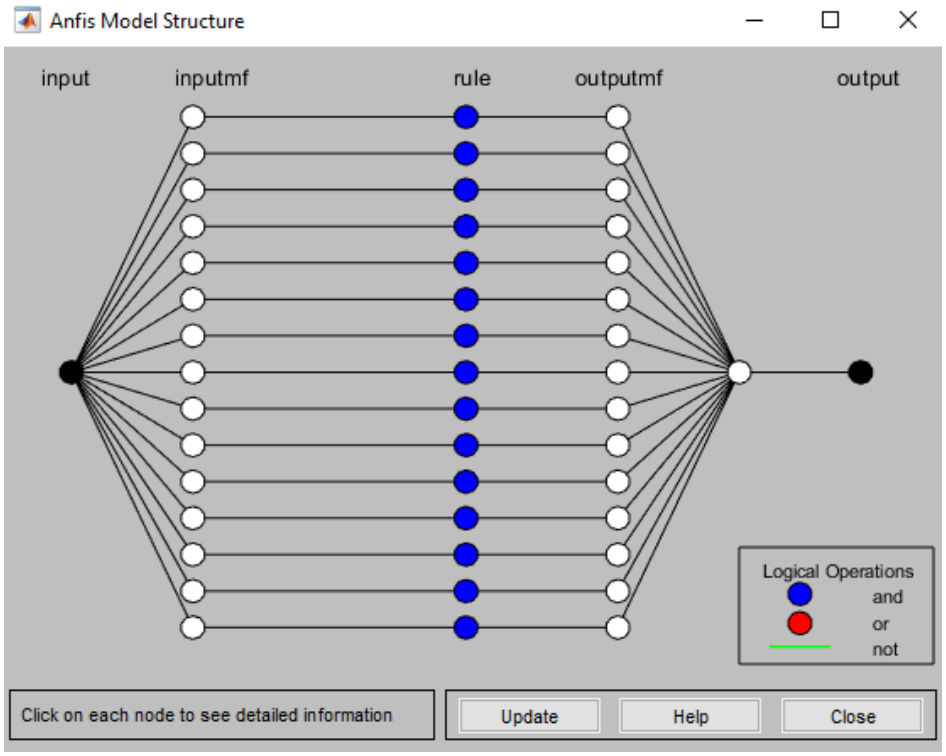


Figure 109. ANFIS model structure

This figure shows the general layout of the created fuzzy inference system using the ANFIS toolbox in ATLAB. All 5 layers are shown. The first layer specifies the number of the input entities. Such entities describe the system's degrees of freedom. In this case study only one input is allotted (oscillator mass or spring stiffness). Corresponding degree of membership to the specified input is determined using the membership functions which has been studied in detail. In this step which is known as the fuzzification layer, the premise (antecedence) set is formed. Strength fuzzy rule sets are generated in the rule layer. Such firing strength is normalized in the third layer. In the fourth layer, the normalized firing strength is taken, and the consequence set is created. Such values are de-fuzzified and inserted into the last layer. Eventually, in the last step, the inserted values are aggregated, and the final single output value is determined.

After designing the fuzzy inference systems (FISs), it is practical to adapt and adjust the PVEH with respect to the desired characteristics available in the background. One important note pertains to the high resonance frequency of piezoelectric vibration-based energy harvesters. As mentioned in the above section, it particularly highlights the issue when the size of the energy harvester is scaled down. This means that small-size PVEH systems have high resonance frequency which is mostly unapproachable by the excitation (driving) frequency. Specifically, in such cases, it is imperative to either supply the high frequency or to adapt the internal features of the energy harvester system by manipulating the vibrational factors. Accordingly, following case study is provided:

Adapting the PVEH to an external source with excitation frequency of $f_e = 5\ Hz$

Two fuzzy inference systems are designed which can estimate the proper value of the oscillator mass or the spring constant to yield the resonance frequency as close as possible to the given excitation frequency.

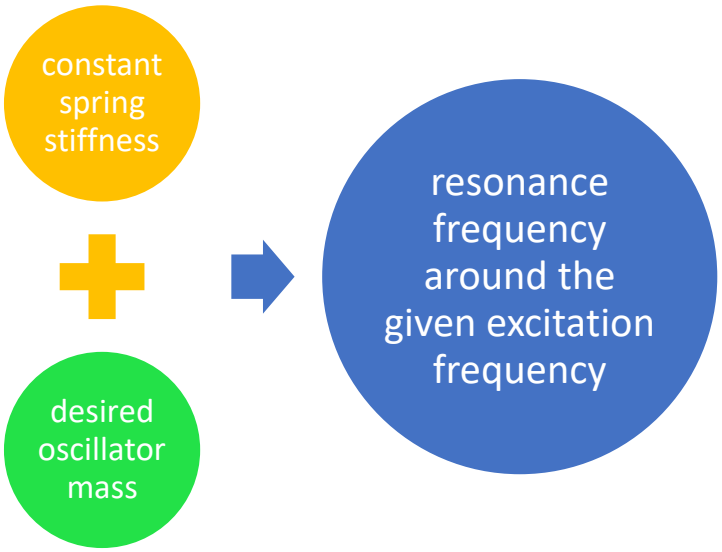


Figure 110. Schematic of constant spring stiffness and varying oscillator mass

This figure visually conveys the process of which, the oscillator mass is to be adapted and the spring stiffness is kept constant ($r_s = 0.1$). The outcome is supposed to yield resonance frequency to a value close to the driving frequency which is already available in the background.

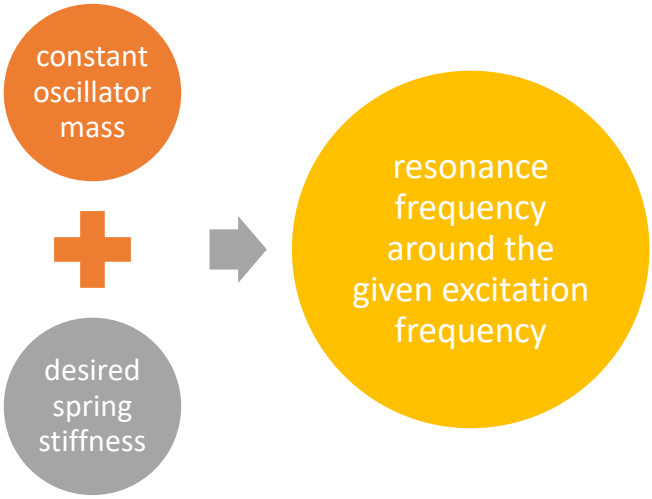


Figure 111. Schematic of constant oscillator mass and spring stiffness

This figure shows the other adaptation in which the spring stiffness is supposed to be adjusted to yield the resonance frequency around the given driving frequency. In this case obviously the oscillator mass is considered to be constant and same weight as the cantilever ($r_m = 1$).

Table 44. Desired excitation (driving) frequency and corresponding design parameters

| FIS | $f_e$ | $r_m$ | $r_s$ |
|---|---|---|---|
| Generalized-Bell shaped | 5 $Hz$ | 1.24571875 | 0.1 |
| Triangular | 5 $Hz$ | 1 | 0.0802915 |

Running the generated fuzzy inference systems (FISs) with the given excitation frequency, the desired value for the oscillator mass is 1.2457 times the cantilever mass if the spring stiffness is constant and 0.1 times the flexural rigidity (bending stiffness) of the cantilever. If the oscillator mass is kept constant and identical to the mass of the cantilever, the desired stiffness of the spring should be 0.08029 times the flexural rigidity of the cantilever. Applying either of such cases is expected to yield the PVEH with the fundamental resonance frequency close to the driving frequency. To verify and evaluate soundness of the artificial intelligence-based fuzzy inference procedure used, the desired oscillator mass and spring constant values are to be employed in the analytical-numerical closed-form solution which is derived in the preceding chapters:

$$r_s r_m(\lambda_n L)(sinh(\lambda_n L)\, cos(\lambda_n L) - cosh(\lambda_n L)\, sin(\lambda_n L)) - (r_s - r_m(\lambda_n L)^4)(1 + cos(\lambda_n\, L)\, cosh(\lambda_n\, L)) = 0 \tag{6.1}$$

To find the roots of the nonlinear transcendental equation, a plot of the equation with the given mass ratio and stiffness ratio values is needed.

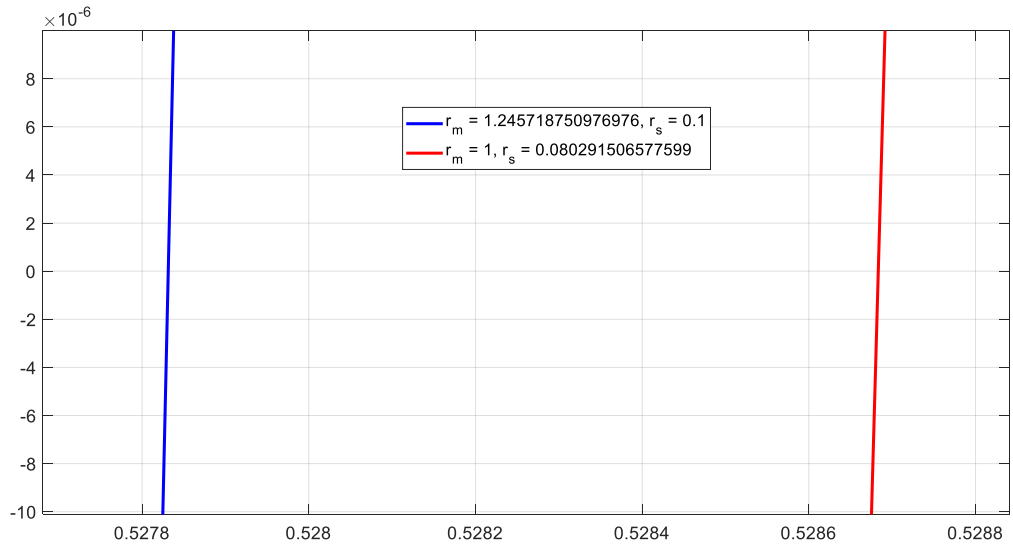


Figure 112. First eigenvalue around the desired frequencies

According to the plot, the first root for the first case is: 0.5278, and the eigenvalue of the second case is: 0.5287.

Table 45. Eigenvalues solved numerically via VPASOLVE

| $(r_m, r_s)$ | Initial guess for the roots | Roots solved by VPASOLVE method |
|---|---|---|
| (1.245718750976976,0.1) | 0.5278 | 0.5279142476403003291724787770084 5 |
| (1, 0.080291506577599) | 0.5287 | 0.5287888216930933924222612088894 5 |

Providing the initial guesses viewed in the plot section into the VPASOLVE algorithm, the roots (eigenvalues) of the system using the numerically solved method are reported in the above table. Using such eigenvalues, the resonance frequency of the cantilever-oscillator-spring piezoelectric vibration-based energy harvester (PVEH) is obtainable:

Table 46. Angular and linear frequencies found via closed-form expression

| $(r_m, r_s)$ | Hyperbolic coefficient | $\omega_1\ (rad/sec)$ | $f_1\ (Hz)$ |
|---|---|---|---|
| (1.24571875,0.1) | 1.8991483 | 31.3606607 | 4.99120417 |
| (1, 0.0802915) | 1.89603977 | 31.4646547 | 5.0077553 |

Obviously, the desired oscillator mass and the desired spring stiffness values found by the fuzzy inference system yield the resonance frequency of the system almost 5 Hz. In other words, after finding the desired mass and stiffness ratios by means of the fuzzy regressor, the analytical closed-form solution was used to assess the verification and soundness of the trained fuzzy estimator (approximator). Inserting the desired oscillator mass value yields in system resonance at: 4.991204174782064; and employing the desired spring stiffness value results in system resonance at: 5.007755322962248. Both cases show great accuracy as the first one has an error of around 0.155% and the second one has an error of around 0.176%. Finally, the voltage frequency response function (FRF) is plotted for the adaptive systems. The voltage FRF is analytically derived in the preceding chapters.

$$v(t) = \frac{\sum_{n=1}^{\infty} \frac{-j\Theta_n(\rho A\gamma_n + m_o{\gamma_n}^o){\omega_e}^3 Y_0}{B_n({\omega_n}^2 - {\omega_e}^2 + j2\zeta_n\omega_n\omega_e)}}{\frac{1}{\tau_c} + j\omega_e + \sum_{n=1}^{\infty} \frac{j\Theta_n\chi_n\omega_e}{B_n({\omega_n}^2 - {\omega_e}^2 + j2\zeta_n\omega_n\omega_e)}} e^{j\omega_e t} \tag{6.2}$$

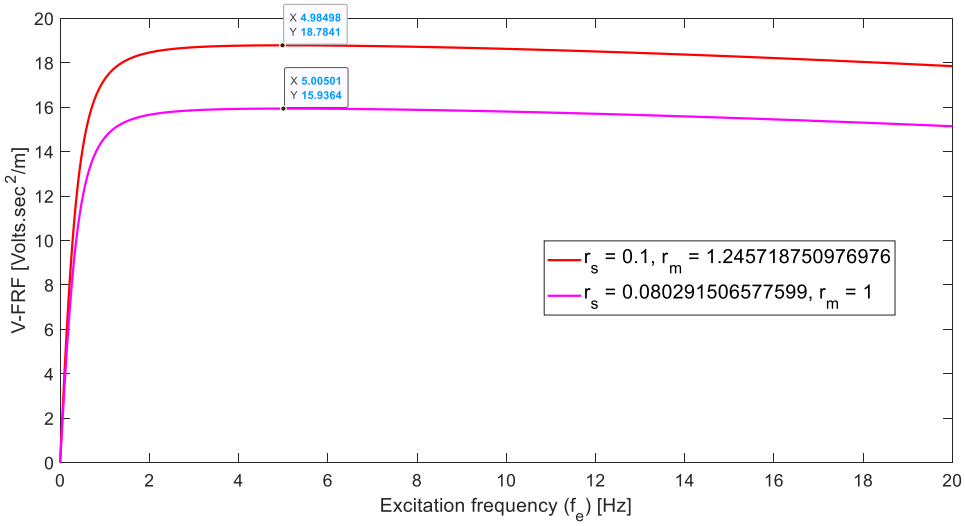


Figure 113. Voltage frequency Response function (FRF)

In the above figure, the voltage frequency response function is plotted with respect to the excitation frequency. It is evident the resonance frequencies of both case studies (varying oscillator mass and constant spring stiffness; varying spring stiffness and constant oscillator mass) match to the given driving (excitation) frequency. Expectedly, the maximum value of the voltage takes place at the resonance frequency of the systems ($f_e = 4.992, 5.008\ Hz$). In such adaptive PVEHs, neural network fuzzy inference is capable of finding proper oscillator mass and/or spring stiffness to fit the resonance frequency of the system to the driving frequency available in the background. One of the vital points refers to the fact that since there are two design parameters in the system, two potential solutions can be found per each case study. Another finding refers to the gradation and mutation of the parameters. In details, with $r_m = 1$, corresponding stiffness ratio is 0.080291506577599. While if a stiffer spring is adopted, heavier oscillator mass is required to meet the desired situation. So, both parameters exhibit complementary mutation. If one of the parameters is increased the other one also needs to be reinforced.

## 6.4 Conclusion

In this chapter, the major focus is to devise adaptive piezoelectric vibration-based energy harvesters (PVEHs) so that the harvester is adjustable to the available sources of excitation. Such an adaptive system is crucially important particularly in practical applications as the excitation resource is not adjustable. The mismatch between the excitation (driving) frequency and the resonance frequency of the harvester system leads to an insignificant amount of harvested electric power. To remedy such an issue, adjustable PVEHs are of crucial importance. Particularly, in the proposed model of PVEHs, there are two design parameters (the oscillator mass and the spring stiffness). Adopting various values of each parameter leads to different voltage FRF and the harvester's performance. In the adaptive case study, it is assumed the harvester is supposed to be tuned so that the resonance frequency of the system reaches the specific value of the excitation (driving) frequency. This is an inverse engineering problem in nature. Employing neural network fuzzy inference system, a decent regressor model is trained to estimate the desired values of the oscillator mass and/or the spring stiffness. In this response, eight types of built-in membership functions (MFs) along with different numbers of each function were tested. Finally, 14 Generalized-Bell shaped and 15 triangular functions were employed to train the function approximator. It is assumed the PVEH is excited with a driving frequency of $f_e = 5Hz$. Using the designed fuzzy regressor, desired values of the design parameters are found as: $(r_m, r_s) = (1, 0.0802915)$ or $(r_m, r_s) = (1.24571875, 0.1)$. At the end, to validate and verify authenticity of the designed neural network fuzzy inference system, the voltage frequency response function (FRF) derived analytically-numerically is utilized.

The desired values of the design parameters are inserted into the mentioned voltage function and the final result is plotted. Findings reveal the correctness and competency of the designed adaptive PVEH as the maximum amount of the extractable voltage occurs around the given driving frequency. Such adaptive PVEHs can be highly applicable in industrial sectors to generate significant amount of electric energy as an alternative power source.

# CHAPTER 7. EXPERIMENTAL SETUP

## 7.1 Preliminaries of Statistical Data Visualization

In the preceding chapters, analytical-numerical analysis of the novel proposed model of the piezoelectric vibration-based energy harvester (PVEH) is accomplished. Furthermore, neural network fuzzy inference system is developed to approximate the harvestable voltage frequency response function. Finally, to optimize the proposed model, soft computing algorithms including: neural networks, fuzzy logic, and genetic optimization are employed to find the optimal values of the oscillator mass and spring stiffness constant. In this chapter, experimental setup is implemented to observe and record the electric voltage values capturable from the PVEH. The main difference between the former chapters and the current one pertains to the type of input excitation. In the former chapters, harmonic base excitation is considered as the input. However, in this experimental section the PVEH system is triggered by impact-driven excitations. Such impact-driven excitation is a random (stochastic) process in nature and there is no measurable factor. The reason for adopting different types of input is to assess the superiority of the proposed model, a standard criterion should be used. It means, to evaluate and verify a harvester system's performance, harmonic base excitation is mostly chosen as an accepted standard scale. After validating the proposed model, it is considered to record a simple PVEH (including a pure cantilever) response with respect to a type of excitation which most often takes place in the real world. Realistically, such an input is mostly a random process. For example, the piezoelectric energy harvesters mounted in subway or in airport hall; are subject to human foot stepping. Such a stochastic motion occurs with no controlled inputs. Thus, to cover such realistic triggers, impact-driven

excitations is considered in this chapter. In this chapter, experimental setup implementation is done. Data logging and data visualization is another important task.

## 7.2 Exploratory data analysis

Data visualization is the very first step to analyze and interpret the dataset. So, in this section data is rendered in an explanatory format to explore it through statistical plotting with interactive graphics and descriptive statistics. As mentioned in the above section, the excitation type in this section is random impact-driven trigger. It is well-established that any random process initiated with random inputs (excitations) results in random output. To visualize the data, a well-clear definition of the response and predictor variables need to be expressed. For such a random process, the harvested electric voltage is considered as the response variable and the iteration number is considered the response or independent variable. To visualize such a 2-D (two dimensional) dataset, scatter plot, bivariate histograms and boxplots are usually the most common plots utilized. Since the 2-D dataset is a single-variable distribution, univariate plots suffice perfectly.

Figure 114. Experimental setup of the piezoelectric energy harvester

The above figure is a snapshot of the experimental setup. Major components include substrate, piezoelectric patch, clamp, multi-meter with data logging capabilities, smart device or laptop, hammer, multi-meter test leads and alligator clips. Each excitation is triggered by means of the hammer impact. The multi-meter is set for 10 seconds of time interval capturing the maximum amount of the generated voltage. This procedure is repeated 100 times.

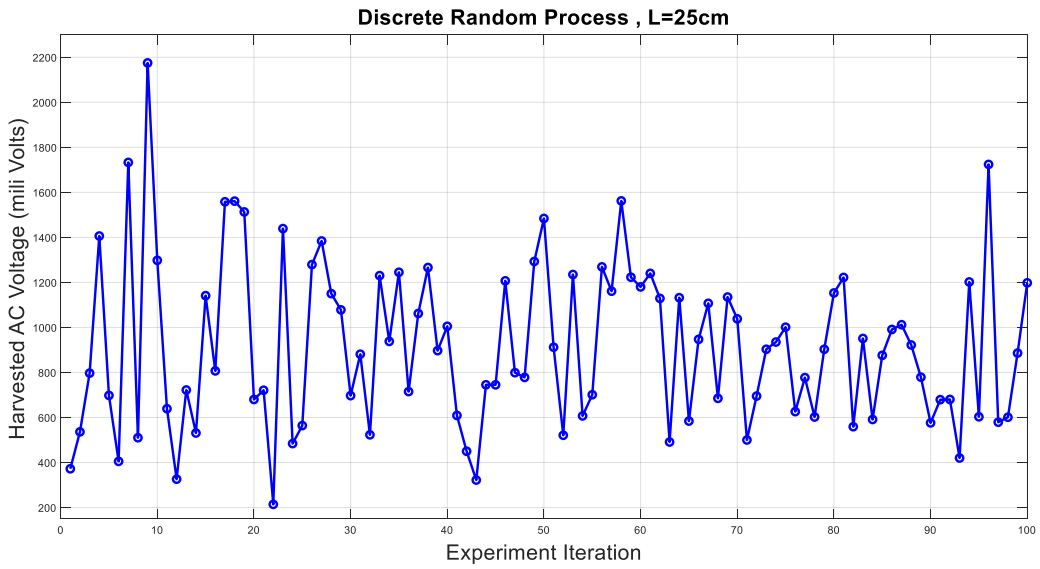


Figure 115. Harvested AC voltage with respect to the experiment iteration

In the above figure, collected dataset from the experimentation is plotted. The maximum value of captured voltage with respect to the iteration number is shown on the figure. However, such a presentation of dataset is rarely used, the plot shows data distribution perfectly.

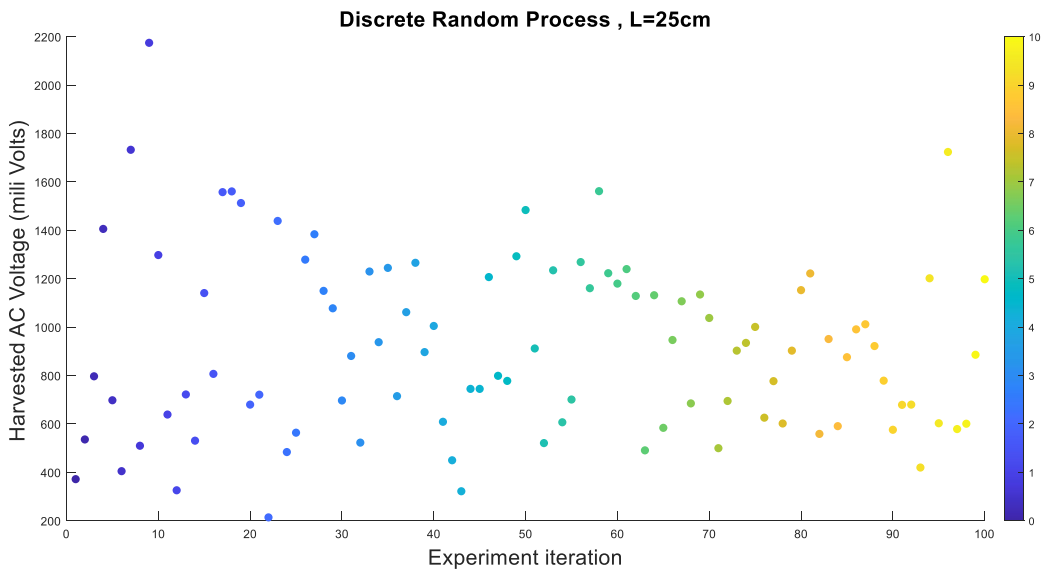


Figure 116. Scatter plot of impact-driven excitation

Another way to demonstrate and represent the dataset is to use the scatter plots. In this figure, the maximum amount of harvested alternating current voltage from the impact-driven excitation of the energy harvester is shown in a scatter plot fashion. Data distribution implies randomness of the dataset which is expected due to the nature of inputs. Such a scatter plot is provided to reveal the relationship between the two variables (the iteration number of the experiment and the maximum amount of the harvested voltage). It is observed that the maximum amount of the alternating current (AC) voltage recorded (logged) is captured per experiment iteration. The iteration is accomplished 100 times. The provided scatter plot discloses the fact that there are no trends detectable in the plot between the predictive and the response variables. This is an endorsement of the randomness of the impact-driven excitations using the hammer.

Another visualizing method is to use the boxplot. Boxplot reveals the summary of the statistics in the correlational coupling between the two variables.

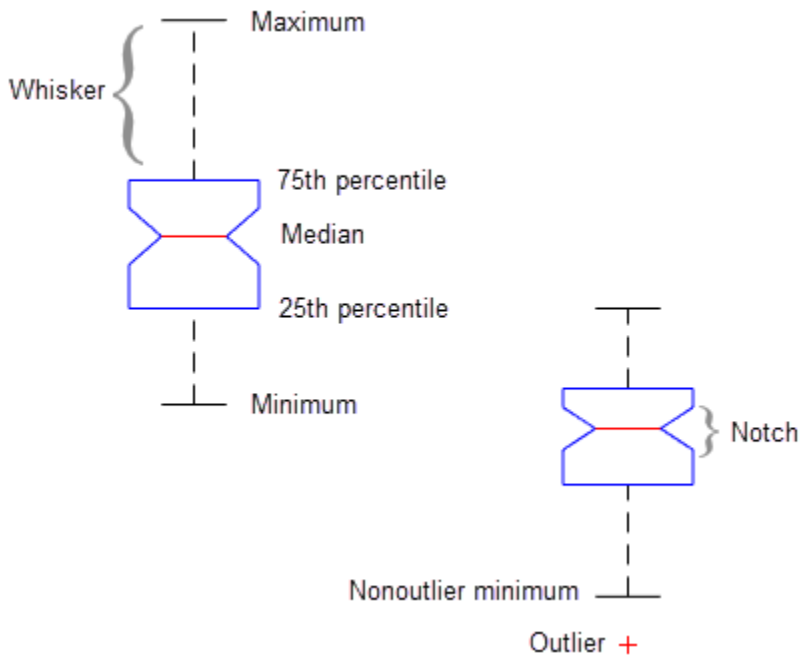


Figure 117. Box plot features

In this figure, the whisker is utilized to demonstrate the variability of the outside of the upper and lower quartiles. Form a box plot following information is derivable:

- The bottom and top of each box are the 25th and 75th percentiles of the sample, respectively. The distance between the bottom and top of each box is the interquartile range.
- The red line in the middle of each box is the sample median. If the median is not centered in the box, the plot shows sample skewness.
- The whiskers are lines extending above and below each box. Whiskers go from the end of the interquartile range to the furthest observation within the whisker length (the adjacent value).

- Observations beyond the whisker length are marked as outliers. By default, an outlier is a value that is more than 1.5 times the interquartile range away from the bottom or top of the box. However, you can adjust this value by using additional input arguments. An outlier appears as a red + sign.
- Notches display the variability of the median between samples. The width of a notch is computed so that boxes whose notches do not overlap have different medians at the 5% significance level. The significance level is based on a normal distribution assumption, but comparisons of medians are reasonably robust for other distributions. Comparing box plot medians is like a visual hypothesis test, analogous to the *t* test used for means.

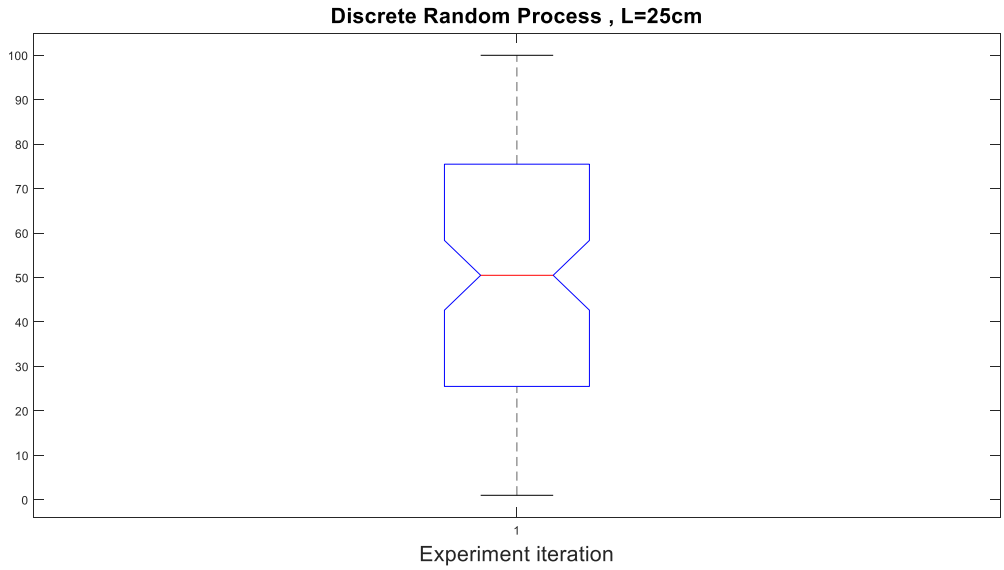


Figure 118. Box plot for the experiment iteration

The above figure shows the box plot for the number of iterations in the dataset shown on the horizontal axis of the scatter plot. Since the iteration number is merely the

numbers of experimentation test number, the box plot is a well-centered plot. It means that the minimum value is 2, the maximum value is 100, 25$^{th}$ percentile is aligned on the 25$^{th}$ iteration, 75$^{th}$ percentile shows the 75$^{th}$ number the test is run, and median is 50 which is indeed the median number between 1 to 100.

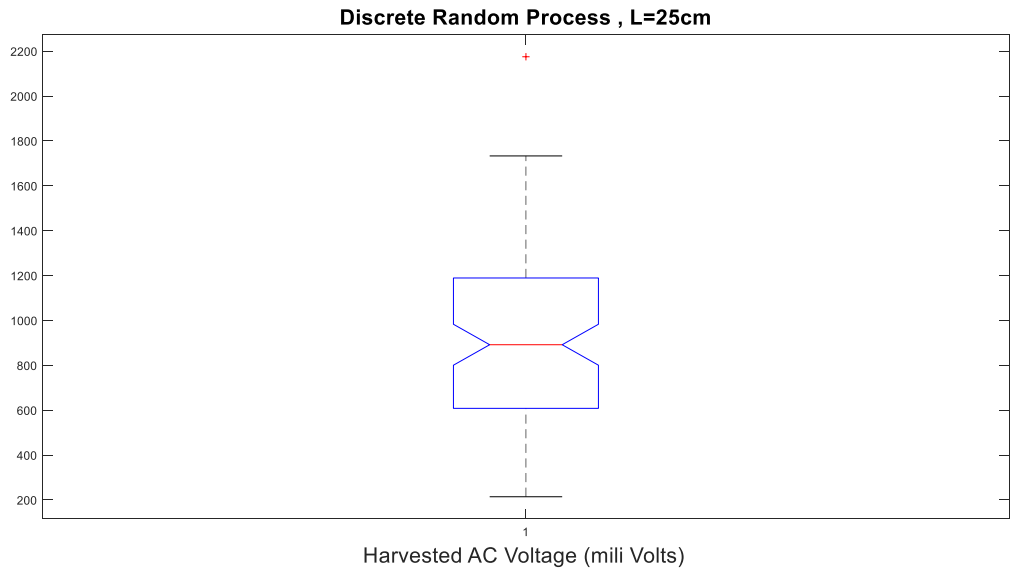


Figure 119. Box plot for the harvested voltage

Box plot for the harvested AC Voltage is expectedly not well-centered and represents distribution of random dataset. Besides to the minimum and maximum values, an outlier is also detected at the top. Detailed information in this regard is shown and stated in the following figure.

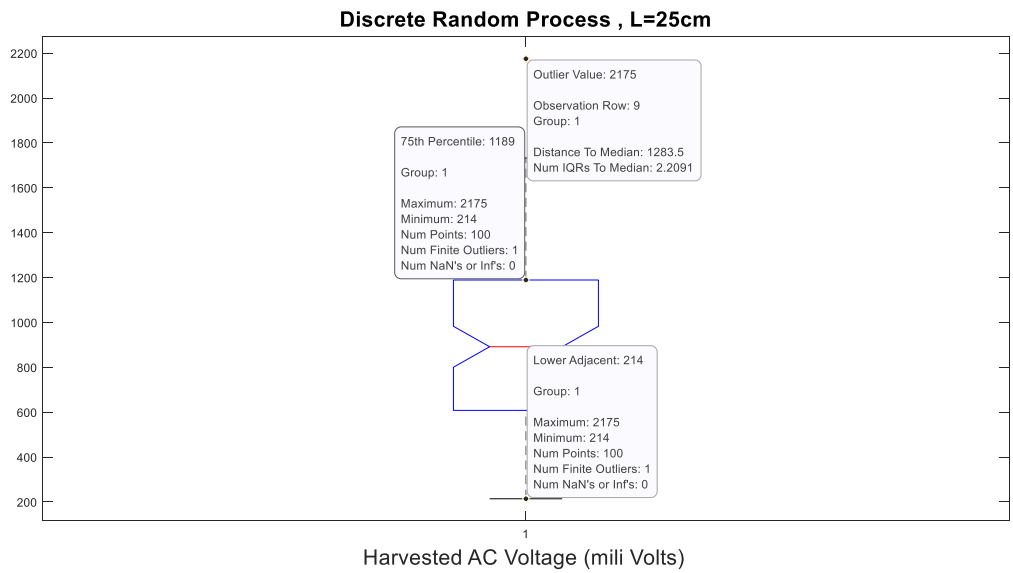


Figure 120. Box plot highlights

Table 47. Box plot summary of information

| | |
|---|---|
| Number of points/observations | 100 |
| Minimum value | 214 mV |
| Maximum value | 2175 mV |
| Lower adjacent | 214 mV |
| $25^{th}$ percentile | 608 mV |
| Low notch | 800.283 mV |
| median | 891.5 mV |
| High notch | 982.717 mV |
| $75^{th}$ percentile | 1198 mV |
| Upper adjacent | 1733 mV |
| Outlier value | 2175 mV |
| Distance to median of the outlier value | 1283.5 |
| Number of IQRs to median | 2.2091 |
| Mean (average) | 916.17 mV |
| Median (middle) | 891.5 mV |
| Skewness | 0.5981 |
| Kurtosis | 3.2438 |
| Interquartile range | 590 |
| Observation row | 9 |
| Standard deviation | 365.0446 |
| Variance | $1.3326 \times 10^6$ |

Figure 120 is duplicated for the maximum alternating current (AC) voltage values captured on the multi-meter with data cursor information. Such data is summarized in Table 50.

It is noteworthy the outlier value detection in MATLAB is by default 1.5 interquartile ranges (IQRs) below the first quartile or above the third quartile. According to the table, the mean value is bigger than the median value. Such a dataset is right skewed. This finding is approved because of the positive value of the skewness. Besides, the kurtosis value is bigger than 3 meaning that the voltage dataset has a larger peak than a normal distribution.

After the scatter plot and the box plot, the histogram is another graph which is highly useful in showing the data distribution. Histogram or bar graph reveals the major features of data.

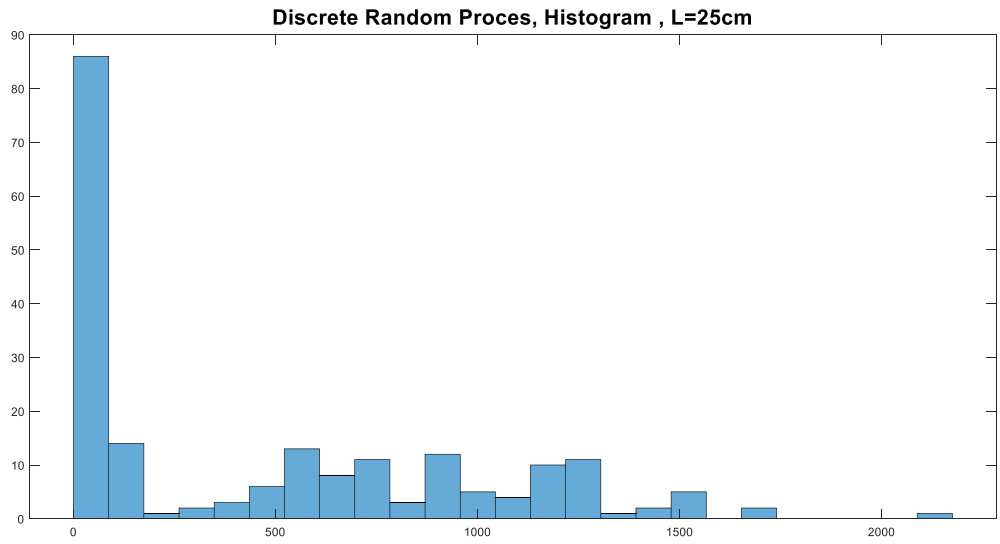


Figure 121. Histogram of the impact-driven experiment dataset

Based on the figure, the voltage values are not normally distributed, which is an expected trait for a random process. There is also a useful scatter plot with marginal histograms.

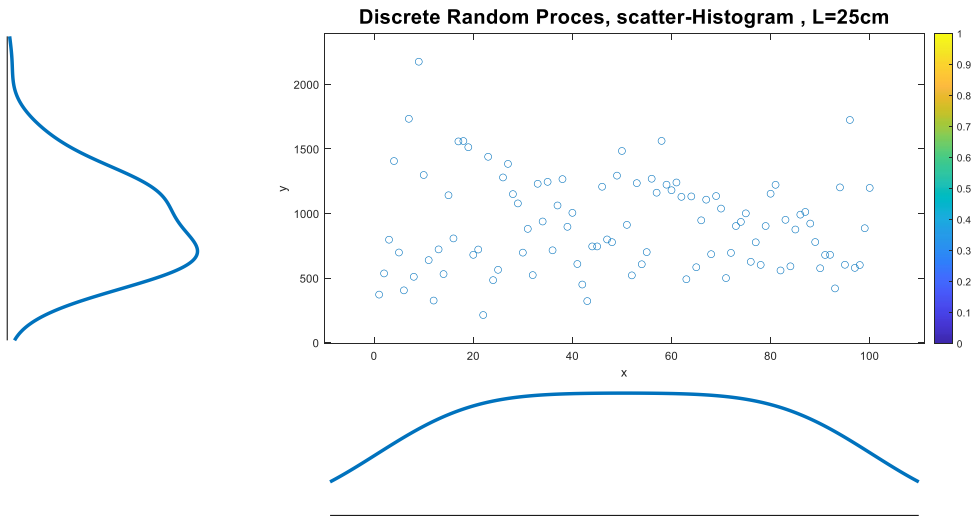


Figure 122. Scatter-Histogram of the impact-driven experiment dataset

Figure 122 embeds the scatter plot and the histogram plot in a single snap. Findings confirm those found from the above figures; x-axis shows a normal distribution as it pertains to the iteration number. Y-axis (vertical) displays data distribution of a random process. The data shows a right-shifted skewness meaning that population of the data is concentrated between 500 and 1300.

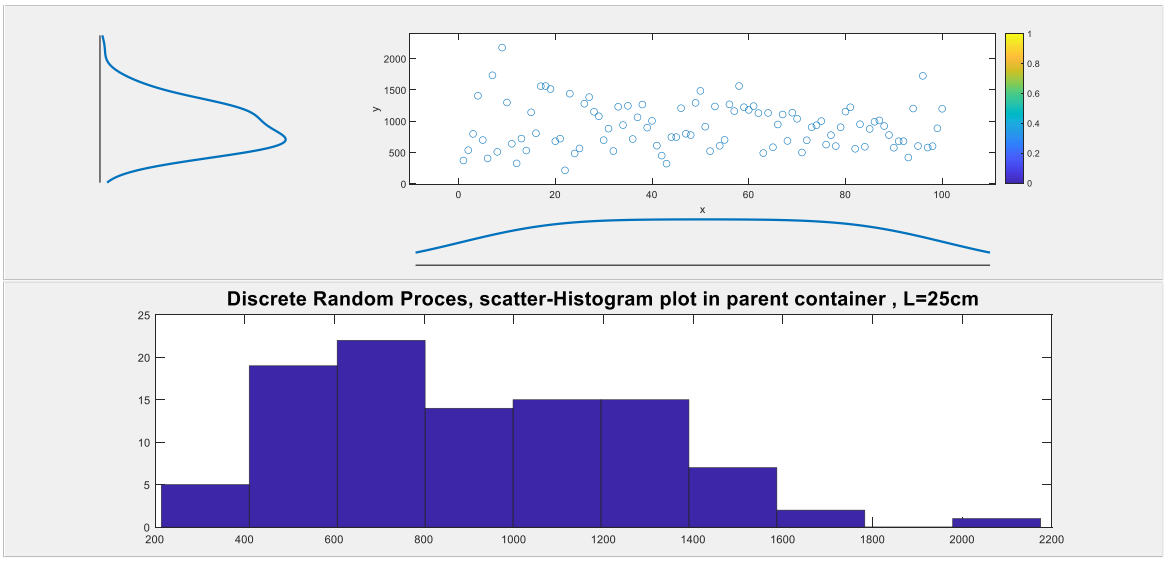


Figure 123. Scatter-Histogram of the impact-driven experiment dataset in parent container

Same figure is duplicated here including the bar graphs along with the scatter plot and the histogram plot. Such a comprehensive plot including all three plots is called scatter-histogram with parent container. The bar graph conveys the same findings of the scatter-histogram plot meaning that the most-dense section of the data distribution belongs to the voltages between 500 and 1300. Outside this interval, few numbers of the dataset are located.

It is also good to state how much electric power ($P$) is generated by running the piezo-electric vibration-based energy harvester. Recoding the electric current ($i$) and using the formula to of electric power ($P = Vi, P = V^2/R_l$); following values are obtained:

In Table 51, minimum harvested electric power is 0.0458 mW, maximum value is: 4.7306 mW, mean value is: 0.8394 W. RFID systems usually require a value between 0-10 mW to be able to transmit data. As the RFID reader antenna and components work based on the passive tags, such a PVEH device is capable of providing enough amount of energy to run the RFID system.

Table 48. Box plot summary for the electric power generated from the PVEH in experimental setup.

| Number of points/observations | 100 |
|---|---|
| Minimum value | 0.0458 mW |
| Maximum value | 4.7306 mW |
| Lower adjacent | 0.0458 mW |
| 25th percentile | 0.3697 mW |
| Low notch | 0.6405 mW |
| median | 0.7948 mW |
| High notch | 0.9657 mW |
| 75th percentile | 1.4352 mW |
| Upper adjacent | 3.0033 mW |
| Outlier value | 4.7306 mW |
| Mean (average) | 0.8394 mW |
| Median (middle) | 0.7948 mW |

7.3 Clustering the dataset.

For clustering the voltage dataset based on the fuzzy logic, one can utilize either fuzzy C-Means or Subtractive clustering techniques to identify clusters within the dataset. Then, using the Sugeno-type of FIS one can model the behavior of the energy harvester system. Before proceeding, clustering is required to be explained shortly: Clustering of numerical dataset forms the basis of several system modeling and classification algorithms. Main purpose of clustering is to identify chief natural groupings of data from a large set to yield a concise and succinct representation of the system's behavior. In MATLAB, cluster information can be used to generate Sugeno-type of the fuzzy inference system (FIS). Such a fuzzy system can model the behavior of the dataset utilizing minimum numbers of rules in the most efficient way. Fuzzy rules partition themselves according to the fuzzy qualities which are associated with each of the clusters.

Fuzzy C-Means clustering: Fuzzy C-means (FCM) is a data clustering technique wherein each data point belongs to a cluster to some degree which is determined by grade of a membership. This technique provides a method showing how to group data points that populate some multidimensional space into a specific number of different clusters. The command line function ‘fcm’ (fuzzy c means clustering) initiates with an initial guess for the cluster centers, which are intended to highlight and coincide with the mean location of each cluster. However, the nominated initial guess for these cluster centers is most likely incorrect. ‘fcm’ assigns every single data point a membership grade for each cluster. By iteratively updating the cluster centers and the membership grades for each data point, ‘fcm’ iteratively moves the cluster centers to the right location within a dataset. This iteration is based on minimizing an objective (cost/loss) function representing the distance from any given data point to a cluster center weighted by that data point's membership grade. In MATLAB, the command line function ‘fcm’ outputs a list of cluster centers along with several membership grades for each data point. Fuzzy qualities of each cluster disclosed by ‘fcm’, can be taken to build the fuzzy membership functions and the fuzzy inference system (FIS).

Subtractive clustering: as for the cases in which, there is no clear idea of how many clusters there should be for a given set of data, subtractive clustering is a fast, one-pass algorithm for estimating the number of clusters and the cluster centers for the dataset. In MATLAB, the cluster estimates obtained from the ’subclust’ function, can be used to initialize iterative optimization-based clustering methods (fcm) and model identification methods (like anfis). The ‘subclust’ function finds the clusters using the subtractive clustering method.

First the voltage dataset is clustered using the C-Means method. The pertinent code is written in MATLAB at the command line. Using the mentioned method, one needs to first clarify the number of clusters. Assuming 3 clusters for the experimental dataset, options should be determined as well. Options in 'fcm' (fuzzy C-means clustering) is a row vector including 4 elements. The first element (options(1)) is the exponent of the fuzzy partition matrix shown by 'U'. before proceeding further, the fuzzy partition matrix is a $N_c$ by $N_d$ matrix. $N_c$ representing the number of rows is identical to the number of clusters. $U(i,j)$ indicates the degree (grade) of membership of the $j^{\text{th}}$ data point in the $i^{\text{th}}$ cluster. For a given datapoint, the sum of the membership values of all clusters is equal to 1. In other words, sum of the entities of each column of the fuzzy partition matrix is equal to 1 ($\sum_{j=1}^{N_j} U_{i,j} = 1$). The first element on the options matrix controls the amount of fuzzy overlap between different clusters. In MATLAB the default value for such an exponent is 2. Greater values of this exponent indicate greater overlaps. It means with big exponent values; cluster boundaries are less crips and have more overlaps. In such a case which happens with big (wide) datasets, the calculated cluster centers are probably very close to each other. In such a case, each datapoint has approximately the same amount of membership in all clusters. In most of the clustering cases, it is recommended to adopt small values of option(1) (fuzzy partition matrix exponent) which leads to less overlap between fuzzy clusters. However, this number should be bigger than 1 to cover all of the datapoints in a dataset. The second entity of the option matrix is options(2) which pertains to the maximum number of iterations. This value is considered by 100 as default. Obviously increasing the option(s) leads to more computations but more accuracy. Third entity is the minimum improvement value of objective function between two successive

(consecutive) iterations. Default value is $10^{-5}$. Optimization in clustering will stop if the objective function improvement between the last two final iterations is less than this third entity. This entity determines the accuracy of clustering. The last entity of the option matrix is a verbose function of 'true' or 'false'. This option enables MATLAB to either display or hide the objective function values for each iteration and loop. With all this explanation, classifying the dataset into the specific cluster with largest membership value is done.

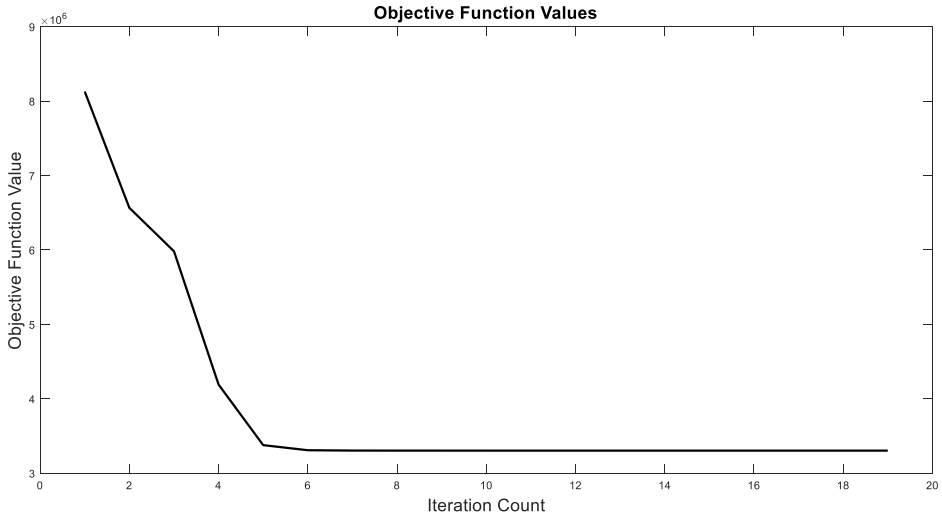


Figure 124. C-Means clustering objective function improvement.

Figure 124 shows the objective function values versus iteration counts with 0.0005 as the minimum function improvement. Obviously, throughout the initial iterations (<5) the objective function decreases sharply and steeply. After about 5 iterations the slope of decrement is reduced and the optimization algorithm stops around 70 iterations where the improvement between the last two functions is less than 0.0005.

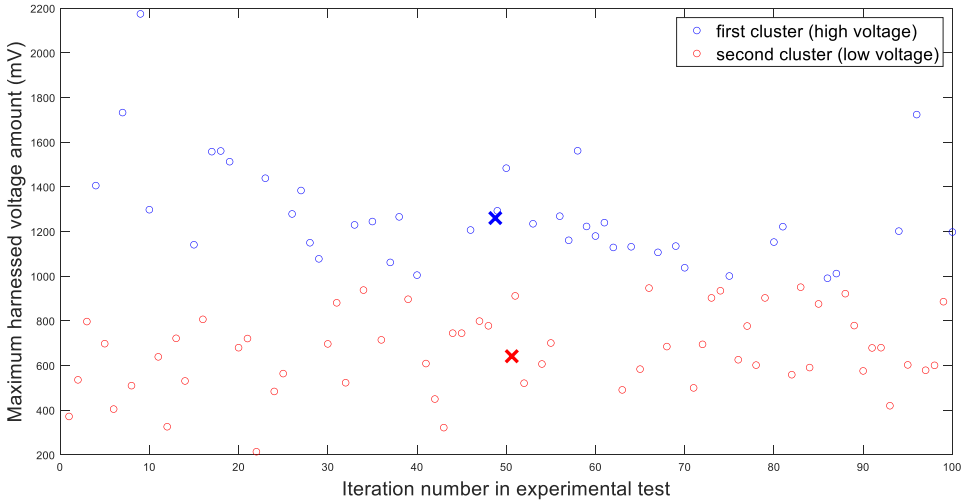


Figure 125 experimental data clusters

Figure 125 shows the clustering of the voltage dataset into two various clusters. Certainly, the number of elements in each cluster does not necessarily equate with the other cluster. In this clustering effort, 47 elements exist in the third cluster, 42 in the second and 11elements appear in the first cluster. The center of each cluster is depicted in cross marks. Fuzzy partition matrix is considered as 2, maximum number of iterations is set to 500, and minimum objective function improvement is considered as 0.0005.

Using the ‘genfis’ function, it is viable to train the corresponding fuzzy inference system (FIS) for the accomplished clustering algorithm. To customize the fuzzy inference system according to the clustering options, one can specify the system using ‘genfisOptions’ function using the ‘option’ matrix which is already used in clustering the dataset.

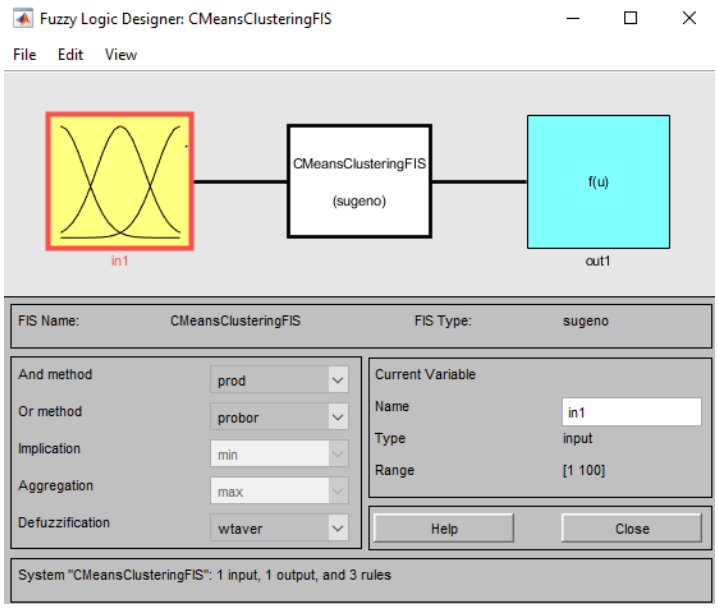


Figure 126 Fuzzy logic designer for C-Means clustering

Figure 126 shows the designed Sugeno type of fuzzy inference system for clustering using C-Means method. And method is ‘prod’, Or method is ‘probor’, implication is ‘min’ and Defuzzification is ‘wtaver’. Range of the system is [1, 100].

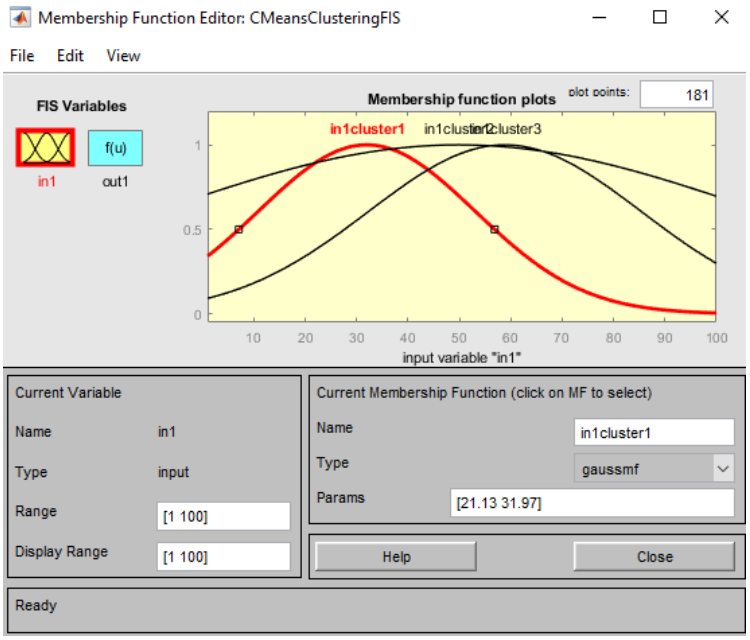


Figure 127 Fuzzy membership function editor for C-Means clustering

Two Gaussian membership functions are used and shown with diverse statistical parameters and ranges. Such functions are generated due to the adoption of two clusters as well as the type of dataset and type of clustering algorithm.

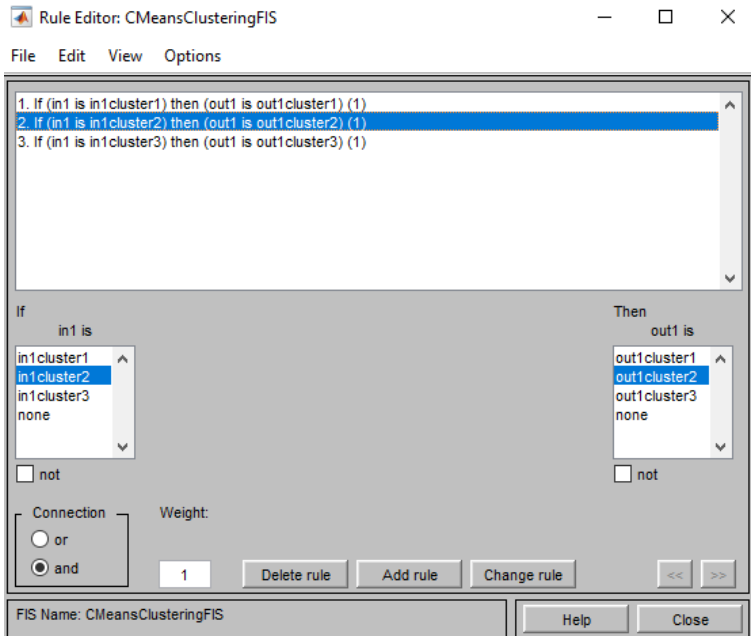


Figure 128 Rule editor for fuzzy C-Means clustering

The rule editor shows the two fuzzy rules derived from the clustering based on C-means and two clusters. Connection between the rules are based on the ‘and’ method and a unit identical weight.

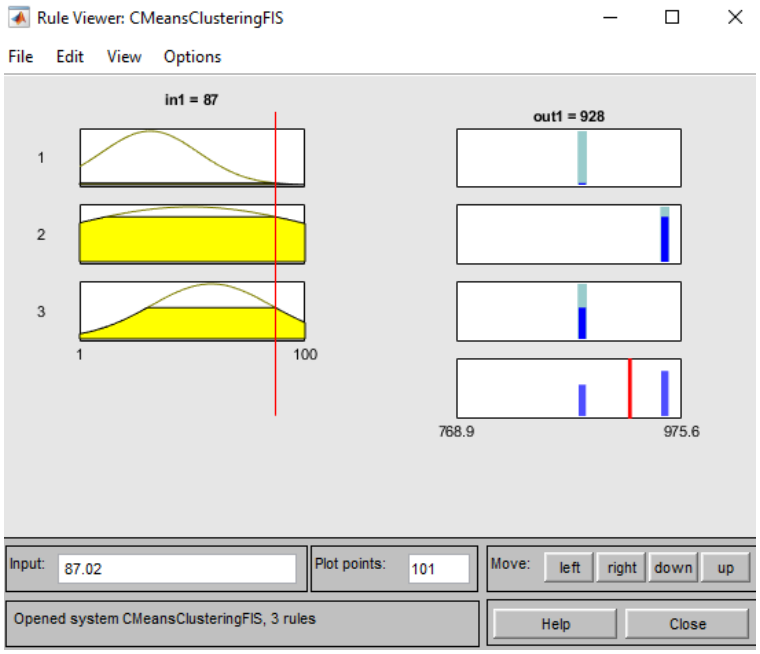


Figure 129 Rule viewer in fuzzy C-Means clustering

Rule viewer of the generated clustering algorithm shows the instinct rules and how inputs lead to a specific cluster as the output. Dragging the red line crossing the input boxes leads to instant changes in the output boxes and the aggregated outcome cluster, respectively.

Further analysis over C-Means clustering can be accomplished in terms of adjusting the amount of overlap between different fuzzy clusters and to see how this option(1) (fuzzy partition matrix exponent) alters the performance of the clustering algorithm.

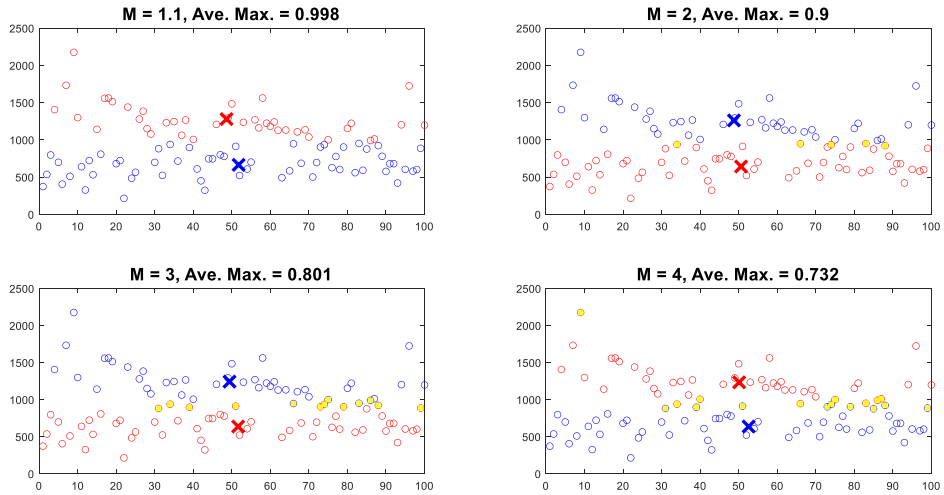


Figure 130 Exponent of fuzzy partition matrix effect over overlap in clusters

Considering four disparate values of fuzzy partition matrix exponent as $M = 1.1, 2, 3, 4$ and keeping constant values of other option values; clustering figure shows that for smaller numbers of M, crisper boundaries are observed and big values of M result in datapoints which belong to two or even more clusters. A given datapoint is classified into the cluster for which it has the highest membership value. A maximum membership value of 0.5 indicates that the point belongs to both clusters equally. The datapoints with marked yellow cross signs have maximum membership values below 0.6. These points have a greater degree of uncertainty in their corresponding membership. More datapoints with low maximum membership values indicate a greater degree of fuzzy overlap in the clustering result. The average maximum membership value shown by Ave. Max. provides a quantitative description of the overlap. In short, bigger average maximum values occurs with smaller fuzzy partition matrix exponent which shows crisp clusters with small or no overlaps. Conversely, increasing the M leads to smaller average maximum values and more overlapped clusters which decreases the efficacy of the clustering algorithm.

Another method of clustering is using the 'subclust' function and subtractive clustering technique. Subtractive clustering assumes that each datapoint is a potential cluster center. Thus, the algorithm calculates the likelihood that each data point would define a cluster center based on the density of the surrounding data points. Then algorithm chooses the data point with the highest potential for being the first cluster center and removes all data points near the first cluster center. The vicinity is determined using a parameter named cluster influence range. Then, algorithm m chooses the points with the highest potential for being the next cluster center. This whole procedure is being repeated until the data is within the influence range of a cluster center. Despite the C-Means clustering, the subtractive type yields the number of clusters automatically. The alternative parameter here is the influence range. Mostly, small number of influence range results in smaller cluster sizes and more clusters. Conversely, bigger influence range results in less clusters and less fuzzy rules. This parameter is ranged from 0 to 1.

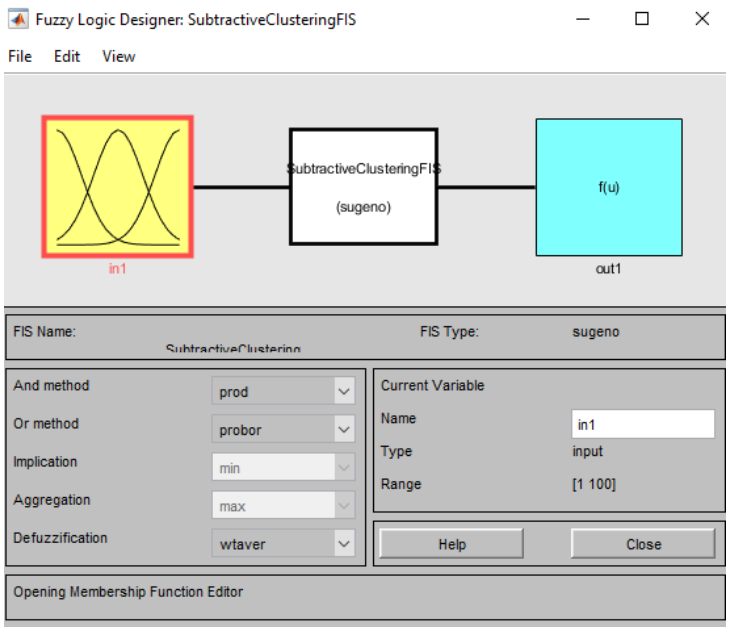


Figure 131 Fuzzy logic designer for subtractive clustering

Figure 131 displays the generated clustering fuzzy inference system (FIS) using subtractive method. It is good to note that the mentioned clustering algorithm is generated in MATLAB at the command line. The fuzzy system is established based on the Takagi Sugeno inference system with single input (iteration number in experiment) and single output (maximum harnessed voltage in an impact-driven excitation).

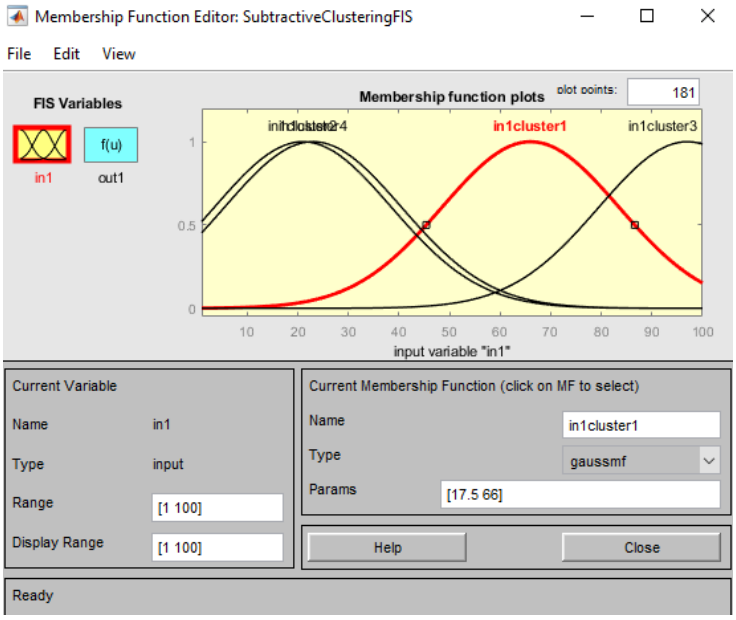


Figure 132 Fuzzy membership function editor for subtractive clustering

Figure 132 shows the membership functions forming the fuzzy rules and the fuzzy inference system. Clustering the experimental dataset into two different clusters leads to adoption of four different types of Gaussian membership function expanding over various ranges.

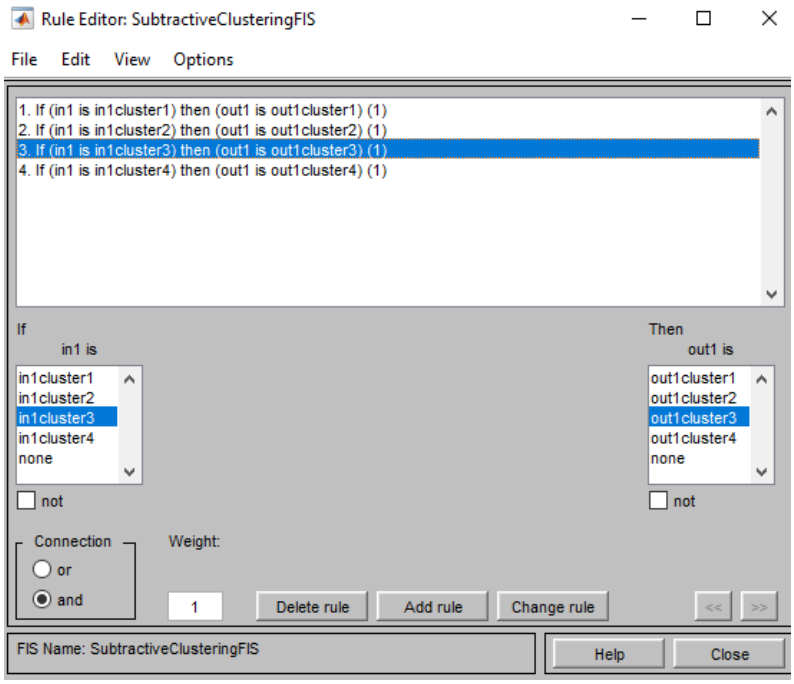


Figure 133 Rule editor for fuzzy subtractive clustering

Fuzzy rule set is depicted in verbose format in the above figure. Using four membership functions leads to four fuzzy inference rules. The connection type in rules is based on ‘and’ method and unit identical weight is taken per rule.

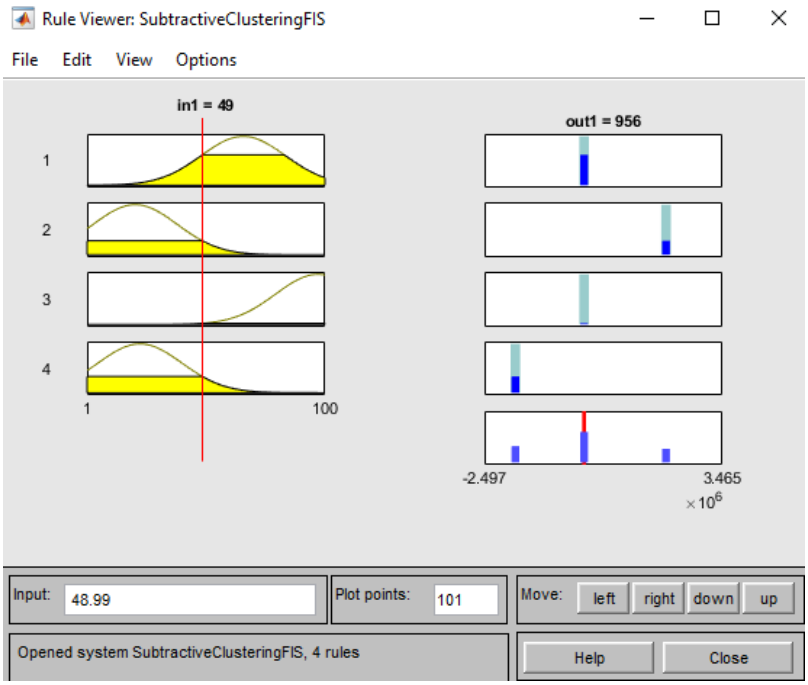


Figure 134 Rule viewer for subtractive fuzzy clustering

Rule viewer figure illustrates the fuzzy rules in visual setting. For this clustering type (subtractive), four fuzzy rules are shown on the left, and the outcome on the right. The last box including the numeric range is the aggregated value of the fuzzy clustering. Dragging the red line crossing the input boxes instantly ends up in variations in output which renders instant fuzzy changes.

## 7.4 Conclusion

In this chapter to evaluate the capability of a piezoelectric vibration-based energy harvester (PVEH) to convert mechanical energy into electric energy, a simple experimental energy harvester setup is implemented. Unlike to the other chapters of this dissertation, excitation trigger type is applied by means of the impact-driven impulses. However, in the former chapters the excitation is based on the harmonic base excitations.

The reason to choose two different types of excitations pertains to the fact that, in the former chapters main concern is modeling, analysis, optimization and design of a modified energy harvester. To show the superiority of such harvester model, a standard criterion is chosen to compare and validate the supremacy of the proposed model relatively. However, in the current chapter major concern is to test the capability of a mere cantilever piezoelectric vibration-based energy harvester which is excited by a realistic trigger similar to what is happening in the real world. In this response, impact-driven excitation is considered as the input. The experimental setup is implemented and the harvested electric voltage is captured and recorded for data visualization purposes. According to the nature of the impact driven excitations, collected voltage dataset is a random dataset with no detectable patterns. The experimentation is run for 100 iterations. It is noteworthy that running different iterations will lead to different dataset distributions. The current dataset is valid for only the 100 iterations accomplished at the specific run in the research laboratory, and running the setup for the next time is expected to result in different dataset.

# CHAPTER 8. CONCLUSION

## 8.1 Overview

The work presented in this dissertation covers an exploration into generating electrical energy from mechanical vibration energies using the piezoelectric transduction method. The primary goals of the work were to devise and potentially improve upon the state-of-the-art technologies to convert vibration energy into electric energy. Developing a technology of energy harvesting based on vibrations and piezoelectricity has great potential as an alternative power source for low-power and ultra-low-power electronics. This is especially important, as the newer generation of electronic devices require very small amounts of energy to run.

This chapter reviews the contributions made to developing piezoelectric vibration-based energy harvesters (PVEHs).

## 8.2 Improvements in understanding the vibration response of a configuration.

Initial energy harvester devices included a single mass-spring system. Such a lumped-parameter system has a single degree of freedom which limits the amount of harvestable energy and the device application. New energy harvester modules are distributed-parameter systems with infinite degrees of freedom and a cantilever beam. The cantilever is equipped with piezoelectric patches on top (uni-morph), and both top and bottom surfaces (bi-morph). Mechanical oscillations of the beam can result from motions which have a connection to the cantilever configuration. The source of oscillations can be generated from flow, acoustic, or physical contact. In this work, the source of vibrations simulates or is due to an operator applying random impact-driven excitations. Since the

amount of harvestable energy vitally depends on the vibratory behavior of the cantilever, it is important to analyze the system considering the influential parameters. These parameters impact the response of the system in terms of the resonance frequency and frequency bandwidth. Piezoelectric vibration-based energy harvesters convert the mechanical energy into electric energy most efficiently when the system is in resonance. Thus, identifying the resonance frequencies, mode shapes, and frequency bandwidth is crucial to increase the efficacy and the generated amount of energy.

In the initial chapters of this work, temperature and rotatory parameter effects upon the frequency variation are studied. To model the temperature effects, an extended Hamilton's principle is used along with the following assumptions: one-dimensional and steady-state heat transfer with no heating source. The rotary element is modeled with respect to a constraint equation between the lateral deformations of the cantilever beam and the rotational orientation of the element. Deriving the governing equations of motion and solving for the first three modes of vibration, it was observed that temperature can impact the frequency bandwidth but does not affect the amount of extractable voltage. This is mainly because temperature fluctuations affect the resonance frequency. Modifications of the Rotatory element have a similar effect in decreasing the resonance frequencies. Such a consideration of changes in the temperature and rotary element can be important for understanding energy harvesters working in ambient with severe temperature fluctuations, or if the cantilever is being rotated by a rotor or servomechanism. Also, different boundary conditions of clamped-free and clamped-clamped cantilevers are considered accompanied with different types of solution in the spatial domain (Galerkin's and Navier's methods).

The importance of using the proper solution method is demonstrated, particularly with respect to symmetric and asymmetric boundary conditions.

### 8.3 Importance of integrating a sub-system of oscillator-spring to the cantilever

Conventional energy harvesters are comprised of a cantilever with or without a tuning mass at the tip end. These conventional systems usually have two important drawbacks: the amount of generated energy is insignificant, and the operational (effective) frequency bandwidth is not wide enough. Such challenges decrease the application of PVEHs in the real world. On the other hand, with recent improvements in electronics and semi-conductor technologies, new devices including RFID passive tags and components require only a small amount of energy to operate. Such a promising point encourages scholars to develop conventional PVEHs to render enough amount of energy along with widened effective frequency bandwidth.

As a novel sub-system integration, a mass-spring system was integrated to the tip end of the beam. Such an integration increases the degrees of freedom and the generalized coordinate systems adding to the complexity of the analysis. The additional complexity is due to the relative motion or oscillation of the oscillator (mass) with respect to the oscillations of the tip end of the cantilever. The elastic support of the oscillator also reflects back vibratory energy to the cantilever. To derive the governing equations of motion, extended Hamilton's principle as an energy method was adopted. Unlike systems of conventional PVEHs, a system of three partial differential equations (PDEs) are coupled in this case. The mechanical equations of the cantilever and the oscillator are coupled to the integral PDE of the electric circuit. Such a sub-system integration has another impact

in regard to the boundary conditions. Deflection, slope, and bending moment of the cantilever are similar to that of a conventional cantilever as the first three boundary conditions were unchanged. However, the spring restoring forces effect significantly alters the shearing force boundary condition of the cantilever. Such a mutation results in a new nonlinear transcendental characteristic equation which is an explicit function of the mass of the oscillator and spring stiffness (or mass and stiffness ratios). Galerkin's modal decomposition method was initially adopted to separate the spatial and temporal domains of the cantilever-oscillator-spring system. Solving the mentioned nonlinear transcendental characteristic equation numerically revealed the initial effect of the restoring forces of the spring and inertia of the oscillator.

In other words, replacing the rigid support with an elastic support renders the restoring forces' impact over the oscillatory response of the cantilever. Such an impact was observed in both resonance frequency and effective frequency bandwidth. It was understood that the new system had the first resonance frequency at the vicinity of the origin and smaller than the conventional system's first resonance. Accordingly, the mode shapes of the cantilever were dramatically changed. Such a mutation can be severe or minor, depending upon the amount of oscillator mass and spring stiffness. Another finding pertains to the second resonance frequency, which takes place around the first resonance of the conventional system. In short, integration of the oscillator-spring system with the cantilever at the tip end enables the designer with tuning capability in resonance frequency and frequency bandwidth. More importantly, the effect of the oscillator inertia emerges in the amount of harvestable voltage.

Based on the results summarized in Table 52, it is inferable that the harvestable energy can be increased by six times. Realization of such an increment depends on the values of the mass and stiffness ratios and is vitally important to increasing the efficiency of the PVEHs. Another finding pertains to the initial resonance at the first mode which takes place at frequencies smaller than the conventional harvesters' first resonance. This is particularly important and helpful as for most cases, the incoming (driving) vibration frequency covers a range smaller than the first resonance of the structure. This way, the smaller resonance taking place at smaller frequency spectrum provides the resonance and generation of peak values in the harvestable energy.

Table 49. Harvested voltage by oscillator-spring sub-system integration.

| $r_s$ | $r_m$ | Maximum voltage | Percentage (%) |
|---|---|---|---|
| 1E+10 | 0 | 4.847469 | 49.47116 |
| 0.01 | 0.01 | 3.344365 | 3.12311 |
| 100 | 0.01 | 3.342263 | 3.05829 |
| 0.01 | 1 | 15.77137 | 386.3084 |
| 1 | 1 | 14.64587 | 351.6036 |
| 100 | 1 | 13.61919 | 319.9463 |
| 0.01 | 2 | 27.34958 | 743.3213 |
| 100 | 2 | 24.38628 | 651.9481 |

Based on the results summarized in the above table, it is inferable that harvestable energy can be increased by six times. Such an increment depends on the values of the mass and stiffness ratios and is vitally important to increase the efficiency of the PVEHs. Another finding pertains to the initial resonance at the first mode which takes place at frequencies smaller than the conventional harvesters' first resonance. This is particularly

important and helpful as for most cases, the incoming (driving) vibration frequency covers a range smaller than the first resonance of the structure. This way, the smaller resonance taking place at smaller frequency spectrum provides the resonance and generation of peak values in the harvestable energy.

## 8.4 Importance of optimizing the cantilever-oscillator-spring energy harvester

In the next step of developing the PVEHs, finding those optimal values of the oscillator mass and spring stiffness (constant) were considered. This tuning was aimed to harvest the biggest amount of electric energy from a given vibration energy.

In most cases, modifying the mechanical and geometrical properties of a cantilever is not a realistic idea due to limits in size and material. This means that changing the vibratory response of the system according to the desired pattern is not easy. To address such an issue, mass of the oscillator and stiffness of the spring were considered as the tuning parameters to optimize the behavior of the cantilever towards the desired state. A specific range of values for the oscillator mass and spring stiffness were considered. The objective function to be maximized was the voltage function. Using analytical-numerical methods, an explicit voltage function was derived. To optimize such a function with genetic algorithms, there were two main challenges. The voltage function encompasses several complicated coefficients which are functions of the mode shapes at different modes. This leads to extreme computational costs as the genetic algorithm runs on successive iterations of high numbers. The bigger challenge referred to the process of solving the nonlinear transcendental characteristic equation which was accomplished numerically. In this process, a developed root-solving algorithm dependent on a reasonable

value of the initial guess was used. To support the solver with a good initial guess, the characteristic equation was visualized by plotting. This step requires human action and cannot be automated by the software.

To overcome such issues, a soft computing technique was investigated. Specifically, the analytical-numerical voltage function was used to obtain over 230 case studies to train a reliable approximator (regressor) algorithm. The mentioned algorithm was implemented using adaptive-neuro-fuzzy-logic principles. Fuzzy inference system (FIS) handles the nonlinearity of the voltage dataset and provides accurate estimations for unknown values of the variables. Neural networks were used in parallel to the fuzzy logic to train the inference system more efficiently. Such efficiency yields more accuracy (precision) of the function approximator algorithm along with reasonable computational costs. In tuning the fuzzy-based function approximator, several types of membership functions (MFs) and various combination of fuzzy rules along with different rule weights were verified and compared based on the root-mean-square-error (RMSE) values. Gaussian, and Generalized-Bell-shaped membership functions with 64 fuzzy rule sets showed better capability in estimating the unknown voltage values. To avoid the under-fitting issue, a high number of fuzzy rule sets were required. However, taking so many rule sets deteriorates the approximator algorithm in terms of generalization. This is known as the over-fitting issue. To avoid generalization problems, a specific division of dataset was considered as a checking (validation) dataset. Multiple adaptive-neuro-fuzzy-inference-systems (ANFIS) were implemented as inputs to the genetic algorithm. Different types of genetic algorithm selection types were also implemented to find the optimal solution. All combinations of different fuzzy systems and genetic selections yield the same results for

the optimum value of the oscillator mass and spring stiffness ($r_m = 2, r_s = 100$). At the end, to evaluate the accuracy of the result obtained from the soft computing technique, results were compared against the analytical-numerical results in terms of harvestable voltage in the frequency-domain. A comparison showed the soundness and correctness of the soft computing algorithms, meaning that the optimal values of the oscillator mass and spring stiffness indeed yield the most amount of harvestable electric voltage.

In summary, it was observed that integration of the oscillator-spring sub-system to the cantilever not only impacts the amount of harvestable energy, but also it is viable to tune and optimize such a multi-system energy harvester to deliver the most amount of harvestable energy.

In a similar effort, the objective or utility (fitness) function was chosen to be the operational (effective) frequency bandwidth. As mentioned earlier, another drawback with conventional PVEHs pertains to the narrow effective bandwidth. Widening this bandwidth is crucial to increase the efficiency of the PVEHs. Integrating the oscillator-spring sub-system provides the chance to alter and widen the effective bandwidth. To optimize this widening process, soft computing techniques were adopted to train an adaptive-neuro-fuzzy-inference-system to approximate the resonance frequencies for unknown values of the oscillator mass and spring stiffness. The approximator was used as input to the genetic algorithm to find the optimal values. It is noted that, as the ANFIS is supported by Takagi-Sugeno type of fuzzy logic, two separate fuzzy-inference-systems (FISs) are required per initial and final frequencies in the effective (operational) frequency bandwidth ranges. This is because of the nature of Takagi-Sugeno type of the FIS, in which unlike to the Mamdani FIS, the supporting algorithm handles single/multiple-input-single-output (S/MISO).

Trapezoidal and Gaussian functions with 49 and 64 fuzzy rule sets were used. After finding the optimal values, they were used in the analytical-numerical expression for the voltage frequency response function (FRF) to evaluate the soundness of the designed soft computing algorithm. Comparison showed that the optimal values nominated by the soft computing algorithm result in an optimal effective (operational) frequency bandwidth. The corresponding optimal values of the mass and stiffness ratios were $r_m = 2.5, r_s = 100$.

### 8.5 Importance of designing an adaptive PVEH according to a given excitation

An important case for an energy harvester would be an identifiable given excitation (driving) frequency to the energy harvester. This means if the amount of the driving frequency and the range is detectable, the easiest method to increase the harvestable amount of energy is to adjust the harvester system's parameters to guarantee resonance. In order to avoid changing the mechanical and the geometrical properties of the cantilever, oscillator mass and spring stiffness can be changed. This problem is designing an adjustable PVEH according to the given excitation information, in which resonance is expected to yield the peak amount of harvestable energy. Due to the challenges mentioned in the above section, a fuzzy-based regressor was similarly designed to estimate the proper values of the design parameters (mass of the oscillator and spring stiffness). Neural networks were also utilized to tune the system for better accuracy and avoid the overfitting and generalization issues. It was assumed in this investigation that the driving (excitation) frequency from the ambient was $5Hz$. Using the Generalized-Bell-shaped and Triangular membership functions with 14 and 15 fuzzy rule sets, $r_m = 1.246,\ r_s = 0.1$ and $r_m = 1$, $r_s = 0.0803$ are the values delivered by the fuzzy-based regressor to ensure resonance will

take place. To verify the correctness, such values were used in the analytical-numerical expression for the voltage frequency response function (FRF) to observe the resonance frequency values.

Table 50. Estimated values of the resonance frequency using ANFIS

| $(r_m, r_s)$ | $f_1$ (Hz) |
|---|---|
| (1.245718750976976,0.1) | 4.991204174782064 |
| (1, 0.080291506577599) | 5.007755322962248 |

It is observed that the designed ANFIS systems are accurate enough to estimate the proper value of the oscillator mass and spring stiffness to yield resonance and match the excitation (driving) frequency with natural frequency of the cantilever.

8.6 Importance of experimental setup to observe the amount of harvestable voltage and energy

To experimentally and practically evaluate the amount of harvestable voltage and electric power, an experimental setup was designed and examined. The major difference is, in the real world, total control over the excitation or driving frequency cannot be guaranteed, and the excitation often looks like a random process. To follow this randomness, the excitation type in the experimental section was impact-driven inputs. The harvested voltage and current were recorded in a data-logging multi-meter per each iteration of the experiment. In a set of 100 times of execution; mean, and maximum values of the generated power were: $P = 0.839\ mW, 4.7306\ mW$.

Table 51 Harvested power by oscillator-spring integration

| | |
|---|---|
| Minimum value | 0.0458 mW |
| Maximum value | 4.7306 mW |
| Lower adjacent | 0.0458 mW |
| 25th percentile | 0.3697 mW |
| median | 0.7948 mW |
| 75th percentile | 1.4352 mW |
| Upper adjacent | 3.0033 mW |
| Mean (average) | 0.8394 mW |

As most of the RFID components require less only several milliwatts to transmit the data, the generated energy from the harvester assembly should be successful in supplying enough power to run the RFID system for passive components with ultra-low-power electronics. It is also good to note that, depending on the storage type and resistance, one can slightly change the value of the applicable energy. At the end of the experimentation, fuzzy C-means type of clustering was implemented to cluster the experimental dataset into three different types: low-energy, mid-energy, and high-energy clusters. Different values of the fuzzy partition matrix exponent ($M$) were used to cluster the data with decent overlap and uncertainty. A relationship between the mentioned fuzzy partition matrix exponent with the average maximum membership value ($Ave\ Max$) was also addressed. Findings revealed that it is important to find the proper value of the matrix exponent along with the average maximum membership value to cover all the datasets while the uncertainty of clustering is minimized. In this work, the proper value of the fuzzy partition matrix exponent was $M = 1.1$ and that of the average maximum value of the membership was $Ave\ Max = 1$. Decreasing the $Ave\ Max$ was identical to increasing the

$M$ value, which resulted in less crisp boundaries and more uncertainty. It was also verified that choosing $M < 1$ results in missing cluster points. This means that some datasets were abandoned and did not belong to any of the clusters. Finally, different types of data visualizations (scatter plot, box plot, histograms) were used to show the distribution of the harvested voltage data.

## 8.7 Summary of contributions

As a final summary: in this work, conventional piezoelectric vibration-based energy harvester (PVEH) devices were developed by integration of oscillator-spring sub-system. It was observed that, based on the analytical-numerical results, the proposed model renders significantly more harvestable voltage than the conventional energy harvesters. This increase is directly tied to the inertia of the oscillator and stiffness of the spring, which dramatically alters the vibratory response of the cantilever. Optimal values of the oscillator mass and spring constant were found using soft computing techniques which were established based on: adaptive-neuro-fuzzy-inference-system and genetic algorithms. Amongst various architectures of fuzzy logic systems, Gaussian, Generalized-Bell-shaped, and Trapezoidal functions were used to determine the membership degree of fuzzy sets. Genetic algorithms were implemented with 200 initial solution population and 50 times of iteration and 100 population of initial solution and 100 iteration times. Random, roulette wheel, and tournament selection methods were deployed to achieve the optimal solution. Based on the random nature of genetic algorithm in selecting the initial solutions, the evolution path differs per each algorithm execution time. This means that it cannot be pre-defined which selection method exceeds in computational costs. However, all three

different types of selection methods and various combinations of fuzzy logic yield identical optimal solutions for the design parameters. Two different sets of optimal values were found to maximize the harvestable voltage and to widen the effective (operational) frequency bandwidth. In the next step, designing an adjustable PVEH was reported. It was assumed the driving (excitation) frequency is a given and identifiable value. Determining the proper mass and stiffness ratios were the parameters investigated. These values should be obtained corresponding to the driving frequency so that resonance would take place. In other words, shifting the natural frequency of the cantilever towards the pre-defined value of the driving frequency was the identified problem. Fuzzy logic was used to design a function approximator to estimate the proper values of the ratios. Ultimately, the soundness of the designed fuzzy inference system was verified by using the analytical-numerical method. In the last chapter, an experimental setup was implemented and different tests were executed to record the harvestable amount of voltage. It was observed that the piezoelectric vibration-based energy harvester is capable of generating up to 4.7 mW, which can be sufficient to supply power for ultra-low-power RFID components to transmit data.

## 8.8 Future work

Developing piezoelectric vibration-based energy harvesters is in demand for several reasons. With the advent of smart cities and ultra-low-power electronics a new generation of electric devices like sensors and actuators are needed; these devices require small energy amount to run. Additionally, batteries can cause environmental issues and replacing used batteries can be difficult and increase labor costs. On the other hand,

developing energy harvesters has the potential to provide sufficient amounts of harvestable energy. As a result, developing harvesters from a dynamic perspective would be essential to overcome the issues of insignificant harvested energy and narrow bandwidth. As an extension of the work presented in this dissertation, designing parallel beams with piezo patches would further improve the functionality of the harvester. The single beam with piezoelectric patch was capable of generating up to 4.7 mW. A good parallel beam design would increase this amount. Another consideration would be the storage type of harvestable energy. It is important to design a proper storage device to minimize the amount of energy which is wasted in the storage process. From an analytical-numerical perspective, considering nonlinearity between mechanical and electrical coupling would be a case study. In this case, derivation of the voltage steady-state response would be the most challenging part. In the soft computing algorithms, one might develop the fuzzy inference system (FIS) to increase the accuracy in prediction of unknown voltage values for complicated harvester configurations. Such development would modify the fuzzy rules, fuzzy membership functions, or the inference type (Mamdani, fuzzy type-II). Modifying the geometry and configuration of the energy harvester would be another case study. It would necessitate a concurrent design process for a system containing multiple cantilever-oscillator-spring subsystems. The challenge would be how to connect these subsystems in terms of boundary conditions (interfaces) from both modeling and experimental perspectives. Such interfaces transfer the oscillations from one subsystem to another. This would require a deep understanding of the transfer functions that describe resulting subsystems. Potential areas of future work are summarized in the following list:

1- Designing parallel beams with piezoelectric patches.

2- Developing the storage type of energy.

3- Developing analytical-numerical methods to handle nonlinearity of mechanical-electrical coupling.

4- Developing soft computing technique from fuzzy inference system perspective.

5- Developing configuration by designing multiple PVEHs.

APPENDICES

APPENDIX 1. Technical Parameters and Terminology

In this appendix, technical parameters and the corresponding terminology are represented.

$L$ is length of beam aligned with $x$-direction

$b$ is beam width (both substrate and piezoelectric layers have identical width)

$h_s$ is thickness of substrate

$h_p$ is thickness of each piezoelectric layer

$g(t)$ is base translation

$h(t)$ is base rotation

${T_1}^s$ is normal (axial) stress at substrate (along $x$-direction)

$E_s$ is Young's modulus of substrate (modulus of Elasticity)

$S_1$ is axial (normal) strain in the $x$-direction

Piezoelectric constitutive relation:

$$D_3 = d_{31}{T_1}^p + {\varepsilon_{33}}^T E_3$$

$${T_1}^s = E_s S_1$$

$$S_1 = E_p {T_1}^p + d_{31} E_3$$

$${T_1}^p = E_p(S_1 - d_{31} E_3)$$

$${\varepsilon_{33}}^s = {\varepsilon_{33}}^T - {d_{31}}^2 E_p$$

$$E_3 = -{}^{v(t)}\!/_{(2h_p)}$$

$$D_3 = d_{31}E_pS_1 - \varepsilon_{33}{}^s\frac{v(t)}{2h_p}$$

$$C_p = \frac{\varepsilon_{33}{}^s bL}{h_p}$$

$$v(t) = R_l i(t) = R_l \dot{q}_3$$

$$i(t) = \frac{dq_3(t)}{dt}$$

$D_3$ is electric displacement

$d_{31}$ is piezoelectric coupling coefficient

$T_1{}^p$ is stress of the piezoelectric layers in the $x$-direction

$\varepsilon_{33}{}^T$ is permittivity at constant stress

$E_3$ is electric filed through $z$-direction

$E_p$ is elastic modulus at constant electric field

$\varepsilon_{33}{}^s$ is permittivity at constant strain

$C_p$ is capacitance

$v(t)$ is voltage across resistive road ($R_l$)

$R_l$ is resistance

$q_3(t)$ is electric charge

$i(t)$ is electric current

$\alpha_s$ is thermal expansion coefficient $w_b$is base motion with respect to Euler (fixed) coordinate axis in space $(X - Y - Z)$

$w_{rel}(x, t)$ is beam transverse (lateral) translation (displacement) (deflection) with respect to Lagrangian coordinate attached to base $(x - y - z)$

$U_k$ is kinetic energy term

$U_s$ is potential strain energy term

$U_{th}$ is potential energy term due to thermal stress

$W_e$ is electrical energy term

$T^{th}$ is thermal stress

$\rho$ is density

$A$ is cross section area including substructure, top and bottom PZT layers

$A_s$ is cross section of substructure layer

$I_s$ is second moment of inertia of substructure

$I_p$ is second moment of inertia of PZT layer

$Q_p$ is first moment of cross area of PZT layer

$L$ is Lagrangian operator

$W_{nc}$ is non-conservative work resulted from dissipating forces, and external forces

$c_a$ is viscoelastic damping coefficient

$W_{c_a}$ is non-conservative work due to viscoelastic dissipating force

$c_s$ is Kelvin-Voigt damping coefficient (also called as strain-rate damping coefficient)

$W_{c_s}$ is non-conservative work due to Kelvin-Voigt (strain-rate) dissipating force

$W_{R_l}$ is non-conservative work due to dissipating force of resistive load

$H(x)$ is Heaviside function

$\delta(x)$ is Dirac delta function

$t$ is time variable (temporal variable)

$x$ is space variable through beam length (spatial variable)

$\gamma_n = \phi_n(L)$

$$\Gamma_2 = \frac{E_p Q_p d_{31}}{h_p}$$

$$\Gamma_1 = \Gamma_2 R_l$$

$$\chi_n = \Gamma_2 \left.\frac{d\phi_n}{dx}\right|_{x=L}$$

$$\tau_c = \frac{C_p}{2} R_l$$

$$\Gamma_3 = \frac{2}{C_p} \Gamma_2$$

$$\Theta_n = \Gamma_3 \left.\frac{d\phi_n}{dx}\right|_{x=L}$$

$$\gamma_n{}^w = \int_0^L \phi_n(x)dx$$

The above parameter pertains to the analytical-numerical closed-form expression of the voltage function frequency response function.

APPENDIX 2. Dataset

In this appendix, the dataset obtained by means of the analytical-numerical closed-form solution is provided. For different values of stiffness ratio and mass ratio; the nonlinear transcendental characteristic equation is solved numerically using the ROOTSOLVER algorithm in MATLAB. To provide the decent initial guess, the mentioned characteristic equation is plotted and visually assessed. Such a visual inference enables us to estimate the initial guess. Such an estimation helps the algorithm to find the numerical solution of the equation. This process is accomplished for the first three vibration modes (first three roots). Besides, the amount of harvested voltage at the first resonance is also gathered and collected.

Dataset

| $r_m$ | $r_m$ | Resonance voltage | $\lambda_1 L$ | $\lambda_2 L$ | $\lambda_3 L$ |
|---|---|---|---|---|---|
| 0.0001 | 0.0001 | 4.393729 | 0.999991 | 1.875121 | 4.694092 |
| 0.0001 | 0.0005 | 4.365127 | 0.668735 | 1.875119 | 4.694092 |
| 0.0001 | 0.001 | 4.366918 | 0.562337 | 1.875119 | 4.694092 |
| 0.0001 | 0.005 | 4.410254 | 0.376057 | 1.875119 | 4.694092 |
| 0.0001 | 0.01 | 4.467924 | 0.316225 | 1.875119 | 4.694092 |
| 0.0001 | 0.05 | 4.931851 | 0.211472 | 1.875119 | 4.694092 |
| 0.0001 | 0.1 | 5.512044 | 0.177826 | 1.875119 | 4.694092 |
| 0.0001 | 0.2 | 6.672468 | 0.149534 | 1.875119 | 4.694092 |
| 0.0001 | 0.3 | 7.832898 | 0.135119 | 1.875119 | 4.694092 |
| 0.0001 | 0.4 | 8.99333 | 0.125742 | 1.875119 | 4.694092 |
| 0.0001 | 0.5 | 10.15376 | 0.11892 | 1.875119 | 4.694092 |
| 0.0001 | 0.6 | 11.31419 | 0.113621 | 1.875119 | 4.694092 |
| 0.0001 | 0.7 | 12.47463 | 0.109326 | 1.875119 | 4.694092 |
| 0.0001 | 0.8 | 13.63506 | 0.105736 | 1.875119 | 4.694092 |
| 0.0001 | 0.9 | 14.79549 | 0.102668 | 1.875119 | 4.694092 |
| 0.0001 | 1 | 15.95593 | 0.099999 | 1.875119 | 4.694092 |
| 0.0001 | 2.5 | 33.36242 | 0.079526 | 1.875119 | 4.694092 |
| 0.0001 | 5 | 62.37334 | 0.031623 | 1.875119 | 4.694092 |
| 0.0001 | 7.5 | 91.38411 | 0.060427 | 1.875119 | 4.694092 |
| 0.0001 | 10 | 120.395 | 0.056234 | 1.875119 | 4.694092 |
| 0.0001 | 100 | 1164.786 | 0.031623 | 1.875119 | 4.694092 |

Dataset (continued)

| $r_m$ | $r_m$ | Resonance voltage | $\lambda_1 L$ | $\lambda_2 L$ | $\lambda_3 L$ |
|---|---|---|---|---|---|
| 0.001 | 0.0001 | 4.814921 | 1.777528 | 1.875892 | 4.694101 |
| 0.001 | 0.0005 | 4.441202 | 1.189089 | 1.875285 | 4.694101 |
| 0.001 | 0.001 | 4.404222 | 0.99991 | 1.875269 | 4.694101 |
| 0.001 | 0.005 | 4.417401 | 0.668684 | 1.875258 | 4.694101 |
| 0.001 | 0.01 | 4.471409 | 0.562294 | 1.875257 | 4.694101 |
| 0.001 | 0.05 | 4.932486 | 0.376029 | 1.875256 | 4.694101 |
| 0.001 | 0.1 | 5.512339 | 0.316201 | 1.875256 | 4.694101 |
| 0.001 | 0.2 | 6.672594 | 0.265893 | 1.875256 | 4.694101 |
| 0.001 | 0.3 | 7.832967 | 0.240261 | 1.875256 | 4.694101 |
| 0.001 | 0.4 | 8.993367 | 0.223588 | 1.875256 | 4.694101 |
| 0.001 | 0.5 | 10.15378 | 0.211457 | 1.875256 | 4.694101 |
| 0.001 | 0.6 | 11.3142 | 0.202035 | 1.875256 | 4.694101 |
| 0.001 | 0.7 | 12.47462 | 0.194397 | 1.875256 | 4.694101 |
| 0.001 | 0.8 | 13.63504 | 0.188014 | 1.875256 | 4.694101 |
| 0.001 | 0.9 | 14.79546 | 0.182559 | 1.875256 | 4.694101 |
| 0.001 | 1 | 15.95589 | 0.177813 | 1.875256 | 4.694101 |
| 0.001 | 2.5 | 33.36232 | 0.14141 | 1.875256 | 4.694101 |
| 0.001 | 5 | 62.37309 | 0.118911 | 1.875256 | 4.694101 |
| 0.001 | 7.5 | 91.38389 | 0.107448 | 1.875256 | 4.694101 |
| 0.001 | 10 | 120.3947 | 0.099992 | 1.875256 | 4.694101 |
| 0.001 | 100 | 1164.785 | 0.056229 | 1.875256 | 4.694101 |
| 0.01 | 0.0001 | 4.940796 | 1.87489 | 3.162544 | 4.694213 |
| 0.01 | 0.0005 | 4.942672 | 1.872677 | 2.11743 | 4.694192 |
| 0.01 | 0.001 | 4.818833 | 1.771247 | 1.882501 | 4.69419 |
| 0.01 | 0.005 | 4.493757 | 1.188034 | 1.876909 | 4.694188 |
| 0.01 | 0.01 | 4.509148 | 0.999098 | 1.876751 | 4.694188 |
| 0.01 | 0.05 | 4.940139 | 0.668175 | 1.876644 | 4.694188 |
| 0.01 | 0.1 | 5.516316 | 0.56187 | 1.876631 | 4.694188 |
| 0.01 | 0.2 | 6.674741 | 0.472476 | 1.876625 | 4.694188 |
| 0.01 | 0.3 | 7.834498 | 0.426931 | 1.876623 | 4.694188 |
| 0.01 | 0.4 | 8.994584 | 0.397304 | 1.876622 | 4.694188 |
| 0.01 | 0.5 | 10.1548 | 0.375747 | 1.876621 | 4.694188 |
| 0.01 | 0.6 | 11.31509 | 0.359005 | 1.876621 | 4.694188 |
| 0.01 | 0.7 | 12.47541 | 0.345433 | 1.876621 | 4.694188 |
| 0.01 | 0.8 | 13.63575 | 0.334092 | 1.87662 | 4.694188 |
| 0.01 | 0.9 | 14.79612 | 0.324398 | 1.87662 | 4.694188 |
| 0.01 | 1 | 15.95649 | 0.315965 | 1.87662 | 4.694188 |
| 0.01 | 2.5 | 33.36255 | 0.251277 | 1.876619 | 4.694188 |
| 0.01 | 5 | 62.37306 | 0.211298 | 1.876619 | 4.694188 |
| 0.01 | 7.5 | 91.38368 | 0.19093 | 1.876619 | 4.694188 |

Dataset (continued)

| $r_m$ | $r_m$ | Resonance voltage | $\lambda_1 L$ | $\lambda_2 L$ | $\lambda_3 L$ |
|---|---|---|---|---|---|
| 0.01 | 10 | 120.3943 | 0.17768 | 1.876619 | 4.694188 |
| 0.01 | 100 | 1164.782 | 0.099917 | 1.876619 | 4.694188 |
| 0.1 | 0.0001 | 4.940831 | 1.874914 | 4.69318 | 5.624802 |
| 0.1 | 0.0005 | 4.944718 | 1.874106 | 3.761139 | 4.695735 |
| 0.1 | 0.001 | 4.949399 | 1.872972 | 3.164933 | 4.695309 |
| 0.1 | 0.005 | 4.971562 | 1.852912 | 2.139529 | 4.6951 |
| 0.1 | 0.01 | 4.883741 | 1.729368 | 1.927657 | 4.695079 |
| 0.1 | 0.05 | 5.019191 | 1.177801 | 1.892798 | 4.695062 |
| 0.1 | 0.1 | 5.558237 | 0.991179 | 1.891328 | 4.69506 |
| 0.1 | 0.2 | 6.698303 | 0.833766 | 1.890678 | 4.695059 |
| 0.1 | 0.3 | 7.851951 | 0.753474 | 1.890472 | 4.695059 |
| 0.1 | 0.4 | 9.008969 | 0.701224 | 1.890372 | 4.695059 |
| 0.1 | 0.5 | 10.16733 | 0.663198 | 1.890312 | 4.695059 |
| 0.1 | 0.6 | 11.32637 | 0.633661 | 1.890272 | 4.695059 |
| 0.1 | 0.7 | 12.48579 | 0.609715 | 1.890244 | 4.695059 |
| 0.1 | 0.8 | 13.64545 | 0.589704 | 1.890223 | 4.695059 |
| 0.1 | 0.9 | 14.80527 | 0.572597 | 1.890206 | 4.695059 |
| 0.1 | 1 | 15.9652 | 0.557716 | 1.890193 | 4.695059 |
| 0.1 | 2.5 | 33.36862 | 0.443552 | 1.890123 | 4.695058 |
| 0.1 | 5 | 62.37781 | 0.372986 | 1.8901 | 4.695058 |
| 0.1 | 7.5 | 91.38772 | 0.337032 | 1.890092 | 4.695058 |
| 0.1 | 10 | 120.3979 | 0.313644 | 1.890088 | 4.695058 |
| 0.1 | 100 | 1164.779 | 0.176376 | 1.890078 | 4.695058 |
| 1 | 0.0001 | 4.940834 | 1.874916 | 4.693598 | 7.853492 |
| 1 | 0.0005 | 4.944798 | 1.874162 | 4.691006 | 4.691006 |
| 1 | 0.001 | 4.949741 | 1.87321 | 4.685132 | 5.63714 |
| 1 | 0.005 | 4.988812 | 1.865249 | 3.765823 | 4.710472 |
| 1 | 0.01 | 5.03645 | 1.854395 | 3.188059 | 4.70629 |
| 1 | 0.05 | 5.38122 | 1.733853 | 2.281226 | 4.704209 |
| 1 | 0.1 | 5.826954 | 1.569956 | 2.118633 | 4.703997 |
| 1 | 0.2 | 6.869668 | 1.36091 | 2.055256 | 4.703895 |
| 1 | 0.3 | 7.983736 | 1.240005 | 2.038224 | 4.703861 |
| 1 | 0.4 | 9.119869 | 1.158369 | 2.030465 | 4.703844 |
| 1 | 0.5 | 10.26537 | 1.097911 | 2.026043 | 2.026043 |
| 1 | 0.6 | 11.41568 | 1.050472 | 2.02319 | 4.703828 |
| 1 | 0.7 | 12.56879 | 1.011757 | 2.021197 | 4.703823 |
| 1 | 0.8 | 13.72367 | 0.979252 | 2.019727 | 4.703819 |
| 1 | 0.9 | 14.87974 | 0.95137 | 2.018598 | 4.703816 |
| 1 | 1 | 16.03664 | 0.927049 | 2.017704 | 4.703814 |
| 1 | 2.5 | 33.42283 | 0.738976 | 2.013009 | 4.703802 |

Dataset (continued)

| $r_m$ | $r_m$ | Resonance voltage | $\lambda_1 L$ | $\lambda_2 L$ | $\lambda_3 L$ |
|---|---|---|---|---|---|
| 1 | 5 | 62.4251 | 0.621871 | 2.011494 | 4.703798 |
| 1 | 7.5 | 91.43198 | 0.562064 | 2.010995 | 4.703797 |
| 1 | 10 | 120.4402 | 0.523124 | 2.010746 | 4.703796 |
| 1 | 100 | 1164.801 | 0.294272 | 2.010077 | 4.703794 |
| 10 | 0.0001 | 4.940834 | 1.874917 | 4.69362 | 7.853942 |
| 10 | 0.0005 | 4.944805 | 1.874167 | 4.691693 | 7.849936 |
| 10 | 0.001 | 4.949771 | 1.873231 | 4.689188 | 7.842302 |
| 10 | 0.005 | 4.989569 | 1.865783 | 4.664468 | 6.717245 |
| 10 | 0.01 | 5.039496 | 1.856572 | 4.616387 | 5.747117 |
| 10 | 0.05 | 5.445959 | 1.787147 | 3.802011 | 4.851922 |
| 10 | 0.1 | 5.969812 | 1.711244 | 3.36328 | 4.817149 |
| 10 | 0.2 | 7.054585 | 1.590672 | 3.05076 | 4.804366 |
| 10 | 0.3 | 8.168464 | 1.500225 | 2.92519 | 4.800617 |
| 10 | 0.4 | 9.297953 | 1.429603 | 2.857754 | 4.798827 |
| 10 | 0.5 | 10.43647 | 1.372476 | 2.815819 | 4.797779 |
| 10 | 0.6 | 11.58062 | 1.324944 | 2.787276 | 4.797091 |
| 10 | 0.7 | 12.72847 | 1.284506 | 2.766619 | 4.796605 |
| 10 | 0.8 | 13.87889 | 1.249489 | 2.750987 | 4.796242 |
| 10 | 0.9 | 15.03116 | 1.218726 | 2.738751 | 4.795962 |
| 10 | 1 | 16.1848 | 1.191379 | 2.728915 | 4.795739 |
| 10 | 2.5 | 33.5492 | 0.966743 | 2.675184 | 4.79455 |
| 10 | 5 | 62.54149 | 0.818536 | 2.657086 | 4.794159 |
| 10 | 7.5 | 91.54402 | 0.741338 | 2.651038 | 4.794029 |
| 10 | 10 | 120.5495 | 0.690691 | 2.648012 | 4.793965 |
| 10 | 100 | 1164.886 | 0.389622 | 2.639834 | 4.79379 |
| 100 | 0.0001 | 4.940834 | 1.874917 | 4.693622 | 7.85397 |
| 100 | 0.0005 | 4.944806 | 1.874168 | 4.691745 | 7.850772 |
| 100 | 0.001 | 4.949774 | 1.873233 | 4.689401 | 7.846668 |
| 100 | 0.005 | 4.98964 | 1.865833 | 4.670742 | 7.80902 |
| 100 | 0.01 | 5.039768 | 1.856766 | 4.64768 | 7.747153 |
| 100 | 0.05 | 5.450654 | 1.790782 | 4.479469 | 6.870913 |
| 100 | 0.1 | 5.982183 | 1.721639 | 4.31837 | 6.32721 |
| 100 | 0.2 | 7.079243 | 1.613902 | 4.119489 | 5.981544 |
| 100 | 0.3 | 8.200411 | 1.532585 | 4.007969 | 5.859089 |
| 100 | 0.4 | 9.334168 | 1.46809 | 3.937914 | 5.79752 |
| 100 | 0.5 | 10.47529 | 1.4151 | 3.89008 | 5.760671 |
| 100 | 0.6 | 11.62108 | 1.370406 | 3.855416 | 5.736196 |
| 100 | 0.7 | 12.77002 | 1.331943 | 3.829168 | 5.718778 |
| 100 | 0.8 | 13.92118 | 1.298312 | 3.808613 | 5.705755 |
| 100 | 0.9 | 15.07396 | 1.268522 | 3.792086 | 5.695655 |

Dataset (continued)

| $r_m$ | $r_m$ | Resonance voltage | $\lambda_1 L$ | $\lambda_2 L$ | $\lambda_3 L$ |
|---|---|---|---|---|---|
| 100 | 1 | 16.22796 | 1.241854 | 3.778511 | 5.687593 |
| 100 | 2.5 | 33.59304 | 1.016947 | 3.699358 | 5.644405 |
| 100 | 5 | 62.58461 | 0.864164 | 3.670598 | 5.630158 |
| 100 | 7.5 | 91.58657 | 0.783665 | 3.660726 | 5.625428 |
| 100 | 10 | 120.5916 | 0.730604 | 3.655736 | 5.623066 |
| 100 | 100 | 1164.922 | 0.412886 | 3.642076 | 5.616702 |
| 1000 | 0.0001 | 4.940834 | 1.874917 | 4.693622 | 7.853972 |
| 1000 | 0.0005 | 4.944806 | 1.874168 | 4.69175 | 7.85084 |
| 1000 | 0.001 | 4.949774 | 1.873233 | 4.689422 | 7.846942 |
| 1000 | 0.005 | 4.989648 | 1.865838 | 4.671229 | 7.816475 |
| 1000 | 0.01 | 5.039795 | 1.856785 | 4.64953 | 7.780166 |
| 1000 | 0.05 | 5.451109 | 1.791132 | 4.509785 | 7.553285 |
| 1000 | 0.1 | 5.983379 | 1.722632 | 4.392538 | 7.381221 |
| 1000 | 0.2 | 7.081699 | 1.616151 | 4.254162 | 7.205836 |
| 1000 | 0.3 | 8.203702 | 1.535788 | 4.175835 | 7.119579 |
| 1000 | 0.4 | 9.338008 | 1.471977 | 4.125608 | 7.068809 |
| 1000 | 0.5 | 10.4795 | 1.419477 | 4.090703 | 7.035472 |
| 1000 | 0.6 | 11.62556 | 1.375141 | 4.065051 | 7.011937 |
| 1000 | 0.7 | 12.77469 | 1.336941 | 4.04541 | 6.994446 |
| 1000 | 0.8 | 13.926 | 1.303506 | 4.029891 | 6.980942 |
| 1000 | 0.9 | 15.07889 | 1.273864 | 4.017322 | 6.970202 |
| 1000 | 1 | 16.23298 | 1.247307 | 4.006934 | 6.961458 |
| 1000 | 2.5 | 33.59845 | 1.022628 | 3.945158 | 6.911804 |
| 1000 | 5 | 62.59006 | 0.869427 | 3.922164 | 6.894296 |
| 1000 | 7.5 | 91.592 | 0.788581 | 3.914201 | 6.888349 |
| 1000 | 10 | 120.597 | 0.735256 | 3.910161 | 6.885354 |
| 1000 | 100 | 1164.926 | 0.415624 | 3.899053 | 6.877198 |
| 10000 | 0.0001 | 4.940834 | 1.874917 | 4.693622 | 7.853973 |
| 10000 | 0.0005 | 4.944806 | 1.874168 | 4.691751 | 7.850847 |
| 10000 | 0.001 | 4.949774 | 1.873233 | 4.689424 | 7.846969 |
| 10000 | 0.005 | 4.989648 | 1.865838 | 4.671276 | 7.817091 |
| 10000 | 0.01 | 5.039798 | 1.856787 | 4.649707 | 7.782428 |
| 10000 | 0.05 | 5.451154 | 1.791167 | 4.51243 | 7.583295 |
| 10000 | 0.1 | 5.983498 | 1.722731 | 4.398835 | 7.444772 |
| 10000 | 0.2 | 7.081944 | 1.616375 | 4.265791 | 7.308254 |
| 10000 | 0.3 | 8.204032 | 1.536107 | 4.190705 | 7.241545 |
| 10000 | 0.4 | 9.338394 | 1.472365 | 4.142573 | 7.202176 |
| 10000 | 0.5 | 10.47993 | 1.419916 | 4.109115 | 7.176236 |
| 10000 | 0.6 | 11.62601 | 1.375616 | 4.084518 | 7.157866 |

Dataset (continued)

| $r_m$ | $r_m$ | Resonance voltage | $\lambda_1 L$ | $\lambda_2 L$ | $\lambda_3 L$ |
|---|---|---|---|---|---|
| 10000 | 0.7 | 12.77517 | 1.337444 | 4.065676 | 7.14418 |
| 10000 | 0.8 | 13.92648 | 1.304029 | 4.050784 | 7.133589 |
| 10000 | 0.9 | 15.07939 | 1.274402 | 4.038717 | 7.125152 |
| 10000 | 1 | 16.23349 | 1.247856 | 4.028742 | 7.118273 |
| 10000 | 2.5 | 33.599 | 1.023204 | 3.969354 | 7.079013 |
| 10000 | 5 | 62.59062 | 0.869962 | 3.947217 | 7.065083 |
| 10000 | 7.5 | 91.59256 | 0.789081 | 3.939545 | 7.060341 |
| 10000 | 10 | 120.5975 | 0.735729 | 3.935652 | 7.057951 |
| 10000 | 100 | 1164.927 | 0.415903 | 3.924945 | 7.051433 |
| 100000 | 0.0001 | 4.940834 | 1.874917 | 4.693622 | 7.853973 |
| 100000 | 0.0005 | 4.944806 | 1.874168 | 4.691751 | 7.850847 |
| 100000 | 0.001 | 4.949774 | 1.873233 | 4.689424 | 7.846971 |
| 100000 | 0.005 | 4.989648 | 1.865838 | 4.671281 | 7.817152 |
| 100000 | 0.01 | 5.039798 | 1.856787 | 4.649725 | 7.782647 |
| 100000 | 0.05 | 5.451158 | 1.79117 | 4.512691 | 7.586022 |
| 100000 | 0.1 | 5.98351 | 1.72274 | 4.399454 | 7.450435 |
| 100000 | 0.2 | 7.081969 | 1.616397 | 4.266935 | 7.317372 |
| 100000 | 0.3 | 8.204065 | 1.536139 | 4.192169 | 7.252462 |
| 100000 | 0.4 | 9.338433 | 1.472404 | 4.144245 | 7.214169 |
| 100000 | 0.5 | 10.47997 | 1.41996 | 4.110932 | 7.18894 |
| 100000 | 0.6 | 11.62606 | 1.375663 | 4.08644 | 7.171074 |
| 100000 | 0.7 | 12.77521 | 1.337494 | 4.067679 | 7.157762 |
| 100000 | 0.8 | 13.92653 | 1.304081 | 4.052849 | 7.147461 |
| 100000 | 0.9 | 15.07944 | 1.274456 | 4.040833 | 7.139254 |
| 100000 | 1 | 16.23354 | 1.247911 | 4.0309 | 7.132562 |
| 100000 | 2.5 | 33.59906 | 1.023261 | 3.971754 | 7.094364 |
| 100000 | 5 | 62.59068 | 0.870016 | 3.949704 | 7.080808 |
| 100000 | 7.5 | 91.59262 | 0.789131 | 3.942063 | 7.076192 |
| 100000 | 10 | 120.5976 | 0.735777 | 3.938185 | 7.073866 |
| 100000 | 100 | 1164.927 | 0.415931 | 3.927519 | 7.067521 |
| 1000000 | 0.0001 | 4.940834 | 1.874917 | 4.693622 | 7.853973 |
| 1000000 | 0.0005 | 4.944806 | 1.874168 | 4.691751 | 7.850847 |
| 1000000 | 0.001 | 4.949774 | 1.873233 | 4.689424 | 7.846972 |
| 1000000 | 0.005 | 4.989648 | 1.865838 | 4.671281 | 7.817158 |
| 1000000 | 0.01 | 5.039798 | 1.856787 | 4.649726 | 7.782669 |
| 1000000 | 0.05 | 5.451159 | 1.791171 | 4.512717 | 7.586292 |
| 1000000 | 0.1 | 5.983512 | 1.722741 | 4.399516 | 7.450995 |
| 1000000 | 0.2 | 7.081971 | 1.616399 | 4.267049 | 7.318273 |
| 1000000 | 0.3 | 8.204069 | 1.536143 | 4.192315 | 7.253541 |

Dataset (continued)

| $r_m$ | $r_m$ | Resonance voltage | $\lambda_1 L$ | $\lambda_2 L$ | $\lambda_3 L$ |
|---|---|---|---|---|---|
| 1000000 | 0.4 | 9.338437 | 1.472408 | 4.144412 | 7.215354 |
| 1000000 | 0.5 | 10.47998 | 1.419964 | 4.111113 | 7.190196 |
| 1000000 | 0.6 | 11.62606 | 1.375668 | 4.086632 | 7.17238 |
| 1000000 | 0.7 | 12.77522 | 1.337499 | 4.067879 | 7.159105 |
| 1000000 | 0.8 | 13.92654 | 1.304086 | 4.053055 | 7.148833 |
| 1000000 | 0.9 | 15.07944 | 1.274461 | 4.041044 | 7.140649 |
| 1000000 | 1 | 16.23354 | 1.247917 | 4.031115 | 7.133975 |
| 1000000 | 2.5 | 33.59906 | 1.023267 | 3.971994 | 7.095884 |
| 1000000 | 5 | 62.59068 | 0.870021 | 3.949953 | 7.082365 |
| 1000000 | 7.5 | 91.59262 | 0.789136 | 3.942314 | 7.077762 |
| 1000000 | 10 | 120.5976 | 0.735781 | 3.938438 | 7.075441 |
| 1000000 | 100 | 1164.927 | 0.415934 | 3.927776 | 7.069114 |

REFERENCES


[1] S. Priya and D. J. Inman, *Energy harvesting technologies*, vol. 21. Springer, 2009.

[2] Y. K. Tan and S. K. Panda, "Review of energy harvesting technologies for sustainable wireless sensor network," *Sustain. Wirel. Sens. networks*, pp. 15–43, 2010.

[3] Y. K. Tan, *Sustainable energy harvesting technologies: Past, present and future*. BoD–Books on Demand, 2011.

[4] J. J. Roh, A. Kunnathur, and M. Tarafdar, "Classification of RFID adoption: An expected benefits approach," *Inf. Manag.*, vol. 46, no. 6, pp. 357–363, 2009.

[5] Z. Q. Phua, "Target Read Operation of Passive Ultra High Frequency RFID Tag in a Multiple Tags Environment," 2017.

[6] Z. Yi, Z. Q. Phua, V. NB Rangel, and J. M. Parker, "Experimental Investigation on Tags Placement Affecting the Efficient Encoding of Multiple Passive UHF RFID Tags With Unique Identifiers," 2016.

[7] A. M. Whitney, "Indoor-wireless Location Techniques and Algorithms Utilizing UHF RFID and BLE Technologies," 2019.

[8] E. W. T. Ngai, K. K. L. Moon, F. J. Riggins, and Y. Y. Candace, "RFID research: An academic literature review (1995–2005) and future research directions," *Int. J. Prod. Econ.*, vol. 112, no. 2, pp. 510–520, 2008.

[9] X. Qing and Z. N. Chen, "Proximity effects of metallic environments on high frequency RFID reader antenna: Study and applications," *IEEE Trans. Antennas Propag.*, vol. 55, no. 11, pp. 3105–3111, 2007.

[10] M. Safaei, H. A. Sodano, and S. R. Anton, "A review of energy harvesting using piezoelectric materials: state-of-the-art a decade later (2008–2018)," *Smart Mater. Struct.*, vol. 28, no. 11, p. 113001, 2019.

[11] J. Chen *et al.*, "Networks of triboelectric nanogenerators for harvesting water wave energy: a potential approach toward blue energy," *ACS Nano*, vol. 9, no. 3, pp. 3324–3331, 2015.

[12] M. Q. Le *et al.*, "Review on energy harvesting for structural health monitoring in aeronautical applications," *Prog. Aerosp. Sci.*, vol. 79, pp. 147–157, 2015.

[13] K. Tao *et al.*, "Piezoelectric ZnO thin films for 2DOF MEMS vibrational energy harvesting," *Surf. Coatings Technol.*, vol. 359, pp. 289–295, 2019.

[14] A. Erturk, "Piezoelectric energy harvesting for civil infrastructure system applications: Moving loads and surface strain fluctuations," *J. Intell. Mater. Syst. Struct.*, vol. 22, no. 17, pp. 1959–1973, 2011.

[15] Z.-W. Fang, Y.-W. Zhang, X. Li, H. Ding, and L.-Q. Chen, "Integration of a nonlinear energy sink and a giant magnetostrictive energy harvester," *J. Sound Vib.*, vol. 391, pp. 35–49, 2017.

[16] M. K. Stojčev, M. R. Kosanović, and L. R. Golubović, "Power management and energy harvesting techniques for wireless sensor nodes," in *2009 9th International Conference on Telecommunication in Modern Satellite, Cable, and Broadcasting Services*, 2009, pp. 65–72.

[17] S. F. Ali, M. I. Friswell, and S. Adhikari, "Analysis of energy harvesters for highway bridges," *J. Intell. Mater. Syst. Struct.*, vol. 22, no. 16, pp. 1929–1938, 2011.

[18] Y. Qi, N. T. Jafferis, K. Lyons Jr, C. M. Lee, H. Ahmad, and M. C. McAlpine,

"Piezoelectric ribbons printed onto rubber for flexible energy conversion," *Nano Lett.*, vol. 10, no. 2, pp. 524–528, 2010.

[19] Y. Zhang, T. Wang, A. Luo, Y. Hu, X. Li, and F. Wang, "Micro electrostatic energy harvester with both broad bandwidth and high normalized power density," *Appl. Energy*, vol. 212, pp. 362–371, 2018.

[20] C. W. Lim, G. Zhang, and J. N. Reddy, "A higher-order nonlocal elasticity and strain gradient theory and its applications in wave propagation," *J. Mech. Phys. Solids*, vol. 78, pp. 298–313, 2015.

[21] A. Babaei, A. %J M. of A. M. Rahmani, and Structures, "On dynamic-vibration analysis of temperature-dependent Timoshenko microbeam possessing mutable nonclassical length scale parameter," pp. 1–8, 2018.

[22] A. Babaei, A. Rahmani, and I. %J A. of M. E. Ahmadi, "Transverse vibration analysis of nonlocal beams with various slenderness ratios, undergoing thermal stress," vol. 66, no. 1, pp. 5–24, 2019.

[23] A. Rahmani, A. Babaei, and S. Faroughi, "Vibration characteristics of functionally graded micro-beam carrying an attached mass," *Mech. Adv. Compos. Struct.*, 2019.

[24] M. Song, Y. Gong, J. Yang, W. Zhu, and S. Kitipornchai, "Nonlinear free vibration of cracked functionally graded graphene platelet-reinforced nanocomposite beams in thermal environments," *J. Sound Vib.*, vol. 468, p. 115115, 2020.

[25] A. Babaei and C. X. Yang, "Vibration analysis of rotating rods based on the nonlocal elasticity theory and coupled displacement field," *Microsyst. Technol.*, vol. 25, no. 3, pp. 1077–1085, 2019.

[26] A. Babaei and A. Rahmani, "Vibration analysis of rotating thermally-stressed gyroscope, based on modified coupled displacement field method," *Mech. Based Des. Struct. Mach.*, pp. 1–10, 2020.

[27] A. Mahi, E. A. A. Bedia, A. Tounsi, and I. Mechab, "An analytical method for temperature-dependent free vibration analysis of functionally graded beams with general boundary conditions," *Compos. Struct.*, vol. 92, no. 8, pp. 1877–1887, 2010.

[28] Y. S. Touloukian, "Thermophysical Properties of High Temperature Solid Materials. Volume 5. Nonoxides and their Solutions and Mixtures, Including Miscellaneous Ceramic Materials," Thermophysical and Electronic Properties Information Analysis Center Lafayette, 1966.

[29] B. Akgöz and Ö. Civalek, "Vibrational characteristics of embedded microbeams lying on a two-parameter elastic foundation in thermal environment," *Compos. Part B Eng.*, 2018.

[30] H. Shafiei and A. R. Setoodeh, "An analytical study on the nonlinear forced vibration of functionally graded carbon nanotube-reinforced composite beams on nonlinear viscoelastic foundation," *Arch. Mech.*, vol. 72, no. 2, pp. 81–107, 2020.

[31] A. A. P. Zanoosi, "Size-dependent thermo-mechanical free vibration analysis of functionally graded porous microbeams based on modified strain gradient theory," *J. Brazilian Soc. Mech. Sci. Eng.*, vol. 42, no. 5, 2020.

[32] H.-C. Li, L.-L. Ke, J. Yang, S. Kitipornchai, and Y.-S. Wang, "Free vibration of variable thickness FGM beam submerged in fluid," *Compos. Struct.*, vol. 233, p. 111582, 2020.

[33] A. Babaei, M.-R. S. Noorani, and A. %J M. technologies Ghanbari, "Temperature-dependent free vibration analysis of functionally graded micro-beams based on the

modified couple stress theory," vol. 23, no. 10, pp. 4599–4610, 2017.
[34] A. %J S. N. A. S. Babaei, "Longitudinal vibration responses of axially functionally graded optimized MEMS gyroscope using Rayleigh–Ritz method, determination of discernible patterns and chaotic regimes," vol. 1, no. 8, p. 831, 2019.
[35] A. Erturk and D. J. Inman, "A distributed parameter electromechanical model for cantilevered piezoelectric energy harvesters," *J. Vib. Acoust.*, vol. 130, no. 4, 2008.
[36] W.-J. Su, J.-H. Lin, and W.-C. Li, "Analysis of a Cantilevered Piezoelectric Energy Harvester in Different Orientations for Rotational Motion," *Sensors*, vol. 20, no. 4, p. 1206, 2020.
[37] M. Rezaei, R. Talebitooti, and S. Rahmanian, "Efficient energy harvesting from nonlinear vibrations of PZT beam under simultaneous resonances," *Energy*, vol. 182, pp. 369–380, 2019.
[38] K. Fan, Q. Tan, H. Liu, Y. Zhang, and M. Cai, "Improved energy harvesting from low-frequency small vibrations through a monostable piezoelectric energy harvester," *Mech. Syst. Signal Process.*, vol. 117, pp. 594–608, 2019.
[39] M. L. Dehsaraji, M. Arefi, and A. Loghman, "Size dependent free vibration analysis of functionally graded piezoelectric micro/nano shell based on modified couple stress theory with considering thickness stretching effect," *Def. Technol.*, 2020.
[40] Z. Tadi Beni, S. A. Hosseini Ravandi, and Y. Tadi Beni, "Size-dependent nonlinear forced vibration analysis of viscoelastic/piezoelectric nano-beam," *J. Appl. Comput. Mech.*, 2020.
[41] D. Tan, A. K. Kemenov, and A. Erturk, "Nonlinearities in resonant dynamics of piezoelectric macro-fiber composite cantilevers," in *Active and Passive Smart Structures and Integrated Systems XIII*, 2019, vol. 10967, p. 109670I.
[42] S. Zhou, J. Cao, D. J. Inman, J. Lin, and D. Li, "Harmonic balance analysis of nonlinear tristable energy harvesters for performance enhancement," *J. Sound Vib.*, vol. 373, pp. 223–235, 2016.
[43] F. C. Bolat, S. Basaran, and S. Sivrioglu, "Piezoelectric and electromagnetic hybrid energy harvesting with low-frequency vibrations of an aerodynamic profile under the air effect," *Mech. Syst. Signal Process.*, vol. 133, p. 106246, 2019.
[44] N. G. Stephen, "On energy harvesting from ambient vibration," *J. Sound Vib.*, vol. 293, no. 1–2, pp. 409–425, 2006.
[45] J. M. Renno, M. F. Daqaq, and D. J. Inman, "On the optimal energy harvesting from a vibration source," *J. Sound Vib.*, vol. 320, no. 1–2, pp. 386–405, 2009.
[46] A. Erturk and D. J. Inman, "On mechanical modeling of cantilevered piezoelectric vibration energy harvesters," *J. Intell. Mater. Syst. Struct.*, vol. 19, no. 11, pp. 1311–1325, 2008.
[47] A. Erturk and D. J. Inman, "An experimentally validated bimorph cantilever model for piezoelectric energy harvesting from base excitations," *Smart Mater. Struct.*, vol. 18, no. 2, p. 25009, 2009.
[48] P. Asthana, A. Dwivedi, and G. Khanna, "Finite Element Modeling of a Wideband Piezoelectric Energy Harvester for Ambient Vibration Extraction," in *Advances in VLSI, Communication, and Signal Processing*, Springer, 2020, pp. 549–556.
[49] M. Heshmati and Y. Amini, "A comprehensive study on the functionally graded piezoelectric energy harvesting from vibrations of a graded beam under travelling multi-oscillators," *Appl. Math. Model.*, vol. 66, pp. 344–361, 2019.

[50] H. Fu and E. M. Yeatman, "Rotational energy harvesting using bi-stability and frequency up-conversion for low-power sensing applications: Theoretical modelling and experimental validation," *Mech. Syst. Signal Process.*, vol. 125, pp. 229–244, 2019.

[51] L. Tang and J. Wang, "Modeling and analysis of cantilever piezoelectric energy harvester with a new-type dynamic magnifier," *Acta Mech.*, vol. 229, no. 11, pp. 4643–4662, 2018.

[52] L. Tang and J. Wang, "Size effect of tip mass on performance of cantilevered piezoelectric energy harvester with a dynamic magnifier," *Acta Mech.*, vol. 228, no. 11, pp. 3997–4015, 2017.

[53] A. Aladwani, O. Aldraihem, and A. Baz, "A distributed parameter cantilevered piezoelectric energy harvester with a dynamic magnifier," *Mech. Adv. Mater. Struct.*, vol. 21, no. 7, pp. 566–578, 2014.

[54] A. Aladwani, M. Arafa, O. Aldraihem, and A. Baz, "Cantilevered piezoelectric energy harvester with a dynamic magnifier," *J. Vib. Acoust.*, vol. 134, no. 3, 2012.

[55] X. Zhang, M. Zuo, W. Yang, and X. Wan, "A Tri-Stable Piezoelectric Vibration Energy Harvester for Composite Shape Beam: Nonlinear Modeling and Analysis," *Sensors*, vol. 20, no. 5, p. 1370, 2020.

[56] S. Roundy and P. K. Wright, "A piezoelectric vibration based generator for wireless electronics," *Smart Mater. Struct.*, vol. 13, no. 5, p. 1131, 2004.

[57] A. Babaei, "Forced vibration analysis of non-local strain gradient rod subjected to harmonic excitations," *Microsyst. Technol.*, pp. 1–11, 2020.

[58] A. Babaei, "Forced vibrations of size-dependent rods subjected to: impulse, step, and ramp excitations," *Arch. Appl. Mech.*, 2021, doi: 10.1007/s00419-020-01878-x.

[59] R. Naseer, H. Dai, A. Abdelkefi, and L. Wang, "Comparative Study of Piezoelectric Vortex-Induced Vibration-Based Energy Harvesters with Multi-Stability Characteristics," *Energies*, vol. 13, no. 1, p. 71, 2020.

[60] P. Asthana and G. Khanna, "Development of Vibration Piezoelectric Harvesters by the Optimum Design of Cantilever Structures," in *Nanogenerators*, IntechOpen, 2020.

[61] K. Moon, J. Choe, H. Kim, D. Ahn, and J. Jeong, "A method of broadening the bandwidth by tuning the proof mass in a piezoelectric energy harvesting cantilever," *Sensors Actuators, A Phys.*, vol. 276, 2018, doi: 10.1016/j.sna.2018.04.004.

[62] E. Dechant, F. Fedulov, L. Y. Fetisov, and M. Shamonin, "Bandwidth widening of piezoelectric cantilever beam arrays by mass-tip tuning for low-frequency vibration energy harvesting," *Appl. Sci.*, vol. 7, no. 12, 2017, doi: 10.3390/app7121324.

[63] Y. Jia and A. A. Seshia, "Power Optimization by Mass Tuning for MEMS Piezoelectric Cantilever Vibration Energy Harvesting," *J. Microelectromechanical Syst.*, vol. 25, no. 1, 2016, doi: 10.1109/JMEMS.2015.2496346.

[64] L. G. H. Staaf, A. D. Smith, P. Lundgren, P. D. Folkow, and P. Enoksson, "Effective piezoelectric energy harvesting with bandwidth enhancement by assymetry augmented self-tuning of conjoined cantilevers," *Int. J. Mech. Sci.*, vol. 150, 2019, doi: 10.1016/j.ijmecsci.2018.09.050.

[65] H. Zhao, X. Wei, Y. Zhong, and P. Wang, "A direction self-tuning two-dimensional piezoelectric vibration energy harvester," *Sensors (Switzerland)*, vol. 20, no. 1, 2020, doi: 10.3390/s20010077.

[66] X. Mei, S. Zhou, Z. Yang, T. Kaizuka, and K. Nakano, "A passively self-tuning nonlinear energy harvester in rotational motion: theoretical and experimental investigation," *Smart Mater. Struct.*, vol. 29, no. 4, 2020, doi: 10.1088/1361-665X/ab78b2.

[67] ITU, "ITU Internet report 2005: The internet of things," *ITU Internet Rep. 2005*, 2005.

[68] Y. Khan, "5 Essential Components of an IoT Ecosystem," *G2.com*, 2020. .

[69] T. Sanislav, G. D. Mois, S. Zeadally, and S. C. Folea, "Energy Harvesting Techniques for Internet of Things (IoT)," *IEEE Access*, vol. 9, 2021, doi: 10.1109/ACCESS.2021.3064066.

[70] P. Kamalinejad, C. Mahapatra, Z. Sheng, S. Mirabbasi, V. C. M. Leung, and Y. L. Guan, "Wireless energy harvesting for the Internet of Things," *IEEE Commun. Mag.*, vol. 53, no. 6, pp. 102–108, 2015.

[71] M. Kocakulak and I. Butun, "An overview of Wireless Sensor Networks towards internet of things," in *2017 IEEE 7th Annual Computing and Communication Workshop and Conference (CCWC)*, 2017, pp. 1–6.

[72] H. Akinaga, "Recent advances and future prospects in energy harvesting technologies," *Japanese Journal of Applied Physics*, vol. 59, no. 11. 2020, doi: 10.35848/1347-4065/abbfa0.

[73] G. Dan Moiş, T. Sanislav, S. C. Folea, and S. Zeadally, "Performance evaluation of energy-autonomous sensors using power-harvesting beacons for environmental monitoring in internet of things (IoT)," *Sensors (Switzerland)*, vol. 18, no. 6, 2018, doi: 10.3390/s18061709.

[74] T. D. Nguyen, J. Y. Khan, and D. T. Ngo, "An effective energy-harvesting-aware routing algorithm for WSN-based IoT applications," in *2017 IEEE International Conference on Communications (ICC)*, 2017, pp. 1–6.

[75] F. Yang, A. C. M. Chong, D. C. C. Lam, and P. Tong, "Couple stress based strain gradient theory for elasticity," *Int. J. Solids Struct.*, vol. 39, no. 10, pp. 2731–2743, 2002.

VITA

# Alireza Babaei

## Education

| | |
|---|---|
| **University of Kentucky:** Ph.D. Mechanical Engineering, Dissertation: Mechanical Energy Harvester for Powering RFID Systems Components: Modeling, Analysis, Optimization, and Design | **Anticipated May 2023** |
| **University of Tabriz:** M.Sc. Mechanical Engineering, Thesis: Modeling and Analysis of Micro-Electro-Mechanical-Systems (MEMS) | **Aug 2015** |
| **Zanjan University:** B.Sc. Mechanical Engineering, Thesis: Introduction to MEMS and Vibration Analysis of Cantilever with Attached Mass | **Aug 2013** |